UNIVERSITÉ DE STRASBOURG

UNIVERSITÉ DE STRASBOURG

ÉCOLE DOCTORALE de Physique et Chimie-Physique (ED182)

Institut de Physique et Chimie des Matériaux de Strasbourg

(UMR 7504 CNRS – Unistra)

THÈSE présentée par :
Paula DUEÑAS RAMÍREZ

Soutenance prévue le : **12 novembre 2020**

pour obtenir le grade de : **Docteur de l'université de Strasbourg**

Discipline/ Spécialité : Chimie-physique des matériaux

Ingénierie de nanocomposites recyclables pour l'élimination de polluants

THÈSE dirigée par :

Mme Bégin-Colin Sylvie	Professeur, IPCMS, ECPM, Université de Strasbourg
M Mertz Damien	Chargé de recherche, IPCMS, Université de Strasbourg

RAPPORTEURS :

M Durand Jean-Olivier	Directeur de recherche, Université de Montpellier
M Delpech Fabien	Professeur, Université de Toulouse

EXAMINATEURS :

Mme Hubscher Véronique	Professeur, IPHC, ECPM, Université de Strasbourg
Mme Alem-Marchand Halima	Maître de conférences, Université de Lorraine

A mi investigador y melómano favorito:

Mi papá

Remerciements

Tout au long de ma thèse, on m'a dit qu'il fallait raconter une histoire pour présenter mes projets, et c'est ce que j'ai essayé de faire pour ce manuscrit et les présentations. Cependant, ces histoires n'ont pas pu être racontées sans les nombreuses personnes qui ont participés.

Pour vivre une histoire, il faut un lieu. C'est pourquoi je veux remercier profondément à Nathalie Viart et Pierre Rabu de m'avoir accueillie au sein du Département de Chimie de Matériaux Inorganiques et de l'Institut de Physique et Chimie des Matériaux de Strasbourg pendant ces 3-4 ans.

Je veux remercier mon jury de thèse : Mme Véronique Hubscher, M. Jean-Olivier Durand, M. Fabien Delpech et Mme. Halima Alim-Marchand d'avoir accepté d'y participer, de lire le manuscrit et d'avoir essayé de rendre ma soutenance « la plus normale » possible, malgré la crise sanitaire.

The master minds de cette histoire étaient mes directeurs de thèse : Sylvie Bégin-Colin et Damien Mertz. Merci de m'avoir fait confiance pour ce projet, de m'avoir permis de rencontre d'autres cultures, d'être plus que mes encadrants… Un support et d'avoir su mes donner des mots de réconfort quand j'en ai eu besoin. Je ne pourrai jamais vous remercier assez. Sylvie, merci de m'avoir appris énormément des choses dans le plan scientifique, de me motiver à être meilleure, d'avoir toujours eu du temps pour moi et de m'avoir aidé à trouver/voir mes points forts. Enormément de choses me sont arrivées pendant la thèse, mais tu as toujours été là pour me soutenir. Damien, merci pour ta patience, ton aide, ton temps, tout ce que tu m'as appris et les discussions de séries-musique-bébés qui me seront toujours très précieuses. Je pense que meilleurs directeurs de thèse je n'aurais pas pu avoir.

Pour écrire cette histoire, j'ai eu la chance aussi de travailler avec Anne Carton, qui est devenue une amie et qui m'a donnée l'opportunité de travailler dans son laboratoire et grâce à qui, ces travaux ont été réalisés. Tout ceci, tu l'as fait en parallèle d'une aventure plus importante : être maman de deux petits anges.

Je tiens à remercier aussi à Benoit Pichon qui a été aussi une aide précieuse lors de ces travaux grâce à ses connaissances et sa bonne humeur. Merci aussi à Céline Kiefer qui m'a énormément facilité la vie dans le labo avec toute son aide et qui est un pilier très important pour le bon fonctionnement du labo.

Merci à tous les permanents du DCMI qui ont toujours été disponibles pour répondre à mes questions sur les différents appareils, techniques, phénomènes (avec une touche de bonne humeur à chaque fois): Guillaume Rogez, François Roulland, Daniele Preziosi, Marc Lenertz, Nathalie Viart, Silviu Colis et Christophe Lefèvre. La plupart ont été mes professeurs en école d'ingénieurs, qui me connaissent depuis quelques années et avec qui j'ai eu la chance de partager des moments autour d'un café. Merci d'avoir été là pour participer à ma formation et m'aider à forger mon avenir professionnel.

Cette aventure a été possible avec le travail de Catherine Bonin, Sylvie Maingé, Ratibe Aksoz, Isabelle Kitzinger, José-Francis Radmacher et le service informatique. Grâce à vous tous de m'avoir beaucoup facilité les démarches administratives. Sylvie, je te souhaite une belle retraite !!

Eu sou muito grato a Pr. Maria Soler (et mon portugais si limité s'arrête ici) de m'avoir accueillie dans son laboratoire à l'université de Brasilia. Merci à Isis, Pedro et Hermano de m'avoir « promené » dans la ville et partagé leur culture, grâce à vous, j'ai appris à aimer cette ville si particulière.

Quiero también agradecerle a mi familia: mis tías, tíos, primas, primos, abuelitas y abuelitos, por haberme siempre apoyado y echado porras desde… pues desde que saben que existo☺. Merci à la famille de mon chéri, qui m'a adoptée et encouragé à distance. Un gracias infinito a mis papás, Pablo y Silvia, y a mi hermana, Diana, por siempre darme ánimos incluso cuando empezaba a dudar de mí misma, por la ayuda que siempre me han aportado y por enseñarme que el amor incondicional no conoce distancia. Somos un equipo y siempre lo seremos, este logro va especialmente dedicado para ustedes.

Gracias a Lima por haber aceptado que yo redacte la mayoría de esta tesis en su espacio vital y mostrarme que solo necesitaba de una mano para escribir, l'autre était pour l'utiliser comme oreiller lors de la n-ième sieste de la journée.

En tout dernier, je veux remercier du fond de mon cœur à mon chéri, Kevin Sartori, pour m'avoir supportée pendant ce temps, de m'avoir aidé pendant la rédaction et d'avoir survécu au Paula-Kraken. Maintenant, nous pouvons mettre « docteurs » sur la boîte à lettres ☺.

Abbreviations

AHMPD	2-amino-2-hydroxymethyl-1,3-propanediol
Al-RSN	Aluminum doped raspberry-shaped nanostructures
APD	Automatic peritoneal dialysis
APTES	3-aminopropyltriethoxysilane
BSA^{FITC}	Bovine serum albumin (BSA) labeled with fluorescein isothiocyanate (FITC)
C$_{221}$ or C221	Cryptand [2.2.1.]
CE	4-carboxybenzo-15-crown-5
CRF	Chronical renal failure
CTAB	Cetyltrimethylammonium bromide
CTAC	Cetyltrimethylammonium chloride
CTATos	Cetyltrimethylammonium tosylate
DFoB	Desferrioxamine b / deferoxamine b
DLS	Dynamic light scattering
DMF	N,n-dimethylformamide
EDC	1-ethyl-3-(3-dimethylaminopropyl)carbodiimide hydrochloride
EDTA	Ethylenediaminetetracetic acid
EG	Ethylene glycol
ESRF	End-stage renal failure
FLG	Few layer graphene
FTIR	Fourier Transform InfraRed spectroscopy
HBTU	N,N,N',N'-Tetramethyl-O-(1H-benzotriazol-1-yl)uronium hexafluorophosphate
HD	Hemodialysis
HEPES	4-(2-hydroxyethyl)-1-piperazineethanesulfonic acid
HRTEM	High-resolution transmission electron microscopy
IEP	Isoelectric point
IO	Iron oxide
MWCO	Molecular weights cut off
NC	Nanoclusters
NHS	N-hydroxysuccinimide
NPs	Nanoparticles
NTA	Nitroacetic acid
PAH	Polycyclic aromatic hydrocarbon
PD	Peritoneal dialysis
PDA	Polydopamine
PEI	Polyethyleneimine
PLS	Plate-like lamellar structures
RSN	Raspberry-shaped nanostructures
SA	Succinic acid (chapter IV)
SA	Succinic anhydride (chapter II)
SEM	Scattering electron microscope
STMS	Stellate mesoporous silica nanoparticles
TA	Tannic acid
TEM	Transmission electron microscope
TEOS	Tetraethyl orthosilicate
TGA	Thermal gravimetric analysis
TMOPES	Trimethoxy(2-phenylethyl)silane
XRD	X-ray diffraction
ZP	Zeta potential

General Introduction

Chapter I : Bibliographical Research

Chapter II : Highly chelating stellate mesoporous silica nanoparticles for specific iron removal from biological media

Chapter III : Grafting of crown-ether and cryptand on stellate mesoporous silica for efficient and selective sodium cation purification

Chapter IV : Investigation of phosphate capture enhancement in peritoneal dialysis process using designed iron oxide nanostructures

Chapter V : Depollution perspectives

Résumé en français

General introduction

Silica and iron oxide nanomaterials are widely developed for purification treatments of water, air, and soils. On the one hand, mesoporous silica (MS) nanoparticles are considered as one of the most versatile and successful adsorbents for the removal of environmental pollutants because of their large specific surface area, their low cost-effective synthesis and their easiness of functionalization. On the other hand, iron oxide nanoparticles display magnetic properties and show interesting surface properties with a high affinity for some impurity elements and high functionalization possibilities, making them a nanomaterial of choice to purify media from pollutants. In particular, they may be easily removed from polluted media using a magnet.

However, besides the depollution of soils, oceans and rivers, the "decontamination" of human organisms is also a big challenge for the 21th century and may benefit from advances in depollution methods developed for water and soils. Indeed, some purification problems also exist in medicine and iron oxide and silica nanomaterials could also contribute to the improvement of purification treatments of blood. In that context, we have considered two important health problems: the hemochromatosis due to an iron excess in blood and the kidney failure leading to an excess of toxic elements in the blood.

The hemochromatosis is a genetic illness. Herein, the organism cannot naturally regulate **iron** levels. The iron excess is stocked in the different organs leading to their dysfunction (e.g. cirrhosis, hepatic problems). The current treatment of chelatotherapy presents many side-effects due to the short circulation time of the drugs in the body. Thus, well-designed bionanomaterials could improve this treatment by increasing the circulation time of the chelators.

The kidney failure consists of the dysfunction of at least one kidney. The immediate consequence is that the blood stops to be purified which leads to an accumulation of toxins up to the standard levels. Hemodialysis and peritoneal dialysis are purification treatments, which help at removing very harmful elements from blood such as <u>sodium and phosphate.</u>

Hemodialysis consists of purifying the blood in an extracorporeal route where blood is cleaned thanks to a dialysis machine. During peritoneal dialysis treatment, a designed dialysis solution is introduced into the peritoneal cavity of the patient and for a few hours, the composition of the liquid is balanced with that of the blood compartment. By diffusion and convection mechanisms through the capillaries, toxins and water excesses pass into the dialysate. The dialysate is then drained outside the body before the subsequent provision of new dialysis fluid.

Hemodialysis session lasts from 3 to 5 hours, during which the patient cannot move. At least, three sessions per week are necessary to allow an effective purification. By contrast, the peritoneal dialysis possesses several economic advantages, is more comfortable for patients and is required for children and new-born babies. However, it is less efficient by comparison with hemodialysis. There is therefore a great interest in being able to enhance the peritoneal dialysis efficiency and one solution could be, as for depollution of polluted media, to introduce nanomaterials in the dialysis solutions, which will enhance the sodium and phosphate uptakes.

To improve those treatments, we suggest testing i) mesoporous silica (MS) nanoparticles functionalized with designed and highly specific ligands to improve iron and sodium purifications and ii) iron oxide nanomaterials for phosphate capture.

Indeed, several groups already used functionalized mesoporous silica surfaces to remove heavy metals from water. For example, thiol molecules were used to functionalize silica surface and remove metals such as mercury, cadmium or lead. Molecules containing amine groups are also used to functionalize silica and capture hazardous pollutants: Polyethylenimine was used to uptake cadmium and nickel and aminopropyl group could remove chrome, arsenic, mercury, nickel, cadmium, and lead. All these works show that mesoporous silica adequately functionalized is a well-adapted nano-object to remove metals from liquid media. However, one challenge is the design of ligands able to specifically chelate iron and sodium cations. For hemochromatosis, one successful medical treatment described so far is the chelation therapy with **desferrioxamine B (DFoB).** In this frame, one objective of this PhD work is to graft DFoB at the surface of the MS in order to enhance its chelation capacity.

In the case of sodium purification, we faced the problem to find specific ligand compatible with biological applications. We have selected two different ligands: **crown-ether** and then **cryptand,** which have been reported to have high affinity with sodium in different media.

Among mesoporous silica materials, we chose to synthesize **stellate-shaped mesoporous silica** which displayed high pore sizes, suitable for ensuring a high chelating ligand grafting rate.

For **phosphate** extraction, we chose **iron oxide nanoparticles**. Indeed, iron oxide particles have been widely developed to remove phosphates from polluted media and appear as very suitable compounds to face the challenge to enhance the phosphate removal using peritoneal dialysis. Among iron oxide nanoparticles, we selected iron oxide raspberry-shaped nanostructures, which consist in oriented aggregates/nanoclusters of iron oxide nanograins with a mean diameter ranging from 50 to 500 nm. They display a rather "big size" ensuring that they will not cross the peritoneal membrane. Secondly, they possess interesting magnetic properties, which makes them easy to recover with a magnet from dialysate and thus they may be recycled. Indeed, an earlier study using iron oxide nanoparticles of 40 nm demonstrated that it was possible by adjusting pH to recycle iron oxide nanoparticles and the performance was maintained after several cycles. In addition, these nanostructures are synthesized by a modified polyol-solvothermal process which allow producing large amount of powders

In this context, the objective of my PhD work is to develop new functional materials highly efficient and, if possible, recyclable for iron, phosphate and sodium removal from biological media (blood). Magnetic iron oxide particles will be designed for phosphate removal while mesoporous silica will be coated with designed chelating ligands for iron and sodium removal.

The first chapter (bibliographic part) describes the hematochromatosis and the peritoneal dialysis tratments as well as the current challenges. Then, the nano-objects that will be used to face these challenges are described. They consist in mesoporous silica coated with chelating ligands and magnetic raspberry-shaped iron oxide nanostructures.

The second chapter is centred on the elaboration of stellate mesoporous silica particles grafted with desferrioxamine to treat hematochromatosis. This material was designed to address purification issues encountered with the uptake of **iron** excess in the body.

The third chapter is dedicated to the improvement of **sodium** extraction by peritoneal dialysis. The previous stellate mesoporous silica particles were grafted with molecules carrying chelating sodium functions (crown-ether and cryptand).

The fourth chapter deals with the design of magnetic iron oxide nanostructures for **phosphate** uptake in peritoneal dialysis. Their synthesis and doping by Al, Co and Zn have been optimized and their capacity to capture phosphate has been evaluated.

Finally, the last chapter presents preliminary experiments that were realized in order to test our nano-object for pollutant removal from water and liquid media. In the first part of the chapter, we have investigated the coating of magnetic iron oxide raspberry shaped particles with mesoporous silica. Here the goal was to combine the high specific surface area and the surface properties of mesoporous silica with the magnetic properties of particles to be able to handle them magnetically. The second part of this chapter consists in the grafting, at the surface of mesoporous silica and iron oxide nanostructures of molecules designed to capture **polycyclic aromatic hydrocarbons** (PAHs). Such materials could contribute to extract PAHs from water and air.

Chapter I
Bibliographical Research

I. Element purification in hematochromatosis disease and emergence of nanoparticles as a treatment

Among metallic pollutants, iron, even if less toxic than heavy metals, is a common constituent of groundwater and may induce taste and other nuisances (discoloration, staining, deposition in distribution systems….).[1] Another major problem with iron is overload in the body which induces strong health problems. In fact, every living organism feeds on iron, this metal being an essential micronutrient for oxygen transport under the hemoglobin form. Furthermore, iron takes part in several metabolic processes such as DNA reparation.[2] Naturally, living organisms tightly regulate the homeostatic level of iron, but due to genetic dysregulations, iron overload can thus occur. Some examples, well-known by doctors, are linked to genetic illness, in the case of hemochromatosis, the production of proteins like hepcidine and hemoglobin are no more controlled and this leads to dysregulation of iron homeostasis storage problems.[3] Acute iron poisoning[4] or medical treatments (e.g. iron supplementation) in diseases such as β-thalassemia[5] can also lead to an iron overload status.

I. 1. Actual medical treatments and desferrioxamine B

To rescue this iron regulation machinery, **one successful medical treatment described so far is the chelation therapy with desferrioxamine B (DFoB)**, a low-molecular weight molecule, engineered by microorganisms to ensure iron (III) uptake. Excreted to their direct environment, those molecules, also termed siderophores, firmly bind ferric ions, and deliver this nutrient to the microorganisms via specific membrane receptors and transport proteins. DFoB, a representative member of this class of siderophores, is a natural linear trihydroxamate-based binder excreted by the bacteria *Streptomyces pilosus* that is known to display a high affinity for Fe^{3+} [6,7] (log $K_{Fe(III)DFoB}$ = 30; pFe = 26.5, with pFe = -log[Fe]$_{free}$ for [Fe]$_0$ = 10^{-6} M and [DFoB]$_0$ = 10^{-5} M at pH 7.4[8,9]. Due to this property, DFoB is very selective for Fe^{3+} as compared to others metal ions of biological interest: Cu^{2+} (log K_{CuDFoB} = 14.1; pCu = 11.2)[10], Zn^{2+} (log K_{ZnDFoB} = 10.1; pZn = 6.6)[11], Ni^{2+} (log K_{NiDFoB} = 10.9)[10] or Al^{3+} (log K_{AlDFoB} = 24.5)[9]. However, DFoB used in its free form in chelation therapy (i.e., administered by blood transfusion) often presents several side effects in patients (e.g., infections and respiratory or gastrointestinal problems) and a low time in the circulation system.[12] A first strategy designed, to avoid several of them, consisted on substituting DFoB by other drugs such as deferiprone[12] or deferasirox[13] that are administered orally. However, these treatments are equally, if not less, effective and still presents several side effects.
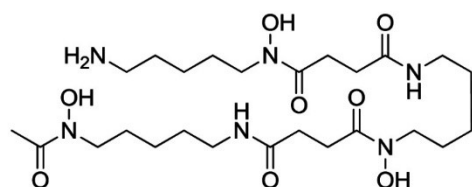
Scheme 1. Desferroxamine molecules (DFoB)

I. 2. Iron chelators supported on micro and nanomaterials

Very few works have been reported on iron chelators fixed on a support. For instance, Liu *et al.*[14] described polymeric nanoparticles functionalized with DFoB for iron uptake in the frame of an Alzheimer treatment. Other groups, such as Farjadian *et al.*[15], investigated the iron capture by a silica support to treat iron overload in children using EDTA binder ligand. Indeed, the use of functionalized nanoparticles (NPs) for pollutant removal applications in biological environments has emerged recently as an important research topic.[16,17] These last years, there were several studies that reported the ability of organic and inorganic nanomaterials to ensure the removal of molecules or ions from different biological media. For example, Pratsinis *et al.*[18] reported on liposomes used to depollute ammonia from mice. Due to the delicate design and also a lower robustness of organic nanomaterials such as liposomes, researches have mainly focused on inorganic NPs.[19–24]

Among all these potential nanomaterials, mesoporous silica (MS) are particularly attractive and are considered as one of the most versatile and successful adsorbents for the removal of environmental pollutants in recent years.[25] Due to their large specific surface area (*ca.* 500 m²/g), their cost-effective synthesis and the easiness of functionalization, these materials –functionalized or not– were applied as adsorbents or catalyst supports, but also for medical treatments as drug delivery vehicle.[26–28] Regarding the toxicity aspects, even if several questions remain about their long-term retention because of their slow biodegradability, they were approved by the FDA (Food and Drug Administration) undoubtedly paves the way toward their use in some other specific biomedical treatments. For example, Fu and al. demonstrated a large circulation time of mesoporous silica (MS) by intravenous injection in mice experiments. The MS were mainly stored in spleen and liver, and finally successfully secreted by urine and feces.[29]

Therefore, such mesoporous silica nanomaterials appear as very promising supports for iron removal from biological media. In addition, several reports have shown that the functionalization of large pore MS with macrocyclic or acyclic chelating ligands is of great interest for toxic metals removal, for environmental applications.[30] Thus, the design of large pore MS will be highly desirable regarding this application compared to small pores. Such a strategy is advantageous because large pore silica NPs are prepared according to straightforward and reproducible procedures, while strong chelating ligands would afford very stable metallic complexes.

II. Element purification in peritoneal dialysis treatment of renal failure and emergence of nanoparticles as a treatment

To understand the context of the sodium and phosphate purification, we compare the hemodialysis and peritoneal dialysis as the most used treatments of chronic renal failure. After an analysis of both methods, we focus on the peritoneal dialysis and describe the different phenomena through which the purification is possible. Hence, in a first case, we focus on the sodium purification and the actual solutions for its purification in water. In the same way, for phosphate purification, we analyze the actual solutions to remove phosphates from water. Finally, we briefly explain the kinetics and adsorption model that we used to fit our results.

II. 1. Chronic renal failure

The chronic renal failure (CRF) is a disease which consists of the progressive loss of kidney functions, including homeostasis and extracellular volume balance, phosphocalcic balance, and bone metabolism. When the kidney has a filtration capacity with a glomerular filtration rate of less than 15 ml/min (normally it is above 90 ml/min), the end-stage renal failure (ESRF) is reached. Patients suffering of ESRF cannot remain without a cleansing mechanism. Several treatment options exist for them such as dialysis and transplantation.

II. 2. Medical treatments of chronic renal failure

II. 2. 1. Transplantation

One therapeutic solution for patients with ESRF is kidney transplantation. It allows to regain their renal functions, improving their quality of life. Unfortunately, the wait for a transplant can be long. The lifespan of a transplanted kidney is on average 15 years if there are not complications.

II. 2. 2. Hemodialysis

Hemodialysis (HD) is the most popular method of dialysis. It consists of purifying the blood in an extra-corporeal route (Figure 1). The blood is pumped through the hemodialyzer (blue circle) to purify blood. Herein, toxins and excess of water passes from blood to the dialysis fluid, which is rejected during dialysis (gray route).

A HD session lasts from 3 to 5 hours, during which the patient cannot move. At least, three sessions per week are necessary to allow an effective purification.

Figure 1. Schematization of hemodialysis.[194]

This method has limitations, especially in infants weighing less than 6-8 kg where HD is difficult to perform due to too low a blood volume. Take the example of a 2 kg newborn baby: the blood volume is approximately 90 ml/kg that is to say a total volume of 180 ml. During HD, a volume of blood must be pumped out of the body to purify it (the extra-corporeal volume). This can be a maximum of 10 % of the whole blood, which here represents 18 mL. However, HD machines often cannot achieve such low volumes. Moreover, for children, it is difficult to stay calm during the whole HD session.

II. 2. 3. Peritoneal dialysis

Contrary to HD, peritoneal dialysis (PD) can be applied on infants, newborn babies, even in pre-matures, because it is independent of the blood volume.
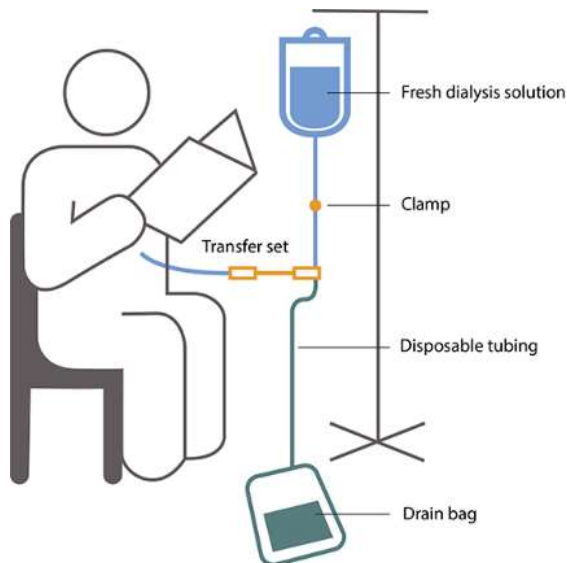
Figure 2. Schematization of a peritoneal dialysis.[195]

In this treatment, a designed dialysis solution is introduced into the peritoneal cavity of the patient. For a few hours, the composition of the liquid is balanced with that of the blood compartment. By diffusion and convection mechanisms through the capillaries, toxins and water excesses pass into the dialysate. This is then drained outside the body before the subsequent provision of new dialysis fluid. The duration of the exchanges varies according to the needs of the patient and the chosen technique. During the PD sessions, the patient does not need to be branched to a machine, and they have a movement liberty, that is another reason to be a suitable treatment for patients.

II. 2. 4. Targeted elements by dialysis

In both dialysis, to purify the blood, the main pollutants targeted are summarized in the next table, as well, their symptoms and consequences.

Table 1. Targeted elements by dialysis, standard levels, symptoms in case of excess of the standard levels and consequences.

Element	Standard levels	Symptom	Consequence
Water	/	• Hypertension	• Puffiness • Bloating • Weight gain
Sodium (hyper-natremia)[31]	135-150 mmol/L		• Heart attack • High blood pressure
Phosphate (hyper-phosphatemia)	25-45 P-mg/L	• Cramps • Heart rhythm disturbances	• Calcium lack in bones (osteo-dystrophy) • Phosphorous deposition on the blood vessels causing heart problems and arteritis • Hyperparathyroidism • Heart attack
Potassium (hyper-kalemia)[32]	3.5-5 mmol/L	• Tiredness • Muscle pain and cramps • Trouble of breathing • Unusual heartbeat	• Heart attack
Others pollutants: Urea[33] Creatinine Uric acid Magnesium Chlorine …	2.5 et 7.6 mmol/L 50-110 µmol/L 120-420 µmol/L 0.65-1.05 mmol/L 96-106 mmol/L	• General fatigue • Loss of appetite • Disgust for meat • Nausea and morning vomiting • Nocturnal cramps • Drowsiness in the day • Troubles of sleeping at night • Confusion • Pale skin • Tachycardia • Xerostomia (dry mouth)	• Platelet dysfunction and bleeding • Encephalopathy • Peripheral neuropathy

Among these pollutants, we will focus on phosphate and sodium. At high concentrations, they are particularly dangerous, even, mortal, that is why, they are surnamed "killers".

If we compare the sodium rates, with the HD, 8 %[34] of the initial sodium concentration is removed, about PD, only 6 % can be removed in very long sessions (24 hours). In parallel, the phosphates are more easily removed by HD (50-60 %) than with the PD (40 %). Indisputably, HD is more effective than PD.

II. 2. 5. Costs and strategy

In 2017, 88 000 patients were treated for end-stage renal disease in France, 40 000 of them were kidney transplanted and 48 000 cases were treated with dialysis (and only 7 % from them by peritoneal dialysis).[35] Contrary to the common thought, PD presents several advantages.

The annual costs per patient for the different treatment modalities are:

- € 92,000 for hemodialysis
- € 65,000 for peritoneal dialysis
- € 90,000 for the 1st year of transplantation and € 20,000 for the following years

In France, end-stage renal disease is totally covered by health insurance.

In addition to the cost, PD has many advantages for the patient: the possibility of being autonomous in the treatment, fewer hospitalizations are needed, less quantity of side treatments as anti-coagulants, and the possibility to perform the treatment during the night/sleep. This last point reinforces their use in children and new-born babies.

To increase the effectivity of the PD, it is possible to modify the dialysis solution. In the case of sodium and phosphates, a possible solution could be the introduction of biocompatible materials which presents an affinity with sodium or phosphates.

In the next lines, to better understand the peritoneal dialysis, we will explain the principle, the mechanisms involved in the ion/molecule purification from blood and some disadvantages of this treatment which we can also solve.

II. 3. Focus on Peritoneal Dialysis

The peritoneum is the largest serous membrane in the body. This membrane surrounds all the organs of the abdominal cavity, delimiting a peritoneal cavity. It has an exchange surface area of 1 to 2 m² in adults.[36] However, this surface is very complex to measure because it contains numerous villi and *ex vivo* measurements are difficult.

Clinically, the peritoneal cavity is used as a drug delivery route and to purify blood instead of the kidney. For this, as shown in figure 2, approximately 1 to 2 L of a dialysis fluid of controlled composition are introduced through a catheter. This catheter is previously inserted by a surgical operation into the peritoneal cavity.

II. 3. 1. Anatomy of the peritoneal membrane and three pores model
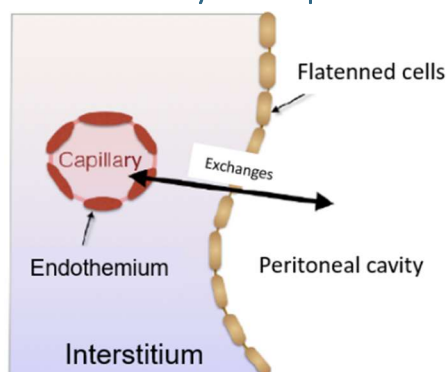
Figure 3. Anatomy of the peritoneal membrane

The peritoneal membrane covers the entire peritoneal cavity (Figure 3). It is composed by a layer of flattened cells and an underlying area of varying thickness (the interstitium) containing lymphatic vessels, blood capillaries, and nerves.[37] The exchange between the blood and the peritoneal cavity needs to cross the endothelium of the capillaries, flattened cells (mesothelial cells), and the space between both.[38,39]

The passage through the membrane was proposed for the first time in 1993, and is described by the three-pores

model.[36,40,41] This model of peritoneal transport is used extensively for modeling peritoneal fluid and solute transport:

- Ultra-small pores. These are the most numerous, they correspond to aquaporins and have a radius of 2 to 4 Å. They only allow the passage of water by osmosis, through the cells.
- Small pores. They have a radius of 40 to 55 Å, allowing water and solutes of low to medium +molecular weight to pass through convection (osmotic and hydrostatic pressure gradient) and diffusion (concentration gradient) processes.
- Large pores: their radius of 250 to 300 Å allows the transport of large molecules by convection (hydrostatic pressure gradient) and diffusion processes.

Thanks to this model, the two possible mechanisms of exchanges are (in this context the term convection does not have the same meaning as in physics. Here, it represents the combined effects of hydrostatic and osmotic pressure):

- Diffusion (figure 4). A movement of molecules according to their concentration gradient is observed.
- Convection/osmosis. The molecules move thanks to the hydrostatic pressure gradient. The intra-peritoneal pressure is lower than capillary hydrostatic pressure, it pushes molecules from the blood to the dialysis solution. This is possible thanks to the osmotic gradient (figure 4) created by the presence of glucose (or other osmotic agent) in the dialysis fluid.
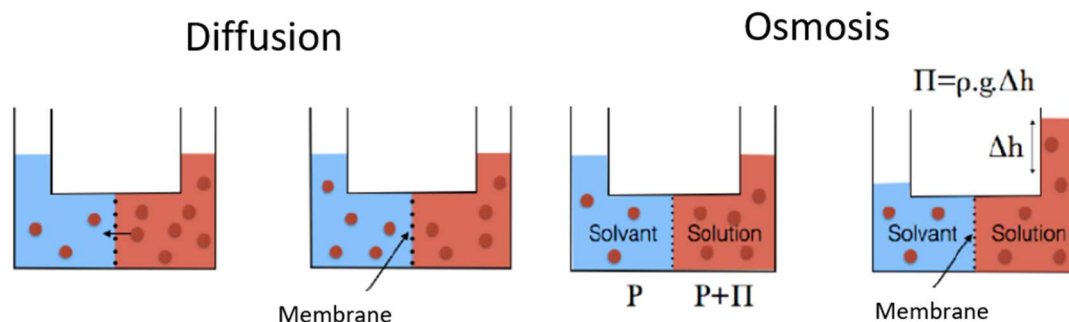
Figure 4. Representation of diffusion and osmosis phenomena.

Interestingly, lymphatics vessels are also involved in the absorption of molecules from the peritoneal cavity. They are able to absorb molecules with a radius greater than 50 Å.[42,43] This means that toxins introduced into the peritoneal cavity that do not pass directly into the blood may, depending on their diameter, pass into the lymph system before finally ending up in the blood.

II. 3. 2. Protocol of peritoneal dialysis in Hospitals

In the Hautepierre hospital, the used dialysis solution is a second-generation double chamber "sleep safe" from Fresenius Medical Care (Glucose 126 mM, Ca^{2+} 1.75 mM, Na^+ 134 mM, Mg^{2+} 0.5 mM, Cl^- 101.5 mM). The difference with a dialysis solution of first generation is the storage of the solution. In the second generation, glucose is kept at very low pH, separate from bicarbonate buffer and electrolytes to avoid toxic glucose degradation products. [44]

The continuous ambulatory peritoneal dialysis (CAPD) is a manual method. At each cycle, a dialysis solution is introduced into the peritoneal cavity of the patient. It is then generally left for four to five hours. The volume of the dialysis solution varies depending on the patient, from a few mL (in newborns babies) to 2.5 L (in adults). At the end of the session, the liquid is drained into another bag before reintroducing new dialysis fluid. Generally, this cycle is carried out three times a day and once in the night. This long exchange helps to purify the phosphate, having a particularly slow removal.[35,36]

The automatic peritoneal dialysis (APD) is a more recent method and allows patients to be more independent. Short exchanges automatically take place at night thanks to a special machine.

During the day, this method can be used to perform a long trade. This method is practical for children, who can then go to school without having to change their pocket during the day, but also for adults who do not want to be constrained during their daily work.[35,36] It also allows for a more individualized prescription and reduces the number of manipulations, thus reducing the risk of infections.

As said before, during a PD, the volume of the fluid is adapted according to the body surface. The use of a large volume makes possible to use a larger surface area of the peritoneal membrane and, therefore, to dialyze better. It should be noted that a too large volume leads to a loss of effectiveness of the PD, discomfort or complications for the patient (breathing difficulties, hernias).

In children under 2 years of age, the introduced volume is around 800 ml/m² of body surface area. Over 2 years, it varies from 1200 ml to 1400 ml/m².[45] The measurement of intraperitoneal pressure is thus useful for clinical monitoring (generally not exceeding 14 cm of water).

II. 4. Sodium Excess - Hypernatremia

In medicine, sodium overload pathology is called hypernatremia (serum [Na+] > 150 mM).[46] As said before, suffering patients present different symptoms as a function of the gravity of the overload: hyperpnea, muscle weakness, insomnia, lethargy and, ultimately, coma.[47,48]

II. 4. 1. Actual medical treatments

Depending on the case, hypernatremia can be treated by dialysis. In a first approach, hemodialysis (HD) allows quick removal of sodium excess, a better control over other electrolytes remedies, this method is only considered in complicated cases with extremely severe sodium levels[49], in most of them sodium decreased by 19 to 20 mM within four hours of dialysis.

On the other hand, for a classical PD, to remove sodium, sessions must be long (>6h). The issue is long sessions (>4 hours) are responsible of peritoneal inflammation which can limit further sessions, the reason is glucose in the dialysis solution forms toxic degradation products which are responsible of peritoneal membrane degradation.[42,44] Moreover, during a PD session, nutriments are also removed, and the growth of children could be affected.[50]

For an optimal treatment, Fischbach *et al.*[51] proposed a varying time and dialysis solution volume in adapted automated peritoneal dialysis session (A-APD), nevertheless, this method can still be performed. The aim of next generation treatments is to improve the sodium and phosphate purification thanks to the addition of elements in the dialysis solution to reduce dialysis sessions time.

II. 4. 2. Extraction of sodium by crown-ether and cryptands

Sodium element is not commonly expressed as dangerous, and few investigations have been developed. However, a high sodium concentration in water (>20 mg/l)[52,53] is not adapted to human consumption as it is may lead to hypertension problems.[54]

For instance, solutions for sodium purification in industry and laboratories present many disadvantages as toxic side products, nonspecific uptake and often expensive. Some examples of them are charged membranes[55], ionic liquids (i.e., monensin as organic extractor for sodium.[56] Unfortunately, they are not compatible with medical treatments.

On a molecular point of view, highly chelating molecules such as crown-ethers and cryptands (Nobel price 1984 Lehn, Pedersen et Cram) have been demonstrated as highly selective for different ions. In 1967, Pedersen accidentally synthesized and isolated the first crown ether: the dibenzo 18-crown-6, able to selectively capture potassium cation[57], the increase of the number of known crown ethers helped to understand and appreciate the limits of size and the study of binding properties of these new macrocycles. Based on the discovery of Pedersen, Lehn and his team developed cryptands. Crown-ether are cyclic compounds consisting on a ring of several ether groups; meanwhile, cryptands contains two bridgehead atoms (nitrogen, phosphorous…) connected by three bridges.[58] The advantages of crown-ethers over cryptands is the easiness of synthesis process, so, less expensive. On the other hand, cryptands are more selective for certain ions. The thermodynamics stability of those complex depends on the match of cavity and cation size. Generally, cryptands have bigger stability constant because the rigidity of the cage matches better with the ion ionic radii. Despite such molecules appear as ideals systems to chelate and extract any cation from a biological media, several issues that are quite similar to those existing for the administration of molecular drugs from drug delivery nanocarriers can be addressed also for depollution.
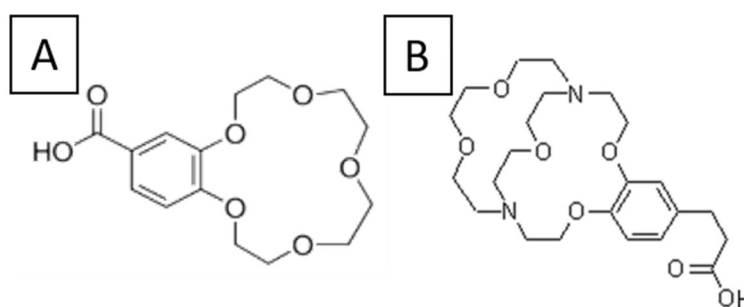
Scheme 2. A. CE: 4-carboxybenzo-15-crown-5. B. Cryptand [2.2.1.]

Indeed, given their small molecular size, their use in complement to hemodialysis or peritoneal dialysis would be rather limited because a rapid renal filtration or easy crossing of peritoneal membranes (given the pore size channels in the peritoneal membrane that are between 2 and 4 Å for the ultra-small pores, 40-55 Å for the small pores and 150-300 Å for the big pores).[36,40,41]

Finally, for this investigation, we have to ensure that the homeostatic levels of this cation remains superior to a limit value for the safety of such treatment because depletion of some relevant ions could be risky. A depletion of sodium could produce cardiovascular problems as hypotension episodes[34].

II. 5. Phosphate excess - Hyperphosphatemia

Phosphates are naturally present and essential in reactions of metabolism.[59] In a healthy person, 85 % of the totality of phosphate belong to the bone (as hydroxyapatite $Ca_5(PO_4)_3(OH)$), 14% is found in tissue and 1% is extracellular.[60] In blood serum, phosphate exists in two forms, dihydrogen phosphate (H_2PO_4) and its salt, mono-hydrogen phosphate (HPO_4^{2-}).[61]

As said previously, to ensure a well-functioning of a metabolism, the normal phosphate concentration in an adult is 25 to 45 P-mg·L^{-1}, while in children, the normal range is 4 to 7 P-mg·L^{-1}.[62] Control of phosphates accumulation is crucial to prevent hyperparathyroidism, biological abnormalities, osteodystrophy and cardiovascular disease.[63]

II. 5. 1. Dephosphatation methods

To decrease phosphates rates in organism, research hardly worked in medical treatment for hyperphosphatemia. For example, an adapted diet can reduce intake of phosphorous, but this can promote the malnutrition. Most of the time intestinal phosphorus chelators are used. They are based on calcium salts but can generate an excessive intake of calcium. An excess of calcium exposes to the risk of hypercalcemia and adynamic osteopathy which could develop of calcifications on the arterial media in hemodialysis patients.[64] Naturally, dialysis is also used, but it is not sufficient to balance the phosphorus levels.

To improve PD, we looked to add a nano-micromaterial in the peritoneal solution. For that, we reviewed the actual solutions to phosphates problems in environment. Some used methods are reverse osmosis, biological removal, adsorption, chemical precipitation, membrane, ion exchange...[65] The most widely used technique in industry (due to its cost effective and environmentally sound), is the biological process.[66] In fact, a variety of bacteria, called polyphosphate-accumulating organisms, has the ability of consuming the contained phosphorus in wastewater. However, the inconvenient of this technique is the limitation of temperature range, sludge quality and settlement, pH, cations, volatile fatty acids, and overall, the danger to use it in a medical treatment.

Looking at the different investigations about removal of phosphates in water, the adsorption phenomenon is often used because of the easy operating conditions and its versatility in the different media.[67] Among absorbents, metal oxide nanoparticles have been already used and could be good candidates for phosphates removal in the peritoneal dialysis treatments.

II. 5. 1. 1. Metals oxide nanoparticles for dephosphatation

The high affinity of phosphorus-based ions towards metals or (hydr)oxides metal is widely exploited in many industrial applications. The most common process is the phosphating of metal surfaces, to ensure the protection of ferrous or non-ferrous metallic materials against corrosion. In the water treatment industry, the adsorption of phosphates by (hydr)oxides metals, mainly iron hydroxides, has been shown to be a very effective method to remove phosphorus from wastewater.[68–70]

In the past, many groups studied phosphate adsorption using metal oxide nanoparticles for environmental applications.[71–81] The next presented materials are claimed as the most performant to the best of our knowledge. The adsorption capacity, the zero charged pH and their optimal pH conditions are summarized in the table 2.

Cerium Oxide Nanoparticles (CeO₂), generally used for catalysis, optical films and fuel cells. They were proved to be efficient for the removal of chromium, arsenate and phosphate in wastewater. These NPs are promising because of their low production price as they are composed of the most abundant rare earth oxides and because they possess promising properties in hazardous conditions as acid or basic media.[82]

Amorphous zirconium oxide Nanoparticles (ZrO₂) is another already tested solution for phosphate capture. Zirconium oxide is a good adsorbent choice for water treatment since it is not toxic. As CeO_2, ZrO_2 has an interesting resistance to acids, bases and oxidants, a high thermal stability and is slightly soluble in water).[83]

The two first materials can be also combined to create a cerium-zirconium binary oxide. This oxide presents the combined advantages of the lonely oxides and high adsorption capacities of phosphorus. Moreover, for other applications, the modulation of Ce/Zr ratio demonstrated better catalytic properties due to their different structures, surface areas and stability.[84]

Cobalt Hydroxide Nanoparticles (Co(OH)₂) proved their capacity to adsorb phosphates under different parameters such as temperature, time and pH. Cobalt based materials can therefore be useful for dephosphatation but it remains a rare metal.[85]

Lanthanum. Another material which showed a specific affinity for phosphates is lanthanum oxide and hydroxide. It forms an insoluble specimen: $LaPO_4$ with 1:1 stoichiometry.[86] This specific affinity makes them some of the most effective adsorbent for phosphate removal. Nevertheless, lanthanum is a rare earth atom, and due to its difficulty of extraction and the social controversy around it, its utilization for dephosphatation might not worth it.[87,88]

Aluminum. As lanthanum, aluminum showed an important affinity under its oxide and hydroxide form.[89] Aluminum has demonstrated satisfactory results as phosphate binder for medical treatments. Though, under certain structures, it has been strictly restricted: absorbed aluminum cation demonstrated severe toxicity.[90]

Iron. Finally, several groups showed than phosphate and Fe^{3+} have the ability to form a strongly bonded binuclear complex.[75] Magnetic properties and chemical stability make iron oxide nanoparticles a good choice for biomedical and environmental applications. Their magnetic properties allow them to be removed/extracted by external magnetic fields. Using those properties, one can easily separate the nanoparticles from the wastewater. [91]

To improve these materials, some groups also designed core-shell nanoparticle such as Fe_3O_4@mZrO₂.[92] Under the different forms of iron oxide, we focus on the spinel iron oxide structure because of their interesting magnetic properties. Therefore, obtaining bare nanoparticles with strong magnetic properties will probably help getting better results concerning phosphate's adsorption.

Table 2. Phosphate adsorption capacity of different type of nanoparticles reported in the literature.

Type of Nanoparticles	Optimized pH	pH_{ZC}	Phosphate Adsorption Capacity (P-mg/g)	Ref.
Cerium Oxide	7	-	0.3-0.4	82
Zirconium Oxide	6.2	-	99.0	83
Cerium-Zirconium Oxide	2-6	-	112.2	84
Lanthanum Oxycarbonate	-	9.3	415.4	86
Cobalt Hydroxide	2	8	49.3	85
Aluminum Oxide	7.1	8.1	33.4	89
Iron oxide (magnetite)	2.4	6.2	40-100	75,91

According with the previous table, several materials promise to enhance phosphates removal in PD. Lanthanum, zirconium, cerium-zirconium or graphene-based materials have impressive results: adsorption capacities of more than 100 P-mg·g^{-1}. However, the potential toxicity is the major limit for bio-applications. According to the expertise of the team using iron oxide NPs for medical applications[93,94], we will focus on iron-based materials from aqueous solutions to perform PD *in vitro* experiments.

II. 5. 1. 2. Adsorption mechanisms and kinetics

The phenomenon itself consists of a chemisorption and/or physisorption of phosphates with metal oxide.

Briefly, depending on the strength of the interaction adsorbent-adsorbate, the adsorption is described as a physisorption or a chemisorption process. Physisorption characterizes all weak electrostatic interactions including Van der Waals interactions, dipole-dipole and London forces. Typical values of these bonds range from 0.2 to 4 kJ/mol.[95] These bonds are considered as the weakest ones of chemical interactions and can be easily broken. Chemisorption occurs when the adsorbate covalently bounds to the substrate via the sharing-transfer of electrons. The energy of these interactions are two orders of magnitude stronger than that of physisorption. Some interactions are "between" both, for example, the strength of hydrogen-bound interactions lies between that of physisorbed and chemisorbed species (12–30 kJ/mol[95] but is often described as a physisorbed interaction. Moreover, the formation of chemisorbed adsorbant-adsorbate bonds can originate from physisorbed interactions and hydrogen-bound species, making the rate of condensation dependent upon the rates of both physisorption and chemisorption.

Iron oxide materials demonstrated a strong affinity with phosphate. These interactions were well studied by T. J. Daou *et al.*[75] using NPs of 39 nm of diameter, synthetized by coprécipitation. Indeed, the affinity between phosphates molecules and iron oxide nanoparticle has two possible origins.

➢ electrostatic interactions between the Fe-OH$_2^+$ sites and phosphates anions (Figure 5).

> ➢ ligand exchanges: an oxygen from the phosphate molecule will replace an oxygen of the hydroxyl group on surface.[96,97]

All the oxides present an amphoteric behavior and the surface is charged due to the protonation/deprotonation of the Fe-OH sites. However, all the OH are not equivalent, and generally, less than 20 % of the sites are ionizable. During his research work, Daou demonstrated that the number of captured phosphates molecules (3.3 molecules/nm²) is superior to the number of active sites (2.2 sites/nm²). It means that the capture of phosphates also involves inactive sites. Finally, phosphates interact with sites of two different natures: the positively charged (Fe-OH$_2^+$) and the hydroxyls Fe-OH to form complexes with phosphates.[98–100] Daou *et al.*[75] were the first to characterize the formation of a stable monoprotonated binuclear iron-phosphate complex on magnetite nanoparticles (scheme 3): (FeO)$_2$(PO)(OH). This last was determined by FTIR spectroscopy and X-Photoemission studies. Finally, they proved that the magnetic properties were not modified after phosphatation.
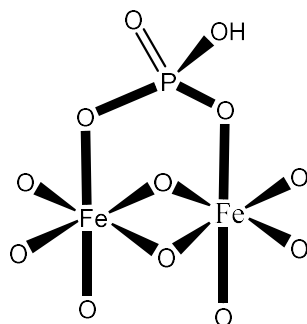
Scheme 3. Schematic representation of the interactions between the phosphate anion and the surface of iron oxide NPs.[101]

In our system, as for the NPs synthesized by coprecipitation, the RSN also have Fe-OH sites which are able to capture phosphates. An increase of pH leads to a change of the main species in solution from H$_3$PO$_4$ to PO$_4^{3-}$ (Figure 5) and a passage from positive to negative zeta potential of RSN (+16 mV to –20 mV, isoelectric point: 5.5). In our experiments (pH 3 and pH 7), the main species in solution are H$_2$PO$_4^-$ and HPO$_4^{2-}$, these anions interact with the surface of the RSN. Additionally, the typical isoelectric point of iron oxide is 6.5-7[96], is our study, the value is 5.5, this could confirm a small layer of ethylene glycol on the surface of the material.
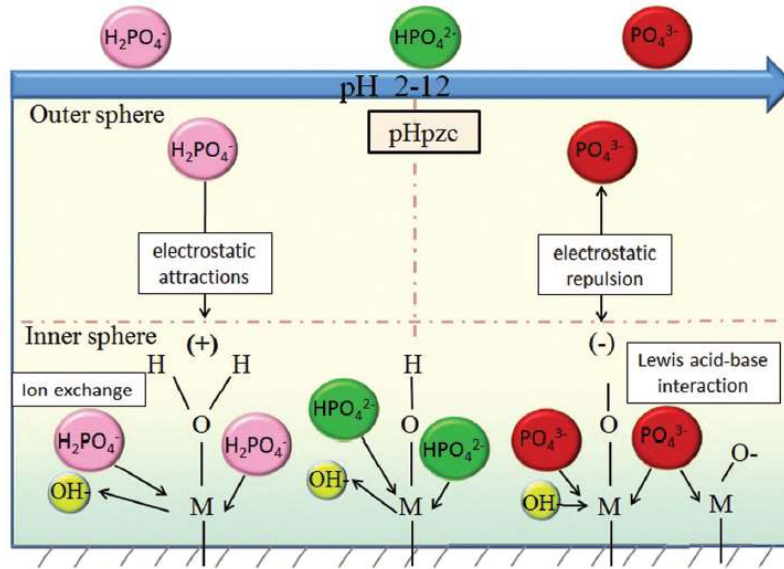
Figure 5. Phosphate sorption mechanisms of metal (hydr)oxides.[102]

Kinetics and adsorption isotherm models

Kinetics model

The pseudo-first and pseudo-second-order kinetic models are the most used to fit the capture of phosphate ions. This is the reason why we used them to characterize the capture of phosphate with RSN and Al-RSN.

Pseudo-first-order model. This model was proposed by Lagergren at the end of the 19th century.[103] This model suggests a diffusion-controlled process, also considered as physisorption because the rate-limiting step is independent on the concentrations of adsorbent and phosphate.[104] In the next equation, q_e is the maximum adsorbed amount at the equilibrium (P-mg·g-1), k_1 the pseudo-first-order rate constant (h^{-1}) and t the time (h).

$$q(t) = q_e \times (1 - e^{-k_1 t})$$

Pseudo-second-order model. This model was proposed in the middle of the 80's by Ho and McKay[105] and popularized in the end of the 90's. Here, the limiting step is the surface adsorption of chemisorption and the phosphate removal is based on physiochemical interactions. Here, k_2 is the pseudo-second-order kinetic rate constant (g·P-mg^{-1}·h^{-1}).

$$q(t) = \frac{k_2 q_e^2 t}{1 + k_2 q_e t}$$

Isotherms Models

In a first approach, we can assume that the S, L, H, C isotherm models allows to understand the interactions between phosphates. However, in a more precise method, different models were used to characterize more precisely the phosphate adsorption: Langmuir, Freundlich and Redlich-Peterson.
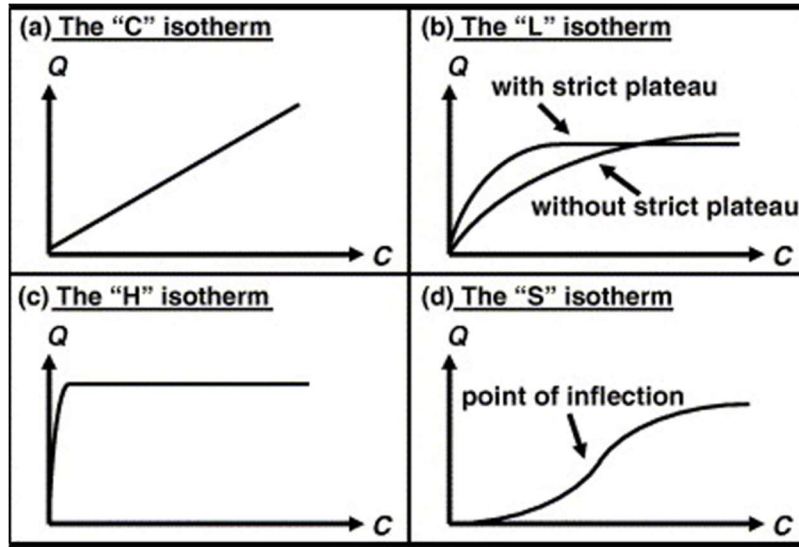
Figure 6. Four main types of isotherm curves.[106]

The "C" Isotherm (linear): An increasing slope at any concentration. This curve is linked to a homogeneous repartition of the adsorbent substance, maybe due to an increase of the adsorbent's sites with the concentration.

The "L" Isotherm: A slope which decreases with the increase of concentration, providing a concave curve. It denotes a strong affinity of the adsorbent with the compound and a diminution of the number of adsorbents sites. This isotherm proposes a progressive saturation of the surface. For this kind of isotherm, two sub-groups are proposed: "with a strict plateau" (solid presents a limited sorption) and "without strict plateau" (a clear sorption is not visible).

The "H" Isotherm: Another version of the L isotherm curve with a very high initial slope, showing a stronger affinity between adsorbed substance and the adsorbent. Here, the affinity is much stronger.

The "S" Isotherm: an increasing slope with a sigmoidal shape having an inflection point. The affinity of the absorbent in function of the adsorbed substance is variable and is the result of two different mechanisms.

Concave Isotherm models

Langmuir was the first model, here, all adsorption sites do not interact with each other's, and they are also equivalent in term of energy. The case of a monolayer coverage is considered in a homogeneous adsorbent surface. Here, at equilibrium, a saturation point is reached where no further adsorption can occur. This model is presented by the formula:

$$q_e = q_m \frac{K_L \times C_e}{1 + K_L \times C_e}$$

Where, q_e is the adsorbed quantity at the equilibrium (P-mg·g^{-1}): q_m is the maximal adsorbed quantity of the monolayer (P-mg·g^{-1}); K_L is the Langmuir equilibrium constant of adsorption (depending of the temperature in L·P-mg^{-1}); and C_e is the concentration at equilibrium (P-mg·L^{-1}).[107]

The Freundlich model proposes different types of adsorption sites of different energy with the same entropy, distributed according to an exponential law as a function of the heat of adsorption. This

expression includes heterogeneous surfaces and assumes that as the adsorbate concentration increases so does the concentration of adsorbate on the adsorbent surface. If the fitting model is adapted, we can determine the quality of the adsorption.

$$q_e = K_F \times C_e^{1/n}$$

Where, K_F is the Freundlich's constant (L·g^{-1}); $1/n$ is the heterogeneity factor, also expressed as $n = Q_0/RT$ where Q_0 is the energetic constant linked to the numeric distribution of sites.

The last choosen model was ***the Redlich-Peterson*** and designated by a "three parameter equation". Contrary to the other models, this one ca be used over a wide range of concentrations.

$$q_e = \frac{K_R \times C_e}{1 + a_R \times C_e^g}$$

At high concentration, this equation is equivalent to the Freundlich isotherm, and, if *g*=1, it is equivalent to the Langmuir isotherm. Here, K_R and *g* are the Redlich-Peterson constants. The ratio of K_R/a_R indicates the adsorption capacity.

III. Features and properties of the nanoparticles used in this work

III. 1. Silica Nanoparticles

Silicon is the second most common element on the Earth (almost 25%), commonly found under the form of silica (SiO_2) in sand. Since 1970's, non-porous silica synthesis has been widely studied and then since 1990's and 2000's, mesoporous silica synthesis was widely developed. In general, silica materials are known to be safe, biocompatible, and easily functionalized. Therefore, the applications are very large: from chemical sensors, catalysis, drug delivery to biomaterials.[108]

III. 1. 2. Synthesis of silica nanoparticles

Historically, non-porous silica nanoparticles or coatings were mostly synthesized using the Stöber process. It consists in the hydrolysis and condensation of a silica precursor for instance tetraethyl-ortho-silicate (TEOS) which is the most used. Ammonia is usually used as catalyst for spherical particles formation in alcoholic solutions. With this process, silica spheres, from 50 to 520 nm diameters can be obtained. [109]
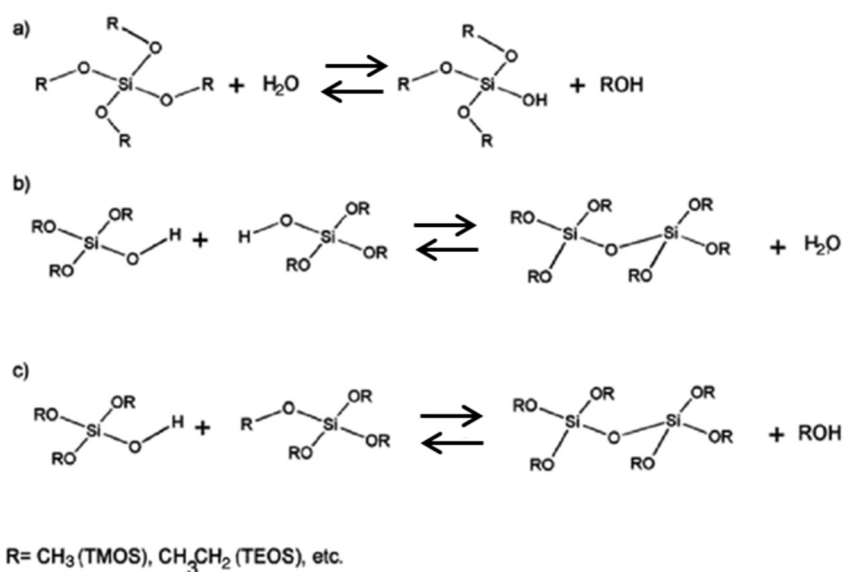
Figure 7. Stöber process. A) Hydrolysis step. B) and C) The condensation step. Typically, in a cosolvent (water-ethanol) under acidic or basic conditions.[110]

This process can be easily explained following the Figure 7. In the hydrolysis step (a), the silica precursor is hydrolyzed by water thanks to the ammonia catalyst, and reactive silanols groups are formed. Then, in condensation steps (b and c), when two silanol groups (or a silanol and a silica precursor) react together, they form a siloxane bridge (Si-O-Si) and release a water molecule (or corresponding alcohol).[110] In this process, there exists a competition between hydrolysis and condensation steps. This regulates the equilibrium between growth of NPs. The process can be catalyzed by an acidic or a basic solution. In the case of acid catalysis, the hydrolysis step is faster and leads to the formation of a continuous cross-linked network. Nonetheless, when the reaction occurs under basic conditions, the condensation is the faster step, and silica NPs are synthesized.[111]

Later in 1992, the Mobil Corporation laboratories stared the production of highly structured mesoporous silica by a modified Stöber process in the presence of surfactants[112], which was called the M41-S family. To obtain a porous silica, surfactants form micelles and these micelles are used as templates. To change the morphology of porosity, the micellar phases (hexagonal, cubic, lamellar) must be different. Based on the positively charged surfactant cetyltrimethyl ammonium (CTA$^+$) structure, and according to different micellar phases, MCM-41 (hexagonal structure), MCM-48 (cubic) and MCM-50 (lamellar) mesoporous silica materials have been obtained after sol-gel with TEOS. Those results allowed the scientific community to improve the properties of silica NPs and their potential applications such as catalysis or drug delivery.

Regarding the possibility for increasing the pore size, in 2013, Zhang *et al.*[113] reported the synthesis of monodispersed mesoporous silica nanoparticles with a high porosity (ca. 15nm), according to an easy route, allowing the production of large scale large pore silica NPs. This method based on soft-templating synthesis, showed a limited aggregation, and allowed to achieve a well-defined pore structure, uniform morphologies, and particle size control. In this work, TEOS was used as silica precursor in the presence of Cetyltrimethylammonium p-toluenesulfonate (CTATos) surfactant and 2-Amino-2-(hydroxymethyl)-1,3-propanediol (AHMPD), a small organic amine acting as a basis which leads to the formation of large pore of ca. 15 nm after silica polymerization. When sol-gel process is conducted with CTAB surfactant, silica with smaller pore size of 3 nm are synthesized. The main difference here comes from the interaction between CTA$^+$ and Tos$^-$ which are much stronger than between CTA$^+$ and Br$^-$. Indeed, tosylate groups strongly compete with silicate adsorbing and polymerizing around the micelles, resulting in micelles packed together, and thus in large pores. Br- has a weak interaction with CTA$^+$ and thus silicate polymerization can be done around the full surface of CTAB micelles resulting in pore having the size of the micelles (3 nm). The Figure 8 summarizes the differences between the sol gel process with CTAB and CTATos.
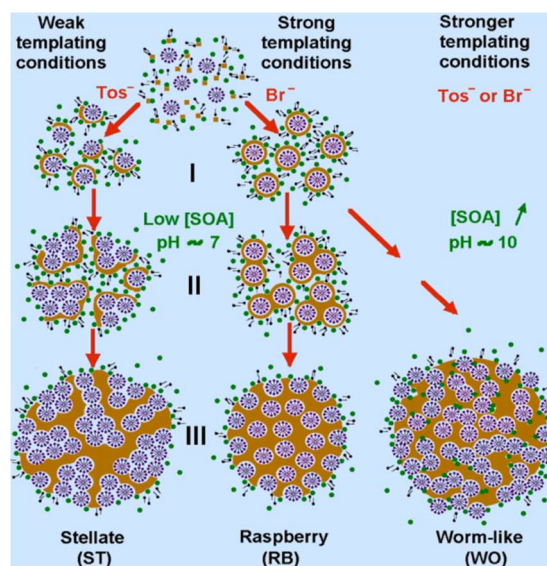
Figure 8. Synthesis mechanisms of stellate, raspberry and worm-like pore network of mesoporous silica.

Interestingly, stellate mesoporous silica (STMS) functionalized with macrocyclic ligands would be of great interest for toxic metal removal either for environment or for medical applications as silica NPs are biocompatible and such ligands allow strong and specific metal coordination.

III. 1. 3. Silica nanoparticles for Purification in Nanomedicine

These last years, there were several studies that reported the ability of organic and inorganic nanomaterials to ensure the removal of molecules or ions from different biological media. For example, Pratsinis *et al.*[18] reported on liposomes used to depollute ammonia from mice. Due to the delicate design and also a lower robustness of organic nanomaterials such as liposomes, researches have mainly focused on inorganic NPs.

Among all these potential nanomaterials, mesoporous silica (MS) are particularly attractive and are considered as one of the most versatile and successful adsorbents for the removal of environmental pollutants in recent years.[25] Due to their large specific surface area (ca. 500 m²/g), their cost-effective synthesis and the easiness of functionalization, these materials –functionalized or not– were applied as adsorbents or catalyst supports, but also for medical treatments as drug delivery vehicle[26,28]

Several groups have already investigated the functionalization of silica surfaces for the capture of different families of pollutants (metals, toxine-bacteria, molecules…). In the case of metallic pollutants, the main experiments concern the extraction of heavy metals from water. For example, thiol molecules are often used to functionalize silica surface and remove heavy metals as mercury [114–116], cadmium[117] or lead.[74,117] Molecules containing amine groups are also very used to functionalize silica and capture hazardous pollutants: Polyethylenimine (PEI) was used to capture cadmium and nickel[118] and aminopropyl groups could capture chrome, arsenic, mercury[119], nickel, cadmium and lead.[120] All these works showed a high potential to remove heavy metals from water, however, the chosen groups are not specific, and it could be an obstacle for some applications.

III. 2. Iron Oxide Nanoclusters

III. 2. 1. Iron oxide structure and magnetic properties

Iron oxide (IO) can exist as sixteen diverse forms including oxides, hydroxides, and oxide-hydroxides. Iron oxides are inexpensive and durable pigments in paints, make-up, coatings and colored concretes, but is also present in steel industry. For this project, our interest is focused on iron oxide spinel structures the magnetite (Fe_3O_4) phase and the maghemite (γ-Fe_2O_3), ones which is the fully oxidized form of magnetite.

More precisely, magnetite and maghemite have a spinel structure. This structure has as chemistry formula AB_2X_4 (space group: Fd-3m). The atoms X form a face-centered cubic system (fcc), the atoms A are placed in the tetrahedral sites and the atoms B in the octahedral sites.

In case of magnetite (Figure 9), the primitive cell is composed by 56 atoms among these, 32 oxygen anions form the fcc system, 8 cations Fe^{3+} occupies tetrahedral sites (Td), and a half of octahedral sites are occupied by Fe^{2+} and Fe^{3+} cations. Thus, magnetite has a general formula $[(Fe^{3+})_{Td}(Fe^{2+}Fe^{3+})_{Oh}](O^2)_4$. The structure is called "inverse spinel" because trivalent cations occupy the tetrahedral sites.

In maghemite, all the Fe^{2+} cations of magnetite are oxidized in Fe^{3+} (in addition, there are apparition of vacancies sites, noted □). The proposed formula is $[(Fe^{3+})_{Td}(Fe^{3+}_{5/3}\square_{1/3})_{Oh}](O^{2-})_4$.[121]
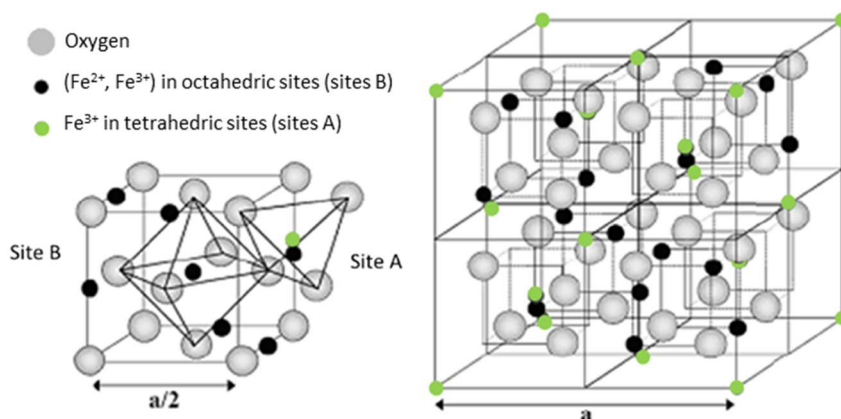
Figure 9. Primitive cell of the inverse spinel structure of magnetite.[122]

Magnetic Structure

Ferrites with a spinel structure are ferrimagnetic materials below the Néel temperature. Fe^{3+} and Fe^{2+} support 4 and 5 μ_B of moment. In the inverse spinel structure, the magnetic moments of Td sites are signed opposed to those of Oh sites. In magnetite, Fe^{2+} and Fe^{3+} in Oh sites are coupled antiparallelly (scheme 4). The magnetic moment of Fe^{3+}_{Oh} is cancelled by those of Fe^{3+}_{Td}, so, the magnetic moment is 4 μ_B corresponding to the contribution of Fe^{2+}_{Oh} (calculated from $M=M_{Oh}-M_{Td}$, the sublattice magnetic moments). For maghemite, one Fe^{3+}_{Td} is opposed to 5/3 of one Fe^{3+}_{Oh}, so magnetic moment decreased and becomes 3.3 μ_B.
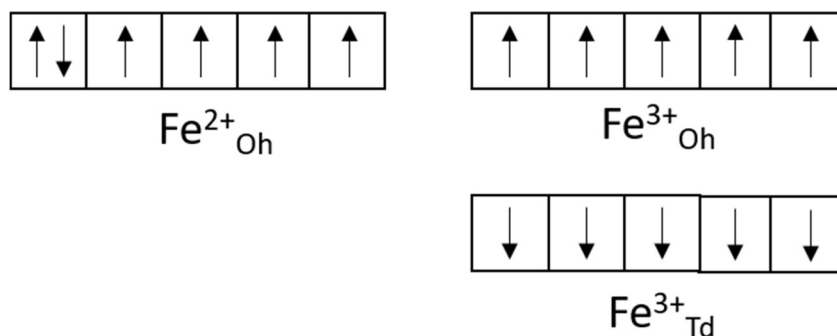
Scheme 4. Spin distribution in magnetite material.

In the bulk state, the magnetization saturation is 92 emu·g^{-1} for magnetite and 74 emu·g^{-1} for maghemite. In fact, the values of magnetization saturation and others magnetic values (coercivity or blocking temperature) depend on the morphology and size of magnetic particles.

III. 2. 2. Reduction to nanoscale

Even if nanoparticles were used for different old cultures as Romans (4th century) in colored glasses, the first person to talk about the "nanometer" was Richard Zsigmondy (Nobel Prize in chemistry 1925), he used this term for characterizing the size of the particles from gold colloids viewed with a microscope.[123] A second key year for nanoworld was 1959: during the American Physical Society meeting at the California Institute of Technology, Richard Feynman presented his iconic lecture: ''There's Plenty of Room at the Bottom''. For the first time in history, the theory of manipulating objects of a "very small" scale was presented as an important research axis.[124] The golden age of nanoworld officially started in the beginning of 21st century, a boom of researches around the world and revolutionary applications in different fields thanks to their unexpected properties.[125]

Iron oxide nanoparticles (NPs) with diameters ranging from 1 and 100 nanometers find applications in environmental catalysis[126,127], imaging in nanomedicine[128,129], drug delivery[130], environmental remediation.[131] Those materials are considered as promising thanks to their low-cost production, abundancy, easy controllable synthesis, and magnetic properties.

The main interest of iron oxide nanoparticles is that the reduction to nanoscale leads to new properties by comparison with bulk such as a high surface/volume ratio and a superparamagnetic behavior.

III. 2. 2. 1. Superparamagnetism

Magnetic domain

In this part, the impact of the nanosize on magnetic properties will be explained.

In the bulk form, iron oxide, as any magnetic material, is composed by several magnetic domains (Weiss domains, figure 10.A) delimited by Bloch walls. The value of saturation magnetization M_S corresponds to the magnetization when all moments are aligned under an applied magnetic field, the remnant M_r is the is the measured magnetization after an external magnetic field is removed, and finally, the coercivity H_C corresponds to the intensity of the external magnetic field to apply in order to demagnetize the material (Figure 10.C).

When the size is reduced, the number of domains decreases until a single domain whose magnetization at room temperature is stable over time: we speak of blocked monodomain nanoparticles. It occurs for a given diameter D_{CR} (Figure 10.A) depending on the materials. For magnetite, the value is 128 nm and for maghemite, 166 nm. Herein, the hysteresis loop is open as for the bulk (Figure 10.C).

If the size is decreased again and the NPs' diameter becomes smaller than to a delimited diameter D_{SPM} (25 nm for magnetite and 30 for maghemite), the magnetocrystalline effective energy becomes lower than thermal energy (K_BT). In that case, the magnetization turns randomly at room temperature. The average time between two reversals is called the Neel relaxation time. This time is generally extremely short and the magnetization therefore appears zero, then, the hysteresis cycle is closed (Figure 10. B), without coercivity H_C or remanent magnetization M_r. We speak in this case of superparamagnetism.[132] This property is highly researched for applications in biomedicine (as contrast agent for MRI - Magnetic Resonance Imaging) where it allows obtaining stable colloidal suspension of

nanoparticles without magnetic interactions (inducing their aggregation). However, for other applications like data storage, this property is not suited, because moments must stay blocked above room temperature.
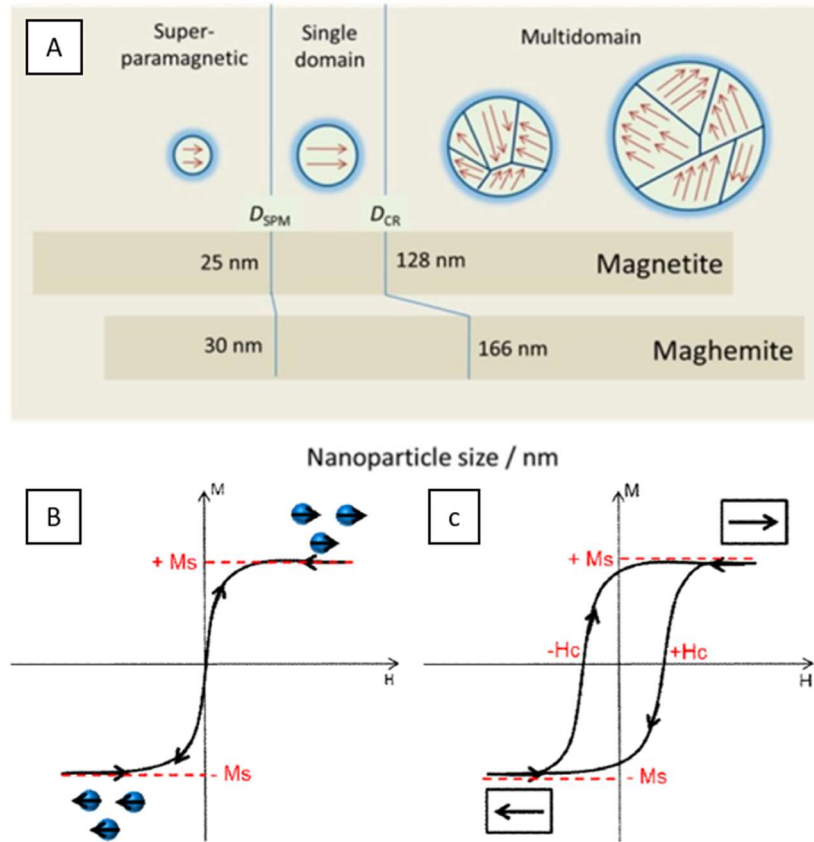
Figure 10. A. Magnetic domain evolution of magnetite and maghemite depending on their size.[133] B. Magnetization curve of a superparamagnetic material and C. Magnetization curve of a hard material with the characteristics hysteresis loop.[122]

Magnetic anisotropy

The bulk magnetic anisotropy energy must include other energy contributions at the nanoscale such as the shape energy (E_{Sh}) and the surface energy (E_S) c, the formula is:

$$E_{a\ total}=E_a+E_{Sh}+E_S$$

$$\text{Where, } E_a=K\cdot V\cdot \sin^2\theta$$

K is the magnetic anisotropy constant of the material, V is the volume of particle depending on D_{SPM} and the angle between the easy magnetization axis and the magnetization direction.

Here, the shape anisotropy (E_{Sh}) refers to the magnetization and his relationship with the shape of the sample. In fact, the emergence of a demagnetized field is created in the material and opposites the external magnetic field. Naturally, the material will want to compensate the external field to be stable. This contribution can be minimized if the magnetization of the system aligns with the longest magnetization axis of the sample. It expression is $E_{Sh}= \frac{1}{2} \cdot \mu_0 \cdot V \cdot (N_x M_x^2+ N_y M_y^2+ N_z M_z^2)$. Where μ_0 is the vacuum permeability ($4\pi \times 10^{-7}$ kg·m·A^{-2}·s^{-2}), N_i and M_i are the projection of the demagnetization and the magnetization polarization (mA).

The last element of our equation is the surface anisotropy E_S: this element has a strong contribution in the nanoscale. In fact, the difference of symmetry between the atoms of the center and the surface of the nanoparticle is different in a short distance: the surface atoms have less neighbors helping to orientate the magnetic moment perpendicularly to the surface. This contribution increases when the ratio of atoms of surface under atoms of core increases, in other words, when the size decreases. This phenomenon is expressed by $E_S = K_S \cdot V \cdot \sin^2 \alpha$, where K_S is the surface anisotropy and α the angle between the magnetization vector and the surface normal.

Other effects linked to the nanosize

The reduction of size induces also a modification of surface and volume. Thus, new phenomena which modify the magnetic measured values by comparison of those measured with the bulk phase.

In fact, when the size of particles decreases, the percentage of the atoms in surface is no more negligible compared to atoms in the core. In case of magnetite, the Fe^{2+} ions on the surface are more sensitive to oxidation due to their direct contact with oxygen of the air. Consequently, they are easily oxidized to form Fe^{3+} cations and vacancies and lead to a maghemite shell and even to an oxidation gradient from the nanoparticle surface up to the core. Finally, the initial magnetite NPs are often core-shell NPs, composed by a core of magnetite and an oxidized shell (assimilated to maghemite). This oxidation modifies the composition of NPs and contributes to decrease the magnetization saturation value (Magnetite: 92 emu·g^{-1}; maghemite: 74 emu·g^{-1}).

Moreover, another effect which is no more negligible is the "spin canting". In fact, surface atoms generate a local anisotropy: magnetic moments align perpendicularly to the surface and not to the direction of the applied magnetic field or the easy magnetization axis, this contribution decreases the global magnetization of the NPs.[134–136]

Other defects inside the structure have also consequences in the magnetic behavior. Vacancies, impurities, dislocations or composition disorder can modify the properties.[137] This is why the atoms distributions inside the structure and its strong link with magnetic properties was reported.[138]

III. 2. 2. 2. Raspberry-shaped nanostructures (RSNs)

Synthesis methods

There exist numerous methods that allow to synthesize ferrite NPs. The next parts very briefly describe the different methods of single nanoparticles synthesis and, more on details, the synthesis of ferrite raspberry-shaped nanostructures (RSNs).

Several methods of synthesis are used to obtain bare iron oxide nanoparticles ($Fe_{3-d}O_4$): co- precipitation, solvothermal, thermal decomposition, via sol-gel, etc... It was demonstrated that variation of parameters may influence on the shape, size, composition. This affects directly the properties of NPs. Thus, the current challenge of synthesis is to adapt the experimental conditions and to obtain the targeted NPs and properties.

The next table summarizes the most known NPs synthesis methods as well as their advantages and inconvenients:

Table 3. Different methods of NPs' synthesis, their advantages and disadvantages.[139]

Method	Conditions	Temperature (°C)	Reaction time	Solvent	Size (nm)	Morphology control	Yield
Coprecipitation	Very sample	20-90	Minutes	Water	<20	Average	High
Microemulsion	Complex	20-50	Dozens of minutes	Water/Organic	<50	Good	Poor
Polyol	Very simple	>180	Dozens of minutes	Polyol	<10	Very good	Average
Hydrothermal	Single but under high pressure	>200	Hours	Water- water/ethanol	<1000	Very good	Average
Thermal Decomposition	Complicated	200-400	Hours	Organic	<20	Very good	High

However, as my PhD project deals with RSNs which consist of oriented aggregates of nanocrystals, I will develop below the different synthesis methods of aggregates of nanocrystals.

Synthesis methods of aggregates of nanoparticles

The nanostructures are aggregates of nanoparticles, and in the case of iron oxide, these objects present interesting magnetic and structural properties. Consequently, they are good candidates for numerous applications. For example, in microwave communication devices, nanostructures are used in magnetodielectric polymer composites, for which, high permeability (μ) and permittivity (ε) and minimal dielectric and magnetic loss (tan σ) are the target properties. That means that magnetic particles have to display high saturation magnetization, mean H_c and to present a homogeneous dispersion in polymers (easy surface to modify). In electrical energy storage, iron oxide particles are promising as electrode materials for lithium-ion batteries[140] or supercapacitors[141] Polyacrylic acid capped nanostructures have already been used in biomedicine as theranostics vehicles: they provide a better diagnostic quality than the commercial product "Endorem®" and therapy by magnetic hyperthermia. [142]

As explained before, the magnetic properties of IONPs are strongly dependent on size of the grains and the smaller is the nanosize, the lower is the saturation magnetization due mainly to a higher oxidation of the magnetite phase and also high surface spin canting and defects. The formation of nanoclusters or nanoaggregates by assembling IONPs has the potential to overcome the low magnetization saturation values by maintaining a superparamagnetic behavior. Besides, other properties are improved: increase of the particle size by keeping properties of NPs (big specific area surface, numerous active sites).

For depollution applications, the researched properties for this PhD work are to be low cost, easily produced, to be magnetic and capture pollutants with a high yield. In fact, these materials possess a low cost production, a relatively high specific surface area and can be removed from polluted media by using a magnet.

The next sections will focus on the different synthesis methods of aggregates of nanocrystals and finally focus on the polyol method.

General concept and main methods

Several groups worked on the elaboration of nanoclusters of iron oxide. Two main types of methods have been reported: the "two-steps" and the "single step" methods.

The "two-steps" methods consists in synthesizing NPs and functionalizing the NPS with designed ligands (Table 4). These ligands will promote clusters' formation either by their added low amount the ligand amount is not high enough to stabilize all the nanoparticles and thus nanoparticles aggregate and ligands coat aggregates) (Scheme 5.A) or by their design which promote interaction between ligands (Scheme 5.B). These methods provide clusters with a rather no-controlled morphology and polydisperse sizes, as well as with a lowest saturation magnetization than nanocluster obtained by the "single step" method.

Scheme 5. Controlled assembly of functionalized NPs. A. By insufficient ligands on the surface. B. By interaction between the ligands.

The "single step" method focuses on the controlled nanocrystals aggregation which occurs during the synthesis process. Here, the size of nanoclusters is better controlled, and the saturation magnetization value is often higher than the nanoclusters formed by the "two-steps" method. These methods are summarized in table 4 with their principle, advantages and inconvenients. To explain this method, a mechanism is proposed in the next part.

Both methods lead to nanoclusters displaying a high saturation magnetization. Because of the easiness of the polyol method, their interesting results, scaling up potential and the previous works of my research group, the next part will focus on this method which will be used in my PhD works. A mechanism will be proposed to explain the formation of nanoclusters.

Table 4. Different methods of nanoclusters' synthesis, main principle, size aggregates and grains, magnetic properties, the advantages and disadvantages of the methods.[143]

Methods			Principle	Size aggregate (nm) Size grain (nm)	Magnetic properties	Advantages and inconvenients
Controlled assembly of functionalized NPs	"Two steps method": 1. Synthesis of monodispersed IONPs 2. Formation of nanoclusters	Ligand-etching	Replace the original capping or introduce a capping with weakly bond ligands, consequently, IONPs are destabilized and form nanoclusters	157±34 4-5[144]	Ms:69.3 emu·g^{-1} Hc:/ TB: 40 K	+ Easy NPs synthesis +Several -Long process because of several steps -Shape control -Expensive -Difficult to scale up
		Solvophobic method	IONPS functionalized with hydrophobic ligand coated with surfactants to form micelles structures and construction of nanostructures	65-204 8[145]	Ms:76-95 emu·g^{-1} Hc:2.6-8.8 Oe TB: 40 K	
		Matrix encapsulation	Method by assisted matrix as ptroteins, polymers and silica[146–149]	80-120 10[147,148]	Ms:40-46 emu·g^{-1} Hc:/ TB: 71 K	
Controlled aggregation	"Single step method" Formation of single IONPs and spontaneous aggregation in a single step	Microwave[4]	Iron salts in presence of capping molecules in a polyol solvent introduced in a microwave for few minutes (T > 200°C)	27-52[153,15] /	Ms:32-58 emu·g^{-1} Hc:43-62Oe TB: /	+Fast and easy +Cheap +Possibility to scale up -Very sensitive to experimental conditions
		Solvothermal	Iron salts in presence of ligand-capping molecules to passivate nanocrystal surface in a reducing solvent.	37[152] 4	Ms:64 emu·g^{-1} Hc:6.2 Oe TB: 200 K	
		Polyol	Iron salts in presence of capping molecules in a polyol solvent at very high temperature (>200°C)	150-250 5-60[153,154]	Ms:75-80 emu·g^{-1} Hc:126-372 Oe TB: 23-35 K	

III. 2. 2. 3. Case of Polyol method - Synthesis parameters

This method attracted researches since 1999 because of its facility to prepare particles of reducible metals (such as silver[155], palladium, platinum[156] or less noble metals (copper, or even iron, nickel or cobalt[157]). Subsequently, this method was adapted for the synthesis of particles of various oxides such as Cu_2O[158,159], V_2O_5[160], SnO_2[161], $MnCo_2O_4$[162] or iron oxide.[163–167] Polyol solvents, the heart of the synthesis, are particularly interesting because α-diols and etherglycols are hydrogen-bonded liquids and apt to dissolve many ionic organic compounds. They possess high boiling temperature and experiments can be performed up to 200 °C under atmospheric pressure.[168]

In the polyol solvothermal methods, reactants (iron precursor, polyol and other additives) are introduced in an autoclave and heated. The obtained nanoclusters are constituted of aggregated nanocrystals following a common crystallographic orientation. Their saturation magnetization is higher than that of single NPs and closer to that of the bulk. In addition, the nanoclusters keep a superparamagnetic behavior in spite of their high particle size.

Synthesis Conditions-brief review

Several groups already worked and performed the synthesis of magnetic nanoclusters by the polyol method. The next table (table 5) summarizes several published works and their different reactants.

About **solvent**, the advantage of this process lies in the multiple roles of the solvent polyol. Polyols are polar solvents. The dipole moment of ethylene glycol (EG) in the gas phase is 2.28 D[169], greater than that of water (1.85 D) and ethanol (1.65 D). In the liquid phase, the dielectric constant ε of EG is 38, higher than that of ethanol (24), but significantly lower than that of water (78.5). Thus, polyols are able of (partially) dissolving many metal precursors. Moreover, polyols are also protic solvents. The protons of the alcohol functions in ethylene glycol are very weak acids but nevertheless superior to those of monoalcohols because their basic form is stabilized by the inductive attracting effect of the two alcohol functions. Several groups chose ethylene glycol (EG). They justified their choice because EG has a high boiling point solvent, is a reducing agent and allows the rotation and orientation of NPs before the contact with neighboring clusters.[170] Other groups also performed the synthesis in other polyol solvents. Cheng *et al*. used 1,2-Polyethylene glycol (PG) and showed PG has a stronger reductive ability than EG. The growth of IONPs is dramatically accelerated in PG, and after a long time (16 hours), clusters collapse and form porous NPs.

Other groups also decided to add **surfactants, strong coordinated-agents, or templates-growth**, generally, these molecules played an important role in determining the cluster morphology (figure 5). Some of them are ethylene diamine (EDA)[171], sodium citrate[172], sodium dodecyl benzene sulfonic (SDBS), polyacrylic acid (PAA)[173], dodecyl diamine (DDA)[174], polyvinyl pyrrolidone (PVP, K30)[163,175] or water[176]. In general, their mechanism of action is similar: their amount modifies the size of cluster and nanocrystals. For example, with citrates: when more citrates; are added, the nanoclusters are smaller. Indeed, citrate is adsorbed on the nanocrystal surface and this results in an electrostatic repelling force between the nanocrystals. On the other side, the surface tension of nanocrystals forces nanocrystals to aggregate and to reduce the surface energy of the nanocrystals. In this case, to form nanoclusters,

a competition of two forces (aggregation and electrostatic interactions) takes place. This mechanism is similar with the other ligands.
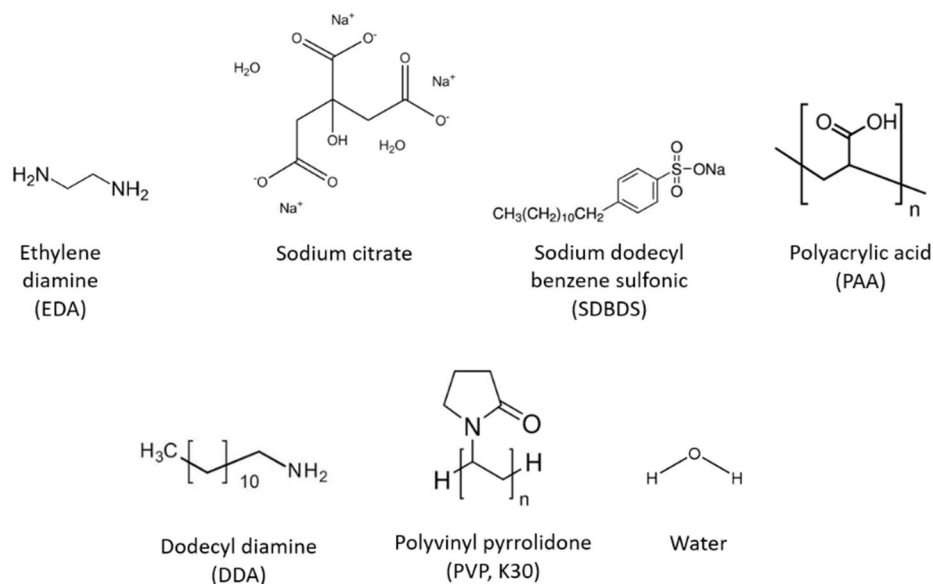
Figure 11. Molecules used as surfactant for template-growth.

About urea, in the studies of Cheng, it also acts as a homogeneous precipitator and as it decomposes in ammonia, it provides hydroxyl ions.[166,172]

Other groups also decided to add *catalyzers* like succinic acid[166] and sodium hydroxide[176], however, their precise role was not explained.

Additionally, another interesting research was made by the team of Zhang. They focused on ***the cooling rate*** and demonstrated an effect on the nanoclusters morphology. In their experiments, the solutions, after heating at 200°C for 12 hours, were cooled down by varying the conditions: furnace cooling (Figure 12. a), air cooling (Figure 12. b) and ice-water cooling (Figure 12. c). The figure 6 was taken from their journal article and clearly shows that, as for samples a and b, the temperature decreases quickly during the first 4 hours; regarding sample c, the minimal temperature was reached after 10 minutes. Concerning the nanostructures, theirs sizes were of about 700, 600 and 500 nm, respectively. Indeed, the two first cooling conditions allowed a continuous growth of the nanostructures (but with more cracks), the third method freezed the nanostructures at the end of the reaction. These differences can be attributed to ***the Ostwald ripening effect.*** Moreover, this result agrees with observations of other groups which investigated the nanoclusters characteristics at different reaction times (Figure 13). The Ostwald ripening effect explains the growth of nanoparticles over time**.** According with the Gibbs-Thompson equation and Fick's first law, the chemical potential of particles decreases when size increases.[177] Visually, smaller internal crystals are dissolved and redeposited on the surfaces of external ones. In the polyol synthesis, the small nanocrystals of the center have a higher surface energy than the external, over time, to reduce their energy, they dissolve, and the others grow. At this point, we can consider than the formation of aggregates is followed by a "recrystallization" process.
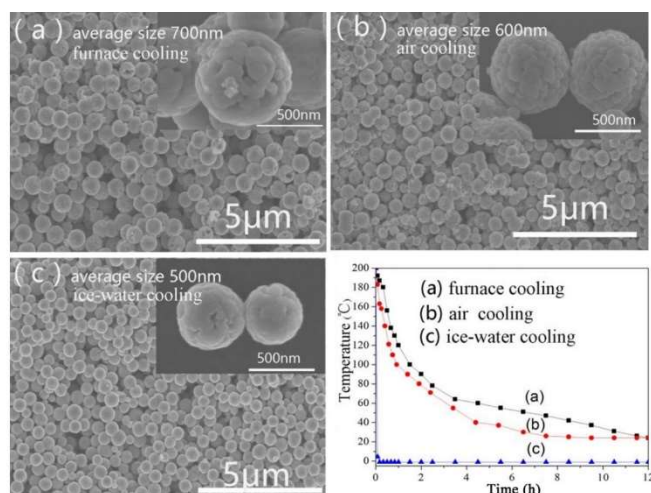
Figure 12. The morphology of nanoclusters synthesized by polyol process (200°C for 12 h) after testing different cooling methods a) by furnace cooling, b) by air cooling and c) by ice-water cooling. Temperature-time plots for the different cooling methods. Taken from Hong *et al.*[178]
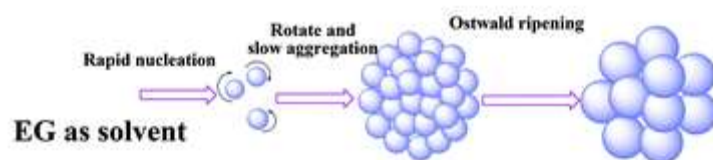
Figure 13. The morphology evolution of nanoclusters in polyol process. Modified from Cheng *et al.*[170]

It is difficult to compare the different syntheses between them because of the very different experimental conditions. However, concerning the size of nanoclusters and grains, in most of the works, nanoclusters synthesized in EG are bigger than 100 nm, and nanograins display mean size between 10 and 50 nm. Concerning magnetic properties, many nanoclusters have exhibited a superparamagnetic behavior with a saturation magnetization between 40 and 99 emu·g^{-1}.

As a global observation, it is apparently necessary to use a template-growth system to form nanoclusters. Because of the complexity to understand this reaction, in 2017, a study of my group proposed a mechanism to understand the nanoclusters synthesis. The next section will focus on their results and investigated properties of the nanoclusters called raspberry-shaped nanostructure (RSN) as this method will be used here to synthesize RSNs.

Table 5. Different nanoclusters' conditions, iron precursor, used solvent and additional reactants. For the characteristics of the synthesized objects: size of aggregates and grains and magnetic properties.

Iron source	Solvent	Other reactants	Reaction time (h)	T (°C)	Size (nanocluster and grain in nm)	Magnetic properties	Ref
$FeCl_3 \cdot 6H_2O$	EG	• EDA	12	200	200-300 50	Hollow : Ms: 68 emu·g^{-1} Mr: 13 emu·g^{-1} Hc: 94 Oe Full : Ms: 85 emu·g^{-1} Mr: 4 emu·g^{-1} Hc: 47 Oe	171
$Fe(acac)_3$	EG	• PVP	36	140-145	100 5	Ms: 42.8 emu·g^{-1} Mr: 7.0 emu·g^{-1} Hc: 44 Oe	163
$FeCl_3 \cdot 6H_2O$	EG	• PVP • HCOONa	6-15	180	100 12	Ms: 57.2-83.8 emu·g^{-1} Mr: 7.0 emu·g^{-1} Hc: 44 Oe	175
$FeCl_3 \cdot 6H_2O$	EG	• Sodium citrate dihydrate • Urea	6	200	40-300 6-11 nm	Ms: 58-73 emu·g^{-1} Mr: 7.0 emu·g^{-1} Hc: 44 Oe	172
$FeCl_3 \cdot 6H_2O$	EG	• Urea	24 – 72	198	260	Ms: 79.58 emu·g^{-1} Mr: 19.1 emu·g^{-1} Hc: 133.5 Oe	164
$FeCl_3 \cdot 6H_2O$	EG	• Urea • Succinic acid	8 - 24	200	300 19-27	Ms: 70-77 emu·g^{-1} Mr: / Hc: /	170
$FeCl_3 \cdot 6H_2O$	1,2-PG	• Urea • Succinic acid	2 - 32	200	50 15-25 *after 8h, nanoclusters are completely dissolved, and porous NPs of 30 nm are formed	Ms: 60 emu·g^{-1} Mr: / Hc: /	
$FeCl_3 \cdot 6H_2O$	EG	• NaAc • *Cooling rate: furnace cooling, air cooling, ice-water cooling*	12	200	500-700	Ms: 82.6-99 emu·g^{-1} Mr: / Hc: /	178
$FeCl_3 \cdot 6H_2O$	EG	• NH_4Ac	8 - 12	200	400	Ms: 82.2 emu·g^{-1}	179

$FeCl_3 \cdot 6H_2O$	EG	• NH$_4$Ac	12 - 24	200	173-177 *hollow diameter 57-136	Ms: 81 emu·g^{-1} Mr: 22 emu·g^{-1} Hc: 250 Oe	180
$FeCl_3 \cdot 6H_2O$	EG	• NaAc • SDBS-concentration	12	200	289-173 20-16	Ms: 60-90 emu·g^{-1} Mr: 4.5-3 emu·g^{-1} Hc: 34.5-37 Oe	173
$FeCl_3 \cdot 6H_2O$	EG	• NaAc • PAA (W$_M$= 1800)	12 - 48	200	197	Ms: 50 emu·g^{-1} Mr: 1 emu·g^{-1} Hc: 8.9 Oe	
$FeCl_3 \cdot 6H_2O$	EG	• DDA	12	220	210 30	Ms: 68-79 emu·g^{-1} Mr : / Hc : /	174
$FeCl_3 \cdot 6H_2O$	EG	• HCOONa • PVP, K30	15	180	240 10-14	Ms: 83.5 emu·g^{-1} Mr : / Hc: 0 Oe	175
$FeCl_3 \cdot 6H_2O$	EG	• DDA • NaOH • Water	12	220	15-234 14-21 *polyhedral shape	Ms: 83.8-90.3 emu·g^{-1} Mr : / Hc: /	176

Mechanism by Gerber et al.[154]

In our laboratory, we have developed the synthesis of nanostructures by using $FeCl_3.6H_2O$, urea and succinic acid in ethylene glycol as reactants. The proposed mechanism is illustrated in scheme 6.
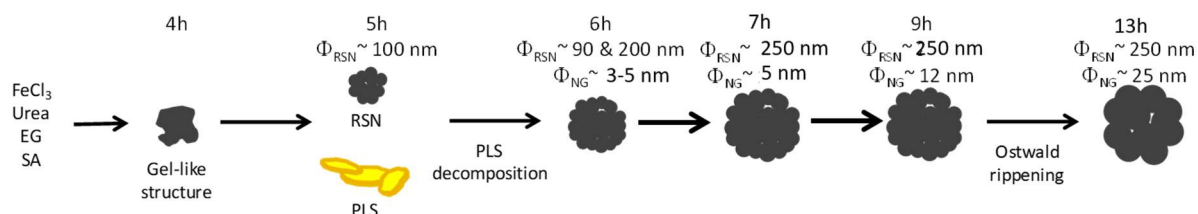
Scheme 6. Reaction steps of the synthesis of magnetite RSN.[154]

Gerber *et al.* performed characterizations at different reaction times and evidence, in particular, the formation of an intermediate iron precursor with a plate morphology which acts as a secondary iron source. s. They propose from these observations the following mechanism: during the first hours, the decomposition of urea in ammonia (and the formation of OH^- and NH_4^+) allows the co-precipitation of iron oxide nanocrystals which form aggregates. Moreover, synthesis conditions and ammonia also allow the deprotonation of EG and, consequently, it coordinates with iron to form an iron alkoxide under the form of plate-like lamellar structures (PLS). At 5 h of reaction, PLS and small RSN (co-precipitation formation) are simultaneously observed. At this step, urea is totally decomposed and iron cations are coprecipitated and formed the first RSN, or are present in the PLS. After 5h, the growth of the first RSNs occurs thanks to the decomposition of PLS, so size of grains stays constant while nanocluster size increases. Between 5 and 7 h, some PLS are still present in the reaction media. After 7h, when no more PLS are available, RSN attained their maximum size. As for the previous presented works, the last step is attributed to the Ostwald ripening process: a solubilization–recrystallization of nanograins located in the center of RSNs, so the size of RSN does not increases but the size of nanograins do. Depending on the reaction time for Ostwald ripening, hollow RSNs may be thus obtained.

Properties by Gerber et al.[153]

Here, Gerber *et al.* synthesized RSN of different size of grains and investigated their composition and magnetic properties.

These nanostructures exhibit unusual properties: a composition close to magnetite due to the prevention of Fe^{2+} from oxidation (resulting from a lot of coherent interfaces between grains) and interesting magnetic properties (saturation magnetization higher than single nanoparticles and keeping a superparamagnetic behavior due to the orientated aggregation of nanograins in RSNs). Gerber *et al.* synthesized RSN of similar sizes but with different nanocrystal size (Figure 8): 250 nm for RSN (± 70 nm) and nanocrystals of 5 nm (RSN5), 55 nm (RSN25) and 60 nm (RSN60). These different nanocrystal sizes were obtained by tuning the heating reaction time (7 hours for RSN5 and 13 hours for RSN25) or the iron chloride concentration (four times more concentrated for RSN60 and 7 h of reaction time).
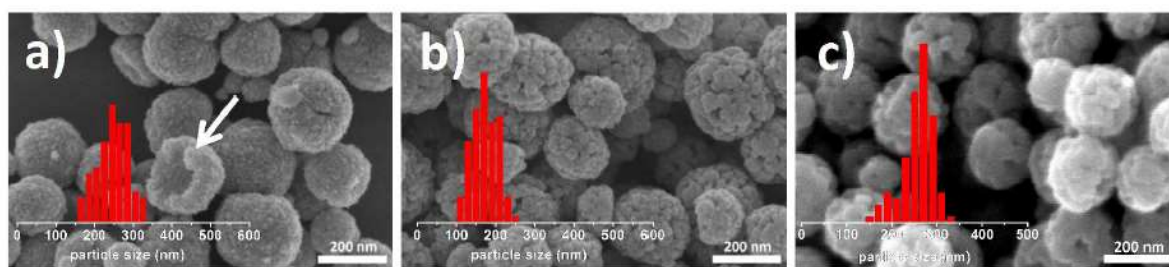
Figure 14. SEM Images and particle size distributions of a) RSN5, b) RSN25 and c) RSN60. From Gerber *et al.*[153]

Mossbauer spectrometry and a fitting procedure using a spherical core-shell system (core-shell model with magnetite as core and maghemite as shell) allowed to calculate the ratio of magnetite and maghemite. Indeed, composition of RSN is a mix of magnetite-maghemite, this variation depends on the partial oxidation of the nanograins. RSN5 has an estimated composition of about 30 % in magnetite and about 70 % for RSN25. Moreover, for both samples, the magnetite fraction is higher than that of isolated nanograins: single NPs of 5 nm are considered as fully oxidized in maghemite,[137,181,182] and for single NPs of 20 nm synthesized by thermal decomposition contains about 55 % of magnetite.[137] Therefore, the raspberry morphology prevents Fe^{2+} from oxidation.

To better understand the magnetic behavior of RSN, different magnetic measurements were performed.

The magnetization curves at 300 K of the three samples are characteristic of superparamagnetic NPs (Figure 9. B), and curves at 5 K display hysteresis loops of blocked magnetic domains (Figure 9. C). When temperature decreases, the increase of coercive fields (H_C) and remanent magnetization (M_R) with the grain size is ascribed to the effect of dipolar interactions and magnetic anisotropy of nanocrystals. Furthermore, all the samples displayed high magnetization saturation at 300 K (76.2, 80.9 and 75.3 $emu \cdot g^{-1}$ for RSN5, RSN25 and RSN60), this values are close to bulk magnetite state.[137,182] For RSN5 and RSN25, M_S is higher than that for single 5 and 20 nm NPs.

In the case of single NPs, this M_S value is generally lower than values of maghemite (74 $emu \cdot g^{-1}$) and magnetite (92 $emu \cdot g^{-1}$) in bulk state. This behavior is justified by the presence of defects in the crystal structure (due to the oxidation of Fe^{2+}) and by the spin canting in the surface or volume of the NPs (consequently, dependent of the size of NPs).[137] In the case of RSN, Gerber *et al.* demonstrated a reduction of the oxidation of Fe^{2+} of nanograins compared to single NPs, this could contribute to the enhancement of M_S. In addition, the oriented aggregation of nanograins in RSN favors a large interface between magnetic monodomains, finally, it reduces surface and volume defects compared to single NPs, thus the M_S is enhanced.

The temperature dependent measurements of magnetization (Figure 15. A, ZFC/FC curves) are different from a typical plot of superparamagnetic nanoparticles. As for superparamagnetic NPs, Gerber *et al.* expected to observe a maximum ZFC value related to the blocking temperature T_B (at this temperature, the crossover between superparamagnetic and ferrimagnetic states takes place), when any maximum is found in the zero field cooled (ZFC) curves. However, we know that the maximum of the ZFC curve, assimilated often to the blocking temperature, is shifted towards higher temperature when there are dipolar interaction between particles in the sample. In fact, ZFC/FC curves suggest that strong

47

dipolar interactions exist in the sample. In this work, it was suggested that the oriented aggregation of nanocrystals favors strong dipolar interactions between nanograins.[183] The contribution observed at 30 K in the three ZFC curves did not correspond to the T_B for the size of grains. It is attributed to the resulting strong collective properties in RSNS which may result in a superspin glass, or possibly a super ferromagnetic state. Such feature has already been observed in assemblies of nanoparticles of similar sizes.[137,182]
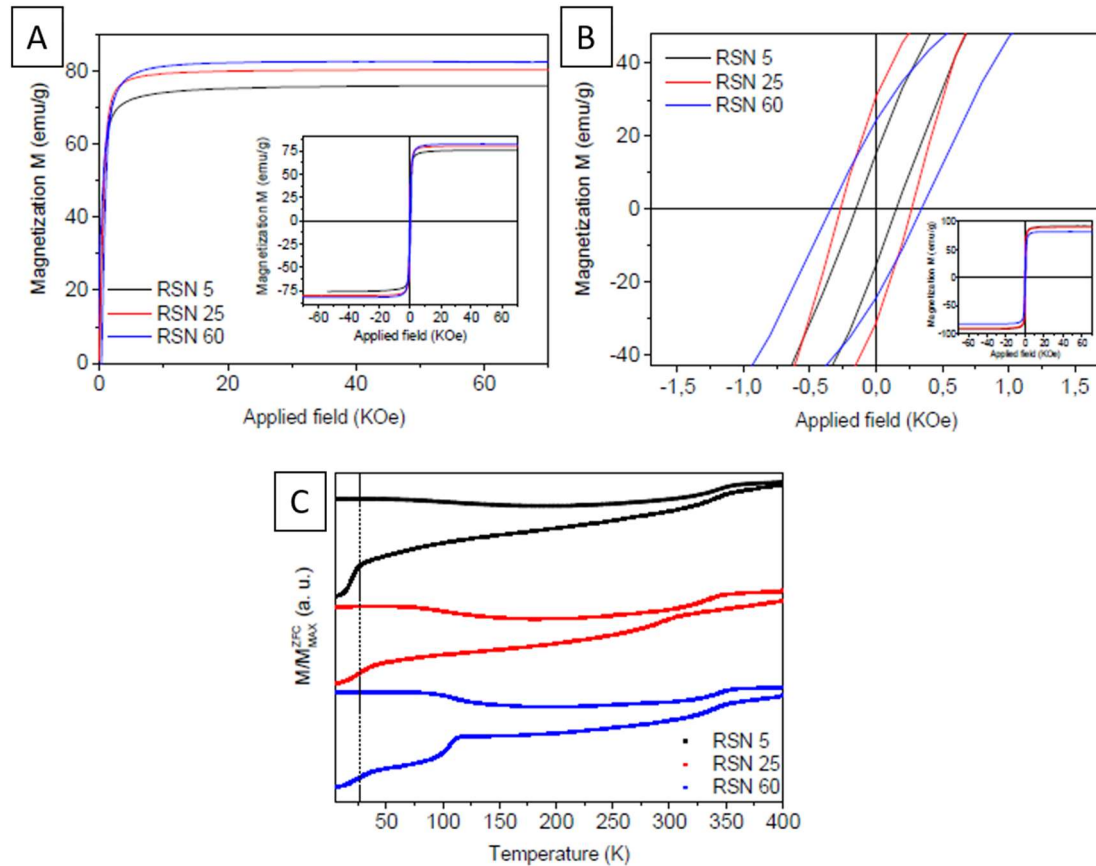
Figure 15. Magnetic properties of RSN5, RSN25 and RSN60 samples. Magnetization curves against an applied magnetic field A. at 300 K and B. at 5 K. C. Magnetization curves against temperature recorded under a static field (ZFC/FC curves). Modified from Gerber *et al.*[153]

Doping of iron oxide nanostructures

During this research project, we got our attention to the doping of iron oxide structures with zinc, cobalt and aluminum in order to tune magnetic properties or to enhance phosphate adsorption for application in peritoneal dialysis. The goal is to modify the magnetic properties, in particular to obtain the same or higher values of M_S. For that, other atoms are introduced into the spinel structure. The formula of these ferrites is $M_xFe_{3-x}O_4$ where M is the introduced cation. As saw before, the general formula of the spinel structure is $[M^{2+}_{1-y}Fe^{3+}i]_{Td}[M^{2+}iFe^{2+}_{1-i}Fe^{3+}]_{Oh}O_4$. Here, for i = 0 the spinel is termed as normal, for i = 1 is inverse (i.e. magnetite) and for 0 < I < 1 is a mixed spinel.

Naturally, some articles reported on the doping of iron oxide nanoclusters and the difficulties of doping magnetite nanoclusters. The next table summarizes the published results on doping of nanostructures with cobalt, magnesium, manganese, copper and nickel. However, any scientific article about

nanostructure doped with aluminum was found. Indeed, the doping of nanostructures with Al (detailed in chapter IV) will be interesting to improve the phosphate capture. To show the effect of aluminum doping, the presented results were only the ones found in a bibliographic review and compared to IONPs of the same size and synthesis method.

Table 6 shows that the most remarkable change for Co doping is on the coercivity values. The addition of this element allows an increase of the Hc value up to 240 Oe, but with saturation magnetization Ms close to magnetite nanocluster.

Comparing the different ferrite composition, in Table 6 and Figure 16 from Chen *et al.* [184], we can clearly observe that all doping experiments conducted to a decrease of the saturation magnetization. The sample with the smaller measured M_S is the Ni doped magnetite, the value is between 43-49 emu·g^{-1} vs 80-90 emu·g^{-1} for magnetite. For the other elements (Co, Mn, Mg and Cu) the M_S value is closer to magnetite (measured values are between 60 and 75 emu·g^{-1}). As for IONPs, this can be explained by the modification of cation distribution inside the structure or supplementary induced defects. In the same way, the morphology was often modified: the size of the nanocluster (from 280 to 1500 nm) and of the nanograins are different between each synthesized sample under the same synthesis conditions. Chen *et al.* demonstrated than in polyol synthesis of nanostructures, the M^{2+} cations affected particle morphology: Co, Cu, and Zn-doped ferrites formed hollow-mesoporous structures and the Mg, Mn and Ni doped ferrites formed mesoporous structures. As we saw before, these modifications affect the magnetic properties.

Table 6. IO nanoclusters doped with different elements and doping of NPs with Al. Chemical formula, synthesis method, size of nanostructures and grains in nm, and recorded magnetic properties.

Doping element	Group	Formula	Synthesis method	Size aggregates and size grains (nm)	Magnetic Properties
Co	Li *et al.*[185]	$Co_xFe_{3-x}O_4$	Polyol	Nanocluster 360 Grain 13.4	Ms: 69 emu·g^{-1} Mr: 14.46 emu·g^{-1} Hc: 242.8 Oe
	Chen *et al.*[184]	$Co_xFe_{3-x}O_4$	Polyol	Nanocluster 280	Ms: 74.5 emu·g^{-1} Mr: 18.4 emu·g^{-1} Hc: 460.2 Oe
Mg	Chen *et al.*[184]	$Mg_xFe_{3-x}O_4$	Polyol	Nanocluster 350	Ms: 63.9 emu·g^{-1} Mr: 0.3 emu·g^{-1} Hc: 5.4 Oe
	Deng *et al.*[186]	$Mg_xFe_{3-x}O_4$	Polyol	Nanocluster 800 Grain: < 30	Ms: 41.7 emu·g^{-1} Hc: 121 Oe
Mn	Chen *et al.*[184]	$Mn_xFe_{3-x}O_4$	Polyol	Nanocluster 350	Ms: 74.2 emu·g^{-1} Mr: 0.2 emu·g^{-1} Hc: 3.9 Oe
Cu	Chen *et al.*[184]	$Cu_xFe_{3-x}O_4$	Polyol	Nanocluster 350	Ms: 67.4 emu·g^{-1} Mr: 0.5 emu·g^{-1} Hc: 7.2 Oe
Ni	Chen *et al.*[184]	$Ni_xFe_{3-x}O_4$	Polyol	Nanocluster 400	Ms: 45.8 emu·g^{-1} Mr: 1.0 emu·g^{-1} Hc: 14.4 Oe
	Deng *et al.*[186]	$Ni_xFe_{3-x}O_4$	Polyol	Nanocluster 300 Grain: < 30	Ms: 49.1 emu·g^{-1} Hc: 139 Oe
	Wang *et al.*[187]	$Al_xFe_{3-x}O_4$	Composite-hydroxide mediated method	Grain: 500-1500	Ms: 43.61 emu·g^{-1} Mr: 6.3 emu·g^{-1} Hc: 110 Oe
Al	Aghazadeh *et al.*[188]	$Al_xFe_{3-x}O_4$	Cathodic electrodeposition method	Grain: 20-30	Ms: 18.37 emu·g^{-1} Mr: 0.13 emu·g^{-1} Hc: 8.73 Oe
	Ehsani *et al.*[189]	$Al_xFe_{3-x}O_4$	Cathodic electrodeposition method Coprecipitation	Grain: 7	Ms: 16.07 emu·g^{-1} Mr: 0.13 emu·g-1 Hc: 8.73 Oe
	Xu *et al.*[190]	$Al_xFe_{3-x}O_4$		Grain: ca. 9	Ms: 22.3 emu·g^{-1}

$M_xFe_{3-x}O_4$ sample	M_s (emu g^{-1})	M_r (emu g^{-1})	H_c (Oe)
$Mg_xFe_{3-x}O_4$	63.9	0.3	5.4
$Mn_xFe_{3-x}O_4$	74.2	0.2	3.9
Fe_3O_4	77.2	5.3	38.8
$Co_xFe_{3-x}O_4$	74.8	18.4	460.2
$Ni_xFe_{3-x}O_4$	45.8	1.0	14.4
$Cu_xFe_{3-x}O_4$	67.4	0.5	7.2
$Zn_xFe_{3-x}O_4$	74.4	1.6	13.5
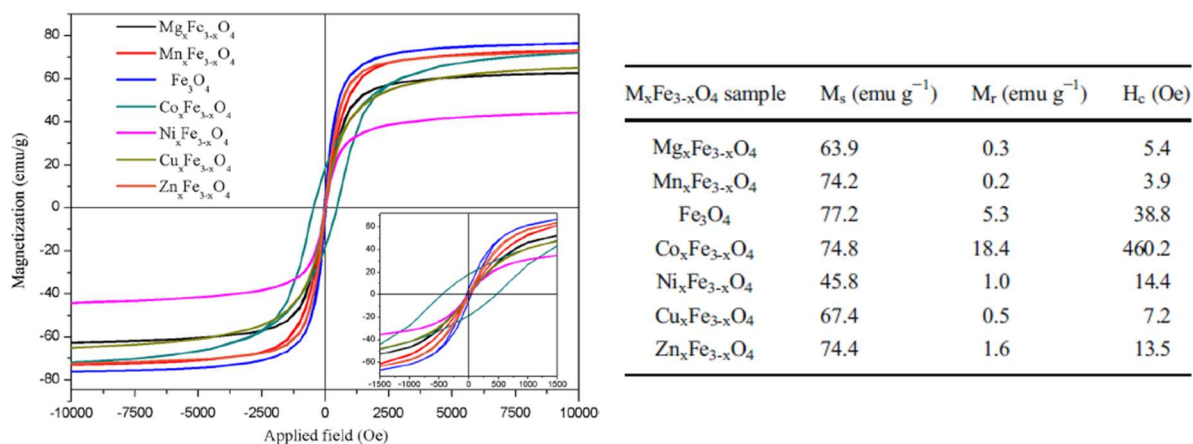
Figure 16. Left: Magnetic hysteresis loops of the ferrites MxFe3-xO4 (M=Mg, Mn,Fe, Co, Ni, Cu, Zn) samples. Right: summary of the different results.[184]

I wanted to treat the case of aluminum separately from the other elements. In fact, few works were performed on nanoparticles doped with Al. However, aluminum could be used as dopant for magnetite because of the similar properties of iron and aluminum cations (size, valence). It should replace Fe^{3+} from the octahedral sides inside the spinel structure.[191] Table 6 shows that for aluminum doping, an important reduction of the saturation magnetization in NPs is observed: it is between 18-22 emu·g^{-1}. Apparently, as Al^{3+} occupies octahedral rather than tetrahedral sites, this reduces the saturation magnetization value.[190]

Mostly, the proof of doping is not well documented and thus, an important step in such doping experiments is to prove the doping of iron oxide (elemental analysis) and to check the structure. To observe the morphology of the synthesized nanostructure, the most often used technics Scanning Electron Microscopy (SEM) and Transmission Electron Microscopy (TEM). In parallel, elementary analysis could be employed, Energy Dispersive Spectrometer (EDS-TEM or EDS-SEM) are the easiest methods to have an idea of the proportion of doping element, to exactly quantify the introduced amount in the sample, methods are Atomic absorption spectroscopy (AAS) or atomic emission spectroscopy (AES) could be employed.

To analyze the structure, X-ray diffraction (XRD) is the main method to identify the crystalline phases, their crystallographic structure, lattice parameter, grain size, crystallite size… Other analysis such as Raman and Fourier-transform infra-red (FTIR) spectroscopies are performed to analyze bonds vibrations of the sample and to suggest the environment of them.

To exhaustive detail structure and element distribution in the particles, characterization with more fine techniques can be performed. It is possible to differentiate atoms in the structure with the Small-Angle X-ray scattering (SAXS) and the angle neutron scattering (SANS). These technics differentiate elements by the signal of electrons or nucleus respectively.[192] X-Ray absorption spectroscopy (XAS) and X-ray magnetic circular dichroism (XMCD) could be used to characterize the environment of specific atoms, its valance state and their site occupancy in the lattice.[193]

Finally, to display the magnetic behavior, magnetic measurements could be performed in a superconductive quantum interference device (SQUID), the magnetic response of samples can be recorded under different conditions (temperature, external magnetic field).

IV. Objectives of the PhD works

The objectives in my PhD work were to develop innovative nano and micro-structured materials for the purification of human body in cases of diseases such as hemochromatosis and renal failures. We have investigated the synthesis of objects that are easy to manipulate from different media, with a large specific surface area, able to capture and release the pollutants that we are targeting. We have thus analyzed two different medical problems which have a common point: the excess of an element in blood due to an illness and have proposed different strategies based on specifically designed materials expecting to improve the standard medical methods.

In a first medical challenge, our goal was to develop a nanomaterial to purify blood in hematochromatosis for which the problem is the iron excess in the body. As seen above, hemochromatosis, a genetic illness which is treated with chelators, however, this treatment presents several side effects due to a short circulation time in blood. To improve the treatment, we must improve the circulation time. Thus, a solution is to fix the iron chelator on a support.

In that context, the originality, which is proposed in this work, is based on the use of a biocompatible material support that is expected to increase the circulation time of the chelating drug and to ensure the selective capture of high iron amount. The development of smart nanoplatforms ensuring a strong complexation of ferric ions, and combining a high level of surface density and a size adapted to circulation in biological environments without aggregation is therefore promising for the efficient, selective and without side-effect removal of biological media but also could be extended to ion removal from ground water. The challenge here is to find a support with high surface specific area and chelating ligands to anchor on this support without affecting their chelating efficiency and selectivity.

In a second medical challenge, we develop a nanomaterial to purify blood in renal failure for which the problem is the excess of various elements in the body such as sodium or phosphate ions. The medical treatment is achieved by peritoneal dialysis where the nanoparticles can foster the purification work. This treatment is applied on patients with chronical or end-stage renal failure. In spite of its economical, adaptability in all age range and its comfort for patients' advantages, hemodialysis is still more performant than peritoneal dialysis (PD) in the same time of sessions. For this project, among the different elements which can be in excess, we focused on sodium and phosphates. Both are considered as extremely dangerous in excess and are difficult to remove from blood (standard levels for sodium 135-150 mM, and phosphate: 25-45 P-mg/L). To improve the PD, the dialysis solution can be improved with the addition of materials designed to increase the removal of toxins.

Hence, to improve those two treatments, our goals were to design nano and microstructured materials and evaluate their efficiency as candidate treatments to purify body.

In the case of iron and sodium excess, **stellate mesoporous silica (STMS) nanoparticles functionalized with cation specific ligands: the desferrioxamine B for iron, and the crown-ether 15-5 and cryptand [2.2.1] for sodium were developed**. On the one hand, the STMS have a big specific surface area (500 $m^2 \cdot g^{-1}$), the surface is easy to modify and are biocompatible. On the other hand, the chosen chelators

have a high affinity with iron and sodium, respectively. This last property should allow to remove selectively the target element.

In the case of phosphate excess, among the different materials, we focused on the use of the magnetite raspberry-shaped nanostructures (RSN) and the aluminum doped raspberry-shaped nanostructures (Al-RSN). These materials have shown a great affinity with phosphates, they possess a high saturation magnetization (Ms=60-80 emu·g^{-1}) which allows an easy magnetic removal from media, and are biocompatible.

Different aspects are combined during this project: fundamental research (particle-pollutant interactions, adsorption isotherm models, complexation of metals), the development of new materials (magnetic particles or recyclable mesoporous silica and with high pollutant sorption / desorption capacity) and the implementation of a technology (easy magnetic recovery and recycling of composites) which can offer new prospects for industrial depollution, improve the success of medical treatments and may be facilitate the dosage of pollutants. Analytical protocols have thus been developed using, for the most part, UV-Visible spectrophotometry because it is a very easy to use, fast and non-destructive method for samples.

As part of my thesis, we worked in collaboration with different research laboratories that master certain analytical techniques (Dr. C. Bertagnolli and Dr. A. Boos-Institut pluridisciplinaire Hubert-Curien, Strasbourg), molecular behavior (Dr. M. Elhabiri-Laboratoire d'Innovation Moléculaire et Applications, Strasbourg), synthesis of chelating molecules (Dr. L. Jierry, Dr. V. Berezhnaia- Institut Charles Sadron, Strasbourg) and nanoparticles synthesis (Pr. P. Kofinas and R. Fedderwitz-University of Maryland, Pr. Y. Piao and Dr. C. Lee-University of Seoul and Dr. D. Bégin and B. Li -Institut de chimie et procédés pour l'énergie, Strasbourg). We have strongly collaborated with the Hautepierre hospital in Strasbourg (Dr. P. Choquet, Dr. A. Zaloszyc and F. Pillods) on the issue of phosphate uptake for peritoneal dialysis.

References

(1)   Sharma, S. K.; Petrusevski, B.; Schippers, J. C. Biological Iron Removal from Groundwater: A Review. *Journal of Water Supply: Research and Technology-Aqua* **2005**, *54* (4), 239–247.

(2)   Puig, S.; Ramos-Alonso, L.; Romero, A. M.; Martínez-Pastor, M. T. The Elemental Role of Iron in DNA Synthesis and Repair. *Metallomics* **2017**, *9* (11), 1483–1500.

(3)   Buffet, C. L'hémochromatose à l'heure de la génétique. *La Presse Médicale* **2007**, *36* (9, Part 2), 1269–1270.

(4)   Westlin, W. F. Deferoxamine in the Treatment of Acute Iron Poisoning: Clinical Experiences with 172 Children. *Clin Pediatr (Phila)* **1966**, *5* (9), 531–535.

(5)   Brittenham, G. M.; Griffith, P. M.; Nienhuis, A. W.; McLaren, C. E.; Young, N. S.; Tucker, E. E.; Allen, C. J.; Farrell, D. E.; Harris, J. W. Efficacy of Deferoxamine in Preventing Complications of Iron Overload in Patients with Thalassemia Major. *New England Journal of Medicine* **1994**, *331* (9), 567–573.

(6)   Ihnat, P. M.; Vennerstrom, J. L.; Robinson, D. H. Solution Equilibria of Deferoxamine Amides. *Journal of Pharmaceutical Sciences* **2002**, *91* (7), 1733–1741.

(7)   Kornreich-Leshem, H.; Ziv, C.; Gumienna-Kontecka, E.; Arad-Yellin, R.; Chen, Y.; Elhabiri, M.; Albrecht-Gary, A.-M.; Hadar, Y.; Shanzer, A. Ferrioxamine B Analogues: Targeting the FoxA Uptake System in the Pathogenic Yersinia Enterocolitica. *J. Am. Chem. Soc.* **2005**, *127* (4), 1137–1145.

(8)   Farkas, E.; Enyedy, É. A.; Csóka, H. A Comparison between the Chelating Properties of Some Dihydroxamic Acids, Desferrioxamine B and Acetohydroxamic Acid. *Polyhedron* **1999**, *18* (18), 2391–2398.

(9)   Evers, A.; Hancock, R. D.; Martell, A. E.; Motekaitis, R. J. Metal Ion Recognition in Ligands with Negatively Charged Oxygen Donor Groups. Complexation of Iron(III), Gallium(III), Indium(III), Aluminum(III), and Other Highly Charged Metal Ions. *Inorg. Chem.* **1989**, *28* (11), 2189–2195.

(10)   Anderegg, G.; L'Eplattenier, F.; Schwarzenbach, G. Hydroxamatkomplexe III. Eisen(III)-Austausch Zwischen Sideraminen Und Komplexonen. Diskussion Der Bildungskonstanten Der Hydroxamatkomplexe. *Helvetica Chimica Acta* **1963**, *46* (4), 1409–1422.

(11)   Farkas, E.; Csóka, H.; Micera, G.; Dessi, A. Copper(II), Nickel(II), Zinc(II), and Molybdenum(VI) Complexes of Desferrioxamine B in Aqueous Solution. *Journal of Inorganic Biochemistry* **1997**, *65* (4), 281–286.

(12)   Bergeron, R. J.; Wiegand, J.; Brittenham, G. M. HBED: A Potential Alternative to Deferoxamine for Iron-Chelating Therapy. *Blood* **1998**, *91* (4), 1446–1452.

(13)   Piga, A.; Galanello, R.; Forni, G. L.; Cappellini, M. D.; Origa, R.; Zappu, A.; Donato, G.; Bordone, E.; Lavagetto, A.; Zanaboni, L.; Sechaud, R.; Hewson, N.; Ford, J. M.; Opitz, H.; Alberti, D. Randomized Phase II Trial of Deferasirox (Exjade, ICL670), a Once-Daily, Orally-Administered Iron Chelator, in Comparison to Deferoxamine in Thalassemia Patients with Transfusional Iron Overload. *Haematologica* **2006**, *91* (7), 873–880.

(14)   Liu, G.; Men, P.; Perry, G.; Smith, M. A. Nanoparticle and Iron Chelators as a Potential Novel Alzheimer Therapy. *Methods Mol. Biol.* **2010**, *610*, 123–144.

(15)   Farjadian, F.; Ghasemi, S.; Heidari, R.; Mohammadi-Samani, S. In Vitro and in Vivo Assessment of EDTA-Modified Silica Nano-Spheres with Supreme Capacity of Iron Capture as a Novel Antidote Agent. *Nanomedicine: Nanotechnology, Biology and Medicine* **2017**, *13* (2), 745–753.

(16)   Kefeni, K. K.; Mamba, B. B.; Msagati, T. A. M. Application of Spinel Ferrite Nanoparticles in Water and Wastewater Treatment: A Review. *Separation and Purification Technology* **2017**, *188*, 399–422.

(17)   Reddy, D. H. K.; Yun, Y.-S. Spinel Ferrite Magnetic Adsorbents: Alternative Future Materials for Water Purification? *Coordination Chemistry Reviews* **2016**, *315*, 90–111.

(18)   Pratsinis, A.; Zuercher, S.; Forster, V.; Fischer, E. J.; Luciani, P.; Leroux, J.-C. Liposome-Supported Enzymatic Peritoneal Dialysis. *Biomaterials* **2017**, *145*, 128–137.

(19)   Khajeh, M.; Laurent, S.; Dastafkan, K. Nanoadsorbents: Classification, Preparation, and Applications (with Emphasis on Aqueous Media). *Chem. Rev.* **2013**, *113* (10), 7728–7768.

(20)   Adeleye, A. S.; Conway, J. R.; Garner, K.; Huang, Y.; Su, Y.; Keller, A. A. Engineered Nanomaterials for Water Treatment and Remediation: Costs, Benefits, and Applicability. *Chemical Engineering Journal* **2016**, *286*, 640–662.

(21)   Khin, M. M.; Nair, A. S.; Babu, V. J.; Murugan, R.; Ramakrishna, S. A Review on Nanomaterials for Environmental Remediation. *Energy Environ. Sci.* **2012**, *5* (8), 8075–8109.

(22)   Simeonidis, K.; Mourdikoudis, S.; Kaprara, E.; Mitrakas, M.; Polavarapu, L. Inorganic Engineered Nanoparticles in Drinking Water Treatment: A Critical Review. *Environ. Sci.: Water Res. Technol.* **2016**, *2* (1), 43–70.

(23) Yang, J.; Hou, B.; Wang, J.; Tian, B.; Bi, J.; Wang, N.; Li, X.; Huang, X. Nanomaterials for the Removal of Heavy Metals from Wastewater. *Nanomaterials* **2019**, *9* (3), 424.

(24) Zhang, X.; Niu, H.; Pan, Y.; Shi, Y.; Cai, Y. Chitosan-Coated Octadecyl-Functionalized Magnetite Nanoparticles: Preparation and Application in Extraction of Trace Pollutants from Environmental Water Samples. *Anal. Chem.* **2010**, *82* (6), 2363–2371.

(25) Cashin, V. B.; Eldridge, D. S.; Yu, A.; Zhao, D. Surface Functionalization and Manipulation of Mesoporous Silica Adsorbents for Improved Removal of Pollutants: A Review. *Environ. Sci.: Water Res. Technol.* **2018**, *4* (2), 110–128.

(26) Vallet-Regí, M.; Ruiz-González, L.; Izquierdo-Barba, I.; M. González-Calbet, J. Revisiting Silica Based Ordered Mesoporous Materials: Medical Applications. *Journal of Materials Chemistry* **2006**, *16* (1), 26–31.

(27) Ménard, M.; Meyer, F.; Parkhomenko, K.; Leuvrey, C.; Francius, G.; Bégin-Colin, S.; Mertz, D. Mesoporous Silica Templated-Albumin Nanoparticles with High Doxorubicin Payload for Drug Delivery Assessed with a 3-D Tumor Cell Model. *Biochimica et Biophysica Acta (BBA) - General Subjects* **2019**, *1863* (2), 332–341.

(28) Wells, C.; Vollin-Bringel, O.; Fiegel, V.; Harlepp, S.; Schueren, B. V. der; Bégin-Colin, S.; Bégin, D.; Mertz, D. Engineering of Mesoporous Silica Coated Carbon-Based Materials Optimized for an Ultrahigh Doxorubicin Payload and a Drug Release Activated by PH, T, and NIR-Light. *Advanced Functional Materials* **2018**, *28* (17), 1706996.

(29) Fu, C.; Liu, T.; Li, L.; Liu, H.; Chen, D.; Tang, F. The Absorption, Distribution, Excretion and Toxicity of Mesoporous Silica Nanoparticles in Mice Following Different Exposure Routes. *Biomaterials* **2013**, *34* (10), 2565–2575.

(30) Hakami, O.; Zhang, Y.; Banks, C. J. Thiol-Functionalised Mesoporous Silica-Coated Magnetite Nanoparticles for High Efficiency Removal and Recovery of Hg from Water. *Water Research* **2012**, *46* (12), 3913–3922.

(31) Effects of Excess Sodium Infographic https://www.heart.org/en/healthy-living/healthy-eating/eat-smart/sodium/effects-of-excess-sodium-infographic (accessed Sep 30, 2020).

(32) High potassium (hyperkalemia) http://www.kidneyfund.org/kidney-disease/chronic-kidney-disease-ckd/complications/high-potassium-hyperkalemia.html (accessed Sep 30, 2020).

(33) Tyagi, A.; Aeddula, N. R. Azotemia. In *StatPearls*; StatPearls Publishing: Treasure Island (FL), 2020.

(34) Kooman, J. P.; Sande, F. V. D.; Leunissen, K.; Locatelli, F. Editorials: Sodium Balance in Hemodialysis Therapy. *Seminars in Dialysis* **2003**, *16* (5), 351–355.

(35) Rottembourg, J.; Rostoker, G. La réalité de la dialyse péritonéale en France : 40 ans après. *Néphrologie & Thérapeutique* **2018**, *14* (7), 507–517.

(36) Bazaev, N. A.; Grinval'd, V. M.; Selishchev, S. V.; Strokov, A. G. A Wearable Device for Low-Flow Detoxification of Human Body by Peritoneal Dialysis. *Biomed Eng* **2018**, *52* (3), 147–151.

(37) van Baal, J. O. A. M.; Van de Vijver, K. K.; Nieuwland, R.; van Noorden, C. J. F.; van Driel, W. J.; Sturk, A.; Kenter, G. G.; Rikkert, L. G.; Lok, C. A. R. The Histophysiology and Pathophysiology of the Peritoneum. *Tissue and Cell* **2017**, *49* (1), 95–105.

(38) Bartosova, M.; Schmitt, C. P. Biocompatible Peritoneal Dialysis: The Target Is Still Way Off. *Front Physiol* **2019**, *9*.

(39) Blackburn, S. C.; Stanton, M. P. Anatomy and Physiology of the Peritoneum. *Seminars in Pediatric Surgery* **2014**, *23* (6), 326–330.

(40) Rippe, B. A Three-Pore Model of Peritoneal Transport. *Perit Dial Int* **1993**, *13 Suppl 2*, S35-38.

(41) Waniewski, J. Mathematical Modeling of Fluid and Solute Transport in Hemodialysis and Peritoneal Dialysis. *Journal of Membrane Science* **2006**, *274* (1), 24–37.

(42) *The Textbook of Peritoneal Dialysis*; Gokal, R., Nolph, K. D., Eds.; Springer Netherlands, 1994.

(43) Yoon, S.-H. *Membrane Bioreactor Processes : Principles and Applications*; CRC Press, 2015.

(44) Schaefer, B.; Bartosova, M.; Macher-Goeppinger, S.; Sallay, P.; Vörös, P.; Ranchin, B.; Vondrak, K.; Ariceta, G.; Zaloszyc, A.; Bayazit, A. K.; Querfeld, U.; Cerkauskiene, R.; Testa, S.; Taylan, C.; VandeWalle, J.; Yap, Y.; Krmar, R. T.; Büscher, R.; Mühlig, A. K.; Drozdz, D.; Caliskan, S.; Lasitschka, F.; Fathallah-Shaykh, S.; Verrina, E.; Klaus, G.; Arbeiter, K.; Bhayadia, R.; Melk, A.; Romero, P.; Warady, B. A.; Schaefer, F.; Ujszaszi, A.; Schmitt, C. P. Neutral PH and Low–Glucose Degradation Product Dialysis Fluids Induce Major Early Alterations of the Peritoneal Membrane in Children on Peritoneal Dialysis. *Kidney International* **2018**, *94* (2), 419–429.

(45) Fischbach, M.; Warady, B. A. Peritoneal Dialysis Prescription in Children: Bedside Principles for Optimal Practice. *Pediatr Nephrol* **2009**, *24* (9), 1633–1642.

(46) Clinical Practice Guidelines : Hypernatraemia https://www.rch.org.au/clinicalguide/guideline_index/Hypernatraemia/ (accessed Feb 26, 2020).

(47) Ross, E. J.; Christie, S. B. Hypernatremia. *Medicine (Baltimore)* **1969**, *48* (6), 441–473.

(48) Adrogué, H. J.; Madias, N. E. Hypernatremia. *New England Journal of Medicine* **2000**, *342* (20), 1493–1499.

(49) Nur, S.; Khan, Y.; Nur, S.; Boroujerdi, H. Hypernatremia: Correction Rate and Hemodialysis https://www.hindawi.com/journals/crim/2014/736073/ (accessed Apr 14, 2020).

(50) Fischbach, M.; Fothergill, H.; Seuge, L.; Zaloszyc, A. Dialysis Strategies to Improve Growth in Children With Chronic Kidney Disease. *Journal of Renal Nutrition* **2011**, *21* (1), 43–46.

(51) Fischbach, M.; Schmitt, C. P.; Shroff, R.; Zaloszyc, A.; Warady, B. A. Increasing Sodium Removal on Peritoneal Dialysis: Applying Dialysis Mechanics to the Peritoneal Dialysis Prescription. *Kidney International* **2016**, *89* (4), 761–766.

(52) Tuthill, R. W.; Calabrese, E. J. Drinking Water Sodium and Blood Pressure in Children: A Second Look. *Am J Public Health* **1981**, *71* (7), 722–729.

(53) Tuthill, R. W.; Calabrese, E. J. Elevated Sodium Levels in the Public Drinking Water as a Contributor to Elevated Blood Pressure Levels in the Community. *Arch. Environ. Health* **1979**, *34* (4), 197–203.

(54) Sapirstein, L. A.; Brandt, W. L.; Drury, D. R. Production of Hypertension in the Rat by Substituting Hypertonic Sodium Chloride Solutions for Drinking Water. *Proceedings of the Society for Experimental Biology and Medicine* **1950**, *73* (1), 82–85.

(55) Duong, H. C.; Duke, M.; Gray, S.; Nelemans, B.; Nghiem, L. D. Membrane Distillation and Membrane Electrolysis of Coal Seam Gas Reverse Osmosis Brine for Clean Water Extraction and NaOH Production. *Desalination* **2016**, *397*, 108–115.

(56) Parmentier, D.; Lavenas, M.; Güler, E.; Metz, S. J.; Kroon, M. C. Selective Removal of Sodium from Alkali-Metal Solutions with Tetraoctylammonium Monensin. *Desalination* **2016**, *399*, 124–127.

(57) Czarnik, A. W. Fluorescent Chemosensors of Ion and Molecule Recognition. In *Interfacial Design and Chemical Sensing*; ACS Symposium Series; American Chemical Society, 1994; Vol. 561, pp 314–323.

(58) Gokel, G. W.; Atwood, J. L.; Lehn, J.-M. *Comprehensive Supramolecular Chemistry. Receptors for Cationic Guests Volume 1, Volume 1,*; Pergamon: New York, 1996.

(59) Fukumoto, S. Phosphate Metabolism and Vitamin D. *Bonekey Rep* **2014**, *3*.

(60) Zaloszyc, A. Rôle de La Voie de Signalisation Gαq/11 Dans La Réponse Osseuse à La Parathormone : Étude Chez Un Modèle Murin Insuffisant Rénal Chronique Avec Inactivation Osseuse de La Voie de Signalisation Gαq/11. Thèse de doctorat, Strasbourg, 2018.

(61) Bansal, V. K. Serum Inorganic Phosphorus. In *Clinical Methods: The History, Physical, and Laboratory Examinations*; Walker, H. K., Hall, W. D., Hurst, J. W., Eds.; Butterworths: Boston, 1990.

(62) Goyal, R.; Jialal, I. Hyperphosphatemia. In *StatPearls*; StatPearls Publishing: Treasure Island (FL), 2020.

(63) Block, G. A.; Klassen, P. S.; Lazarus, J. M.; Ofsthun, N.; Lowrie, E. G.; Chertow, G. M. Mineral Metabolism, Mortality, and Morbidity in Maintenance Hemodialysis. *JASN* **2004**, *15* (8), 2208–2218.

(64) London, G. M.; Guérin, A. P.; Marchais, S. J.; Métivier, F.; Pannier, B.; Adda, H. Arterial Media Calcification in End-Stage Renal Disease: Impact on All-Cause and Cardiovascular Mortality. *Nephrol Dial Transplant* **2003**, *18* (9), 1731–1740.

(65) Terry, P. A. Removal of Nitrates and Phosphates by Ion Exchange with Hydrotalcite. *Environmental Engineering Science* **2008**, *26* (3), 691–696.

(66) Münch, E.; Barr, K. Controlled Struvite Crystallisation for Removing Phosphorus from Anaerobic Digester Sidestreams. *Water Research*. 35th ed. 2001.

(67) Liu, R.; Chi, L.; Wang, X.; Sui, Y.; Wang, Y.; Arandiyan, H. Review of Metal (Hydr)Oxide and Other Adsorptive Materials for Phosphate Removal from Water. *Journal of Environmental Chemical Engineering* **2018**, *6* (4), 5269–5286.

(68) Anderson, M. A.; Tejedor-Tejedor, M. Isabel.; Stanforth, R. R. Influence of Aggregation on the Uptake Kinetics of Phosphate by Goethite. *Environ. Sci. Technol.* **1985**, *19* (7), 632–637.

(69) Miyauchi, H.; Yamamoto, T.; Chitrakar, R.; Makita, Y.; Wang, Z.; Kawai, J.; Hirotsu, T. Phosphate Adsorption Site on Zirconium Ion Modified MgAl-Layered Double Hydroxides. *Top Catal* **2009**, *52* (6), 714–723.

(70) Yeoman, S.; Stephenson, T.; Lester, J. N.; Perry, R. The Removal of Phosphorus during Wastewater Treatment: A Review. *Environ. Pollut.* **1988**, *49* (3), 183–233. https://doi.org/10.1016/0269-7491(88)90209-6.

(71) Yao, W.; Millero, F. J. Adsorption of Phosphate on Manganese Dioxide in Seawater. *Environ. Sci. Technol.* **1996**, *30* (2), 536–541.

(72) Febrianto, J.; Kosasih, A. N.; Sunarso, J.; Ju, Y.-H.; Indraswati, N.; Ismadji, S. Equilibrium and Kinetic Studies in Adsorption of Heavy Metals Using Biosorbent: A Summary of Recent Studies. *J. Hazard. Mater.* **2009**, *162* (2–3), 616–645.

(73) Sousa, A. F. de; Braga, T. P.; Gomes, E. C. C.; Valentini, A.; Longhinotti, E. Adsorption of Phosphate Using Mesoporous Spheres Containing Iron and Aluminum Oxide. *Chemical Engineering Journal* **2012**, *210*, 143–149.

(74) Long, F.; Gong, J.-L.; Zeng, G.-M.; Chen, L.; Wang, X.-Y.; Deng, J.-H.; Niu, Q.-Y.; Zhang, H.-Y.; Zhang, X.-R. Removal of Phosphate from Aqueous Solution by Magnetic Fe–Zr Binary Oxide. *Chemical Engineering Journal* **2011**, *171* (2), 448–455.

(75) Daou, T. J.; Begin-Colin, S.; Grenèche, J. M.; Thomas, F.; Derory, A.; Bernhardt, P.; Legaré, P.; Pourroy, G. Phosphate Adsorption Properties of Magnetite-Based Nanoparticles. *Chem. Mater.* **2007**, *19* (18), 4494–4505.

(76) Parfitt, R. L.; Atkinson, R. J.; Smart, R. S. C. The Mechanism of Phosphate Fixation by Iron Oxides. *Soil Science Society of America Journal* **1975**, *39* (5), 837–841.

(77) Liu, H.; Sun, X.; Yin, C.; Hu, C. Removal of Phosphate by Mesoporous ZrO2. *Journal of Hazardous Materials* **2008**, *151* (2), 616–622.

(78) Liu, H.; Chen, T.; Chang, J.; Zou, X.; Frost, R. L. The Effect of Hydroxyl Groups and Surface Area of Hematite Derived from Annealing Goethite for Phosphate Removal. *Journal of Colloid and Interface Science* **2013**, *398*, 88–94.

(79) Kang, S. A.; Li, W.; Lee, H. E.; Phillips, B. L.; Lee, Y. J. Phosphate Uptake by TiO2: Batch Studies and NMR Spectroscopic Evidence for Multisite Adsorption. *Journal of Colloid and Interface Science* **2011**, *364* (2), 455–461.

(80) D'Arcy, M.; Weiss, D.; Bluck, M.; Vilar, R. Adsorption Kinetics, Capacity and Mechanism of Arsenate and Phosphate on a Bifunctional TiO2–Fe2O3 Bi-Composite. *Journal of Colloid and Interface Science* **2011**, *364* (1), 205–212.

(81) Lǚ, J.; Liu, H.; Liu, R.; Zhao, X.; Sun, L.; Qu, J. Adsorptive Removal of Phosphate by a Nanostructured Fe–Al–Mn Trimetal Oxide Adsorbent. *Powder Technology* **2013**, *233*, 146–154.

(82) Recillas, S.; García, A.; González, E.; Casals, E.; Puntes, V.; Sánchez, A.; Font, X. Preliminary Study of Phosphate Adsorption onto Cerium Oxide Nanoparticles for Use in Water Purification; Nanoparticles Synthesis and Characterization. *Water Sci Technol* **2012**, *66* (3), 503–509.

(83) Su, Y.; Cui, H.; Li, Q.; Gao, S.; Shang, J. K. Strong Adsorption of Phosphate by Amorphous Zirconium Oxide Nanoparticles. *Water Res.* **2013**, *47* (14), 5018–5026.

(84) Su, Y.; Yang, W.; Sun, W.; Li, Q.; Shang, J. K. Synthesis of Mesoporous Cerium–Zirconium Binary Oxide Nanoadsorbents by a Solvothermal Process and Their Effective Adsorption of Phosphate from Water. *Chemical Engineering Journal* **2015**, *268*, 270–279.

(85) Zolgharnein, J.; Dalvand, K.; Rastgordani, M.; Zolgharnein, P. Adsorptive Removal of Phosphate Using Nano Cobalt Hydroxide as a Sorbent from Aqueous Solution; Multivariate Optimization and Adsorption Characterization. *Journal of Alloys and Compounds* **2017**, *725*, 1006–1017.

(86) Rashidi Nodeh, H.; Sereshti, H.; Zamiri Afsharian, E.; Nouri, N. Enhanced Removal of Phosphate and Nitrate Ions from Aqueous Media Using Nanosized Lanthanum Hydrous Doped on Magnetic Graphene Nanocomposite. *Journal of Environmental Management* **2017**, *197*, 265–274.

(87) Hirano, S.; Suzuki, K. T. Exposure, Metabolism, and Toxicity of Rare Earths and Related Compounds. *Environ Health Perspect* **1996**, *104* (Suppl 1), 85–95.

(88) Kyker, G. C.; Cress, E. A. Acute Toxicity of Yttrium, Lanthanum, and other Rare Earths. *Arch. Indust. Health* **1957**, *16* (6), 475–479.

(89) Li, W.; Pierre-Louis, A.-M.; Kwon, K. D.; Kubicki, J. D.; Strongin, D. R.; Phillips, B. L. Molecular Level Investigations of Phosphate Sorption on Corundum (α-Al2O3) by 31P Solid State NMR, ATR-FTIR and Quantum Chemical Calculation. *Geochimica et Cosmochimica Acta* **2013**, *107*, 252–266.

(90) Kazama, J. J. Oral Phosphate Binders: History and Prospects. *Bone* **2009**, *45*, S8–S12.

(91) Hou, L.; Liang, Q.; Wang, F. Mechanisms That Control the Adsorption–Desorption Behavior of Phosphate on Magnetite Nanoparticles: The Role of Particle Size and Surface Chemistry Characteristics. *RSC Advances* **2020**, *10* (4), 2378–2388.

(92) Sarkar, A.; Biswas, S. K.; Pramanik, P. Design of a New Nanostructure Comprising Mesoporous ZrO2 Shell and Magnetite Core (Fe3O4@mZrO2) and Study of Its Phosphate Ion Separation Efficiency. *J. Mater. Chem.* **2010**, *20* (21), 4417–4424.

(93) Parat, A.; Bordeianu, C.; Dib, H.; Garofalo, A.; Walter, A.; Bégin-Colin, S.; Felder-Flesch, D. Dendrimer–Nanoparticle Conjugates in Nanomedicine. *Nanomedicine* **2015**, *10* (6), 977–992.

(94) Cotin, G.; Piant, S.; Mertz, D.; Felder-Flesch, D.; Begin-Colin, S. Chapter 2 - Iron Oxide Nanoparticles for Biomedical Applications: Synthesis, Functionalization, and Application. In *Iron Oxide Nanoparticles for Biomedical Applications*; Mahmoudi, M., Laurent, S., Eds.; Metal Oxides; Elsevier, 2018; pp 43–88.

(95)   Cottrell, T. L. *The Strengths of Chemical Bonds*, 2nd ed.; Butterworths Publications: London, 1958.

(96)   Chitrakar, R.; Tezuka, S.; Sonoda, A.; Sakane, K.; Ooi, K.; Hirotsu, T. Phosphate Adsorption on Synthetic Goethite and Akaganeite. *Journal of Colloid and Interface Science* **2006**, *298* (2), 602–608.

(97)   Antelo, J.; Avena, M.; Fiol, S.; López, R.; Arce, F. Effects of PH and Ionic Strength on the Adsorption of Phosphate and Arsenate at the Goethite–Water Interface. *Journal of Colloid and Interface Science* **2005**, *285* (2), 476–486.

(98)   Guerrero, G.; Mutin, P. H.; Vioux, A. Anchoring of Phosphonate and Phosphinate Coupling Molecules on Titania Particles. *Chem. Mater.* **2001**, *13* (11), 4367–4373.

(99)   Nooney, M. G.; Campbell, A.; Murrell, T. S.; Lin, X.-F.; Hossner, L. R.; Chusuei, C. C.; Goodman, D. W. Nucleation and Growth of Phosphate on Metal Oxide Thin Films. *Langmuir* **1998**, *14* (10), 2750–

(100)   Shafi, K. V. P. M.; Ulman, A.; Dyal, A.; Yan, X.; Yang, N.-L.; Estournès, C.; Fournès, L.; Wattiaux, A.; White, H.; Rafailovich, M. Magnetic Enhancement of γ-Fe2O3 Nanoparticles by Sonochemical Coating. *Chem. Mater.* **2002**, *14* (4), 1778–1787. https://doi.org/10.1021/cm011535+.

(101)   Daou, T. J. Synthèse et Fonctionnalisation de Nanoparticules d'oxydes de Fer Magnétiques. thesis, Strasbourg 1, 2007.

(102)   Li, M.; Liu, J.; Xu, Y.; Qian, G. Phosphate Adsorption on Metal Oxides and Metal Hydroxides: A Comparative Review. *Environ. Rev.* **2016**, *24* (3), 319–332. https://doi.org/10.1139/er-2015-0080.

(103)   Lagergren, S. ZUR THEORIE DER SOGENANNTEN ADSORPTION GELOSTER STOFFE. *KUNGLIGA SVENSKA VETENSKAPSAKADEMIENS HANDLINGAR* **1898**, *24* (4), 1–39.

(104)   Simonin, J.-P. On the Comparison of Pseudo-First Order and Pseudo-Second Order Rate Laws in the Modeling of Adsorption Kinetics. *Chemical Engineering Journal* **2016**, *300*, 254–263.

(105)   Ho, Y. S.; McKay, G. Pseudo-Second Order Model for Sorption Processes. *Process Biochemistry* **1999**, *34* (5), 451–465.

(106)   Giles, C. H.; Smith, D.; Huitson, A. A General Treatment and Classification of the Solute Adsorption Isotherm. I. Theoretical. *Journal of Colloid and Interface Science* **1974**, *47* (3), 755–765.

(107)   Langmuir, I. THE CONSTITUTION AND FUNDAMENTAL PROPERTIES OF SOLIDS AND LIQUIDS. PART I. SOLIDS. *JACS* **1916**, *38* (11), 2221–2295.

(108)   Narayan, R.; Nayak, U. Y.; Raichur, A. M.; Garg, S. Mesoporous Silica Nanoparticles: A Comprehensive Review on Synthesis and Recent Advances. *Pharmaceutics* **2018**, *10* (3).

(109)   Topuz, B.; Şimşek, D.; Çiftçioğlu, M. Preparation of Monodisperse Silica Spheres and Determination of Their Densification Behaviour. *Ceramics International* **2015**, *41* (1, Part A), 43–52.

(110)   Ronda, L.; Bruno, S.; Campanini, B.; Mozzarelli, A.; Abbruzzetti, S.; Viappiani, C.; Cupane, A.; Levantino, M.; Bettati, S. Immobilization of Proteins in Silica Gel: Biochemical and Biophysical Properties. *Current Organic Chemistry* **2015**, *19* (17), 1653–1668.

(111)   Silva, C. R.; Airoldi, C. Acid and Base Catalysts in the Hybrid Silica Sol–Gel Process. *JCIS* **1997**, *195* (2), 381–387.

(112)   Kresge, C. T.; Leonowicz, M. E.; Roth, W. J.; Vartuli, J. C.; Beck, J. S. Ordered Mesoporous Molecular Sieves Synthesized by a Liquid-Crystal Template Mechanism. *Nature* **1992**, *359* (6397), 710–712.

(113)   Zhang, K.; Xu, L.-L.; Jiang, J.-G.; Calin, N.; Lam, K.-F.; Zhang, S.-J.; Wu, H.-H.; Wu, G.-D.; Albela, B.; Bonneviot, L.; Wu, P. Facile Large-Scale Synthesis of Monodisperse Mesoporous Silica Nanospheres with Tunable Pore Structure. *J. Am. Chem. Soc.* **2013**, *135* (7), 2427–2430.

(114)   Li, G.; Zhao, Z.; Liu, J.; Jiang, G. Effective Heavy Metal Removal from Aqueous Systems by Thiol Functionalized Magnetic Mesoporous Silica. *Journal of Hazardous Materials* **2011**, *192* (1), 277–283.

(115)   Mercier, L.; Pinnavaia, T. J. Heavy Metal Ion Adsorbents Formed by the Grafting of a Thiol Functionality to Mesoporous Silica Molecular Sieves: Factors Affecting Hg(II) Uptake. *Environ. Sci. Technol.* **1998**, *32* (18), 2749–2754.

(116)   Aguado, J.; Arsuaga, J. M.; Arencibia, A. Adsorption of Aqueous Mercury(II) on Propylthiol-Functionalized Mesoporous Silica Obtained by Cocondensation. *Ind. Eng. Chem. Res.* **2005**, *44* (10), 3665–3671.

(117)   Rostamian, R.; Najafi, M.; Rafati, A. A. Synthesis and Characterization of Thiol-Functionalized Silica Nano Hollow Sphere as a Novel Adsorbent for Removal of Poisonous Heavy Metal Ions from Water: Kinetics, Isotherms and Error Analysis. *Chemical Engineering Journal* **2011**, *171* (3), 1004–1011.

(118)   Thakur, A. K.; Nisola, G. M.; Limjuco, L. A.; Parohinog, K. J.; Torrejos, R. E. C.; Shahi, V. K.; Chung, W.-J. Polyethylenimine-Modified Mesoporous Silica Adsorbent for Simultaneous Removal of Cd(II) and Ni(II) from Aqueous Solution. *Journal of Industrial and Engineering Chemistry* **2017**, *49*, 133–144.

(119)   Dindar, M. H.; Yaftian, M. R.; Rostamnia, S. Potential of Functionalized SBA-15 Mesoporous Materials for Decontamination of Water Solutions from Cr(VI), As(V) and Hg(II) Ions. *Journal of Environmental Chemical Engineering* **2015**, *3* (2), 986–995.

(120) Heidari, A.; Younesi, H.; Mehraban, Z. Removal of Ni(II), Cd(II), and Pb(II) from a Ternary Aqueous Solution by Amino Functionalized Mesoporous and Nano Mesoporous Silica. *Chemical Engineering Journal* **2009**, *153* (1), 70–79.

(121) Morales, M. P.; Pecharroman, C.; Carreñ, T. G.; Serna, C. J. Structural Characteristics of Uniform γ-Fe2O3 Particles with Different Axial (Length/Width) Ratios. *Journal of Solid State Chemistry* **1994**, *108* (1), 158–163.

(122) Walter, A. Élaboration de Nano-Objets Magnétiques Dendronisés à Vocation Théranostic. These de doctorat, Strasbourg, 2014.

(123) Hulla, J.; Sahu, S.; Hayes, A. Nanotechnology: History and Future. *Hum Exp Toxicol* **2015**, *34* (12), 1318–1321.

(124) Feynman, R. P. There's Plenty of Room at the Bottom. *Engineering and Science* **1960**, *23* (5), 22–36.

(125) Toumey, C. Plenty of Room, Plenty of History. *Nature Nanotechnology* **2009**, *4*, 783–784.

(126) Lin, S.-S.; Gurol, M. D. Catalytic Decomposition of Hydrogen Peroxide on Iron Oxide: Kinetics, Mechanism, and Implications | Environmental Science & Technology. *Environ. Sci. Technol.* **1998**, *32* (10), 1417–1423.

(127) Pereira, M. C.; Oliveira, L. C. A.; Murad, E. Iron Oxide Catalysts: Fenton and Fentonlike Reactions – a Review. *Clay Minerals* **2012**, *47* (3), 285–302. https://doi.org/10.1180/claymin.2012.047.3.01.

(128) Wang, Y. J.; Hussain, S. M.; Krestin, G. P. Superparamagnetic Iron Oxide Contrast Agents: Physicochemical Characteristics and Applications in MR Imaging. *Eur Radiol* **2001**, *11*, 2319–2331.

(129) Basly, B.; Felder-Flesch, D.; Perriat, P.; Billotey, C.; Taleb, J.; Pourroy, G.; Begin-Colin, S. Dendronized Iron Oxide Nanoparticles as Contrast Agents for MRI. *Chem. Commun.* **2010**, *46* (6), 985–987.

(130) Chertok, B.; Moffat, B. A.; David, A. E.; Yu, F.; Bergemann, C.; Ross, B. D.; Yang, V. C. Iron Oxide Nanoparticles as a Drug Delivery Vehicle for MRI Monitored Magnetic Targeting of Brain Tumors. *Biomaterials* **2008**, *29* (4), 487–496.

(131) Peik-See, T.; Pandikumar, A.; Hong Ngee, L.; Nay Ming, H.; Chin Hua, C. Magnetically Separable Reduced Graphene Oxide/Iron Oxide Nanocomposite Materials for Environmental Remediation. *Catalysis Science & Technology* **2014**, *4* (12), 4396–4405.

(132) Teja, A. S.; Koh, P.-Y. Synthesis, Properties, and Applications of Magnetic Iron Oxide Nanoparticles. *Progress in Crystal Growth and Characterization of Materials* **2009**, *55* (1–2), 22–45.

(133) Estelrich, J.; Escribano, E.; Queralt, J.; Busquets, M. A. Iron Oxide Nanoparticles for Magnetically-Guided and Magnetically-Responsive Drug Delivery. *Int J Mol Sci* **2015**, *16* (4), 8070–8101.

(134) Kodama, R. H.; Berkowitz, A. E. Atomic-Scale Magnetic Modeling of Oxide Nanoparticles. *Phys. Rev. B* **1999**, *59* (9), 6321–6336.

(135) Iglesias, Ò.; Labarta, A. Role of Surface Disorder on the Magnetic Properties and Hysteresis of Nanoparticles. *Physica B: Condensed Matter* **2004**, *343* (1), 286–292.

(136) Kachkachi, H.; Ezzir, A.; Noguès, M.; Tronc, E. Surface Effects in Nanoparticles: Application to Maghemite γ-Fe2O3. *Eur. Phys. J. B* **2000**, *14* (4), 681–689.

(137) Baaziz, W.; Pichon, B. P.; Fleutot, S.; Liu, Y.; Lefevre, C.; Greneche, J.-M.; Toumi, M.; Mhiri, T.; Begin-Colin, S. Magnetic Iron Oxide Nanoparticles: Reproducible Tuning of the Size and Nanosized-Dependent Composition, Defects, and Spin Canting. *J. Phys. Chem. C* **2014**, *118* (7), 3795–3810.

(138) Sawatzky, G. A.; Van Der Woude, F.; Morrish, A. H. Mössbauer Study of Several Ferrimagnetic Spinels. *Phys. Rev.* **1969**, *187* (2), 747–757.

(139) Colombo, M.; Carregal-Romero, S.; Casula, M. F.; Gutiérrez, L.; Morales, M. P.; Böhm, I. B.; Heverhagen, J. T.; Prosperi, D.; Parak, W. J. Biological Applications of Magnetic Nanoparticles. *Chem. Soc. Rev.* **2012**, *41* (11), 4306–4334.

(140) Gerber, O.; Bégin-Colin, S.; Pichon, B. P.; Barraud, E.; Lemonnier, S.; Pham-Huu, C.; Daffos, B.; Simon, P.; Come, J.; Bégin, D. Design of Fe3–XO4 Raspberry Decorated Graphene Nanocomposites with High Performances in Lithium-Ion Battery. *Journal of Energy Chemistry* **2016**, *25* (2), 272–277.

(141) Pardieu, E.; Pronkin, S.; Dolci, M.; Dintzer, T.; Pichon, B. P.; Begin, D.; Pham-Huu, C.; Schaaf, P.; Begin-Colin, S.; Boulmedais, F. Hybrid Layer-by-Layer Composites Based on a Conducting Polyelectrolyte and Fe3O4 Nanostructures Grafted onto Graphene for Supercapacitor Application. *J. Mater. Chem. A* **2015**, *3* (45), 22877–22885.

(142) Kostopoulou, A.; Brintakis, K.; Fragogeorgi, E.; Anthousi, A.; Manna, L.; Begin-Colin, S.; Billotey, C.; Ranella, A.; Loudos, G.; Athanassakis, I.; Lappas, A. Iron Oxide Colloidal Nanoclusters as Theranostic Vehicles and Their Interactions at the Cellular Level. *Nanomaterials* **2018**, *8* (5), 315.

(143) Antone, A. J.; Sun, Z.; Bao, Y. Preparation and Application of Iron Oxide Nanoclusters. *Magnetochemistry* **2019**, *5* (3), 45.

(144) Yu, B. Y.; Kwak, S.-Y. Assembly of Magnetite Nanocrystals into Spherical Mesoporous Aggregates with a 3-D Wormhole-like Pore Structure. *J. Mater. Chem.* **2010**, *20* (38), 8320–8328.

(145) Lai, Q.; Zhu, S.; Luo, X.; Zou, M.; Huang, S. Ultraviolet-Visible Spectroscopy of Graphene Oxides. *AIP Advances* **2012**, *2* (3), 032146.

(146) Frka-Petesic, B.; Fresnais, J.; Berret, J.-F.; Dupuis, V.; Perzynski, R.; Sandre, O. Stabilization and Controlled Association of Superparamagnetic Nanoparticles Using Block Copolymers. *Journal of Magnetism and Magnetic Materials* **2009**, *321* (7), 667–670.

(147) Xia, H.; Foo, P.; Yi, J. Water-Dispersible Spherically Hollow Clusters of Magnetic Nanoparticles. *Chem. Mater.* **2009**, *21* (12), 2442–2451.

(148) Xia, H.-B.; Yi, J.; Foo, P.-S.; Liu, B. Facile Fabrication of Water-Soluble Magnetic Nanoparticles and Their Spherical Aggregates. *Chem. Mater.* **2007**, *19* (16), 4087–4091.

(149) Dušak, P.; Mertelj, A.; Kralj, S.; Makovec, D. Controlled Heteroaggregation of Two Types of Nanoparticles in an Aqueous Suspension. *Journal of Colloid and Interface Science* **2015**, *438*, 235–243.

(150) Sathya, A.; Kalyani, S.; Ranoo, S.; Philip, J. One-Step Microwave-Assisted Synthesis of Water-Dispersible Fe3O4 Magnetic Nanoclusters for Hyperthermia Applications. *Journal of Magnetism and Magnetic Materials* **2017**, *439*, 107–113.

(151) Liao, X.; Zhu, J.; Zhong, W.; Chen, H.-Y. Synthesis of Amorphous Fe2O3 Nanoparticles by Microwave Irradiation. *Materials Letters* **2001**, *50* (5), 341–346.

(152) Hemery, G.; Keyes, A. C.; Garaio, E.; Rodrigo, I.; Garcia, J. A.; Plazaola, F.; Garanger, E.; Sandre, O. Tuning Sizes, Morphologies, and Magnetic Properties of Monocore Versus Multicore Iron Oxide Nanoparticles through the Controlled Addition of Water in the Polyol Synthesis. *Inorg. Chem.* **2017**, *56* (14), 8232–8243.

(153) Gerber, O.; Pichon, B. P.; Ulhaq, C.; Grenèche, J.-M.; Lefevre, C.; Florea, I.; Ersen, O.; Begin, D.; Lemonnier, S.; Barraud, E.; Begin-Colin, S. Low Oxidation State and Enhanced Magnetic Properties Induced by Raspberry Shaped Nanostructures of Iron Oxide. *J. Phys. Chem. C* **2015**, *119* (43), 24665–24673.

(154) Gerber, O.; Pichon, B. P.; Ihiawakrim, D.; Florea, I.; Moldovan, S.; Ersen, O.; Begin, D.; Grenèche, J.-M.; Lemonnier, S.; Barraud, E.; Begin-Colin, S. Synthesis Engineering of Iron Oxide Raspberry-Shaped Nanostructures. *Nanoscale* **2016**, *9* (1), 305–313.

(155) Pileni, M. P. Nanocrystal Self-Assemblies: Fabrication and Collective Properties. *J. Phys. Chem. B* **2001**, *105* (17), 3358–3371.

(156) Andrade Sales, E.; Benhamida, B.; Caizergues, V.; Lagier, J.-P.; Fiévet, F.; Bozon-Verduraz, F. Alumina-Supported Pd, Ag and Pd–Ag Catalysts: Preparation through the Polyol Process, Characterization and Reactivity in Hexa-1,5-Diene Hydrogenation. *Applied Catalysis A: General* **1998**, *172* (2), 273–283.

(157) Viau, G.; Fiévet-Vincent, F.; Fiévet, F. Nucleation and Growth of Bimetallic CoNi and FeNi Monodisperse Particles Prepared in Polyols. *Solid State Ionics* **1996**, *84* (3), 259–270.

(158) Ammar, S.; Jouini, N.; Fiévet, F.; Stephan, O.; Marhic, C.; Richard, M.; Villain, F.; Cartier dit Moulin, Ch.; Brice, S.; Sainctavit, Ph. Influence of the Synthesis Parameters on the Cationic Distribution of ZnFe2O4 Nanoparticles Obtained by Forced Hydrolysis in Polyol Medium. *Journal of Non-Crystalline Solids* **2004**, *345–346*, 658–662.

(159) Huang, L.; Peng, F.; Yu, H.; Wang, H. Synthesis of Cu2O Nanoboxes, Nanocubes and Nanospheres by Polyol Process and Their Adsorption Characteristic. *Materials Research Bulletin* **2008**, *43* (11), 3047–3053.

(160) Uchaker, E.; Zhou, N.; Li, Y.; Cao, G. Polyol-Mediated Solvothermal Synthesis and Electrochemical Performance of Nanostructured V2O5 Hollow Microspheres. *J. Phys. Chem. C* **2013**, *117* (4), 1621–1626.

(161) Courtel, F. M.; Baranova, E. A.; Abu-Lebdeh, Y.; Davidson, I. J. In Situ Polyol-Assisted Synthesis of Nano-SnO2/Carbon Composite Materials as Anodes for Lithium-Ion Batteries. *Journal of Power Sources* **2010**, *195* (8), 2355–2361.

(162) Liu, L.; Yang, Y. Shape-Controlled Synthesis of MnCo Complex Oxide Nanostructures via a Polyol-Based Precursor Route and Their Catalytic Properties. *Superlattices and Microstructures* **2013**, *54*, 26–38.

(163) Zhu, Y.; Zhao, W.; Chen, H.; Shi, J. A Simple One-Pot Self-Assembly Route to Nanoporous and Monodispersed Fe3O4 Particles with Oriented Attachment Structure and Magnetic Property. *J. Phys. Chem. C* **2007**, *111* (14), 5281–5285.

(164) Guan, N.; Wang, Y.; Sun, D.; Xu, J. A Simple One-Pot Synthesis of Single-Crystalline Magnetite Hollow Spheres from a Single Iron Precursor. *Nanotechnology* **2009**, *20* (10), 105603.

(165) Xuan, S.; Wang, Y.-X. J.; Yu, J. C.; Cham-Fai Leung, K. Tuning the Grain Size and Particle Size of Superparamagnetic Fe3O4 Microparticles. *Chem. Mater.* **2009**, *21* (21), 5079–5087.

(166) Cheng, C.; Xu, F.; Gu, H. Facile Synthesis and Morphology Evolution of Magnetic Iron Oxide Nanoparticles in Different Polyol Processes. *New J. Chem.* **2011**, *35* (5), 1072–1079.

(167) Liu, H.; Ji, S.; Zheng, Y.; Li, M.; Yang, H. Modified Solvothermal Synthesis of Magnetic Microspheres with Multifunctional Surfactant Cetyltrimethyl Ammonium Bromide and Directly Coated Mesoporous Shell. *Powder Technology* **2013**, *246*, 520–529.

(168) Brayner, R.; Fiévet, F.; Coradin, T. *Nanomaterials: A Danger or a Promise?: A Chemical and Biological Perspective*; Springer Science & Business Media, 2012.

(169) Lide, D. R. *CRC Handbook of Chemistry and Physics: A Ready-Reference Book of Chemical and Physical Data*; CRC Press, 1995.

(170) Cheng, C.; Xu, F.; Gu, H. Facile Synthesis and Morphology Evolution of Magnetic Iron Oxide Nanoparticles in Different Polyol Processes. *New J. Chem.* **2011**, *35* (5), 1072–1079.

(171) Zhu, L.-P.; Xiao, H.-M.; Zhang, W.-D.; Yang, G.; Fu, S.-Y. One-Pot Template-Free Synthesis of Monodisperse and Single-Crystal Magnetite Hollow Spheres by a Simple Solvothermal Route. *Crystal Growth & Design* **2008**, *8* (3), 957–963.

(172) Cheng, C.; Wen, Y.; Xu, X.; Gu, H. Tunable Synthesis of Carboxyl-Functionalized Magnetite Nanocrystal Clusters with Uniform Size. *J. Mater. Chem.* **2009**, *19* (46), 8782–8788.

(173) Liang, J.; Ma, H.; Luo, W.; Wang, S. Synthesis of Magnetite Submicrospheres with Tunable Size and Superparamagnetism by a Facile Polyol Process. *Materials Chemistry and Physics* **2013**, *139* (2), 383–388.

(174) Yu, D.; Sun, X.; Zou, J.; Wang, Z.; Wang, F.; Tang, K. Oriented Assembly of Fe3O4 Nanoparticles into Monodisperse Hollow Single-Crystal Microspheres. *J. Phys. Chem. B* **2006**, *110* (43), 21667–21671.

(175) Yuan, H.; Wang, Y.; Zhou, S.-M.; Lou, S. Fabrication of Superparamagnetic Fe3O4 Hollow Microspheres with a High Saturation Magnetization. *Chemical Engineering Journal* **2011**, *175*, 555–560.

(176) Cao, S.-W.; Zhu, Y.-J.; Chang, J. Fe3O4 Polyhedral Nanoparticles with a High Magnetization Synthesized in Mixed Solvent Ethylene Glycol–Water System. *New J. Chem.* **2008**, *32* (9), 1526–1530.

(177) Chang, Y.; Teo, J. J.; Zeng, H. C. Formation of Colloidal CuO Nanocrystallites and Their Spherical Aggregation and Reductive Transformation to Hollow Cu2O Nanospheres. *Langmuir* **2005**, *21* (3), 1074–1079.

(178) Hong, Y.; Shi, H.; Shu, X.; Zheng, Y.; Zhang, Y.; Wu, Y. Controlled Synthesis of Hollow Magnetic Fe3O4 Nanospheres: Effect of the Cooling Rate. *Particuology* **2017**, *33*, 24–28.

(179) Hu, P.; Yu, L.; Zuo, A.; Guo, C.; Yuan, F. Fabrication of Monodisperse Magnetite Hollow Spheres. *J. Phys. Chem. C* **2009**, *113* (3), 900–906.

(180) Nguyen, D. T.; Kim, K.-S. Template-Free Synthesis and Characterization of Monodisperse Magnetite Hollow Nanoparticles Through Solvothermal Process. *Journal of Nanoscience and Nanotechnology* **2013**, *13* (8), 5773–5776.

(181) Santoyo Salazar, J.; Perez, L.; de Abril, O.; Truong Phuoc, L.; Ihiawakrim, D.; Vazquez, M.; Greneche, J.-M.; Begin-Colin, S.; Pourroy, G. Magnetic Iron Oxide Nanoparticles in 10−40 Nm Range: Composition in Terms of Magnetite/Maghemite Ratio and Effect on the Magnetic Properties. *Chem. Mater.* **2011**, *23* (6), 1379–1386.

(182) Demortière, A.; Panissod, P.; Pichon, B. P.; Pourroy, G.; Guillon, D.; Donnio, B.; Bégin-Colin, S. Size-Dependent Properties of Magnetic Iron Oxide Nanocrystals. *Nanoscale* **2011**, *3* (1), 225–232.

(183) Mørup, S.; Bo Madsen, M.; Franck, J.; Villadsen, J.; Koch, C. J. W. A New Interpretation of Mössbauer Spectra of Microcrystalline Goethite: "Super-Ferromagnetism" or "Super-Spin-Glass" Behaviour? *Journal of Magnetism and Magnetic Materials* **1983**, *40* (1), 163–174.

(184) Chen, P.; Cui, B.; Bu, Y.; Yang, Z.; Wang, Y. Synthesis and Characterization of Mesoporous and Hollow-Mesoporous $M_xFe_{3-X}O_4$ (M=Mg, Mn, Fe, Co, Ni, Cu, Zn) Microspheres for Microwave-Triggered Controllable Drug Delivery. *J Nanopart Res* **2017**, *19* (12), 398.

(185) Li, W.; Qiao, X.; Zheng, Q.; Zhang, T. One-Step Synthesis of MFe2O4 (M=Fe, Co) Hollow Spheres by Template-Free Solvothermal Method. *Journal of Alloys and Compounds* **2011**, *509* (21), 6206–6211.

(186) Deng, H.; Chen, H.; Li, H. Synthesis of Crystal MFe2O4 (M=Mg, Cu, Ni) Microspheres. *Materials Chemistry and Physics* **2007**, *101* (2), 509–513.

(187) Wang, X.; Hu, C. G.; Xi, Y.; Xia, C. H.; He, X. S. Al-Doped Fe3O4 Nanoparticles and Their Magnetic Properties. *J Supercond Nov Magn* **2010**, *23* (6), 909–911.

(188) Aghazadeh, M.; Karimzadeh, I.; Reza Ganjali, M.; Malekinezhad, A. Al3+ Doped Fe3O4 Nanoparticles: A Novel Preparation Method, Structural, Magnetic and Electrochemical Characterizations. *Int. J. Electrochem. Sci.* **2017**, *12*, 8033–8044.

(189) Ehsani, M. H.; Esmaeili, S.; Aghazadeh, M.; Kameli, P.; Tehrani, F. S.; Karimzadeh, I. An Investigation on the Impact of Al Doping on the Structural and Magnetic Properties of Fe3O4 Nanoparticles. *Appl. Phys. A* **2019**, *125* (4), 280.

(190)   Xu, J.; Luu, L.; Tang, Y. Phosphate Removal Using Aluminum-Doped Magnetic Nanoparticles. *Desalination and water treatment* **2017**, *58*.

(191)   Mason, T. O.; Bowen, H. K. Electronic Conduction and Thermopower of Magnetite and Iron-Aluminate Spinels. *Journal of the American Ceramic Society* **1981**, *64* (4), 237–242.

(192)   Sartori, K. Studying the Interfacial Exchange Coupling within Ferrite Based Magnetic Nanoparticles Prepared Following to a Succession of Thermal Decomposition Synthesis. These de doctorat, Strasbourg, 2019.

(193)   Sartori, K.; Choueikani, F.; Gloter, A.; Begin-Colin, S.; Taverna, D.; Pichon, B. P. Room Temperature Blocked Magnetic Nanoparticles Based on Ferrite Promoted by a Three-Step Thermal Decomposition Process. *J. Am. Chem. Soc.* **2019**, *141* (25), 9783–9787.

(194)   https://www.klipartz.com/es/sticker-png-hywhy

(195)   https://www.behance.net/gallery/66228279/Illustrator-diagrams

Chapter II
Highly chelating stellate mesoporous silica nanoparticles for specific iron removal from biological media

Introduction

Herein, this work aims at developing a new generation of functionalized large pore silica NPs that could contribute to specific removal of iron in biological environments. Our approach consists in grafting large pore stellate mesoporous silica (STMS) NPs with a specific iron chelator, such as DFoB and evaluating the selective capture of iron(III). The benefit of these NPs design is the high surface area (*ca.* 500 $m^2 \cdot g^{-1}$) of STMS NPs and a suitable pore volume (*ca.* 15 nm) that allow a high grafting rate of DFOB ligands (*ca.* 410 $\mu g \cdot mg^{-1}$ or 730 $nmol \cdot mg^{-1}$ STMS). In our group, we already used such STMS as building blocks either by grafting quantum dots in their pores or by incorporating a magnetic iron oxide core in STMS[37,38] allowing to form new multimodal nanomaterials for magnetic hyperthermia, MRI and fluorescence imaging applications. Here too, the design of large pore MS is highly desirable regarding depollution applications as compared to small pores. However, to the best of our knowledge, the reported strategies on silica supports mainly described non-specific ligands that can chelate together a broad range of heavy metallic species for environmental applications.[1–4] There is therefore an urgent need to develop approaches allowing to extract cations more selectively for bioremediation in human organism or from biological environments, but only a few studies have been focused on this research topic so far.[5,6] In this work, STMS platforms are used for the first time for depollution applications.

To reach such a functionalized nanomaterial, several steps are necessary as pictured in Scheme 1. First, after STMS NPs synthesis by a surfactant mediated sol-gel process[7], a three step covalent binding allows us to efficiently graft DFoB at the surface of silica. Next, DFoB-STMS have been tested for iron(III) uptake properties in HEPES-buffered solutions (physiological pH). Nitrilotriacetic acid (NTA) is used as an auxiliary ligand of iron(III) to prevent its precipitation into insoluble iron(III) hydroxide species and affords a time stable 1:1 stoichiometric FeNTA complex (log K_{FeNTA} = 6.0(3) at pH 7.4 and log $K_{f\,FeNTA}$ ~15-16)[8,9]. The moderate stability of FeNTA ensures successful ligand exchange processes in aqueous solution with $DFoB_{grafted}$ (or DFoB-STMS). Next, the Fe(III) uptake capacities of the newly designed DFOB grafted nanosystems were investigated to get a deeper understanding of the kinetics and thermodynamic aspects of the ligand exchange between NTA and DFoB-STMS. At last, the selectivity of iron(III) uptake of DFoB-STMS with respect to other metal ions (mixture of relevant cations) was investigated as well. The aim of our work was to develop smart nanoplatforms with high efficiency and selectivity towards iron for metal overload treatments.
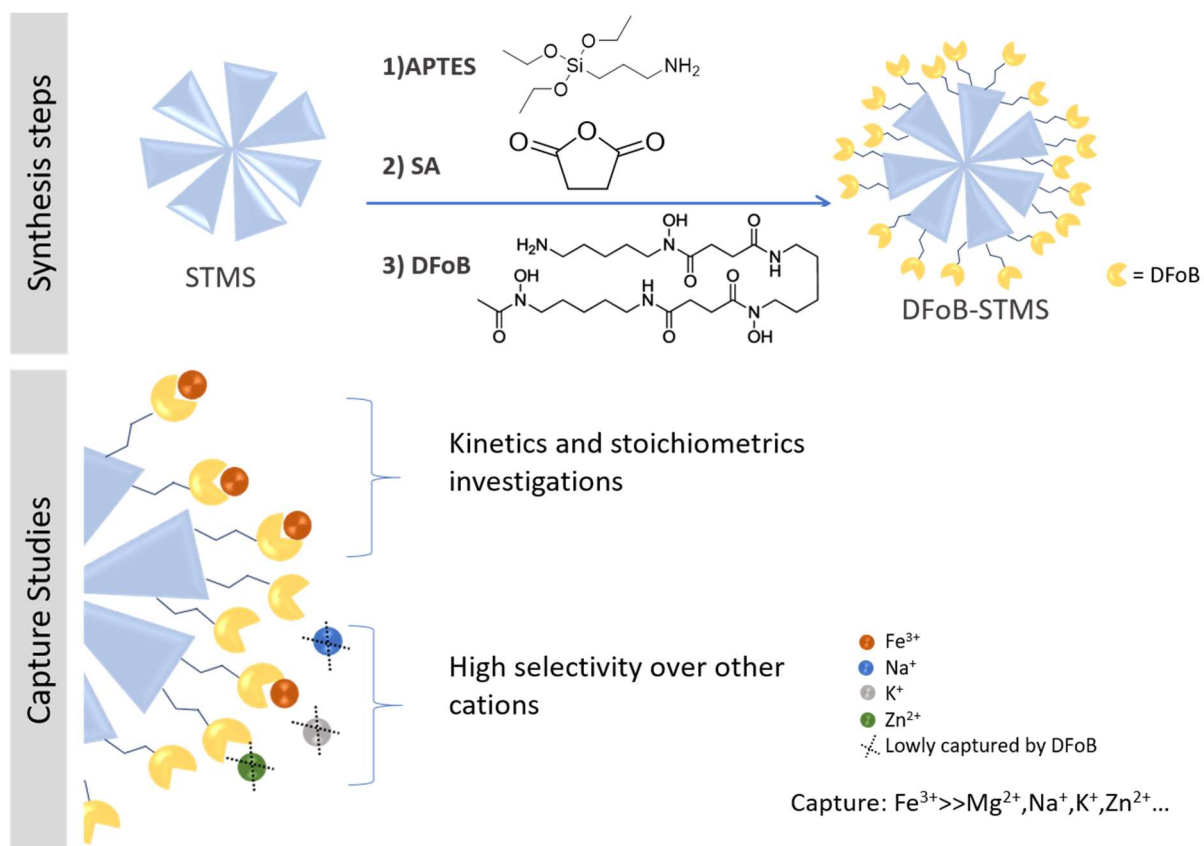
Scheme 1. General concept schematizing the synthesis of the STMS NPs, the grafting of DFoB and the subsequent applications of these materials for metal removal.

II. 1. Experimental Section

Products. Cetyltrimethylammonium tosylate (CTATos, ≥98.0%), 2-amino-2-hydroxymethyl-1,3-propanediol (AHMPD, ≥99.9%), 3-aminopropyltriethoxysilane (APTES, 99%) and succinic anhydride (SA, ≥99%) were purchased from Sigma Aldrich; tetraethyl orthosilicate (TEOS, ≥99.0%) was purchased from Alfa Aesar. 1-ethyl-3-(3-dimethylaminopropyl)carbodiimide hydrochloride (EDC, >98.0%) was obtained from Tokyo Chemical Industry (TCI). Desferrioxamine B (DFoB) was obtained from Ciba-Geigy under its mesylate salt, while ammonium hydroxide sodium (NH_4OH) was purchased from Sigma Aldrich (puriss, p.a.). Fe(III) perchlorate hydrate ($Fe(ClO_4)_3 \cdot xH_2O$, Alfa Aesar (reagent grade), nitrilotriacetic acid trisodium salt, monohydrate (Fluka, prum, > 98%), 4-(2-hydroxyethyl)-1-piperazineethanesulfonic acid (HEPES, Sigma Life Science, ≥99.5%) and perchloric acid ($HClO_4$, normapur, 70% min), $AlCl_3 \cdot 6H_2O$ (99%) from Sigma Aldrich, different salts: NaCl from Carlo Erba (technical grade), $ZnCl_2$ (≥98%), $CaCl_2$ (≥97%) and $Ca(NO_3)_2 \cdot 4H_2O$ (≥98%) from Prolabo, $MgCl_2 \cdot 6H_2O$ (reagent grade) from Merck, KCl (>99%) from Labosi, $MgSO_4 \cdot 7H_2O$ (≥99.5%) from RP Normapur. All the products were used as received.

CAUTION! Perchlorate salts combined with organic ligands are potentially explosive and should be handled in small quantities and with the adequate precautions.[10]

II. 1. 1. Synthesis of stellate mesoporous silica nanoparticles (STMS)

In a 500 mL flask, 3.80 g of CTATos, 0.436 g of AHMPD and 200 mL of distilled water were introduced and stirred at 80 °C up to complete dissolution (about 1h15). Next, 20.55 g (22 mL) of TEOS was added to the mixture, and stirred for 2h at 80 °C. A white precipitate of stellate mesoporous silica denoted STMS was formed and filtered under vacuum. The precipitate was washed three times with distilled water and dried overnight. The resulted powder was calcined at 600 °C for 6h to remove the CTATos surfactant. Next, around 5 g of this white powder was obtained and crushed with a mortar. 1 g of the crushed powder was added to 50 mL of ethanol in a centrifuge tube and sonicated during 10 minutes. About a half of the particles aggregated and fell to the bottom of the tube. The supernatant was separated and the precipitate was dried and then crushed again before adding it to the 50 mL of supernatant to disperse more particles. The suspension was treated with an ultrasound tip for a 20 minutes' cycle, and then the supernatant was isolated from precipitate.

II. 1. 2. Functionalization of the surface

Functionalization of STMS with aminopropyltriethoxysilane (APTES). 25 mL of STMS in ethanol (10 mg·mL^{-1}) were added to 7 mL of ethanol in a tube with 1.2 mL of NH_4OH. The mixture was stirred for 5 minutes, and 5 mL APTES was added. The tube was mixed for 2 hours then separated in two and washed twice with 15 mL ethanol before being re-dispersed in 20 mL of ethanol.

Functionalization of STMS with carboxylic acids and grafting of Desferrioxamine B. A dispersion of the previously APTES-STMS obtained in DMF (15 mL) at 10 mg·mL^{-1} was added dropwise to a tube containing 30 mL of 0.1 M succinic anhydride (SA, 3 mol, 300 mg) in DMF to convert the amine into carboxylic functions. DMF must be anhydrous as water would hydrolyze the SA into succinic acid. The mixture was stirred for 24h, the resulting stellate MS NPs with carboxylic-function groups at their

surface (STMS–COOH) were washed by centrifugation and redispersed in ethanol, repeated 3 times (20 mL). In the next step, 10 mL of COOH-STMS (10 mg·ml^{-1}) was dispersed in Na$_2$CO$_3$ buffer pH 7.2 (10 mg·mL^{-1}), and were brought in contact with DFoB (222.6 mg) bearing amino groups. A first addition of 159 mg EDC as activator agent was achieved and the tube was stirred for 1h. Then, 4 additional add-ons of EDC were performed each hour in order to activate the carboxyl functions left then, the reactional media was stirred overnight before proceeding to several washings with water.

II. 1. 3. Iron capture experiments

Fe(III) stock solutions. Fe(III) perchlorate stock solutions were freshly prepared in water at acidic pH (pH < 1.5) immediately before use and their concentrations were ascertained by UV-visible absorption spectrophotometry (ε^{240} = 4.16 x 10^3 M^{-1} cm^{-1} et ε^{260} = 2.88 x 10^3 M^{-1} cm^{-1})[11]. The glassware used was rinsed after each experiment with a hydrochloric acid solution to remove all traces of iron.

Iron nitroacetic (FeNTA) solution. 25 mL of a stock FeNTA solution (5 × 10^{-3} M) were freshly prepared by adding an aqueous solution of iron(III) (1 equiv.), whose concentration (3.8 × 10^{-2} M) was previously determined (*vide supra*). A slight excess of NTA (1.1 equiv.) with respect to iron(III) was always used to ensure complete complexation of iron(III) and avoid free ferric species in solution at pH = 7.4. The pH of the mixture was then raised to 7.4 with the help of a HEPES buffer (50 mM, pH 7.4).

Kinetics investigations. 0.78 mg of the functionalized DFoB-STMS (equivalent to 0.52 mg STMS) were dispersed in 1.5 ml of a FeNTA solution (2.16·x 10^{-4} M) to ensure a stoichiometric amount at 0.85:1 of FeNTA with respect to DefoB$_{grafted}$ This solution was stirred over different reaction times (from 30 min to 1 day) and then centrifuged at 10 000 g for 10 minutes. The STMS-DFoB-Fe were washed 2 times with 1 mL of the HEPES buffered solution. The supernatants were then analyzed using UV-visible absorption spectrophotometry. An excess of free DFoB was added to the supernatant to ensure complete complexation of the unreacted FeNTA and the corresponding Fe(III) concentrations were evaluated from the absorbance measurement at 430 nm (LMCT absorption band of Fe**DFoB** at 430 nm, ε^{430} = 2950 M^{-1}·cm^{-1})[12].

Thermodynamic investigations. 0.78 mg of the functionalized DFoB-STMS (equivalent to 0.52 mg STMS) were dispersed in 1.5 ml of a FeNTA solution whose concentration was varied from 4.3 x 10^{-5} M to 4.3 x 10^{-4} M to ensure a variable stoichiometric amount in the range 0.17-1.7 :1 of FeNTA with respect to DFoB$_{grafted}$. The mixture was stirred during 30 min and centrifuged at 10 000 g for 10 minutes. The nanoparticles were then washed twice with 1 mL of the HEPES buffered solution. The supernatants were analyzed using UV-visible absorption spectrophotometry using the same protocol than that used for the kinetic study (see above).

Fe(III) selectivity of the DFoB-STMS. These experiments were conducted under two different conditions. In a first serie, the DFoB-STMS NPs (7.7 mg of DFoB-STMS, equivalent to 5.1 mg STMS) were subjected to a HEPES buffered solution (13.2 mL) containing FeNTA (0.27 mM) containing several metal salts of interest used at same concentration: CaCl$_2$, ZnCl$_2$ and MgCl$_2$. Na$^+$ cation was also used at 1.159 mM, a higher concentration than other ions because a NaOH solution (2 M) was necessary to fix the pH of the HEPES solution. In the second approach, 7.7 mg of the DFoB-STMS NPs were dispersed in a

Barth's buffer[13]. This medium was reported to mimic the extracellular brain ionic composition (NaCl 88 mM, KCl 1 mM, $MgSO_4$ 0.82 mM, $NaHCO_3$ 2.4 mM, $CaCl_2$ 0.91 mM, $Ca(NO_3)_2$ 0.33 mM adjusted at pH 7.4 with a HEPES buffered solution at 10 mM). For these two types of experiments, the reaction mixtures were stirred for 30 min, centrifuged and the NPs were washed twice with the HEPES buffered solution. The elements content of the supernatants was analyzed by Inductively Coupled Plasma-Atomic Emission Spectroscopy (ICP-AES).

II. 1. 4. Characterizations techniques

Transmission Electron Microscopy (TEM and TEM-EDX). A transmission electron microscope JEOL 2100 high-resolution microscope operating at 200 kV was used to characterize the size and morphology of the STMS silica. EDX was used to investigate the presence of Fe and Si elements.

Dynamic Light Scattering (DLS) and Zeta Potential (ZP). The zetasizer Nano ZS from Malvern DLS was used to characterize the properties of colloidal suspensions: the hydrodynamic diameter and the dispersity in size in intensity mode. Measurements of surface Zeta potential were performed to get insights into the surface charge of the particles.

Thermal Gravimetric Analysis (TGA). TGA was performed on a TA SDT 600 instrument to measure the loss mass of the sample when the temperature changed. With these results, the amount of organic compound grafted on functionalized inorganic STMS nanoparticles can be quantified.

The Brunauer-Emmett-Teller (BET) nitrogen (N_2) adsorption/desorption isotherms. To characterize the porosity of the silica nanoparticles, adsorption and desorption of nitrogen isotherms were measured on a ASAP 2420 V instrument with around 100 mg of STMS nanoparticles. The Brunauer-Emmett-Teller (BET) method was used to calculate the surface area, and the pore size was obtained according to BJH (Barrett, Joyner and Halenda) model.

UV-visible Absorption Spectrophotometry. For the FeNTA supernatants analyses, 1.1 eq of free DFoB in solution ($DFoB_{free}$) was added to 1 ml of supernatant solution to ensure complete complexation of iron(III). The color changes from light yellow to orange (confirming the NTA-DFoB ligand exchange). The solutions were analyzed (from 200 to 800 nm) with quartz optical cell (Hellma) using either a CARY50 Probe Varian absorption spectrophotometer or an Agilent CARY5000 absorption spectrophotometer maintained at 25.0 (2) °C (Lauda E200 thermostat) between 200 and 800 nm.

Inductively Coupled Plasma-Atomic Emission Spectroscopy (ICP-AES). Iron concentrations of initial and extracted solutions were measured using ICP-AES with a Varian 720 ES instrument.

CHNS elemental analysis. The amino groups grafted on the silica surface (APTES-STMS) were analyzed using a CHNS apparatus.

II. 2. Results and Discussion

II. 2. 1. Synthesis and characterization of stellate mesoporous silica nanoparticles (STMS NPs) suspensions

Mesoporous silica (MS) NPs having a stellate morphology (STMS) were prepared through the sol-gel procedure using the structure directing agent CTATos as described previously[7,14]. Low magnification TEM image in Figure 1.A shows a narrow size distribution of 95±6 nm of nicely structured STMS with a homogenous stellate morphology. A magnified image (Figure 1.B) clearly shows more in detail the stellate pore morphology. The porous properties (*i.e.*, surface area, pore size, pore volume) of the STMS were investigated by BET-nitrogen adsorption (Figure S1). In a typical sample, nitrogen adsorption isotherm provided a surface area S_{BET} of *ca*. 498 m²·g⁻¹ associated with a pore size of 16 nm. These results were consistent with those of the literature by comparing the STMS obtained from Zhang et al.[15] having a surface area S_{BET} of 590 m²·g⁻¹ for particles of 130 nm and a pore size close to 17 nm. The STMS were then dispersed in ethanol or in water (pH=7) and formed excellent colloidal suspensions in those solvents with hydrodynamic diameters (Dh) of *ca*. 164 and 141nm, respectively (Figure 1.C). This colloidal stability is very favourable to a further homogenous functionalization of the NPs. The slightly larger mean hydrodynamic diameter of the STMS particle suspensions by comparison with the mean TEM diameter is attributed to the solvation shell and the inherent effects of NPs distribution in liquid suspensions. Zeta potential (ZP) measurements as a function of the pH in water were also performed (Figure 1.D). The ZP values were found to decrease from 1.8 mV at pH= 1.5 to -15 mV at pH=7.2 and the pH range beyond. The isoelectric point (IEP) of the STMS in water was found at *ca.* pH = 4 which is in agreement with such silica nanomaterials. [16]
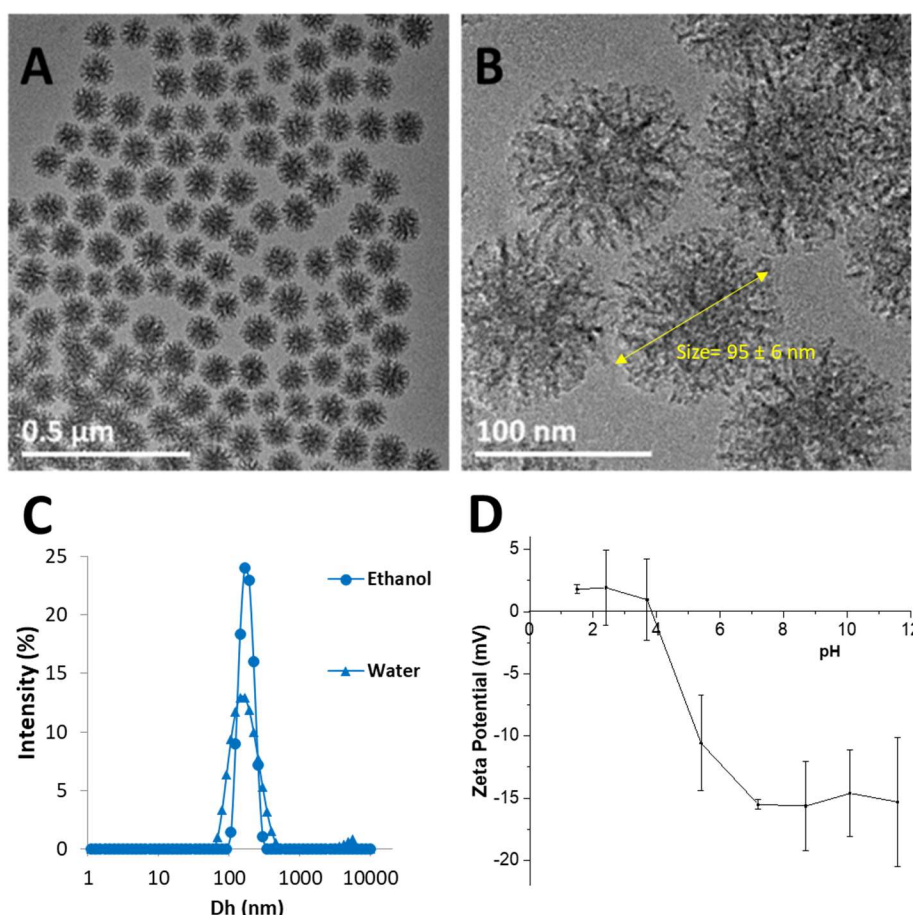
Figure 1. TEM images of STMS at A. low and B. high magnification. C. DLS size distributions in intensity mode in water and in EtOH of the STMS. D. ZP curve of the STMS in water *versus* pH.

II. 2. 2. Silica surface modification with Desferrioxamine (DFoB) ligand

The DFoB grafting at the silica surface requires three surface modification steps as shown in Scheme 2. The first one corresponds to the surface modification with aminopropyltriethoxysilane (APTES) by a condensation reaction in ethanol. In the second step, the amine groups of STMS are transformed into carboxylic acid functions using succinic anhydride (SA) and finally, those carboxylic groups are activated with 1-ethyl-3-3-dimethylaminopropylcarbodiimide hydrochloride (EDC) to react with the terminal amine function of the DFoB ligand.
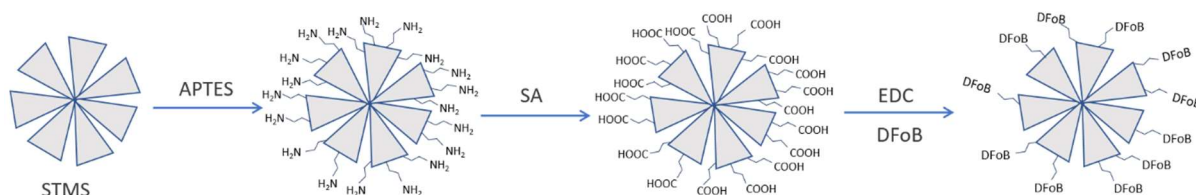
Scheme 2. Scheme describing the grafting of DFoB on STMS. It involves the introduction of carboxylic groups after reaction with APTES-STMS. A last step consists in coupling the EDC-activated carboxylic functions with the amine group of DFoB.

The grafting of APTES onto bare STMS surface to introduce amine terminal functions was obtained via the well-known procedure of silanization. The reaction is done in ethanol where the STMS particles are well dispersed in presence of ammoniac (Stöber-like conditions)[17] to form a NH_2 layer. As the grafting occurs, the surface of STMS is modified and the zeta potential value at same pH (7.2) increased from -15.5 mV to +20.3 mV. The charge reversal and positive value obtained after the reaction is consistent with the presence of ammonium groups of APTES grafted on the STMS. TGA was performed to quantify the organic content of these samples. In Figure 2, for both samples, STMS and APTES-STMS, a first weight loss was observed at 100°C, which was attributed to evaporation of solvent trapped inside the pores, even though the samples are dried before the measurements. For STMS (blue curve), a continuous weight loss is observed between 500 and 700 °C, and corresponds to the dehydroxylation of the silicate frameworks.[15] Several weight losses between 350 °C and 530 °C are linked to the burning of organic molecules grafted on the STMS. The grafting rate, previously defined as the amount of APTES grafted versus the mass of STMS, was then calculated to be at about 129 $\mu g_{APTES} \cdot mg_{STMS}^{-1}$ (weight loss 11%), which leads to a concentration of 2.9 amino functions per nm² (Figure S2). Elemental analysis of C, H and N conducted to a grafting rate of 2.7 NH_2 functions per nm² (Table S2) which is in the same range value than TGA results. Furthermore, grafting is close with these of Schiestel et al. who reported 1.8 amino functions per nm² [18]. Therefore, the grafting of APTES was successfully completed ensuring a good coverage of the STMS NPs surface with amino functions.
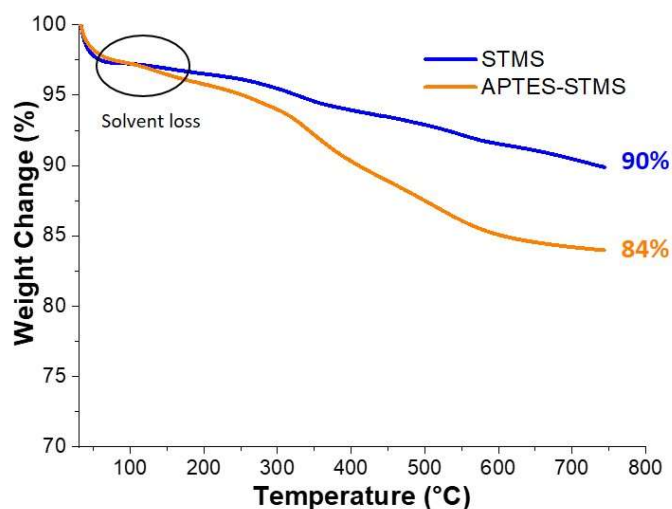
Figure 2. TGA curves of STMS (blue) and APTES-STMS (orange).

The introduction of surface carboxylic groups was performed by reacting the amine functions of APTES-STMS with succinic anhydride (SA) in DMF. The carboxylic acid groups were generated by a ring opening linker elongation reaction of the amine groups with the SA cycle. The formed COOH-STMS bonds were characterized by TGA and ZP measurements. TGA data indicated a weight loss of 17.5 wt% for the APTES and COOH organic layers (grey curve) which corresponds to 6.6 wt% specifically for the COOH grafts on STMS (Figure 3.A) (values without solvent contributions). This allowed to calculate a grafting rate of 84 $\mu g \cdot mg^{-1}$ for COOH groups on STMS which after calculations correspond to a surface density of *ca*. 1 COOH functions per nm², suggesting that *ca.* a third of amine functions have reacted with SA. Moreover, these results are consistent with the values obtained by An *et al.*[20]. With regard to

the surface charge measured at pH 7.2 at each critical steps of the functionalization (Figure 3.B), the inversion of the surface charge values is clearly demonstrated along the different grafting steps: bare (ZP= -13.5 mV); APTES (ZP = + 20.3mV); COOH modified STMs (ZP = -23 mV) which is perfectly consistent with the incorporation of deprotonated carboxylic functions (e.g., pK_a = 4.9 for propionic acid) at the silica surface.

Next, we grafted DFoB onto the COOH-STMS NPs: the continuous activation of the carboxylic groups of the COOH-STMS was achieved by a home-made procedure where sequential additions of EDC reagents are achieved every hour in the presence of DFoB in NaHCO$_3$ buffer at pH 7, with the aim of optimizing the reaction with the amine groups of the DFoB. Thus, coupling reaction of DFoB is carried out continuously throughout the defined reaction time. In the last activation step with the EDC reagent, the reaction mixture was stirred overnight. TGA analysis (Figure 3.A, DFoB yellow curve) allowed determining a grafting rate of about 410 µg of DFoB per mg of STMS (730 nmol·mg^{-1}) corresponding to 0.85 ligand/nm².
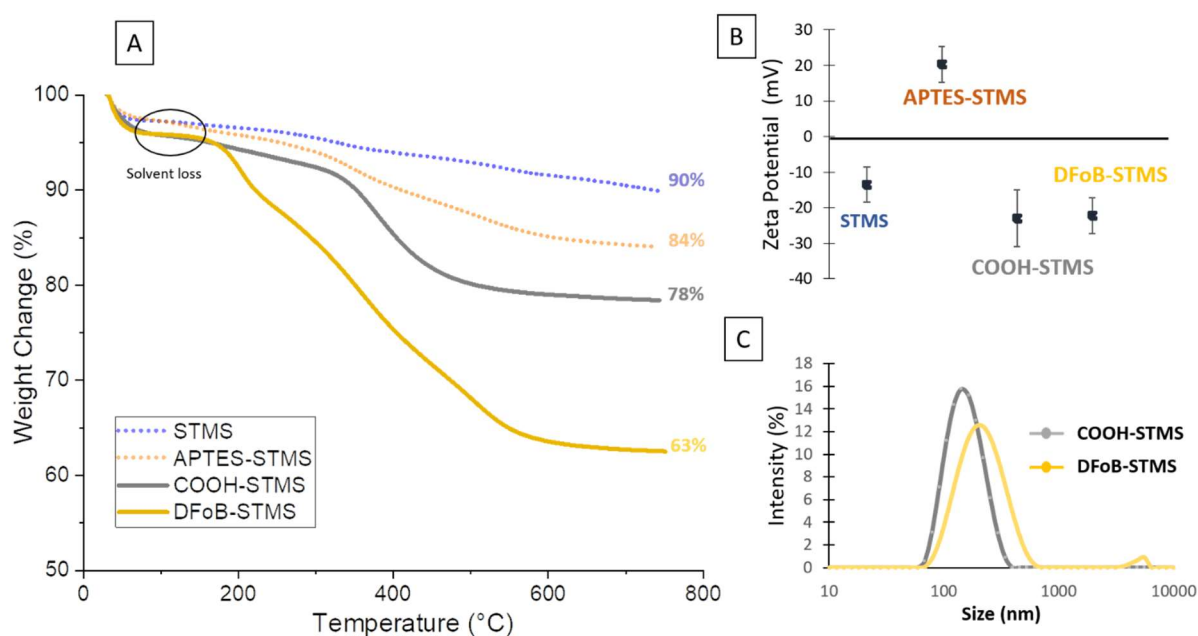
Figure 3. A. TGA and B. ZP of STMS (blue), APTES-STMS (orange), COOH-STMS (gray) and DFoB-STMS (yellow). TGA of STMS (blue) and APTES-STMS (orange) from Figure 2 were represented in dotted lines to highlight the surface modification, step by step. C. DLS size distribution of COOH-STMS (gray) and DFoB-STMS (yellow).

The colloidal stabilities of COOH-STMS and DFoB-STMS (Figure 3.C) were investigated by DLS measurements in HEPES buffered solution (50 mM, pH 7.2). The data demonstrate that the COOH-STMS suspensions display a good colloidal stability with an average hydrodynamic size of *ca*. 164 nm that can be explained by the strong electrostatic repulsions ensured by the terminal carboxylate functions in agreement with the the zeta potential value (ca. -23 mV) of the COOH-STMS. After functionalization by DFoB, the high colloidal stability is maintained with an average hydrodynamic size of ca. 220 nm (DLS, Figure 3.C) in buffered solution (HEPES 50 mM, pH 7.2). This striking result can be explained by the structure of DFoB, which contains hydrophilic fragments that probably contribute to the strong colloidal stability by introducing steric repulsion.

II. 2. 3. Fe(III) uptake by DFoB-STMS: kinetic and stoichiometric parameters

The major objective of this work was to evaluate the ability of the DFoB-STMS NPs to firmly chelate ferric ions in solution and to adress their use as innovative nanoplatforms for the elimination of toxic ions from the human body. A critical point is thus to demonstrate that the immobilization of DeFoB on the silica surface does not affect its chelating efficiency. As the iron capture would have to be performed in biological media such as blood, we have to consider the "state" of iron in such media as iron cations in water easily form hydroxides. In fact, at physiological conditions (pH 7.4), iron(III) does (almost) not exist as free cations in water: the equilibrium concentration of free Fe^{3+} is only about 10^{-18} M ($K_{sp}(Fe(OH)_3) = 2.6 \times 10^{-39}$)[22]. To maintain its solubility and homeostasis under physiological conditions, iron(III) is constantly bound to proteins (*e.g.*, hemoglobin, transferrin) or to low molecular weight moderate chelators such as citrates (*i.e.*, the non-proteinic bound iron is called "labile iron pool). Therefore, we had to find an iron chelating model molecule to mimic the iron state in physiological media. Used as a model of citrate, nitrilotriacetic acid (NTA) is among the most studied organic chelators. In our study, NTA was used with the aim to mimic the biological environment conditions, and the adopted strategy allowed us to stabilize Fe(III) under quasi-physiological conditions (*i.e.*, pH 7.4 and citrate model). It should be noted that DFoB is by far the chelating agent which has a much more powerful Fe(III) chelating constant (log $K_{f\ Fe(III)DFoB}$ = 30; pFe = 26.5)[23] than NTA (log $K_{f\ FeNTA}$ ~15-16; pFe = 17.8)[24]**.** It confirms the feasibility and efficiency of Fe(III) exchange. In the following experiments, FeNTA were therefore incubated with DFoB-STMS and key parameters characterizing the metal capture : capacity capture (nmol.mg^{-1}), efficiency capture (%) and molecular coverage of the DFOB chelate (%) were then evaluated as a function of time (kinetics) and the stoichiometry of the exchange reaction.

$$\textbf{Capacity Capture} = \frac{n_{\text{Fe-captured}}\ (\text{nmol})}{m_{\text{silica}}\ (\text{mg})}$$

$$\textbf{Capture Efficiency} = \frac{n_{\text{Fe-captured}}\ (\text{mol})}{n_{\text{Fe initial}}\ (\text{mol})} \times 100$$

$$\textbf{DFoB}_{\textbf{grafted}}\ \textbf{Coverage} = \frac{n_{\text{Fer-captured}}\ (\text{mol})}{n_{\text{DFoB available}}\ (\text{mol})} \times 100$$

II. 2. 3. 1. Ligand exchange kinetics

When DFoB is grafted at the surface of STMS NPs, the Fe(III) uptake kinetics by ligand exchange between FeNTA and DFoB-STMS could be slower compared to free DFoB. At pH 7.4, only [FeNTA(OH)]$^-$ species is reactive and follows a dissociative interchange mechanism of the Eigen−Wilkins type - independent of the nature of the binding ligand- with $k_{\text{[FeNTA(OH)]}^-}$ values in the order of 10^4 M^{-1}·s^{-1}.[8] Supernatants containing remaining FeNTA have been analyzed directly by UV-visible absorption spectrophotometry (λ_{max} = 270 nm). However, in our experimental conditions (HEPES buffer at 50 mM), the FeNTA absorption was markedly altered by another more intense absorption at about 210 nm (linked to HEPES) which prevents the accurate determination of the iron content (Figure S3.A). To overcome this problem and analyze FeNTA supernatants, free DFoB was added to the supernatant, which rapidly led to the formation of FeDFoB complex which is characterized by a Ligand-to-Fe(III)

charge transfer band (*i.e.*, LMCT) of moderate intensity centered at 430 nm (ε^{430} = 2950 $M^{-1} \cdot cm^{-1}$)[25]. The color changes from light yellow to orange, confirming the exchange of the ligands and the formation of the FeDFoB complex. To ensure more accurate determination of FeNTA using free DFoB, an absorption titration of FeNTA by DFoB was then undertaken, and the absorbance values at 430 nm were plotted as a function of DFoB concentrations (Figure S3.B). Hence, a ligand exchange was shown to be rapid and confirmed the stoichiometry of the reaction (Fe**NTA**:DFoB 1:1).

We then carried out a kinetic exchange study between FeNTA and DFoB-STMS in HEPES buffer at pH 7.4. The mixture (FeNTA:DFoB$_{grafted}$ at a ratio of 0.85:1: at 25°C) was stirred for different reaction times (from 30 min to 1 day) and then centrifuged at 10 000 g. The supernatants were then analyzed using UV-visible absorption spectrophotometry using free DFoB in excess to ensure an accurate determination of the free iron contents.
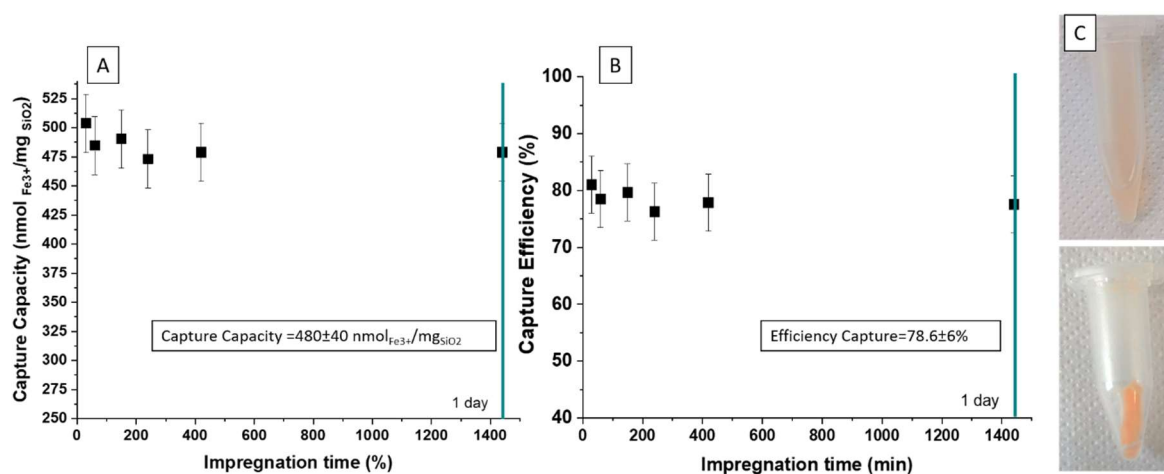
Figure 4. A. Capture capacity and B. capture efficiency of iron(III) by DFoB-STMS using different impregnation times for a ratio FeNTA:DFoB$_{grafted}$ of 0.85:1 at 25°C, pH 7.4. C. Picture showing the orange colored suspension and the centrifuged Fe-DFoB-STMS.

As shown on Figure 4, the values of the capture capacity and efficiency did not significantly change over a 24 hours period with a maximum value reached after 30 minutes of impregnation of DFoB-STMS with FeNTA. According to these data, the metal exchange between FeNTA and DFoB-STMS can therefore be considered as rapid, which is a major advantage for the development of any metal ion removal process. Nevertheless, we were unable to reduce the impregnation time to less than 30 minutes due to the experimental set-up (*i.e.,* centrifugation, washing, measurement of residual FeNTA content by absorption spectrophotometry). In average over this time period, the capacity capture of DFoB-STMS was calculated to be 480 nmol$_{Fe} \cdot mg_{SiO2}^{-1}$ (*i.e.*, 27 µg$_{Fe} \cdot mg_{SiO2}^{-1}$), which corresponds to an capture efficiency of *ca*. 78 % and a coverage of DFoB$_{grafted}$ molecules of *ca*. 66 %. These results are higher to those of other studies conducted with DFoB grafted onto other materials such as nanogel-DFoB, which allow a capture efficiency of 50 % *in vivo* with ferritine (*i.e.,* universal intracellular protein that ensures iron storage) as a source of iron[26]*.* The functionalized DFoB on mesoporous silica surface type MCM-41 allows a capture efficiency of ca*.* 60 % from Fe**EDTA** used as a metal source[27].

In the spectrophotometric study described above, the uptake and efficiency of Fe(III) were demonstrated and quantified indirectly by measuring unreacted FeNTA in the supernatant (*i.e.,* in the

presence of free DFoB). The capture of Fe(III) was also confirmed by analyzing iron within the DFOB-STMS by TEM-EDX. First, TEM images of the FeDFoB-STMS showed the presence of an elastic/viscous coating all around the STMS NPs, confirming a homogenous grafting of DFoB on the STMS (more than 40% wt) (Figure 5.A and B in low and high magnifications). EDX analysis in low and high magnification areas then allowed detecting te presence of iron (attribution Fe-Ka 6.27 and Fe-Kb 7.1 keV for the most intensive pics) and silicon (attribution 1.71 keV) atoms and determining a Fe/Si fraction of *ca.* 2 %. Noteworthy, EDX is a suitable method to detect the presence of such elements however it is not adapted to quantify with precision these elements as the TEM grids used in the preparation may contain silica and the error deviation related to EDX measurements is not negligible at low element %.
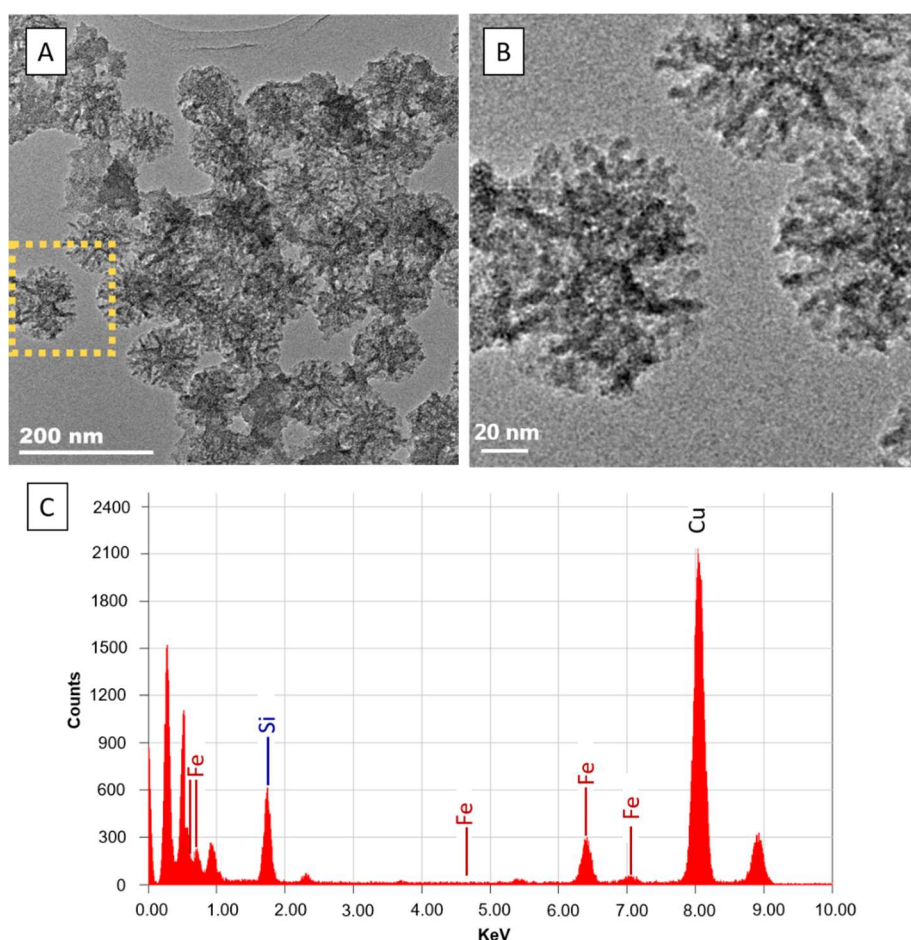
Figure 5. TEM images of FeDFoB-STMS with A. low magnification and B. high magnifications and C. EDX analysis of FeDFoB-STMS NPs.

II. 2. 3. 2. Iron uptake for different ratios and different surface modifications

The capacity uptake of DFoB-STMS suspensions was then measured for different FeNTA:DFoB$_{grafted}$ molar ratios of 0.17, 0.85 and 1.7. The influence of the nature (*i.e.* coating) of the STMS surface: STMS, APTES-STMS or COOH-STMS was also evaluated as a control in this study to evaluate the impact of the supporting system (STMS) and the surface coating (naked, APTES or COOH grafting) on the Fe(III) loading (Figure 6.A and B).

For the three molar ratios, the results of Figure 6.A and B. (yellow curves) displayed the capture capacity and efficiency of our system under different FeNTA concentrations. Over these molar ratio

range, the capture capacity normally increased from 32 to 799 $nmol_{Fe} \cdot mg^{-1}_{STMS}$, while, capture efficiency increased also to reach values of 67% and 65 % at stoichiometries of 0.85 and 1.7:1 meaning in other words that our STMS-DFOB has removed more than 65% of initially introduced iron. Regarding the coverage of DFoB molecules, Figure 6. C shows that the molecular coverage of the DFOB increases importantly from 4% for 0.17:1 stoichiometry, to 58 % for 0.85:1 stoichiometry and reaches finally a coverage of 109 % for 1.7:1 stoichiometry. This last result over 100% at 1.7 equivalent FeNTA, suggests strongly that in addition to a full occupation of the DFOB ligands chelated by Fe(III), an additional binding of FeNTA occurs at the surface of the STMS NPs.
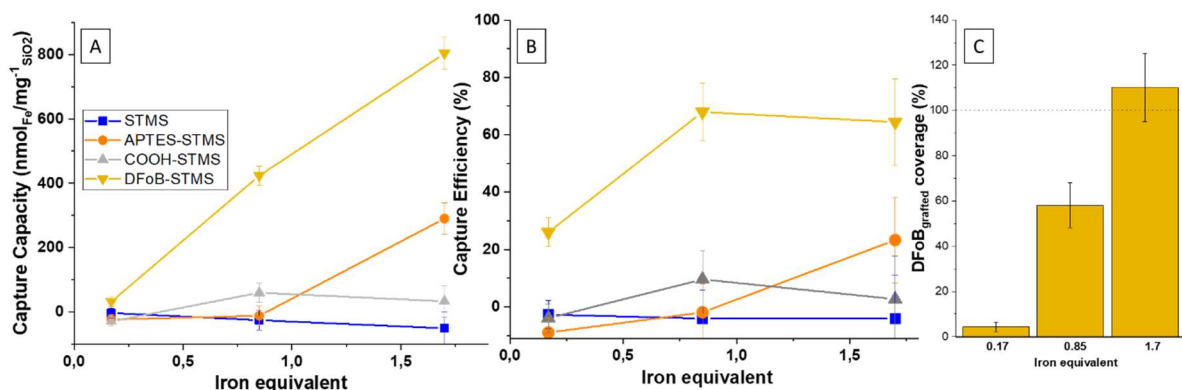
Figure 6. A. Capture capacities and B. efficiencies of STMS (blue), APTES-STMS (orange), COOH-STMS (gray) and DFoB-STMS (yellow) for different FeNTA:DFoB$_{grafted}$ ratios (0.17:1, 0.85:1 and 1.7 :1) with impregnation time of 30 minutes at 25°C, pH 7.4. C. Coverage represents the percentage of DFoB molecules occupied by Fe^{3+} cations. Experiment were repeated three times.

Hence, we assume that parts of the silica surface that are not functionalized with DFoB have a non negligible effect on the iron FeNTA storage. The grafting processes of the different steps has left other functions (APTES and COOH) that could potentially bind to FeNTA. On this last point, the blue and grey curves show that STMS and COOH-STMS are not prone to efficient iron storage (less than 60 $nmol \cdot mg^-$ STMS), whereas iron capture seems to increase significantly with APTES-STMS at a 1.7:1 stoichiometry and thus reach a significant amount of FeNTA loaded with 290 $nmol \cdot mg^{-1}$ APTES-STMS (Figure 6.A). At physiological pH, FeNTA can be written as $[Fe^{III}(CO_2CH_3)_3N.H_2O.OH]^-$ meaning that this ferric complex is therefore negatively charged. As the pK_a of APTES-STMS is *ca*. 8, the surface is therefore partially positively charged at pH 7.4, and the amount of FeNTA adsorbed (orange curve) can be explained by electrostatic interactions between the positively charged surface and the negatively charged Fe(III) complex. Contrary, STMS and COOH-STMS are negatively charged at their surface at pH 7.4. It should be noted that this type of capture with grafted APTES onto silica NPs has previously been described by Wu et al.[28], where they captured CuEDTA^{2-} and CuHEDTA$^-$ complexes. To summarize, the trend observed in iron(III) capture by DFOB-STMS can be explained by two mechanisms: one likely corresponds to strong and selective chelation binding with metal-ligand coordination bonds as the main process, and the other, non-specific and probably electrostatic in nature, could involve weaker binding of iron(III) negatively charged complexes to the positively charged surface (APTES-STMS).

II. 2. 3. 3. Selectivity over other cations of the DFoB-STMS suspensions

Another property of DFoB-STMS suspensions such as their selectivity was thoroughly investigated. The understanding and measurement of selectivity is indeed a key factor to ensure a safe uptake of iron(III) and to restrict the action of these nanomaterials to its sole initial task in a biological organism. In this study, the chelation selectivity of Fe(III) with respect to other important cations of biological interest such as Al^{3+}, Zn^{2+}, Cu^{2+}, Ca^{2+} or Na^+ was evaluated. Indeed, blood is a complex system composed of numerous metal ions essential to the body's functioning. The main idea is therefore to establish whether DFoB-STMS NPs are capable of selectively capturing iron(III) in a complex multi-element environment. Two different media were used to demonstrate that our material can selectively capture iron: a multi-element system consisting of a solution containing different biological cations at the same initial concentration, and the Barth's solution experiment consisting in a preparation which mimics the ionic brain composition. Results are summarized in the next table (Table 1).

Table 1 Capture capacity and efficiency of DFoB-STMS in the two different solutions containing different metal cations. (FeNTA:DFoB_grafted: stoichiometries 0.95:1), impregnation time of 30 minutes at 25°C, pH 7.4 on 7.7 mg of DFOB functionalized STMS). Experiment were performed in duplicate. *A NaOH (2M) solution was used to set the pH.

	Ion	Fe^{3+}	Mg^{2+}	Ca^{2+}	Al^{3+}	Zn^{2+}	K^+	Na^+
Multielement solution	Initial concentration (mM)			0.27±0.03			x	1.159*
	Capture Capacity (nmol_ion/mg_SiO2)	229±4.3	6.6±4.9	1.2±0.7	169±2.3	9.0±1.0	x	155±14
	Capture Efficiency (%)	44.2±1.6	1.1±1.5	0.9±1.3	32.9±0.9	1.9±0.4	x	6.8±1.2
Barth's buffer	Initial concentration (mM)	0.29	0.82	1.32	x	0.04	1.89	90
	Capture Capacity (nmol_ion/mg_SiO2)	428±3.6	174±19.2	437±75	x	9.±3.6	367±1.8	4293±13
	Capture Efficiency (%)	69.2±1.2	8.2±1.7	13.4±4.5	x	8.8±8.2	1.5±0.1	1.9±0.1
log K_f Ion-DFoB		30	9[22]	3[22]	24.5[29]	10.1[30]	/	/

For the multielement solution, the capture capacity and efficiency of iron are lower than in the previous experiments, which is explained mainly by competition between Al^{3+} and Fe^{3+} cations. As compared to the previous study (Figure 4) without any competing cation (*i.e.*, capture capacity of 480 nmol_Fe3+·mg_SiO2 and efficiency of *ca*. 78 % at a stoichiometry FeNTA:DFOB_grafted 0.85:1), the results showed a significant reduction in iron capture (*i.e.*, capture capacity of 229 nmol_Fe3+·mg_SiO2^{-1} and

efficiency *ca*. 44 % at a stochiometry Fe**NTA**:DFOB$_{grafted}$ 0.95:1). Indeed, Al^{3+} and Fe^{3} cations have comparable coordination properties and high complexation constants with DFoB (*i.e.*, log K_{MDFoB} = 30 and 24.5 for Fe^{3+} and Al^{3+}, respectively). Even though the stability constant is higher for FeDFoB, Al^{3+} can competes and distributes within the grafted DFoB. It is noteworthy that the sum of the capture efficiencies for Fe^{3+} and Al^{3+} (*ca.* 77%) is in excellent agreement with that determined from the experiment conducted in absence of any competing metal ions (*ca.* 78%). Concerning the other competing cations Mg^{2+}, Ca^{2+} and Zn^{2+}, their captures were found to be less important, in agreement with the much lower stability constants of the corresponding complexes. As far as Na$^+$ and K$^+$ ions are concerned, no data could be found with DFoB in terms of stability. These adsorption could be possible because, as described before, electrostatic interactions between cations and COOH grafting and naked STMS can occur. Studies were performed concerning this phenomenon: COOH functionnalization was already used for cations capture[31,32] and cations were demonstrated to be attracted by the negative silica surface[33].

Regarding the study with the Barth's solution mimicking the ionic brain composition, where the concentrations of the biological cations (Mg^{2+}, Ca^{2+}, Zn^{2+} and Na$^+$) are higher than that of Fe^{3+} fixed at 0.29 mM (see Table 1, Barth's buffer line), values obtained for iron capture capacity and efficiency (428 nmol$_{Fe3+}$·mg$_{SiO2}$$^{-1}$ and 69%) were found relatively close to the results obtained in the previous kinetic and stoechiometric studies (480 nmol$_{Fe3+}$·mg$_{SiO2}$$^{-1}$ and 78 %). As the Barth's aqueous buffer does not present any Al^{3+} cation, a close relationship can be clearly highlighted on the ability of our DFOB-STMS to efficiently chelate and capture iron in the presence or not of aluminium cation. Regarding the capture capacities for the other cations having I or II valency (Mg^{2+}, Ca^{2+}, Zn^{2+} and Na$^+$), although their capture capacities are quite high, their capture efficiencies remain however low without being negligible, indicating that the homeostatic levels of these cations could be slightly or moderately affected during the selective iron capture. For further investigations, we have to ensure that the homeostatic levels of these cations remain stable for the safety of such treatment because depletion of some relevant ions could be risky, *i.e.,* an depletion of sodium could produce cardiovascular problems as hypotension episodes[34].

II. 2. 3. 4. Recyclability of DFoB-STMS

To assess the recyclability of the DFoB-STMS NPs, the experiments were carried out in two successive cyclic steps: iron trapping and then iron release. The Fe-DFoB complex is very stable at pH 7; however, when the pH is significantly lowered (pH < 1-2), this complex is destabilized following protonation of the DFOB ligand, ultimately leading to its full dissociation. These acidic conditions therefore favor the release of iron from STMS NPs and thus allow the material to be reused in several capture/release cycles. As for the iron capture step previously discussed, we have chosen to work at pH 7.4 with a FeNTA:DFoB grafted ratio of 0.9 :1, while for the iron release step, we employed an aqueous hydrochloric acid solution at pH 1. As it is well known, the sol-gel process is catalyzed in acidic or basic aqueous media[17], so that the shape of STMS in water at pH 1 is retained, but may aggregate irreversibly. A preliminary experiment has been carried out concerning the release time in order to evaluate the impregnation time of NP in the acidic solution necessary to dissociate the metal complexes while avoiding irreversible aggregation.
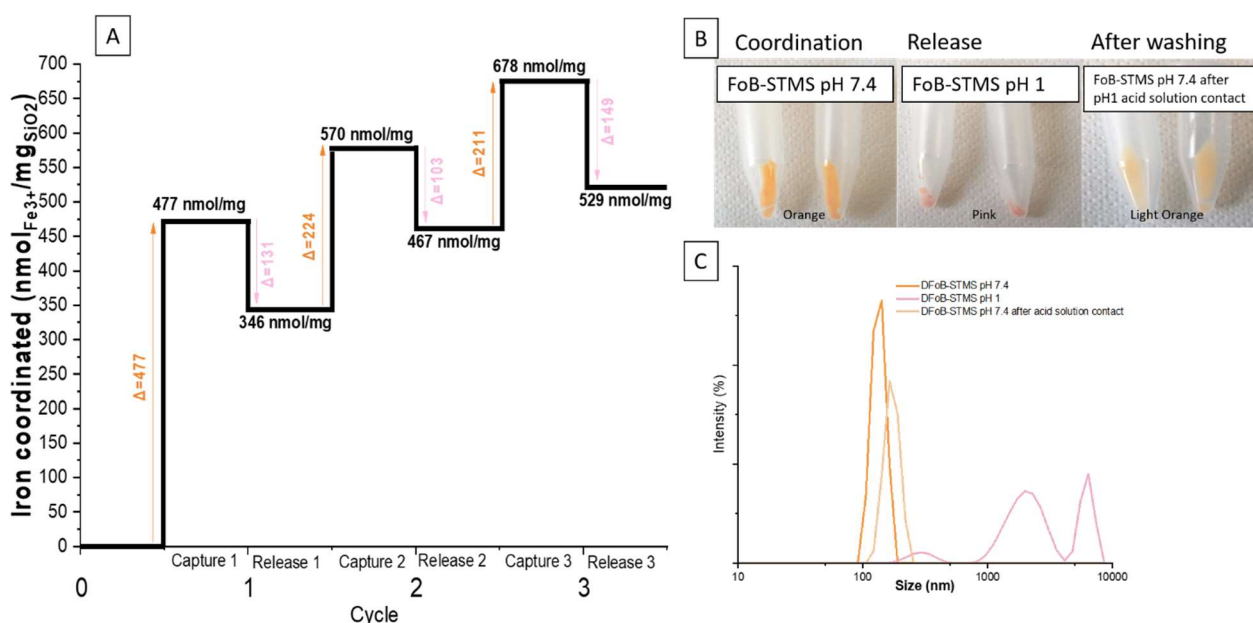
Figure 7. A. Iron inside the DFoB-STMS NPs after 3 cycles of capture/release. Conditions: DFoB_grafted:FeNTA ratio 1:0.9, impregnation time of 30 minutes at 25°C. Release: 30 minutes at 25°C, pH 1. B. Photos of centrifuged FoB-STMS NPs after capture, after release in acidic solution (pH 1) and between release (n-1) and capture (n) at physiological pH. C. Granulometry measurements of DFoB-STMS in water at pH 7.4 (orange), at pH 1 (pink) and at pH 7.4 after acid solution treatment (light orange). All the studies were carried on 10 mg of nanoparticles.

The previous figure displays the amount of iron captured (nmol) in the DFoB-STMS NPs per mg of SiO2. The first capture corresponds to the value determined in previous experiments (ca. 477 $nmol_{Fe}\cdot mg_{SiO2}^{-1}$). The first release triggered by acidic conditions shows that only 131 $nmol_{Fe}\cdot mg_{SiO2}^{-1}$ were dissociated. Subsequent cycles of capture and release show again a high level of captured iron (224 and 211 $nmol_{Fe}\cdot mg_{SiO2}^{-1}$) compared to the released iron (103 and 149 $nmol_{Fe}\cdot mg_{SiO2}^{-1}$). Although DFoB-STMS NPs are effective in chelating iron, only part of this complexed iron could be released. This can be explained by the behavior of the DFoB-STMS NPs at different pH: from a good colloidal stability at physiological pH to agglomeration at low pH (Dh>1000 nm) and a final stability after washings (Figure 7.C). Indeed,

at low pH, agglomeration can alter the diffusion of iron across the STMS NPs, which could explain the low rate of dissociation. Surprisingly, for the second and third capture steps, coordination reactions continue without reaching a saturation value. As seen above, the residual APTES functions could contribute to the iron capture. Another possible explanation relies on the potential formation of binuclear complex with DFoB under acidic conditions.[35] Other groups that have also studied the recyclability of their materials have found improved efficiencies by using other approaches such as ligand exchange between the grafted DFoB and an exogenous competing ligand (EDTA) to capture iron within the supports. Note that the Fe**EDTA** complex is characterized by a formation constant of 10^{25} M^{-1} and a pFe value of 25.1 (to be compared to pFe = 26.5 calculated for DFoB).[27]

Conclusion

In this work, a new nanoplatform efficient/effective for iron removal from complex biological media has been designed. It consists of original mesoporous silica with a large pore stellate morphology on which an iron chelating agent has been anchored. The synthesis of such stellate silica has been reported recently and their use in depollution has never been investigated up to now. By considering the challenges and the targeted application which is the specific removal of iron from a biological medium, desferrioxamine B (DFoB) chelator, already used in its free form for iron capture in body, was also found herein highly relevant when covalently immobilized on silica to efficiently and selectively extract iron(III) alone in solution or combined to a mixture of biological relevant cations. The challenges here were the design of the nanoplatform and the evaluation of its chelating efficiency and selectivity.

As compared to the findings in the litterature, our strategy to use DFOB-STMS offers key advantages:

- Large pore stellate silica NPs are prepared according to a straightforward and reproducible procedure, while chelating DFoB ligands afforded selective iron capture moiety and very stable complexes.

- The grafting of DFoB, to modify the surface of homogeneous stellate silica NPs, was successfully achieved and controlled. It leads to a great coverage of the chelator of 730 $nmol \cdot mg^{-1}$ (*i.e.,* 0.85 ligand·per nm^2).

- Our DFoB-STMS are well dispersed in aqueous buffer at physiological pH before and after iron capture which highlights their efficiency to be used in biological fluids where their non-agglomeration is required;

- The DFoB-STMS are able to capture very fast (in less than 30 minutes) a high amount of iron(III) up to a capture capacity of 480 $nmol_{Fe3+}/mg_{SiO2}$ with a good uptake efficiency (*ca.* 78%) meaning that 78 % of the initial iron is uptaken for a stoichiometry 0.85:1 (FeNTA : DFoB);

- Comparison of the iron uptake by our DFoB-STMS with other surface modification (bare, APTES, COOH) indicates that iron capture of our DFoB-STMS is mainly due to chelation while the other surfaces have slight or moderate non-specific adsorption reaction;

- At last, about the metal selectivity, studies in two different multielement media, showed a high selectivity for iron(III) over other metal ions. For a multielement solution mimicking the extracellular brain ionic composition (Barth's buffer), the iron capture was found to be close to that performed in the absence of competing ions (capture capacity of 428 $nmol_{Fe} \cdot mg_{SiO2}^{-1}$ and capture efficiency of *ca.* 69 %) while in the presence of Al^{3+} that strongly competes with Fe^{3+}, the capture of iron decreased (capture capacity 229 $nmol_{Fe} \cdot mg_{SiO2}^{-1}$ and capture efficiency of *ca.* 44 %). Due to their closely related properties, Al^{3+} and Fe^{3+} thermodynamically distribute within the DFoB-STMS (capture efficiency of *ca.* 77% for both Al^{3+} and Fe^{3+}).

Hence, such works may pave the way towards new nanosystems at the interface between depollution and nanomedecine. Future experiments will aim to investigate such nanoplatforms with other chelating agents to demonstrate the versatility of our design and approach for other biomedical issues.

The introduction of a magnetic core will be also assessed to offer possibility of magnetic separation/recovery of such new nanoplatforms.

References

(1)   Hakami, O.; Zhang, Y.; Banks, C. J. Thiol-Functionalised Mesoporous Silica-Coated Magnetite Nanoparticles for High Efficiency Removal and Recovery of Hg from Water. *Water Res.* **2012**, *46* (12), 3913–3922.

(2)   Heidari, A.; Younesi, H.; Mehraban, Z. Removal of Ni(II), Cd(II), and Pb(II) from a Ternary Aqueous Solution by Amino Functionalized Mesoporous and Nano Mesoporous Silica. *Chem. Eng. J.* **2009**, *153* (1), 70–79.

(3)   Li, G.; Zhao, Z.; Liu, J.; Jiang, G. Effective Heavy Metal Removal from Aqueous Systems by Thiol Functionalized Magnetic Mesoporous Silica. *J. Hazard. Mater.* **2011**, *192* (1), 277–283.

(4)   Dindar, M. H.; Yaftian, M. R.; Rostamnia, S. Potential of Functionalized SBA-15 Mesoporous Materials for Decontamination of Water Solutions from Cr(VI), As(V) and Hg(II) Ions. *J. Environ. Chem. Eng.* **2015**, *3* (2), 986–995.

(5)   Sangvanich, T.; Sukwarotwat, V.; Wiacek, R. J.; Grudzien, R. M.; Fryxell, G. E.; Addleman, R. S.; Timchalk, C.; Yantasee, W. Selective Capture of Cesium and Thallium from Natural Waters and Simulated Wastes with Copper Ferrocyanide Functionalized Mesoporous Silica. *J. Hazard. Mater.* **2010**, *182* (1), 225–231.

(6)   Chang, C.-Y.; Chau, L.-K.; Hu, W.-P.; Wang, C.-Y.; Liao, J.-H. Nickel Hexacyanoferrate Multilayers on Functionalized Mesoporous Silica Supports for Selective Sorption and Sensing of Cesium. *Microporous Mesoporous Mater.* **2008**, *109* (1), 505–512.

(7)   Zhang, K.; Xu, L.-L.; Jiang, J.-G.; Calin, N.; Lam, K.-F.; Zhang, S.-J.; Wu, H.-H.; Wu, G.-D.; Albela, B.; Bonneviot, L.; Wu, P. Facile Large-Scale Synthesis of Monodisperse Mesoporous Silica Nanospheres with Tunable Pore Structure. *J. Am. Chem. Soc.* **2013**, *135* (7), 2427–2430.

(8)   Martin-Benlloch, X.; Haid, S.; Novodomska, A.; Rominger, F.; Pietschmann, T.; Davioud-Charvet, E.; Elhabiri, M. Physicochemical Properties Govern the Activity of Potent Antiviral Flavones. *ACS Omega* **2019**, *4* (3), 4871–4887.

(9)   Anderegg, G. Critical Survey of Stability Constants of NTA Complexes. *Pure Appl. Chem.* **1982**, *54* (12), 2693–2758.

(10) Wolsey, W. C. Perchlorate Salts, Their Uses and Alternatives. *J. Chem. Educ.* **1973**, *50* (6), A335.

(11) Bastian, Robert.; Weberling, Richard.; Palilla, Frank. Determination of Iron by Ultraviolet Spectrophotometry. *Anal. Chem.* **1956**, *28* (4), 459–462.

(12) Kornreich-Leshem, H.; Ziv, C.; Gumienna-Kontecka, E.; Arad-Yellin, R.; Chen, Y.; Elhabiri, M.; Albrecht-Gary, A.-M.; Hadar, Y.; Shanzer, A. Ferrioxamine B Analogues: Targeting the FoxA Uptake System in the Pathogenic Yersinia Enterocolitica. *J. Am. Chem. Soc.* **2005**, *127* (4), 1137–1145.

(13) Budimir, A.; Humbert, N.; Elhabiri, M.; Osinska, I.; Biruš, M.; Albrecht-Gary, A.-M. Hydroxyquinoline Based Binders: Promising Ligands for Chelatotherapy? *J. Inorg. Biochem.* **2011**, *105* (3), 490–496.

(14) Perton, F.; Harlepp, S.; Follain, G.; Parkhomenko, K.; Goetz, J. G.; Bégin-Colin, S.; Mertz, D. Wrapped Stellate Silica Nanocomposites as Biocompatible Luminescent Nanoplatforms Assessed in Vivo. *J. Colloid Interface Sci.* **2019**, *542*, 469–482.

(15) Zhang, K.; Chen, H.-L.; Albela, B.; Jiang, J.-G.; Wang, Y.-M.; He, M.-Y.; Bonneviot, L. High-Temperature Synthesis and Formation Mechanism of Stable, Ordered MCM-41 Silicas by Using Surfactant Cetyltrimethylammonium Tosylate as Template. *Eur. J. Inorg. Chem.* **2011**, *2011* (1), 59–67.

(16) Cui, X.; Zin, W.-C.; Cho, W.-J.; Ha, C.-S. Nonionic Triblock Copolymer Synthesis of SBA-15 above the Isoelectric Point of Silica (PH=2–5). *Mater. Lett.* **2005**, *59* (18), 2257–2261.

(17) Stöber, W.; Fink, A.; Bohn, E. Controlled Growth of Monodisperse Silica Spheres in the Micron Size Range. *J. Colloid Interface Sci.* **1968**, *26* (1), 62–69.

(18) Wang, X.-Y.; Mertz, D.; Blanco-Andujar, C.; Bora, A.; Ménard, M.; Meyer, F.; Giraudeau, C.; Bégin-Colin, S. Optimizing the Silanization of Thermally-Decomposed Iron Oxide Nanoparticles for Efficient Aqueous Phase Transfer and MRI Applications. *RSC Adv.* **2016**, *6* (96), 93784–93793.

(19) Schiestel, T.; Brunner, H.; Tovar, G. E. M. Controlled Surface Functionalization of Silica Nanospheres by Covalent Conjugation Reactions and Preparation of High Density Streptavidin Nanoparticles. *J. Nanosci. Nanotechnol.* **2004**, *4* (5), 504–511.

(20) An, Y.; Chen, M.; Xue, Q.; Liu, W. Preparation and Self-Assembly of Carboxylic Acid-Functionalized Silica. *J. Colloid Interface Sci.* **2007**, *311* (2), 507–513.

(21) An, Y.; Chen, M.; Xue, Q.; Liu, W. Preparation and Self-Assembly of Carboxylic Acid-Functionalized Silica. *J. Colloid Interface Sci.* **2007**, *311* (2), 507–513.

(22) Kiss, T.; Farkas, E. Metal-Binding Ability of Desferrioxamine B. *J. Incl. Phenom. Mol. Recognit. Chem.* **1998**, *32* (2), 385–403.

(23) Farkas, E.; Enyedy, É. A.; Csóka, H. A Comparison between the Chelating Properties of Some Dihydroxamic Acids, Desferrioxamine B and Acetohydroxamic Acid. *Polyhedron* **1999**, *18* (18), 2391–2398.

(24) Elhabiri, M.; Carrër, C.; Marmolle, F.; Traboulsi, H. Complexation of Iron(III) by Catecholate-Type Polyphenols. *Inorganica Chim. Acta* **2007**, *360* (1), 353–359.

(25) Kornreich-Leshem, H.; Ziv, C.; Gumienna-Kontecka, E.; Arad-Yellin, R.; Chen, Y.; Elhabiri, M.; Albrecht-Gary, A.-M.; Hadar, Y.; Shanzer, A. Ferrioxamine B Analogues: Targeting the FoxA Uptake System in the Pathogenic Yersinia Enterocolitica. *J. Am. Chem. Soc.* **2005**, *127* (4), 1137–1145.

(26) Wang, Y.; Liu, Z.; Lin, T.-M.; Chanana, S.; Xiong, M. P. Nanogel-DFO Conjugates as a Model to Investigate Pharmacokinetics, Biodistribution, and Iron Chelation in Vivo. *Int. J. Pharm.* **2018**, *538* (1), 79–86.

(27) Alberti, G.; Emma, G.; Colleoni, R.; Pesavento, M.; Marina Nurchi, V.; Biesuz, R. Novel DFO-Functionalized Mesoporous Silica for Iron Sensing. Part 2. Experimental Detection of Free Iron Concentration (PFe) in Urine Samples. *Analyst* **2014**, *139* (16), 3940–3948.

(28) Wu, L.; Wang, H.; Lan, H.; Liu, H.; Qu, J. Adsorption of Cu(II)–EDTA Chelates on Tri-Ammonium-Functionalized Mesoporous Silica from Aqueous Solution. *Sep. Purif. Technol.* **2013**, *117*, 118–123.

(29) Evers, A.; Hancock, R. D.; Martell, A. E.; Motekaitis, R. J. Metal Ion Recognition in Ligands with Negatively Charged Oxygen Donor Groups. Complexation of Iron(III), Gallium(III), Indium(III), Aluminum(III), and Other Highly Charged Metal Ions. *Inorg. Chem.* **1989**, *28* (11), 2189–2195.

(30) Farkas, E.; Csóka, H.; Micera, G.; Dessi, A. Copper(II), Nickel(II), Zinc(II), and Molybdenum(VI) Complexes of Desferrioxamine B in Aqueous Solution. *J. Inorg. Biochem.* **1997**, *65* (4), 281–286.

(31) Bensacia, N.; Fechete, I.; Moulay, S.; Debbih-Boustila, S.; Boos, A.; Garin, F. Removal of Cadmium (II) from Aqueous Media Using COOH/TUD-1 Mesoporous Solid. Kinetic and Thermodynamic Studies. *Environ. Eng. Manag. J.* **2014**, *13* (10), 2675–2686.

(32) Bensacia, N.; Fechete, I.; Moulay, S.; Hulea, O.; Boos, A.; Garin, F. Kinetic and Equilibrium Studies of Lead(II) Adsorption from Aqueous Media by KIT-6 Mesoporous Silica Functionalized with –COOH. *Comptes Rendus Chim.* **2014**, *17* (7), 869–880.

(33) Peng, L.; Qisui, W.; Xi, L.; Chaocan, Z. Zeta-Potentials and Enthalpy Changes in the Process of Electrostatic Self-Assembly of Cations on Silica Surface. *Powder Technol.* **2009**, *193* (1), 46–49.

(34) Kooman, J. P.; Sande, F. V. D.; Leunissen, K.; Locatelli, F. Editorials: Sodium Balance in Hemodialysis Therapy. *Semin. Dial.* **2003**, *16* (5), 351–355.

(35) Biruš, M.; Bradić, Z.; Kujundžić, N.; Pribanić, M. Iron(III) Complexation by Desferrioxamine B in Acidic Aqueous Solutions. The Formation of Binuclear Complex Diferrioxamine B. *Inorganica Chim. Acta* **1983**, *78*, 87–92.

Chapter III
Grafting of crown-ether and cryptand on stellate mesoporous silica for efficient and selective sodium cation purification

Introduction

Previously, we explained the difficulty to remove certain metal/ions from blood by peritoneal dialysis in the case of a chronic or end-stage renal failure. This treatment showed special difficulties to efficiently remove sodium in less than 4 hours (the time of the session treatment).

In this chapter, to solve the various issues addressed above, we developed new functionalized submicron size materials based on the covalent grafting of high specific sodium chelator on large pore stellate mesoporous silica (STMS) NPs. In this work, we hypothesize that such stellate silica NPs functionalized with crown-ether or cryptands could efficiently contribute to remove sodium from biological environments. Hence, we achieved in a first approach the grafting of the 15-crown-5 ether (CE) on STMS, and in a second approach, of the cryptand [2.2.1] (named cryptand$_{221}$ and abbreviated C$_{221}$). Both macrocycles are well-known for their capacity to strongly bind sodium cations[1] (CE: cavity radius 1.7-2.2 Å [2]/C$_{221}$: 1.1 Å, ionic radius of sodium 0.98 Å). Thus, in this work we present the chemical strategies to efficiently graft CE and C$_{221}$ at the STMS surface. First, CE-STMS are tested for Na$^+$ uptake properties in NaCl solutions under different conditions. Firstly, with the aim to prove our system in optimal conditions sodium cations capture are tested in a co-solvent methanol-water (80%-20% v/v). Secondly, to investigate capture potential in aqueous media, it was achieved in water by varying Na:CE stoichiometry and pH. Then, C$_{221}$-STMS are assessed, only in water media (0.9 and 4.7 Na eq) and the sodium selectivity was tested in a multi-element aqueous solution (at the same concentration and equivalent concentration to the dialysis solution). A last study concerning recyclability of C$_{221}$-STMS, based on ion and ligand exchanges, has been also performed during this work.

The next schema summarizes the different synthesis strategies to graft the ligands and the performed experiments on the systems.
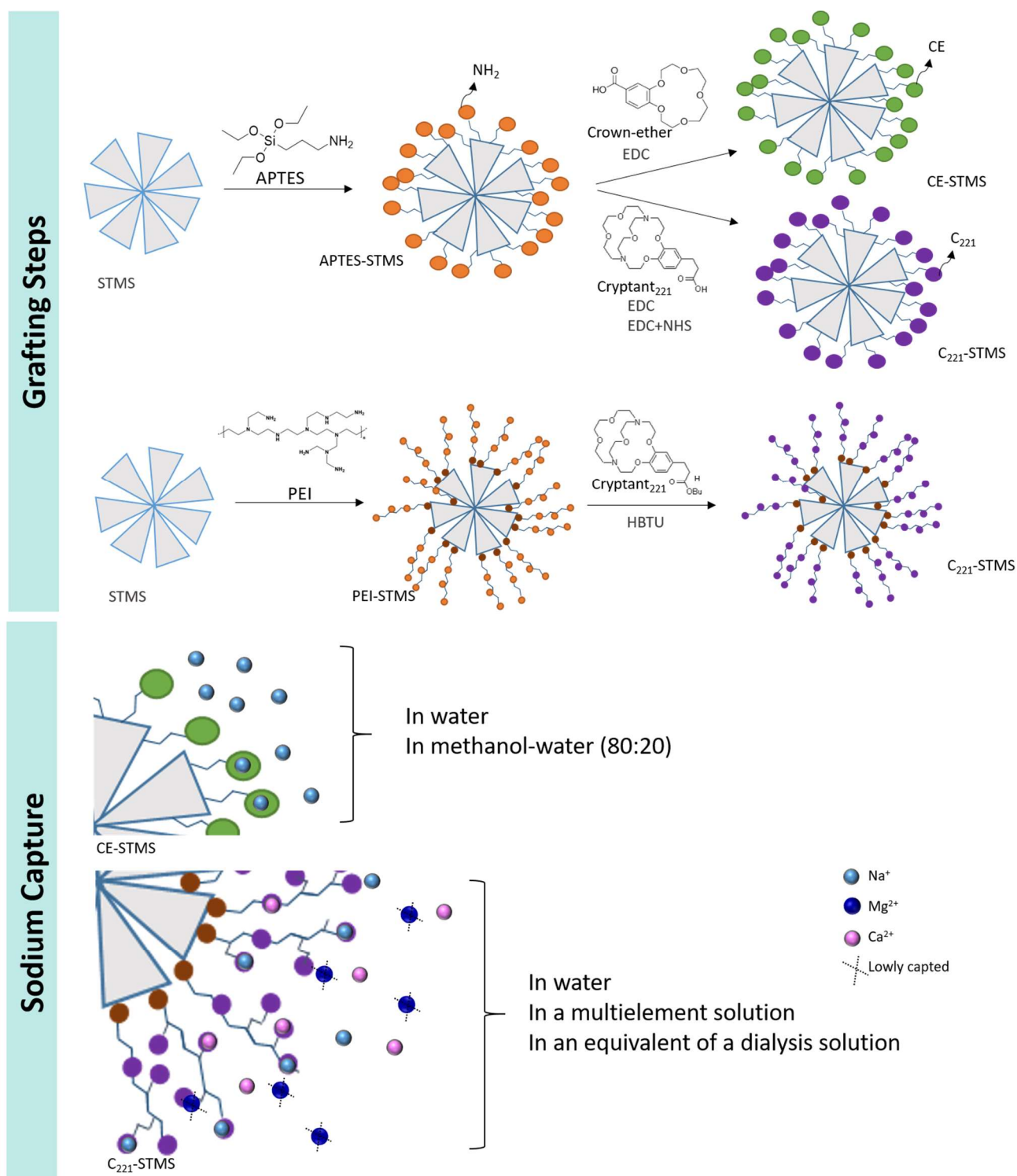
Scheme 1. General concept schematizing the synthesis of the STMS NPs, the grafting of the macrocycles and the subsequent applications of these materials for sodium metal removal.

III. 1. Sodium removal with functionalized mesoporous silica nanoparticles.

III. 1. Experimental Section

Products. 4-carboxybenzo-15-crown-5 (CE) were purchased from Sigma Aldrich, 1-ethyl-3-(3-dimethylaminopropyl)carbodiimide hydrochloride (EDC, >98 %) from Tokyo Chemical Industry (TCI), Ammonium hydroxide Sodium (NH_4OH) and ethylenediaminetetracetic acid (EDTA) from Fluka, N-Hydroxysuccinimide (NHS, -98 %) and Polyethyleneimin, branched (PEI, M.W. 50, 000 – 100, 000, 30 % w/w aqueous solution) from Alfa Aesar, Cryptand [2.2.1] synthesized by Dr. Veronika BEREZHNAIA (team of Dr. Loïc Jierry, Institut Charles Sadron). N,N,N',N'-Tetramethyl-O-(1H-benzotriazol-1-yl)uronium hexafluorophosphate (HBTU, >98 %) from Sigma Aldrich, N,N-Dimethylformamide (DMF, pure) and Methanol from Carlo Erba, NaCl from Carlo Erba (technical grade), $CaCl_2$ (≥97 %) from Prolabo, $MgCl_2 \cdot 6H_2O$ (reagent grade) from Merck.

III. 1. 1. Crown-ether experiments

Grafting of crown-ether. The previously amino grafted STMS, were reacted with the carboxyl functions of carboxybenzo-CE previously activated with EDC in "sequential add-ons" in an HEPES buffer (pH 7.2). For that, 100 mg of STMS-APTES were dispersed in 20 mL of HEPES buffer at pH 7.2 (50 mM, buffered with diluted NH_4OH solution), then 80 mg of CE were added and the solution was stirred 5 min. Then, 234 mg of EDC were added to the solution and this step was repeated each hour (5 consecutive times). After the last addition, the reactional media is let on the stirring wheel for a night (17 h), then the tube is centrifuged (10 000 g, 10 min) and functionalized NPs washed 3 times with distilled water. A part of the synthesis was dispersed in methanol and the other in water.

Sodium Capture with CE-STMS

Cosolvent media. In 4 ml of a methanol-water 80 % - 20 % v/v media, 6 mg of the CE-STMS (4452 nmol of $CE_{grafted}$) nanoparticles were respectively dispersed in two NaCl solutions containing 0.9 molar equivalent of Na ([Na]= $1.1 \cdot 10^{-3}$ M) and 4.7 molar equivalents of Na ([Na]= $5.5 \cdot 10^{-3}$ M) for 1 equivalent of CE. Solutions were stirred during 24 hours and centrifuged at 12000 g during 20 minutes.

Water media. For the tree experiments 6 mg of the functionalized nanoparticles (4452 nmol of $EC_{grafted}$) were respectively added to a centrifuge tube solution containing 6 ml of 0.9 equivalent of Na for 1 equivalent of $CE_{grafted}$ at pH 7 ([Na]= $7.1 \cdot 10^{-4}$ M). The same process was repeated for 4.7 equivalent of Na at pH=5 and at pH= 7 ([Na]= $3.7 \cdot 10^{-3}$ M). The whole was stirred continuously overnight and finally centrifuged at 12000 g for 20 minutes. The supernatants were analyzed by ICP-AES method.

III. 1. 2. Cryptand experiments

Grafting of Cryptant$_{221}$ by EDC on APTES-STMS. By the same way, 24 mg of STMS-APTES were dispersed in 10 mL of HEPES buffer at pH 7.2 (150 mM, buffered with NH_4OH), and 30 mg of Cryptand221 were added on first, and the mix was ultrasonicated during 5 minutes. After, 56 mg of EDC were added to the solution (5 sequential additions spaced by one hours each) and constantly stirring in wheel for a night (17h). The solution is centrifuged (12 000 g, 20 min) and functionalized STMS washed 3 times with distilled water, then dispersed in 5 mL of water.

Grafting of Cryptant$_{221}$ by EDC-NHS on APTES-STMS. Following the same previous principle, the amino grafted STMS were reacted with the carboxyl function of Cryptant$_{221}$ using EDC and NHS to improve the yield of grafting. By the same way, 24 mg of STMS-APTES were dispersed in 10 mL of HEPES buffer at pH 7.2 (150 mM, buffered

with NH_4OH), and 30 mg of Cryptand221 were added on first, and the mix was ultrasonicated during 5 minutes. After, 116 mg of EDC and 232 mg of NHS were added to the solution (5 sequential additions spaced by one hour) and constantly stirred in a wheel for a night (17 h). The solution is centrifuged (12 000 g 20 min) and functionalized STMS washed 3 times with distilled water, then dispersed in 5 mL of water.

Grafting of Cryptant$_{221}$ by HBTU on PEI-STMS. This time, the amino functions are provided by branched Polyethylenimine (PEI). For this, 50 mg of STMS are dispersed in 50 ml of water and 100 mg of PEI are added. The tube was stirred during 2 hours and the PEI-STMS was centrifuged (10 000 g, 10 min) washed several times with water. 24 mg of PEI-STMS nanoparticles were dispersed in 5 mL of DMF. In another flask, 22.68 mg of triethylamine, 30 mg of C_{221} and 85 mg of HBTU were well dispersed in 5 ml of DMF and added to the flask containing the nanoparticles. The whole is stirred in a wheel (17 h). The solution is centrifuged (12 000 g, 20 min) and C_{221}-STMS are washed with ethanol and distilled water, then dispersed in 5 mL of water.

Sodium Capture with C_{221}-STMS

Water media. The protocol applied for CE-STMS functionalized nanoparticles was adapted to C_{221}-STMS NPs. 6 mg of the functionalized nanoparticles (1314 nmol of $C221_{grafted}$) were respectively added to 6.2 mL of a solution containing 0.9 equivalent of Na ([Na]= $1.97 \cdot 10^{-4}$ M) at pH 7, and to 6.4 mL of a solution containing 4.7 equivalent of Na ([Na]= $9.8 \cdot 10^{-4}$ M) at pH 7, all the experiments for 1 eq. of C_{221} grafted. The whole was stirred overnight and finally centrifuged at 12000 G during 20 minutes.

Na(I) selectivity of the C_{221}-STMS. These experiments were conducted under two different conditions. In the first approach, the C_{221}-STMS NPs were subjected to a solution containing Na in combination with a set of metal elements used at the same concentration. 6 mg of C_{221}-STMS were dispersed in 6 mL of a multielement solution containing several metal salts at the same concentration ([Na^+]=[Mg^{2+}]=[Ca^{2+}]=$2.0 \cdot 10^{-4}$ M). These cations are present in the peritoneal dialysis solution.

In the second approach, 6 mg of the C_{221}-STMS NPs were dispersed in 6 mL of an equivalent of dialysis solution of a second-generation double chamber "sleep safe" from Fresenius Medical Care. This medium was used to remove sodium during the peritoneal dialysis ([Na^+]=$5.5 \cdot 10^{-4}$ M (2.6 eq), [Mg^{2+}]=$2.2 \cdot 10^{-6}$ M (0.01 eq) and [Ca^{2+}]=$8.7 \cdot 10^{-6}$ M (0.04 eq). The solution was set at pH=7 with a NH_4OH solution. For this experiment, no glucose was added (contrary to the real solution), to avoid possible effects.

For these two types of experiments, the reaction mixtures were stirred overnight, centrifuged and the NPs were washed twice with milliQ water. The supernatants were analyzed by ICP-AES (following the same protocol as for the previous studies, see above).

Recyclability

Using ion exchange principle: in 1975, Lehn *et al.*, reported the different ion captures of a family of cryptands and the cryptand$_{221}$ showed a higher stability constant in water with Ca^{2+} ion (log K_f=6.95 in water at 25°C, with Ag^+, log K_f=10.6 [1] than with sodium.

For that, the Na-C_{221}-STMS were dispersed in 6.5 ml of a solution containing 100 equivalents of Ca^{2+} at pH 7 and constantly stirred for 3 hours. The solution was centrifuged at 10 000 G during 20 minutes. The Ca-C_{221}-STMS are then redispersed in an EDTA solution (50 eq, pH 7), stirred and centrifuged as previously. This last step is repeated three times. Finally, the C_{221}-STMS could be redispersed in water for another cycle.

III. 1. 3. Characterizations methods

Dynamic Light Scattering (DLS) and Zeta Potential (ZP). The zetasizer Nano ZS from Malvern was used to characterize the properties of colloidal suspensions: the hydrodynamic diameter and the dispersity in size in intensity mode. Measurements of surface Zeta potential were performed to get insights into the surface charge of the particles.

Thermal Gravimetric Analysis (TGA). TGA was performed on a TA SDT 600 instrument to measure the loss mass of the sample when the temperature changed. Consequently, the amount of organic compound grafted on functionalized inorganic STMS nanoparticles can be quantified.

ICP-AES. The measurement of supernatants concentration was performed on a Varian 720 ES instrument. For the co-solvent supernatants, samples were diluted to have less of 5% of methanol in the whole media. In fact, the device is very sensitive to solvent which could cause measurement interferences. The functionalized STMS nanoparticles with CE or C_{221} in aqueous suspensions were brought in contact with sodium cations solutions in different media. Sodium uptake was quantified by dosage of the remaining supernatants by ICP AES and the analytical concentration of sodium was measured.

III. 2. Mesoporous silica nanoparticles functionalized with crown-ether to sodium removal

III. 2. 1. Grafting of Crown-Ether

After the STMS synthesis and the APTES functionalization (described in the previous chapter), the grafting of the crown-ether bearing carboxylic groups was achieved onto the APTES-STMS surface via a peptidic-like coupling. For crown-ether, the acidic functions on the ligands were activated by the carbo-diimide activator agent EDC forming a reactive intermediate product which reacted with the amine functions on APTES-STMS surface. As seen above, the TGA (Figure 1.A) and ZP (Figure 1.B) gave similar results which are : 129 $\mu g_{APTES} \cdot mg_{SiO_2}^{-1}$ and +16 mV, respectively.

TGA quantification (Figure 1.A, CE green curve) allowed determining the grafting of the organic molecule: a first solvent loss is observed at 100 °C (weight loss 95 %), between 350 °C and 680 °C a continuous weight loss is detected linked to APTES and CE molecules grafted on surface (weight loss 71 %). Appling this, the grafting rate is about 223 $\mu g_{CE} \cdot mg_{SiO_2}^{-1}$ corresponding to 742 $nmol_{CE} \cdot mg_{SiO_2}^{-1}$ and 0.9 ligand·nm^{-2}. Similar grafting rate was also found by Azaroon *et al.*[3] with grafted 18-CE-6-Pd on MCM-41, where they succeeded with another method to have ca. 288 $\mu g[18\text{-}CE\text{-}6] \cdot mg_{SiO_2}^{-1}$ (732 $nmol_{CE} \cdot mg_{SiO_2}^{-1}$). Concerning the CE grafting, ZP did not show any change of the value (ZP= +15 mV), this value being in agreement with the absence of charge in the CE molecule[4], nevertheless, ZP study did not permit us to confirm the surface modification.

In a last point, Figure 1. C demonstrates that the CE-STMS suspensions display a good colloidal stability with an average hydrodynamic size of ca. 271 nm.
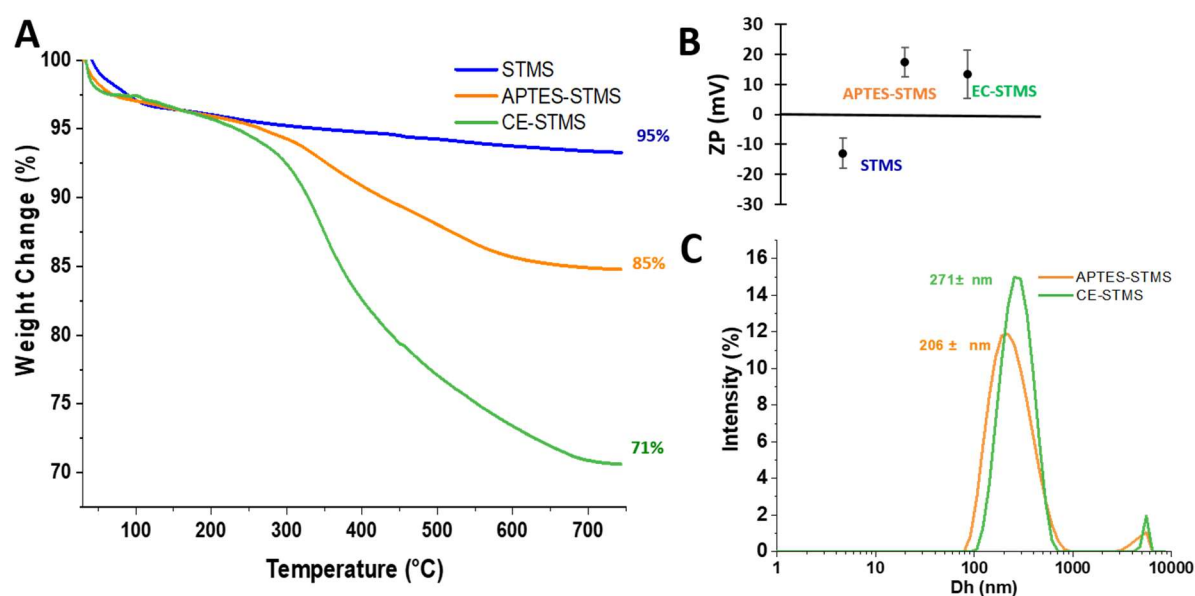
Figure 1. A. TGA and B. ZP of STMS (blue), APTES-STMS (orange), CE-STMS (green) and C. DLS size distribution of APTES-STMS (orange) and CE-STMS (green).

III. 2. 2. Sodium capture with Crown-Ether

III. 2. 2. 1. Co-solvent media and water

Our first system is the functionalized STMS with benzo 15-crown-5. Here, the CE ligands contain a carboxylic acid function which react with the amine functions of previous APTES-STMS NPs. This last reaction is done in ethanol where the STMS particles are well dispersed in presence of ammoniac (Stöber-like conditions) to form a NH_2 layer. Then, we address the ability of CE-STMS to selectively chelate sodium in two different media: methanol-water (80 % - 20% v/v) to investigate the sodium capture in optimal conditions and in water (100%) to work in conditions near to dialysis applications.

The peritoneal dialysis being implemented in biomedical situation; the dialysis solution is generally a multi-ionic aqueous solution (Ca^2, Na^+, Mg^{2+} and Cl^-). However, studies and experiments performed on free CE (no grafted) showed a better constant stability in other solvents or co-solvents (log $K_{f\ in\ water}$= 0.58, log $K_{f\ in\ THF}$>4[5], log $K_{f\ in\ acetonitrile}$=4.91[6]), log $K_{f\ in\ acetone}$=3.68, log $K_{f\ in\ DMF}$=1.97[5]. According to the study of Dishong, a work about the variation of the stability constant of the complex Na**15CE5** in different proportions of a mix methanol-water, the co-solvent chosen was a mix 80-20 % (v/v) methanol-water (log K_f 3.25)=.[7]

We introduced the next parameters to quantify the sodium removal by CE (same equations for the cryptand experiments):

$$\text{Capture Capacity} = \frac{n_{Na\ captured}\ (nmol)}{m_{silica}\ (mg)}$$

$$\text{Capture Efficiency}\ (\%) = 100 \times \frac{n_{Na\ captured}\ (mol)}{n_{Na\ initial}\ (mol)}$$

$$\text{Macrocycle Coverage}\ (\%) = 100 \times \frac{n_{Na\ captured}\ (mol)}{n_{\ grafted\ macrocycles}\ (mol)}$$

We thus tested the sodium capture by the CE-STMS ($CE_{grafted}$=4452 nmol) in this co-solvent (20:80) for two molar stoichiometries Na:CE 0.9:1 and 4.7:1. The results summarized in Table 1 showed that sodium capture was improved, from a capacity capture of 245 $nmol_{Na+}·mg^{-1}_{SiO2}$, for Na:CE 0.9:1 stochiometry, to 1600 $nmol_{Na+}·mg^{-1}_{SiO2}$ for Na:CE 4.7:1 stoichiometry. This values corresponds respectively to a $CE_{grafted}$ coverage of 25 % and 216 %. This shows that the grafting of CE at the STMS surface as compared to free CE does not affect the capacity to efficiently chelate sodium cations. Interesting experiments in cosolvent environment and large excess of sodium indicate an occupancy of Na of 201 % of grafted crown-ether, much more than the initial vacancy sites. The first explanation could be a different stoichiometry than expected, some groups reported stoichiometries 2:1 and 3:2 that suggests a "sandwich structure"[8], nevertheless, this hypothesis could be difficultly verified in our study as CE grafted on STMS could not have enough mobility to form this kind of structure. Another explanation could lay on interactions between Na^+ ions and bare zones on the STMS NPs (negatively charged). Indeed, similar phenomenons occured in other contexts where grafted APTES onto silica NPs (positively charged) were proved to capture negatively charged ferric nitrilotriacetate complex ($FeNTAH^-$)[9]. However, a different behavior of NaCl molecules in methanol could explain this adsorption. To summarize, the trend observed in Na^+ capture by CE-STMS can be explained by two mechanisms: one likely corresponds to strong and selective chelation binding

with metal-ligand coordination bonds, and the other, non-selective and potentially corresponding to weak interactions with the NPs surface or CE ligand.

With the aim to apply our nanoobjects for PD applications, we assessed the sodium capture in aqueous solutions at different pH (pH=7 and 5) and at different Na:CE stoichiometries (0.9:1 and 4.7:1). We found in water for a 0.9:1 stoichiometry conditions at pH =7, only capacity capture of 28 $nmol_{Na+} \cdot mg^{-1}_{SiO2}$ (corresponding to 2.8 % of efficiency and to 3.7 % of coverage). In order to displace the sodium capture equilibrium, the CE-STMS NPs were introduced in a solution with a larger excess of sodium at a stochiometry Na:CE 4.7:1 at pH =7, which yielded to improvement of the capacity capture to 124 $nmol_{Na+} \cdot mg^{-1}_{SiO2}$ (corresponding to 16.7 % of coverage). Similar experiments in a slighthly acidic solution (pH 5) did not allow to improve this results as 108 $nmol_{Na+} \cdot mg^{-1}_{SiO2}$ were obtained (14.5 % of coverage).

Table 1. Efficiency and capacity captures of CE-STMS in two different solutions containing different sodium cations under different conditions. (Na$^+$: CE$_{grafted}$ stoichiometries (0.9:1 and 4.7:1), impregnation time of one night at 25°C, pH 7 and 5 for water experiments, solvent 80-20 % (v/v) methanol-water on 6 mg of functionalized STMS nanoparticles).

	H₂O: MeOH (20:80)		H₂O		
	Na:CE 0.9:1	Na:CE 4.7:1	Na:CE 0.9:1 pH=7	Na:CE 4.7:1 pH=7	Na:CE 4.7:1 pH=5
Efficiency capture (%)	25	31	2.8	2.4	2.1
Capture Capacity ($nmol_{Na+} \cdot mg^{-1}_{SiO2}$)	245	1600	28	124	108
Coverage (%)	25	216	3.7	16.7	14.5

Thus, functionalized CE-STMS NPs were shown less efficient to capture a consequent quantity of sodium in water solution, even with more sodium as compared to organic media. According to studies of ions uptake with crown-ethers, to improve the sodium capture, other solvents than water are able to form a more stable complex for two main reasons. The first one is that the structure of the complex is upgraded by the addition of solvent molecules to complete the complex structure (log $K_{f\ in\ water}$= 0.58, log $K_{f\ in\ chloroform}$= 3.25).[2] The second one is that cations are more strongly solvated in water than methanol, consequently, the solvation sphere increases the cation radius and the match cation-cavity become more difficult.[10] This could explain the behaviour of our system, nevertheless, it is important to emphasize than grafting the CE on a support did not modify the sodium ability of the 15-crown-5 ether.

III. 3. Mesoporous silica nanoparticles functionalized with Cryptant$_{221}$ to sodium removal

Previous experiments showed the capacity of our first material to remove sodium in two different media. Nevertheless, for peritoneal dialysis it is impossible to work with 80 % of methanol due to its toxicity and health problems.[11] To perform our experiments in water, we looked for another ligand with a higher constant complex with sodium: the cryptands, and after the studies of Lehn's group, we decided to focus our study in cryptand [2.2.1] (log K$_{f\ in\ water}$=5.40).[1] Cryptands were shown to be excellent solutions for this, as they possess a higher stability constant complex in water and other solvents. This effect was termed the macrobicyclic cryptate effect, by analogy to the macrocyclic effect.[10] However, as we will see in the next paragraph of this chapter, due to the nature of the molecule, the grafting of the cryptands at the surface of NH$_2$-STMS is more challenging that CE.

III. 3. 1. Grafting of Cryptant$_{221}$

III. 3. 1. 1. Cryptand grafting by EDC

C$_{221}$ cryptand grafting was achieved on a similar way than crown-ether. For that, the molecule cryptant C$_{221}$ bearing a carboxylic group was fully synthesized according to a multistep procedure. As before, the reaction with the amines of NH$_2$-STMS NPs involved the formation peptide bond to link C$_{221}$ cryptands. We used different strategies with different acid activators: EDC, EDC-NHS and HBTU. To better understand each reaction, the reactional mechanisms and the results of grafting are developed below.

In scheme 2, the different steps of this reaction are described. On first, the carboxylic function reacts with EDC, an intermediate O-acylisourea, unstable in aqueous solution. Then, the primary amine grafted on the silica surface forms an amide bond with the previous carboxyl function and isourea.[12]
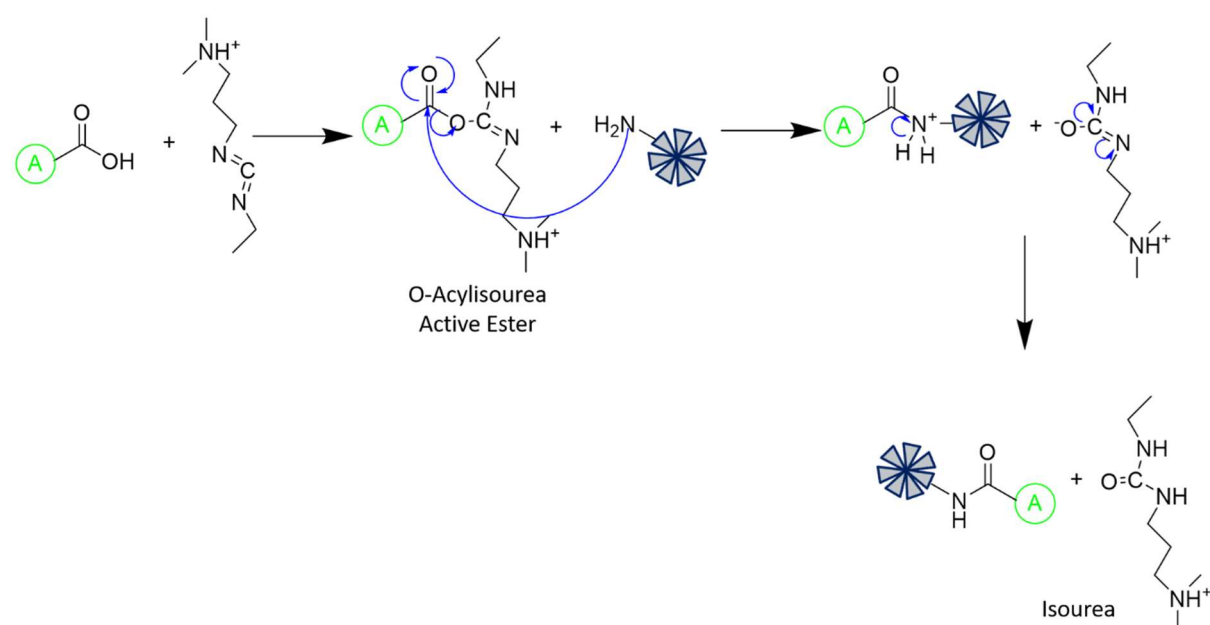
Scheme 2. Mechanism of cryptand grafting by EDC.

As for the CE grafting, the C$_{221}$ grafting was evaluated by thermogravimetric analysis (Figure 2, Cryptand violet curve) at 1.2 µg of C$_{221}$ per mg of STMS (2.7 nmol$_{C221}$·mg$_{SiO2}$$^{-1}$), which is a very low grafting. It may be possible that the cryptand being a bigger molecule than CE, it has a more steric constraint and its reactivity is decreased.

95

It is possible that the intermediary product O-acylisourea was not enough stable in time and did not meet an amine group during the reaction.
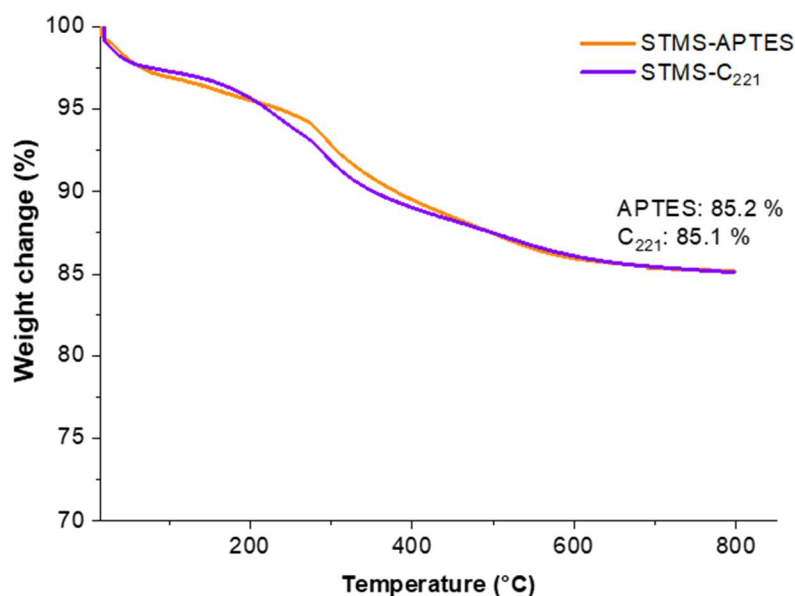
Figure 2. TGA of C_{221}-STMS (violet) grafted by EDC.

III. 3. 1. 2. Cryptand grafting by EDC-NHS

In order to use a more stable intermediate molecule, we adopted the EDC-NHS method.
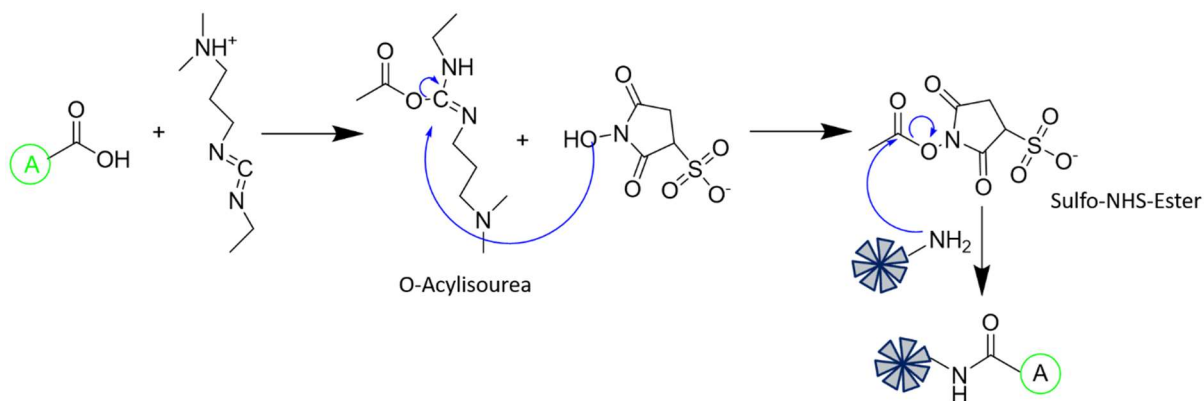
Scheme 3. Mechanism of cryptand grafting by EDC-NHS.

In general, N-hydroxysuccinimide (NHS) is included in the protocol to improve efficiency and to form a more stable amine-reactive intermediate. In scheme 3, the O-acylisourea couples NHS to carboxyls, then, a sulfo-NHS-ester is formed that is more stable (from minutes to hours) than the O-acylisourea. This could allow an efficient conjugation to primary amines at physiologic pH.[12]

Figure 3 showed a slight improvement of the grafting. This time, we could graft 35 µg of C_{221} per mg of STMS (80 $nmol_{C221} \cdot mg_{SiO2}^{-1}$). The result of grafting is better than for the EDC process, confirming that the "sulfo-NHS-ester" intermediate is more stable. Nevertheless, the result can still be improved.
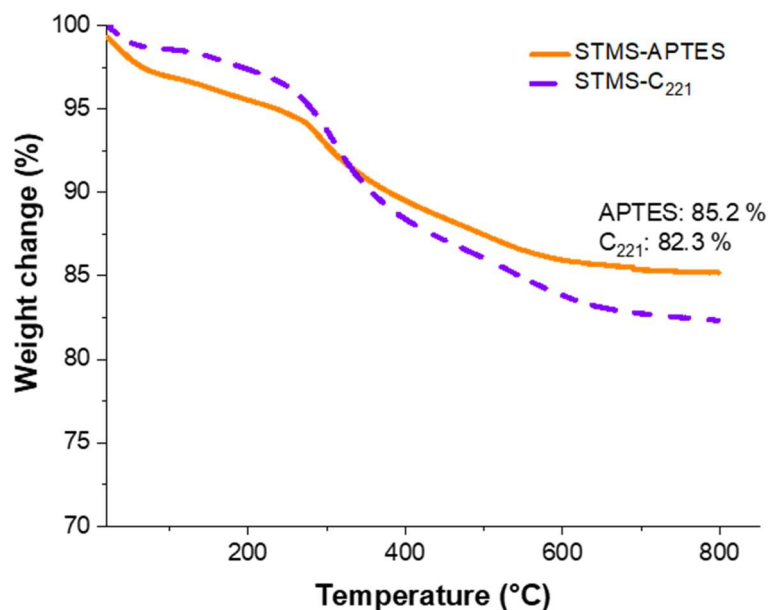
Figure 3. TGA of C$_{221}$-STMS (dash violet curve) grafted by EDC-NHS.

To improve the grafting, we investigated together the grafting of polyamines (PEI) instead of APTES and the use of another activator. The idea is to provide more amine flexible amines functions at the surface of STMS i.e. longer arms/chains with the PEI. The activator is HBTU which is well-known because its intermediate group may be more stable.

III. 3. 1. 3. Cryptand grafting by HBTU

To increase the number of flexible amine groups at the surface of STMS and increase the flexibility of the chains, we changed the APTES function by poly(ethylenimine), PEI: a polymer containing primary and secondary amine functions.

In scheme 4, the carboxylic acid is first deprotonated with a strong base (triethyil amine). Then, the carboxylate group attacks the imide carbonyl carbon of the HBTU. An intermolecular arrangement gives HOBT$^-$ and an ester. Later, HOBT$^-$ attacks this ester to create the activated leaving group HOBT-ester. Finally, amine groups of PEI-STMS displaces the HOBT$^-$ and the cryptand is grafted on the surface by a peptide bond.

97
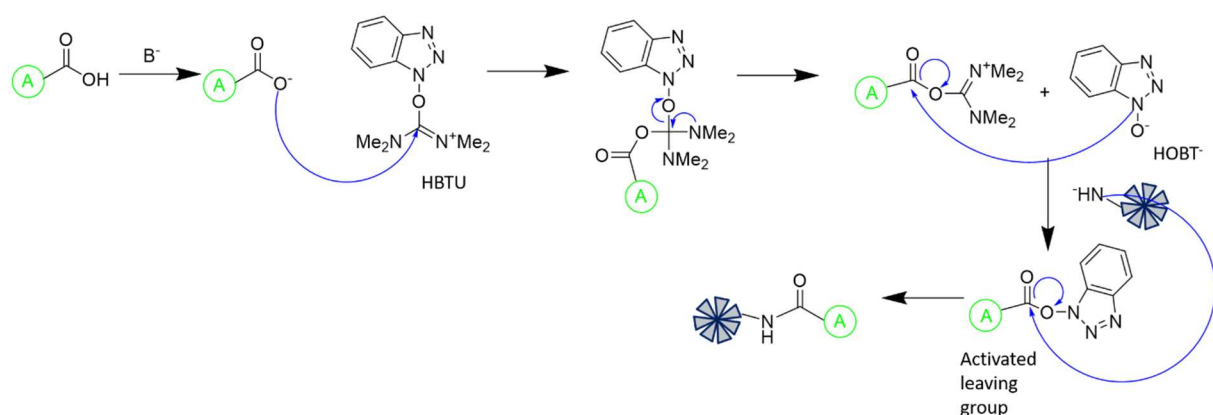
Scheme 4. Mechanism of cryptand grafting by HBTU.

In a first rapid and simple step, the STMS were functionalized with PEI via a sample procedure of electrostatic adsorption. In Figure 4, PEI-STMS and C_{221}-STMS have a first weight loss at 100°C, as for other samples, it was attributed to evaporation of solvent (water), trapped inside the pores. The several weight losses between 200 °C and 730 °C are linked to the burning of organic molecules grafted (polymer chain, ammonium groups) on the samples. The grafting rate was then calculated to be at about 181 $\mu g_{PEI} \cdot mg_{STMS}^{-1}$ (weight loss 79.6 %). In the same way, TGA analysis (Figure 4.A, C_{221} violet curve) allowed to determine a grafting rate of about 96 µg of C_{221} per mg of STMS (219 nmol·mg^{-1}).

Regarding to the surface charge, as explained before (chapter II, iron capture), it is possible to validate the sequential steps of the functionalization (Figure 4.B): bare (ZP= -13 mV); PEI (ZP = +35 mV); C_{221} modified STMs (ZP = +28 mV). These results are perfectly consistent with the incorporation of ammonium groups and non-charged molecules (C_{221}). Finally, the C_{221}-STMS formed excellent colloidal suspensions in water with hydrodynamic diameters (Dh) of ca. 190 nm (Figure 4.C). This colloidal stability is favorable to purify aqueous media for the next experiments.
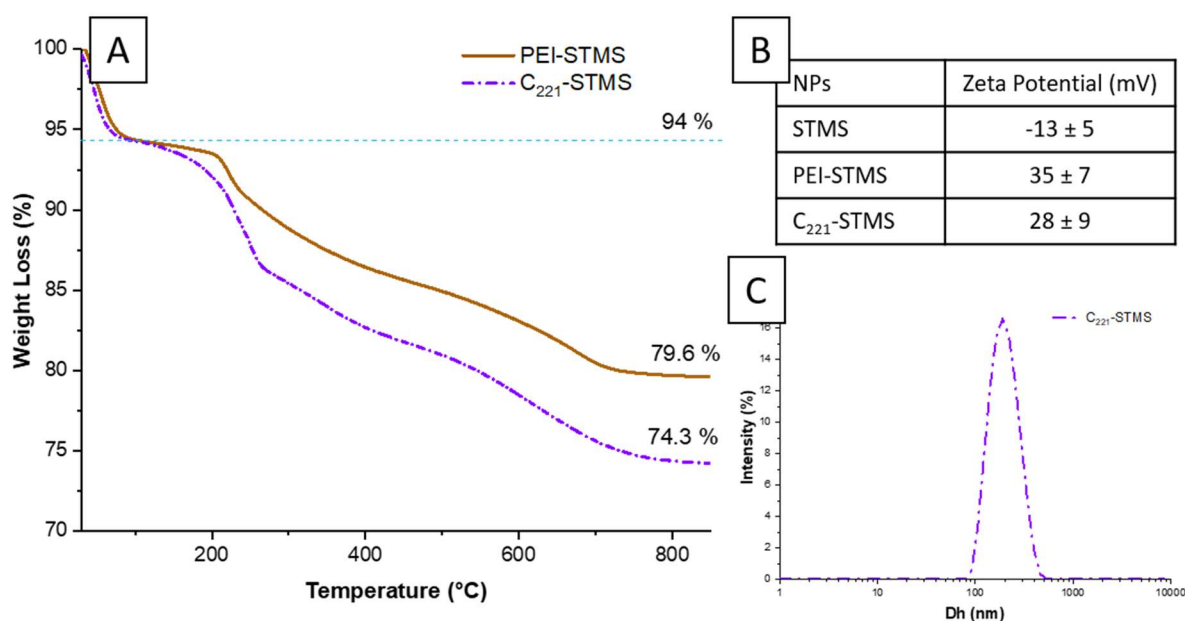
Figure 4. A. TGA of PEI-STMS (brown curve) and C_{221}-STMS (dotted violet curve) grafted with HBTU. **B**. Zeta potential of the samples **C**. DLS size distribution of C_{221}-STMS.

III. 3. 2. Sodium capture with C_{221}

III. 3. 2. 1. Water media.

Contrary to the study with CE-STMS NPs, experiments with C_{221}-STMS (219 $nmol_{C221} \cdot mg_{SiO2}^{-1}$) were directly performed in water. Similarly to the CE-STMS, to demonstrate the potential for PD applications, we assessed the sodium capture in aqueous solutions at different Na:CE stoichiometries (0.9:1 and 4.7:1) and the same pH (pH 7).

This time, in water for a 0.9:1 stoichiometry conditions, the capacity capture was found at 34.1 $nmol_{Na+} \cdot mg^{-1}_{SiO2}$ (corresponding to 12.5 % of efficiency and to 15.5 % of coverage). In the case of a larger excess of sodium (Na:C_{221} 4.7:1), the capture capacity increased to 368 $nmol_{Na+} \cdot mg^{-1}_{SiO2}$ (corresponding to 26.2 % of efficiency and 168 % of cryptand coverage). Comparing with the previous results of CE-STMS, the material containing cryptands is more performant in the stoichiometry 0.9:1 (Na:$macrocycle_{grafted}$). However, for the experiment with a sodium excess (4.7 eq.) the capture capacity is larger than expected (168 % of couvrance). As for the previous system, we have the capture of sodium by the macrocycles and an additionnal adsorption by other parts of the nanomaterials. To see a possible capture by NH_2 of PEI or APTES, further experiments will be improved. Finally, these last results are higher than for CE-STMS under the same conditions. It suggests the high potential of these nanomaterials in the peritoneal dialysis treatment.

Table 2. Efficiency and capacity captures of C_{221}-STMS in two different solutions containing different sodium cations under different conditions. (stoichiometries Na^+:C_{221} (0.9:1 and 4.7:1), impregnation time of one night at 25°C, pH 7 on 6 mg of functionalized STMS nanoparticles grafted at 219 nmol/mg).

	Na:C_{221} (0.9:1) pH=7	Na:C_{221} (4.7:1) pH=7
Capture Capacity ($nmol_{Na+} \cdot mg^{-1}_{SiO2}$)	34.1	368
Efficiency capture(%)	12.5	26.2
Cryptand coverage (%)	15.5	168

In order to validate their future applications, espacially regarding their selectivity, the experiment in the next paragarph will consist in testing the C_{221}-STMS in multielement media.

III. 3. 2. 2. Na(I) selectivity of the C_{221}-STMS

In this part, our aim was to study the chelation selectivity of Na(I) with respect to other cations present in the dialysis solution (Ca^{2+} and Mg^{2+}). As for the iron case in chapter II, we investigated if C_{221}-STMS NPs can selectively uptake sodium (I) in a multi-element environment. Two different media were used to demonstrate that our material can capture sodium without other ion perturbation.

The first medium is a medium where all the cations have the same concentrations with the aim to evidence a selective captation. The solution contains Na^+, Ca^{2+} and Mg^{2+} ($2.0 \cdot 10^{-4}$ M) at pH 7 (multielement solution). Corresponding to 0.9 molar equivalents as compared to C_{221} grafted on STMS ([$C221_{grafted}$]=$2.2 \cdot 10^{-4}$ M).

The second medium mimics a biomedical situation of peritoneal dialysis by using the dialysis solution from Fresenius Medical Care that is provided to patients.[13] It contains cations Ca^{2+} and Mg^{2+} at respectively $2.2 \cdot 10^{-6}$

and $8.7 \cdot 10^{-6}$ M. To model a high level of sodium cations corresponding to renal failure diseases, we set Na$^+$ at $5.5 \cdot 10^{-4}$ M. this corresponds to 20% of the initial concentration. This sodium concentration is justified by the studies of Fischbach *et al.*[14] In their research about sodium removal, they have adapted automatic peritoneal dialysis treatment, and removed around 20 % of the initial sodium concentration. In our study, we aimed at reproducing this reduction by using the strategies of cryptand-grafted stellate mesoporous silica.

Results are summarized in the Table 3.

Table 3. Capture capacity, efficiency and coverage of C$_{221}$-STMS in two different media solutions containing different metal cations. M: C$_{221}$ stoichiometries (0.9:1) for the multielement solution. And M: C$_{221}$ stoichiometries 2.6, 0.04 and 0.01 : 1 (Na$^+$, Ca^{2+} and Mg^{2+}) for the equivalent of peritoneal dialysis. Impregnation time of one night at 25°C, pH 7 on 6 mg of functionalized STMS nanoparticles).

	Ion	Na$^+$	Ca^{2+}	Mg^{2+}
Multielemement solution	**Initial concentration (M)**	$2.0 \cdot 10^{-4}$	
	Capture Capacity (nmol$_{ion}$·mg^{-1}$_{SiO2}$)	5.9	65.5	11.3
	Efficacity Capture (%)	2.2	24.3	4.2
	Cryptand coverage (%)	3	30	5.1
Equivalent to peritoneal dialysis solution	**Initial concentration (M)**	$5.5 \cdot 10^{-4}$	$2.2 \cdot 10^{-6}$	$8.7 \cdot 10^{-6}$
	Capture Capacity (nmol$_{ion}$·mg^{-1}$_{SiO2}$)	20.7	0	0.75
	Efficacity Capture (%)	2.8	0	6.4
	Cryptand coverage (%)	9.5	0	0.03
K$_f$ Ion-C221		$10^{5.40}$	$10^{6.95}$	$< 10^2$

For the multi-element solution, the capture capacity, efficiency and cryptand coverage (5.9 nmol$_{Na+}$·mg^{-1}$_{SiO2}$, 2.2 % and 3 %) of sodium are smaller than in the previous experiments with C221 alone. Moreover, it is observed that calcium capture is much higher than for sodium with a capture capacity 65.5 nmol$_{Ca2+}$·mg^{-1}$_{SiO2}$ (with efficiency and cryptand coverage =24 and 30 %). These differences are explained by a competition between Ca^{2+} and Na$^+$ cations because of their complex constants, the one of Ca-C$_{221}$ (log K$_f$ = 6.95) being higher than those of Na-C$_{221}$ (log K$_f$= 5.40). Concerning magnesium cations, the results agrees with the "small" constant complex (capture capacity 11.3 nmol$_{Mg2+}$·mg^{-1}$_{SiO2}$). Nonethess, the capture of magnesium is close to the one of sodium. This last result may be explained by a change of the complexation constants induced by the aromatic ring. In fact, the effects of benzo and other substituents on the complexation properties were reported to decrease metal ion binding and selectivity. A performed study in cryptand [2.2.2] (well known for a high binding K$^+$) exhibited a decrease of log Kf values and a loss of selectivity.[10] The previous reported values of constant complex are of the naked cryptand, but our cryptand also contains a benzene ring in the structure. So, it can be possible than the affinity of our cryptand is different. Instead of Ca^{2+}>Na$^+$>Mg^{2+}, the selectivity was modified and become Ca^{2+}>Mg^{2+}>Na$^+$. Another interesting result here is the total cryptand coverage, if we add the three results, we obtained a total coverage of 38.1 % with many cryptand cages being still free. Indeed, even if there are different reactivity of the ligands, based on the complex constants and if it is easier to capture calcium than sodium, the captation migh be also highly dependant on cation concentrations.

Furthermore, it is worthy to note that, even if the constants for Ca and Mg are higher than for Na , the cryptand [2.2.1] remains nevertheless the best ligand to capture sodium to the best of our knowledge. Indeed, Ca^{2+} and Mg^{2+} being present in ultra small amount in the peritoneal medium or in blood, they might not interfere with sodium captation. As sodium is the most concentrated specie of this medium as compared to Ca (250 times) and Mg (63 times), we suppose that this capture could be improved despite of the affinities.

Thus, regarding the study in the equivalent medium of peritoneal dialysis, achieved at 2.6 eq of sodium the results showed a higher capture for sodium than the other cations (capture capacity of 20.7 $nmol_{Na+} \cdot mg_{SiO2}^{-1}$). As compared to sodium alone described above achieved at 0.9 equivalents, it is less than the amount at 34.1 $nmol_{Na+} \cdot mg_{SiO2}^{-1}$. This value is between the experiment at the same concentration (5.9 $nmol_{Na+} \cdot mg_{SiO2}^{-1}$) and that of the sodium at 0.9 eq (capture capacity: 34.1 $nmol_{Na+} \cdot mg_{SiO2}^{-1}$). The diminution of the capture could be an effect of the presence of calcium and magnesium. Even if the sample presents a very low quantity of calcium and magnesium, their presence could disturb the behaviour of the cryptands.

To summarize these two studies, a close link could be suggested between the sodium capture and the calcium presence in the solution. Concerning the diminution of the sodium quantity, we succeed to remove around 9 % of sodium. This corresponds to the half value versus the 20 % with the adapted automatic peritoneal dialysis of Fischbach *et al.* who used several cycles of solutions dwells.[14,15] To improve this value, we investigated the possibility to render our system recyclable and to capt this amount at each cycle of peritoneal dialysis.

III. 3. 2. 3. Recyclability

The advantage of covalently anchoring macrocycles forming complexes with cations on a support offers the possibility of recycling. Thus we investigated if after sodium capture, this element can be removed and the NPs be used again.

To assess the recyclability of the C_{221}-STMS NPs, the experiments were carried out in three successive cyclic steps: sodium trapping, then calcium trapping (or sodium replacing) and then calcium release. In fact, and as shown above, the Na-C_{221} cryptate is very stable in water at physiological pH, however, the cryptate **Ca-C$_{221}$** is more stable (log K_f = 6.95[1]) than Na-C_{221}. Nevertheless, Ca^{2+} can form a more stable complex with EDTA (log K_t= 11.[16] Thus, the main idea of this final step is to exchange Ca^{2+} ligands with EDTA to remove all calcium cations from C_{221}-STMS.

To replace sodium per calcium cations inside the STMS, we employed a calcium solution at pH 7 (stoichiometry Ca:C_{221} grafted – 100:1). Finally, for calcium removing, the NPs were dispersed in a EDTA solution containing 50 molar eq of EDTA (calculated from amount of cryptand mole) to remove all the calcium inside the cages. This addition is repeated three times to remove most of the calcium.

Figure 5 summarizes the results of this technique. It was observed that calcium replaces a major part of sodium inside the cages (ca. of 90 %), however, in the next step, just a moderate part (40 %) of these calcium cations could be removed from the cryptands by EDTA. Finally, this method has shown a good performance for a first trial to recycle cryptands.

In a brief review, the other recycle methods were by the protonation of the cryptates in methanol[17] and by a process in eleven steps in aqueous media.[18] These methods are difficult and expensive to adapt to our system. Our method, based on a ligand exchange is moderately long, but low-cost and effective. In future projects, the method can be performed making many wahings with EDTA to remove the totality of those ions.
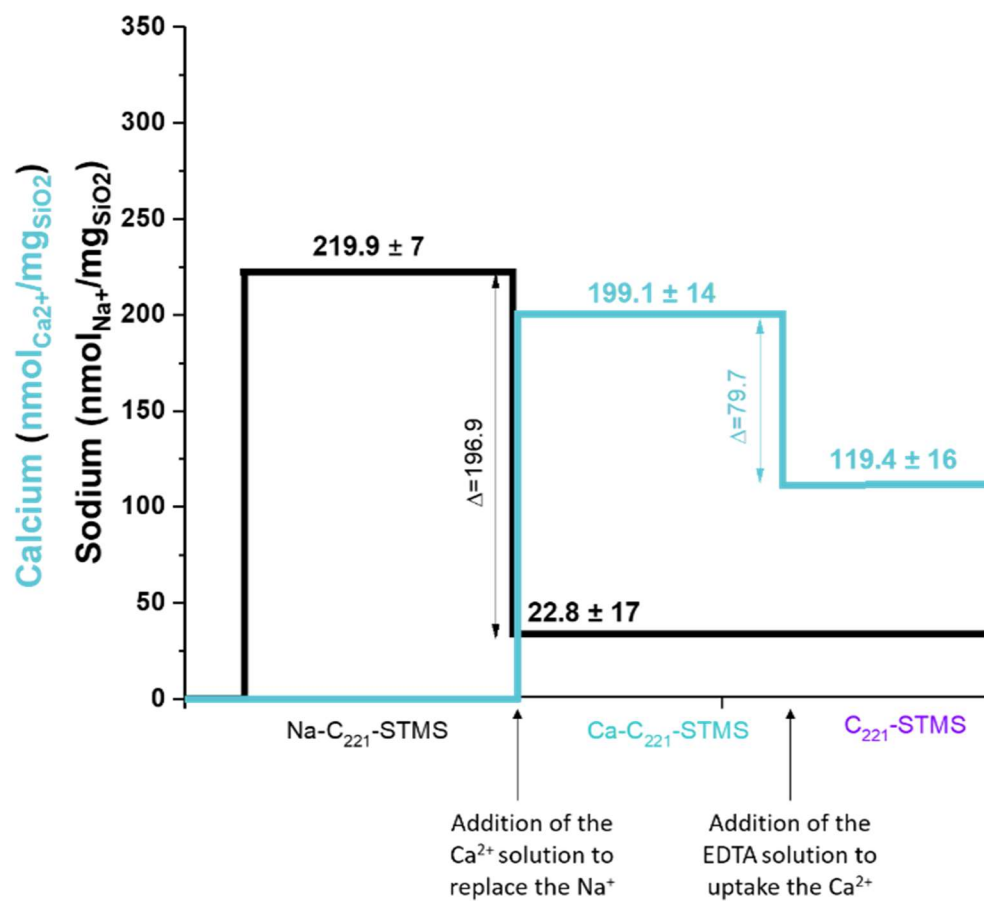
Figure 5. Recyclability Results

Conclusion

In this work, the versatile potential of STMS functionalization with macrocycles allowed them to be applied for specific sodium uptake. The chemical engineering of such well design porous silica material able to selectively capture sodium, is based on the properties of high chelating ligands such as ether crowns and cryptands which were grafted on biocompatible transport stellate silica materials with high specific surface area.

For CE, we showed a grafting of crown-ether on APTES-STMS of 742 $nmol_{CE} \cdot mg^{-1}_{SiO2}$, which was achieved using the EDC strategy. Furthermore, we confirmed that the behavior of $CE_{grafted}$ are similar than of free CE. Indeed, the media is an essential factor to assure the best capture. In a co-solvent media (methanol-water (80 % - 20 % v/v), capture capacity was 245 $nmol_{Na+} \cdot mg^{-1}_{SiO2}$ (25 % of coverage) for a stoichiometry Na:CE 0.9:1 and 1600 $nmol_{Na+} \cdot mg^{-1}_{SiO2}$ for Na:CE 4.7:1 (216 %). This last result suggests two mecanisms of capture: the first by complexation via ligands, the second by non-specific interactions. This results agrees with the complexation behavior of free crown-ether in such solvent.

For cryptand C_{221}, despite of the difficulties to graft it directly on the STMS, we have developed new strategies of functionalization. Thanks to HBTU and polyethyleneimine, we could graft 219 $nmol_{C221} \cdot mg^{-1}_{SiO2}$, an inferior value than for CE-STMS, which could be explained by steric constraint. To increase the grafting, it was assumed that the cryptand cages must be far of the silica, so, the addition of longer chains (i.e. other polymers) could help to obtain greater graftings. This material showed similar capture capacities than for CE-STMS in water for a stoichiometry Na:C_{221} 0.9:1 (34.1 $nmol_{Na+} \cdot mg^{-1}_{SiO2}$ for C_{221} and 28 $nmol_{Na+} \cdot mg^{-1}_{SiO2}$ for CE), however the coverage was found much better (15.5 % vs 3.7 %) given that the ligand density is lower for C_{221}. For a larger excess of sodium (Na: C_{221} 4.7:1), the capture capacity and the coverage increased (368 $nmol_{Na+} \cdot mg^{-1}_{SiO2}$ and 168 %). As for the CE-STMS, this last value could be justified by two modes of binding for sodium : specific complexation via ligands, and the second by non specific interactions with the present amine on PEI.

At last, the capture of sodium, in the multielement media at the same concentration, showed a great affinity with calcium rather than sodium (65.5 $nmol_{Ca2+} \cdot mg^{-1}_{SiO2}$ and 5.9 $nmol_{Na+} \cdot mg^{-1}_{SiO2}$) which is explained by the complexations constants. However, in a medium containing the same elements but with a higher concentration of sodium (equivalent to the peritoneal dialysis solution), and where calcium and magnesium ions are negligible in concentrations, the NPs showed a higher capture capacity in sodium (20.7 $nmol_{Na+} \cdot mg^{-1}_{SiO2}$) face to the other two elements.

Finally, even if this last result display a moderate sodium capture, this material shows nevertheless a high potential for their use in medical treatments. Indeed, avoiding deadly hyponatremia (lack of sodium) does not consist in the massive removal of sodium but more likely to low capture ensuring sodium level regulation at below 150 mM. As the massive removal of sodium ions would be detrimential to our organism, the sodium uptake should be finely controlled and a good compromise between effective sodium uptake and sodium level regulation must be achieved. That is why the combination of sequential low uptakes and recyclability appears as a way to finely control this level.

References

(1)   Lehn, J. M.; Sauvage, J. P. Cryptates. XVI. [2]-Cryptates. Stability and Selectivity of Alkali and Alkaline-Earth Macrobicyclic Complexes. *J. Am. Chem. Soc.* **1975**, *97* (23), 6700–6707.

(2)   Pedersen, C. J.; Frensdorff, H. K. Macrocyclic Polyethers and Their Complexes. *Angew. Chem. Int. Ed. Engl.* **1972**, *11* (1), 16–25.

(3)   Azaroon, M.; Kiasat, A. R. An Efficient and New Protocol for the Heck Reaction Using Palladium Nanoparticle-Engineered Dibenzo-18-Crown-6-Ether/MCM-41 Nanocomposite in Water. *Appl. Organomet. Chem.* **2018**, *32* (4), e4271.

(4)   Etzkorn, F. A. *Green Chemistry: Principles and Case Studies*; Royal Society of Chemistry, 2019.

(5)   Lin, J. D.; Popov, A. I. Nuclear Magnetic Resonance Studies of Some Sodium Ion Complexes with Crown Ethers and [2]-Cryptands in Various Solvents. *J. Am. Chem. Soc.* **1981**, *103* (13), 3773–3777.

(6)   Buschmann, H.-J. The Influence of Acetonitrile on Complex Formation of Crown Ethers Containing Different Donor Atoms. *J. Solut. Chem.* **1988**, *17* (3), 277–286.

(7)   Dishong, D. M.; Gokel, G. W. Crown Cation Complex Effects. 16. Solvent Dependence of the 15-Crown-5 and 18-Crown-6 Equilibriums with Sodium Cation. *J. Org. Chem.* **1982**, *47* (1), 147–148.

(8)   Pedersen, C. J. Crystalline Salt Complexes of Macrocyclic Polyethers. *J. Am. Chem. Soc.* **1970**, *92* (2), 386–391.

(9)   Duenas-Ramirez, P.; Bertagnolli, C.; Müller, R.; Sartori, K.; Boos, A.; Elhabiri, M.; Bégin-Colin, S.; Mertz, D. Highly Chelating Stellate Mesoporous Silica Nanoparticles for Specific Iron Removal from Biological Media. *J. Colloid Interface Sci.* **2020**, *579*, 140–151.

(10)   Hamilton, A. D. 5.21 - Crown Ethers and Cryptands. In *Comprehensive Heterocyclic Chemistry*; Katritzky, A. R., Rees, C. W., Eds.; Pergamon: Oxford, 1984; pp 731–761.

(11)   Tephly, T. R. The Toxicity of Methanol. *Life Sci.* **1991**, *48* (11), 1031–1041.

(12)   Carbodiimide Crosslinker Chemistry - FR //www.thermofisher.com/fr/fr/home/life-science/protein-biology/protein-biology-learning-center/protein-biology-resource-library/pierce-protein-methods/carbodiimide-crosslinker-chemistry.html (accessed Aug 20, 2020).

(13)   Knerr, T. Solution for Peritoneal Dialysis. US6277815B1, August 21, 2001.

(14)   Fischbach, M.; Schmitt, C. P.; Shroff, R.; Zaloszyc, A.; Warady, B. A. Increasing Sodium Removal on Peritoneal Dialysis: Applying Dialysis Mechanics to the Peritoneal Dialysis Prescription. *Kidney Int.* **2016**, *89* (4), 761–766.

(15)   Domenici, A.; Scabbia, L.; Sivo, F.; Falcone, C.; Punzo, G.; Menè, P. Determinants of Sodium Removal with Tidal Automated Peritoneal Dialysis. - Abstract. *Adv. Perit. Dial. Conf. Perit. Dial.* **2012**, *28*, 16–20.

(16)   D., J. V. Stability Constants of Metal-Ion Complexes (Sillen, Lars Gunnar; Martell, Arthur E.). *J. Chem. Educ.* **1965**, *42* (9), 521.

(17)   Perdicakis, M.; Bessière, J. Recyclage Du Cryptand (222). *Anal. Lett.* **1986**, *19* (3–4), 393–401.

(18)   Shih, J.; Lin, L.; Propov, A. *J Inorg Nucl Chem* **1977**, *39*, 553.

Chapter IV
Investigation of phosphate capture enhancement in peritoneal dialysis process using designed iron oxide nanostructures

Introduction

The chronic renal failure (CRF) is a disease which consists of the progressive loss of kidney functions, including homeostasis and extracellular volume balance, phosphocalcic balance, and bone metabolism. Patients suffering of the end-stage renal failure cannot remain without a cleansing treatment. Several treatment options exist for them such as dialysis and transplantation. As transplantation depends on the availability of donated kidneys, dialysis is the most current treatment for this kidney disease. There are two kinds of dialysis: hemodialysis (HD) and peritoneal dialysis (PD). Hemodialysis consists of purifying the blood in an extracorporeal route where blood is cleaned thanks to a dialysis machine. During peritoneal dialysis treatment, a designed dialysis solution is introduced into the peritoneal cavity of the patient and for a few hours, the composition of the liquid is balanced with that of the blood compartment. By diffusion and convection mechanisms through the capillaries, toxins and water excesses pass into the dialysate. The dialysate is then drained outside the body before the subsequent provision of new dialysis fluid. The duration of the exchanges varies according to the needs of the patient and the chosen technique.

If we compare both HD and PD: HD session lasts from 3 to 5 hours, during which the patient cannot move. At least, three sessions per week are necessary to allow an effective purification. This method has also other limitations, especially in infants weighing less than 6-8 kg where HD is difficult to perform due to their too low blood volume.

By contrast, during the PD sessions, the patient does not need to be branched to a machine, and they have movement liberty. In addition to its lower cost, PD has many advantages for the patient: the possibility of being autonomous in the treatment, fewer hospitalizations are needed, less quantity of side treatments as anti-coagulants, and the possibility to perform the treatment during the night/sleep. This last point makes that PD is mainly used for children and new-born babies.

However, after a dialysis of 4 hours, HD and PD respectively remove 50-60 % and 40 % of the initial phosphates which is among the most harmful compounds to remove from blood.[1,2] It crowns HD as the best treatment. However, as underlined above, PD is more comfortable for patients, may thus ensure a better quality of life to all patients and is more adapted for children but HD is the most efficient ones.

Therefore, there is a great interest in improving PD treatment. Most improvement have concerned the duration and sequences of the PD treatment but very few have proposed to work on the dialysate

composition to enhance the caption of biological pollutants. Knowing that among the most harmful compounds to remove from blood are phosphates ones, we propose here to investigate the addition of iron oxide nanoparticles into dialysate to enhance phosphate removal from blood. Indeed, iron oxide particles have been widely developed to remove phosphates from polluted media[3–6] and appear as very suitable compounds to face the challenge to enhance the phosphate removal using PD.

Among iron oxide nanoparticles, we choose iron oxide raspberry-shaped nanostructures (RSN), which consist in oriented aggregates/nanoclusters of iron oxide nanograins with a mean diameter ranging from 50 to 500 nm. They display a rather "big size" ensuring that they will not cross the peritoneal membrane. Secondly, they possess interesting magnetic properties, which makes them easy to recover with a magnet from dialysate and thus they may be recycled. Indeed, an earlier study using iron oxide nanoparticles of 40 nm demonstrated that it was possible by adjusting pH to recycle iron oxide nanoparticles and the performance was maintained after several cycles. In addition, these nanostructures are synthesized by a modified polyol-solvothermal process which allow producing large amount of powders.[7]

Furthermore, it was demonstrated that the doping of iron oxide is also a way to improve the phosphate caption.[4,8,9] The Table 1 shows how the doping of spinel iron oxide nanoparticles may increase the adsorption capacity. However, many missing data on the adsorption capacity of bare spinel iron oxide in the literature compromise the calculation of the increase in adsorption capacity, which would be interesting in the case of our study. In addition, the homogeneous doping of iron oxide nanostructures synthesized by polyol-solvothermal approach remains a challenge. Nevertheless, among doping element, aluminum appears promising and was thus selected to dope RSN to enhance the phosphate removal.

Table 1. Influence of the substituents on magnetite adsorption capacity

Substituents	Adsorption capacity of magnetite ($mg·g^{-1}$)	Adsorption capacity of doped magnetite ($mg·g^{-1}$)	Increase in the adsorption capacity (%)	Ref.
Aluminum	1.21	5.96	492	4
Zinc-aluminum	/	21.8	/	8
Magnesium-aluminum	/	20	/	
Nickel-aluminum	/	17.4	/	
Fe_3O_4@SiO_2-LaO	11.02	27.8	252	10

However, an AOARD program has partially funded these research works and therefore, we have also investigated the doping of RSN by Zn and Co to provide iron oxide nanostructures and doped iron oxide nanostructures to our American and Korean partners in the AOARD project. They had to test them for energy and magneto-dielectric applications. Indeed, these RSN are very suitable for such applications. Magneto-dielectric applications require high *Ms* and low *Hc*[11] when hollow iron oxide nanostructures are interesting structures as electrode battery materials because they can support mechanically the strain induced by the insertion/deinsertion of lithium ions in iron oxide.[11] The doping of iron oxide nanostructures by Co (battery), Zn (magneto-dielectric application) and Al (phosphate removal) was investigated to enhance/improve their properties for targeted applications. I have spent 2 weeks in South Korea to work with our partner on the optimization of the doping of iron oxide nanostructures.

At first, we have worked on the reproducibility of the synthesis of raspberry-shaped iron oxide nanostructures (RSN) of Gerber *et al.*[7] and investigated the doping of RSN by zinc, cobalt and aluminum. We demonstrated the strong impact of starting iron chlorides precursors and of the mixing and reaction times on the nanostructure characteristics (diameter, nanograin size, doping efficiency).

Then, we have investigated the phosphate caption of RSN in water and dialysate and of aluminum doped RSN in water. Finally, we reported on the first experiments performed using a set-up designed by Dr P. Choquet, Dr. A. Zaloszyc and their medicine master student Florence Pillods to simulate the PD process.

The next scheme summarizes the different studies on the RSN and the performed experiments on the RSN and aluminum doped RSN (Al-RSN) for the phosphate removal.
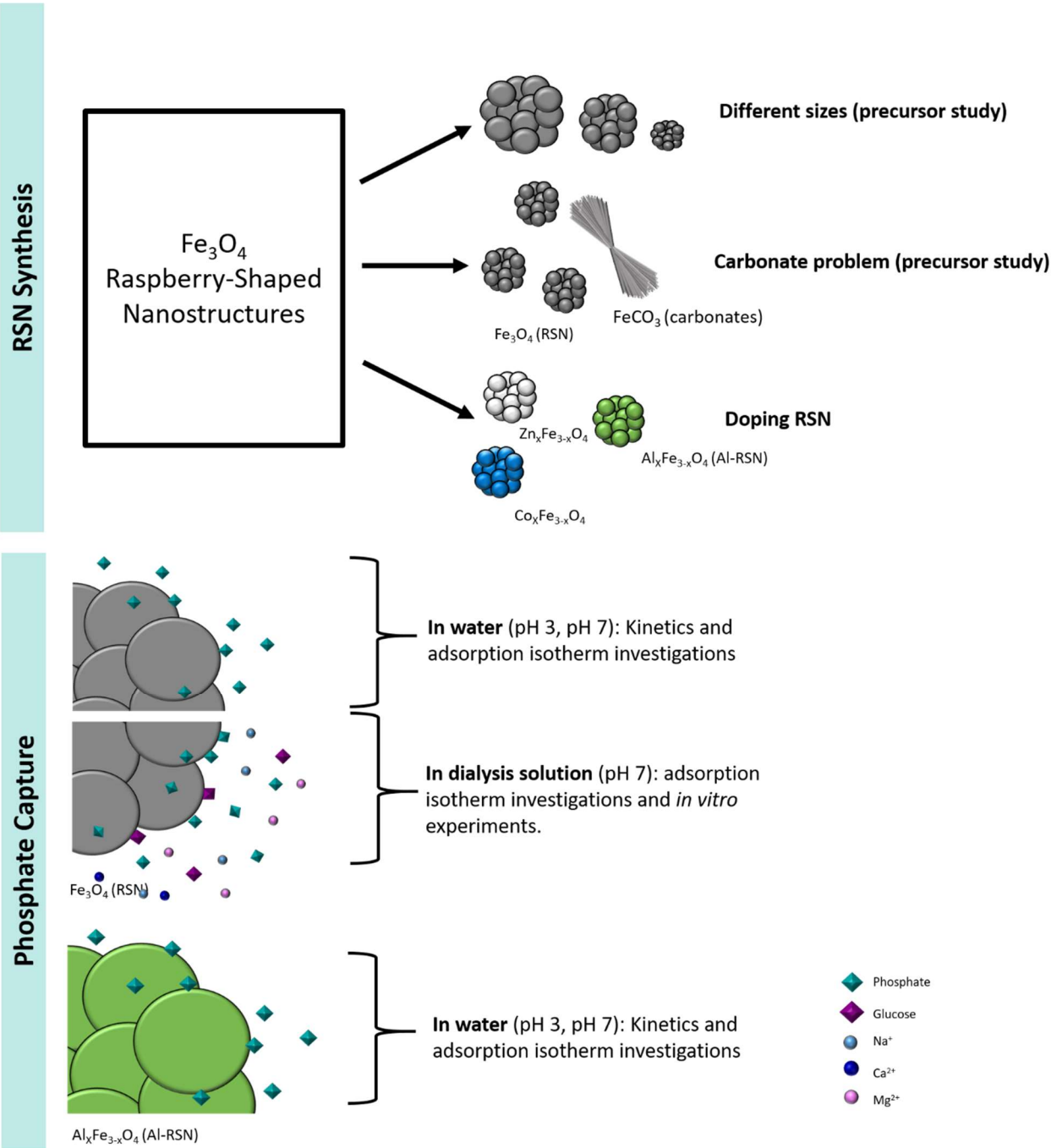
General concept schematizing the different performed investigations on the synthesis of the raspberry-shaped nanostructures and on the evaluation of the RSN and the Al-RSN materials for phosphate removal.

IV. 1. Optimization of the synthesis of iron oxide Nanostructures

IV. 1. 1. Experimental synthesis conditions

Material

Iron (III) chloride hexahydrate (CAS: 10025-77-1), urea 99.3+% (CAS: 57-13-6), ethylene glycol 99% (CAS: 107-21-1), trisodium citrate dihydrate 99% (CAS: 6132-04-3) were supplied by Alfa Aesar. Succinic acid (CAS: 110-15-6), ammonium hydroxide solution 25% (CAS: 1336-21-6) were provided by Sigma Aldrich. CTAB (CAS: 57-09-0) was provided by Roth. Deionized water was used for all experiments.

Magnetite RSN

RSN synthesis. In a typical synthesis $FeCl_3 \cdot 6H_2O$ (1.626 g), succinic acid (0.24 g) and urea (3.6 g) were completely dissolved in ethylene glycol (60 mL) by vigorous mechanical stirring (700 rpm) (during 2 hours or overnight, this parameter is discussed later) and sonication (3 times 20 minutes, changing water of the ultrasound bath). The solution was carefully sealed in a Teflon lined stainless steel autoclave (75 mL capacity) and slowly heated at 200°C at a heating rate of 1.5°C/min. T temperature was kept several hours (between 5 and 10.5 hours) at 200°C. The autoclave was then cooled down to room temperature outside of the oven for 3 hours. The black sediment was separated from supernatant by magnetic decantation. On a first approach, it was washed 3 times with ethanol and 3 times with deionized water to eliminate organic and inorganic impurities. This washing step was improved in this work and will be discussed in this chapter.

Systematically, before each synthesis experiment, the glasses and Teflon containers were cleaned with an acidic solution (HCl, 6 M) for one-hour at least and then washed with deionized water and ethanol.

For the peritoneal dialysis applications, we looked for the synthesis of RSN with the highest specific surface area to remove large amounts of phosphates from aqueous solutions (next part of this chapter). The optimized parameters were the dissolution step by adjusting the stirring time (3 h or overnight) and the reaction time were 6 or 10.5 hours.
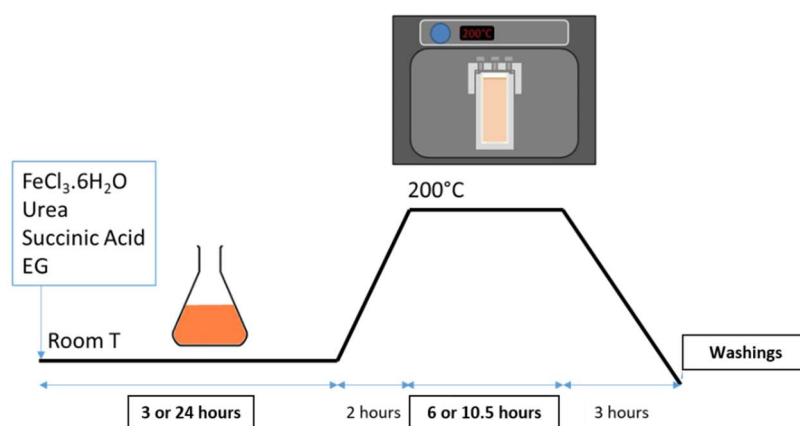
Scheme 1. Synthesis conditions of RSN.

Doped RSN

The same protocol as for the iron oxide RSNs was kept. Zinc chloride ($ZnCl_2 \cdot 6H_2O$) was used as the precursor for zinc, cobalt chloride hexahydrate ($CoCl_2 \cdot 6H_2O$) for cobalt and aluminum chloride hexahydrate ($AlCl_3 \cdot 6H_2O$) for aluminum. The synthesis of doped nanostructures by applying the synthesis protocol of undoped iron oxide RSNs has not been successful. We have therefore investigated this doping step by carrying out the synthesis by substituting cobalt to iron in different 1: X ratio (X= 1, 2, 3, 4, 7, 9 – depending on the synthesis). The total concentration in metal cations was kept at 0.1 mol·L^{-1}.

The first synthesis conditions for each doping element are given below.

Zinc doped RSN. Stirring time for 3 hours and reaction time for 12 hours. A long reaction time is needed to ensure a dispersion of the Zn inside the structure. Indeed, a study of Nguyen *et al.* reported on the formation, at first, of a Zn shell around the RSN with Zn which gradually diffuse when increasing the reaction time.[12]

Cobalt doped RSN. Stirring time for 3 hours or overnight, and reaction time of 10.5, 21 or 30 hours. The two different stirring times evidenced the importance of a good dissolution of $CoCl_2 \cdot 6H_2O$ in the reaction mixture (collaboration with Korean partner in AOARD project).

Aluminum doped RSN. Due to the similarities between Fe^{3+} and Al^{3+} cations (same valence, similar ionic sizes, same hydration), we kept a stirring time of 3 hours and a reaction time of 10.5 hours.
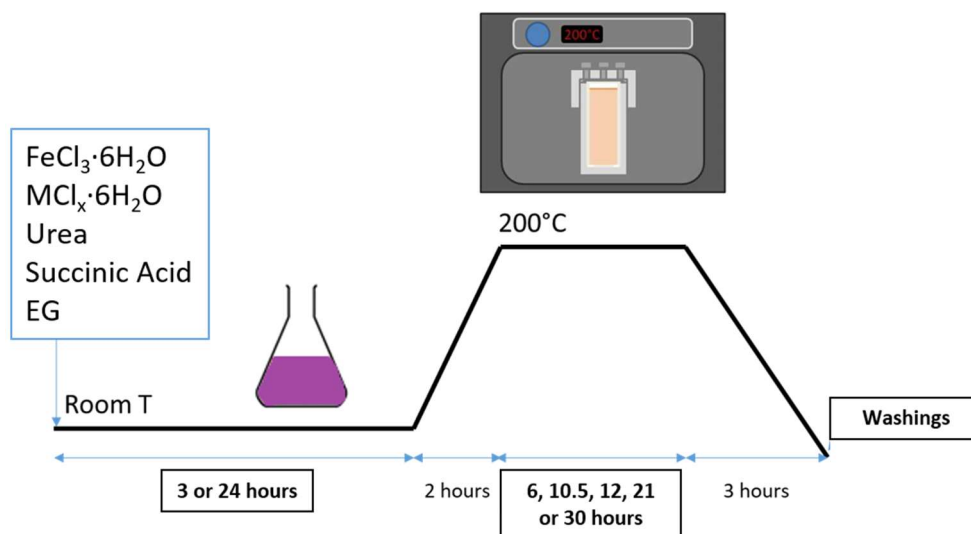
Scheme 2. Synthesis conditions for doped RSN (M=Zn, Co or Al).

IV. 1. 2. Reproducibility of RSN synthesis

We reproduced at first the protocol of Gerber *et al.*[7] by using the same reactants (iron precursor flask: Alfa-Aesar 2) and under the same conditions. Under such experimental conditions, Gerber et al. [7]obtained RSN with a mean diameter of 250 nm and a mean nanograin size of 25 m measured by TEM. The crystallite size determined by XRD profile matching is of 15.5 nm and the saturation magnetization is of 78 emu·g^{-1} (Table 2). We have characterized also these new RSN with SEM-TEM, FITR spectroscopy, X-Ray 1diffraction and magnetic measurements (using a SQUID device).
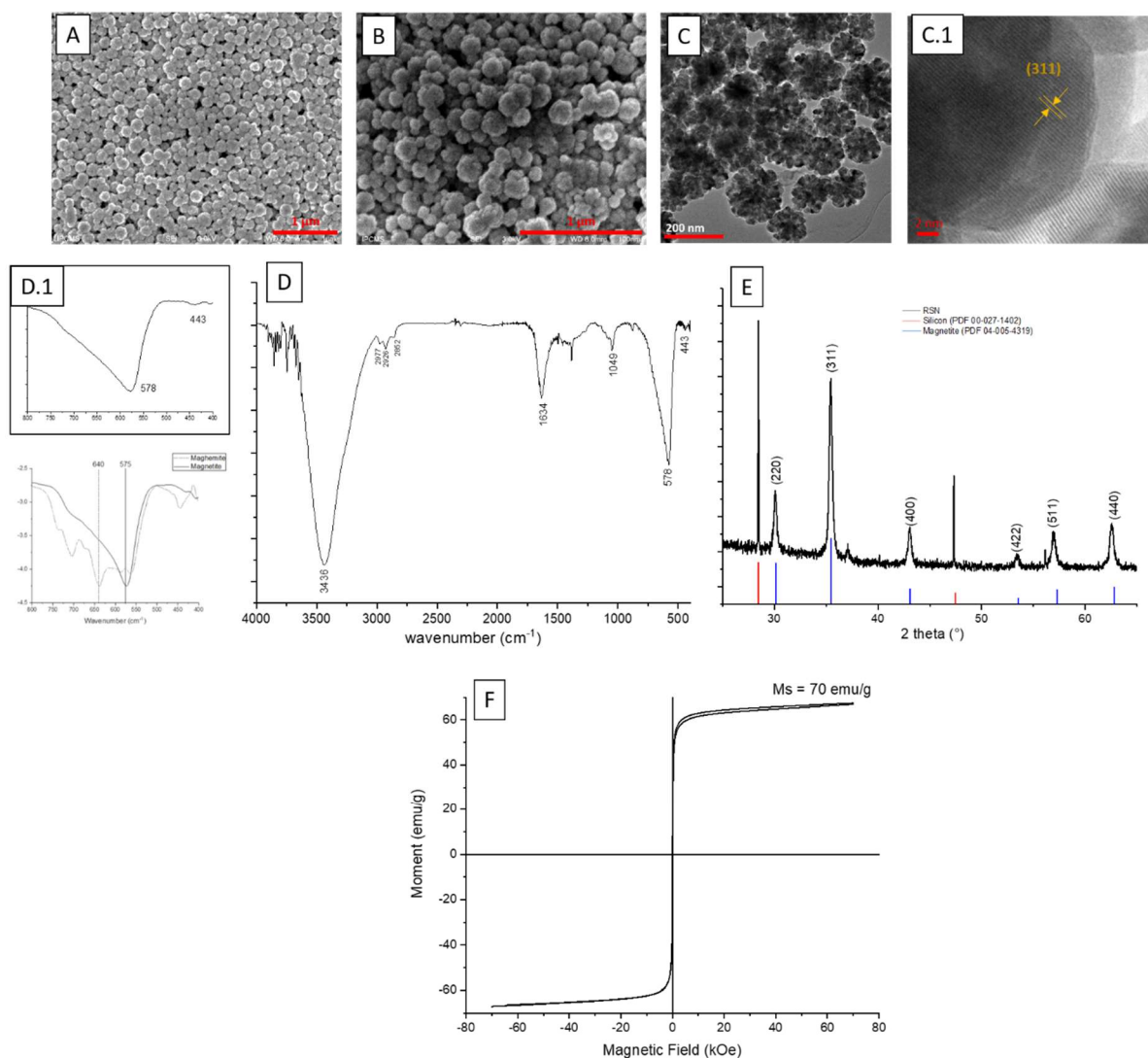
Figure 1. A) and B) SEM images. C) TEM image of RSN. D) FITR spectrum of RSN with D1) Zoom of FTIR spectrum in the range 800-400 cm-1 of RSN and of the magnetite and maghemite phases. E) XRD pattern and F) Magnetization curves of RSN at 300 K.

The SEM images (Figure 1. A and B) are representative of our synthesized RSN. Large nanoclusters with a mean size of 157 ± 42 nm and composed of small nanograins are observed. The **TEM image** (Figure 1. C) confirmed their aggregate morphology. In the high resolution TEM image (Figure 1. C.1), the lattice fringe corresponds to the (311) reflection of the cubic spinel iron oxide. This image shows also the parallel lattice fringes between consecutive grains confirming the oriented aggregation of grains.

Concerning the magnetite and/or maghemite composition of these RSN, **the XRD pattern** (Figure 1. E) displays the characteristic diffraction peaks of an iron oxide spinel structure. No peaks of other phases are visible (hematite, wüstite) suggesting a good purity of the nanoclusters. The crystallite size (determined by profil matching) from the XRD pattern is of 20.2 nm. The lattice parameter determined by profile matching is of 8.399 Å and is slightly higher than that of magnetite (JCPDS file 39-1346). This may be explained by the oriented aggregation of grains which may induce local strains that impact the lattice parameter value.[13]

The **FTIR spectroscopy** allows to discriminate between magnetite and maghemite phases (Figure 1-D1). In fact, in the range 800-400 cm^{-1}, maghemite (the oxidized phase of magnetite) displays broad bands in this wavenumber range. The resolution of these bands depends on the structural order of vacancy sites in maghemite. By contrast, magnetite presents a well-defined band at 570-590 cm^{-1}.[14–17] In the Figure 1 D.1, IR spectrum of RSN presents one well-defined band at 578 cm^{-1} and a shoulder is noticed over higher wavenumbers. This suggests a main composition of magnetite but slightly oxidized. Moreover, the FTIR spectrum exhibits, at 3435 cm^{-1}, a characteristic band of the O-H groups of adsorbed water molecules (water asymmetric stretching). Other bands attributed to water molecules are observed at 1610 cm^{-1} and 1110 cm^{-1} corresponding to the absorbed water antisymmetric stretching and O-H stretching. Small bands around 2911 cm^{-1} are observed and would correspond to CH_2 and CH antisymmetric and symmetric stretchings. Depending on the washing step, a band at 1100 cm^{-1} is also clearly visible, which is related to C=O bond from ethylene glycol (EG). The presence of the band related to EG shows that the washings were insufficient to remove all organic reactants and products. We have performed several washing steps but it was always difficult to remove completely EG.

About the magnetization curve at 300 K (Figure 1.F), we noticed no hysteresis loop confirming the superparamagnetic behavior of the RSN. The measured magnetization saturation (Ms) is of about 70 $emu·g^{-1}$.

Table 2. Comparison of the characteristics of RSN of Gerber *et al.*[13] and our RSN.

		Gerber *et al.*[13] (sample RSN25)	This research
Size of RSN (nm)		245 ± 12	157 ± 42
Size of grains (nm)		25 ± 3	30 ± 6
Crystallite size (nm)		15.5	20.2 ± 0.2
Lattice parameter (Å)		8.39	8.39
Magnetic properties	**Ms ($emu·g^{-1}$)**	78	70

Table 2, the characteristics of our RSNs are compared with those obtained by Gerber et al.[13] Using the same reactants and synthesis conditions, we may notice that the mean diameter of RSN is smaller in our case (245 vs 157 nm) when the mean grain size is higher (25 vs 30 nm). For both materials, the grains size is higher than the crystallite size. Gerber et al.[13] attributed such mismatch between both sizes to the

presence of defects or dislocations resulting from the formation mechanism of the oriented aggregates (coalescence of grains, recrystallization processes).

The lattice parameter is similar and in agreement with the presence of mainly magnetite and its slightly higher value may be explained by the presence of defects. The saturation magnetization ($M_{S, 300K}$) value is also lower (78 vs 70 emu·g^{-1}) and may be explained by the difference in sizes leading to a slightly higher oxidation of magnetite in our RSN: Gerber et al.[13] observed similar results in RSN with larger nanograins (they display lower interfaces which normally contribute to prevent nanograins from oxidation).

To conclude, we used the same reactants and experimental conditions and observed that:

- The diameter of RSN decreased
- The size of nanograins increased
- The magnetization saturation decreased.

However, these new RSN are oriented aggregates of nanograins (HRTEM) and have a main composition of magnetite (XRD+FTIR analysis).
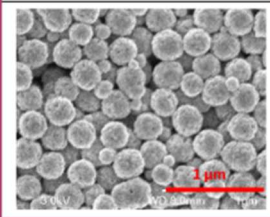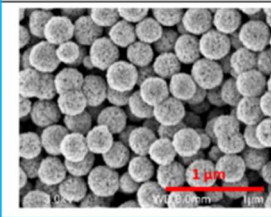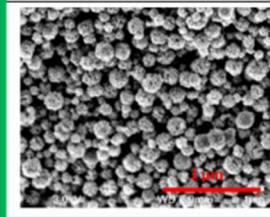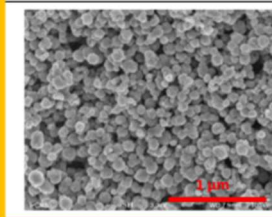
As we have already experienced in the laboratory, the impact of the precursor on the synthesis of nanoparticles, our first explanation on the different mean diameter was the used reactants. Indeed, the iron precursor flask was conserved in the laboratory without particular precautions and we observed an effect of the ageing of the iron precursor. In order to investigate a possible effect of the iron chloride precursor, we have reproduced the RSN synthesis by using different $FeCl_3 \cdot 6H_2O$ precursors provided by different companies or also stocked for different times in the laboratory.

IV. 1. 3. Effect of the commercial nature of hexahydrate iron chloride (III) precursor

IV. 1. 3. 1. Results as a function of the commercial batch

In the following experiments, the sole difference is the brand and batch of hexahydrate iron chloride (III), the other used reactants and the experimental conditions were the same (Table 3). The previous synthesis was performed with the reactant Alfa Aesar-2.

Table 3. Mean crystallite size (deduced from XRD patterns) and mean diameter of RSN as a function of the used iron precursor and representative SEM images of the synthesis.

Brand and lot	Sigma-1	Alfa Aesar-1	Alfa Aesar-2	Acros Organics-1
RSN size (nm)	291±52	296±35	157±42	~100
Grain size (nm)	38±7	26±6	30±6	27±9
Crystallite size (nm)	32.4	19.9	20.2	25.4

The characteristics of RSN obtained using different types of iron precursor are given in Table 3. SEM images show that all experiments gave nanoclusters with an aggregated and spherical morphology but RSNs present different mean sizes of nanocluster, nanograins and crystallites. The RSN display a mean size of 291 ± 52 nm, 29 ± 35 nm, 157 ± 42 nm and 100 nm for the samples from Sigma-1, Alfa Aesar-1, Alfa Aesar-2 and Acros Organics-1, respectively. The nanograin sizes determined from TEM images are 38, 26, 30 and 27 nm respectively and as expected, the crystallite sizes, 32.4, 19.9, 20.2 and 25.4 respectively, are smaller. A connection with the used iron chloride is evident. We have tried to understand why such a discrepancy in the results.

We know that iron chloride is very sensitive to hydrolysis[18] and our first hypothesis was that the iron precursors display different hydration rates. In addition, several groups reported on the effect of water in the polyol synthesis[19,20] and more precisely, in the nanocluster formation. Cao *et al.*[21,22] presented the control of the particle size and size distribution by adjusting the amount of water. In their work, they explained the coordination of water molecules with iron ions is stronger than EG with iron. They observed a modification of the morphology with water: when water is added, the size of grains increases and that of nanoclusters decreases. However, a direct link cannot be confirmed because they also increase the concentration in iron in the initial solution (and several groups already confirmed a link between iron concentration and morphology).[21]

IV. 1. 3. 2. Supplementary Observation: Carbonates Formation

Another problem, that we faced, was the <u>random</u> formation of iron carbonates within the final product. Apparently, these carbonates have not been seen before in such RSN synthesis. Additionally, they are difficult to remove from RSN powder and make that the reaction yield decreases.

The first way (and very often, the only) to detect carbonates is by SEM. Figure 2 shows iron carbonate (siderite) in the SEM images. Because of its composition ($FeCO_3$), the shape of brush is characteristic. [23] In fact, these "forms" are linked to a charge accumulation due to a less conductive behavior (compared to magnetite RSN). In general, iron carbonates were hardly detectable by XRD. Even if in the SEM image we have the impression of a big quantity, the iron carbonates represent less than 5 % of the sample (the necessary percent to be detected by XRD). However, in the only sample with more than 5% of carbonates, we have identified two diffraction peaks (104) and (018) related to iron carbonates (PDF 00-029-0696) (Figure 2).

To explain the formation of this product, we suppose that during the reaction, iron carbonates are formed thanks to CO_2 produced by the decomposition of urea which leads to CO_2 and ammoniac.[7] Once formed, this $FeCO_3$ cannot be decomposed further because of its stability in a large range of temperatures. A similar carbonate formation was reported by Li *et al.*[24] who observed the intermediate formation of cobalt carbonates $CoCO_3$ which decompose to form cobalt ferrite at very high temperatures (> 800 °C).
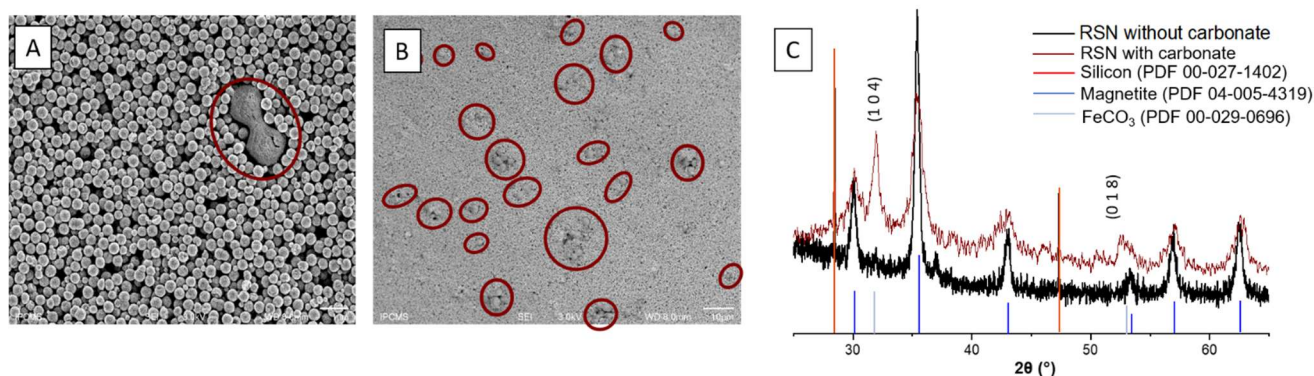
Figure 2. SEM images corresponding to the synthesis of RSN A. without and B. with iron carbonates (brushes). C. XRD pattern of both batches.

One may notice that after the use of a new (unaged) iron chloride precursor, no more carbonates were observed in the synthesis. Therefore, the potential hydration of the reactant could be linked to the carbonates formation.

Finally, all the previous results could be explained by an ageing effect resulting in the gradual hydration of the different iron precursors.

IV. 1. 3. 4. Analysis of FeCl$_3$·6H$_2$O precursors

To understand what happened with the iron chloride, all the previous iron chlorides were characterized to check if the iron chlorides are hydrolyzed or polluted by other substances. XRD, TGA, element analyses and iron quantification experiments were performed.

In a first sight, the color of four iron precursors is different (Figure 3). All of them have different yellow intensity and tonality:

- Sigma 1 has a bright yellow color.
- Alfa Aesar is darker and presents a brown-orange color rather than yellow.
- Alfa Aesar 2 is visually more similar to Sigma's aspect.
- Acros Organics is opaquer.

As well, the morphology of powders is different: Sigma 1 and Alfa Aesar 2 are less compact than Alfa Aesar 1 and Acros Organics.
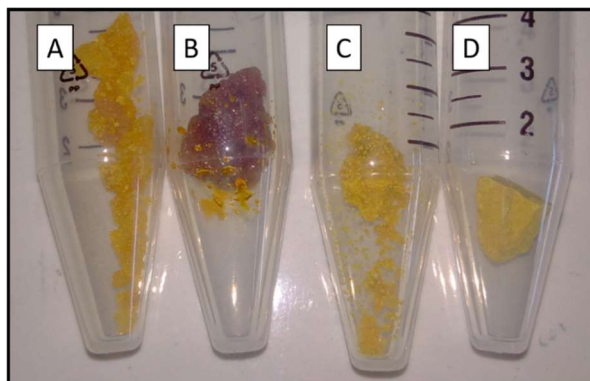
Figure 3. Images of the four flasks containing the different iron precursors: A. Sigma 1, B. Alfa Aesar 1, C. Alfa Aesar 2, and D. Acros Organics 1.

SEM-EDS results

SEM images of the four reactants (Figure 4) show the same morphology: a rough but uniform surface without grains or sheets. Moreover, we do not observe a strong charge of energy in images, which is characteristic of organic and less conductive species.

The results of EDS elementary analysis (Figure 4) show the presence of some element traces. In addition to iron, chloride and oxygen, the reactants also contain:

- Sigma and Alfa Aesar 2: aluminum, magnesium and silicium.
- Alfa Aesar 1: carbone, aluminum and silicium.
- Acros Organics: aluminum and silicium.

These impurities show up a clue. Additionally, we checked the certificates of analysis provided by the different producers. In this case,

- Sigma: traces of arsenic, copper, lead, zinc, phosphates and sulfate.
- Alfa Aesar reactant (1 and 2) do not contain impurities.
- Acros organics: some traces of heavy metals, arsenic and sulfates.

The comparison of our analysis with the furnished data showed a big difference. In truth, the indicated traces are no present, but other traces exist inside the samples. The reasons could be an accidental pollution of the flask by other users (the flasks come from a common use and are shared with other teams), or, less probably, a non-indicated pollution by the producer. However, a link between the synthesized RSN cannot be concluded from these data.

Iron amount determined by relaxometry measurements

This method is used to evaluate the iron amount in a sample in our laboratory. We used it to quantify iron amount in iron perchlorate (III) hydrate reactants (chapter II: iron capture for hemochromatosis). It is also used by other members of the team to quantify the iron concentration in the IONPs suspensions.

To calculate the iron amount, we dissolved a given amount of iron chloride hexahydrate in water and added a determined amount of nitric acid (65 %). Then, the mixture is diluted to reach a final concentration of 2 % in nitric acid. A relaxometry measurement is made in a Brucker Minispec Instrument (60 MHz, 1.41 T) which measures the relaxation time of iron cations. Thanks to a calibration curve which associates the iron concentration to the relaxation time T1, we can determine the iron concentration of the sample. The theoretical iron weight and the experimental one deduced by relaxometry measurements are presented in Table 4.

Table 4. Amount of iron in the different iron precursors determined by relaxometry measurements.

Iron Precursor	Sigma 1	Alfa Aesar 1	Alfa Aesar 2	Acros Organics 1
Iron mass$_{calculated}$ (mg)	1	1	1	1
Iron mass$_{experimental}$ (mg)	0.89	0.93	0.94	0.93
%	-1.5	-6.8	-5.9	-7.1

We can observe that Sigma 1 showed a decrease of 1.5 % of iron quantity, Alfa Aesar 1, 2 and Acros Organics presented 6.8, 5.9 and 7.1 % less, respectively. The batches of iron chloride (III) hexahydrate contain less iron than expected and it suggests a higher water content.

These results would be in agreement with different hydration rate of precursors. <u>So, if the reactant is more hydrated, the diameter of RSN decreases</u>. This observation agrees with the experiment of Cao et al.[21] who observed that when water is added, the size of nanoclusters decreases.

From SEM-EDS results (Figure 4), we determine atomic ratios between some important elements: Fe and Cl (from $FeCl_3$) and Fe and O (from H_2O). In theory, we should observe an atomic Fe/Cl ratio of 0.33 and Fe/O of 0.165. In general, all the samples contain an atomic ratio Fe/Cl slightly higher that the theoretical one (Sigma: 0.35, AA1: 0.36, AA2: 0.38 and Acros 0.44). It may either be due to an increase in Fe or a decrease in Cl. As the Fe amount is lower than expected (Table 3), the increase of this ratio suggests that the amount of chloride decreases (and maybe replaced by another molecule). Comparing with Table 3, the size of RSN seems to decrease with the increase of this ratio.

In addition, the ratio Fe/O is much higher than the expected one: Sigma: 0.33, AA1: 0.30, AA2: 0.38 and Acros: 0.35. It corresponds to an average of 50 % more than expected. It could suggest either a higher amount of iron or a lower amount of molecules providing oxygen such as water or possibly OH. Indeed under hydration, $FeCl_3 \cdot 6H_2O$ should transform into $FeCl_2(H_2O)_4$ and finally to $Fe(H_2O)_6$ (in water). In this evolution, we can note than the ratio Fe/O decreases. Therefore, from all these results, we may conclude that the iron precursors are hydrated. The water for hydration of hexahydrate iron chloride may come from the air if the flaks of the reactant were not carefully stocked.

The difficulty of this investigation is how to evaluate the degree of hydrolysis in the sample (if possible) and also to be sure that we have only hydration and not hydrolysis.

Sample	Fe/Cl	Fe/O
Sigma 1	0.35	0.33
Alfa Aesar 1	0.36	0.30
Alfa Aesar 2	0.38	0.38
Acros Organics 1	0.44	0.37
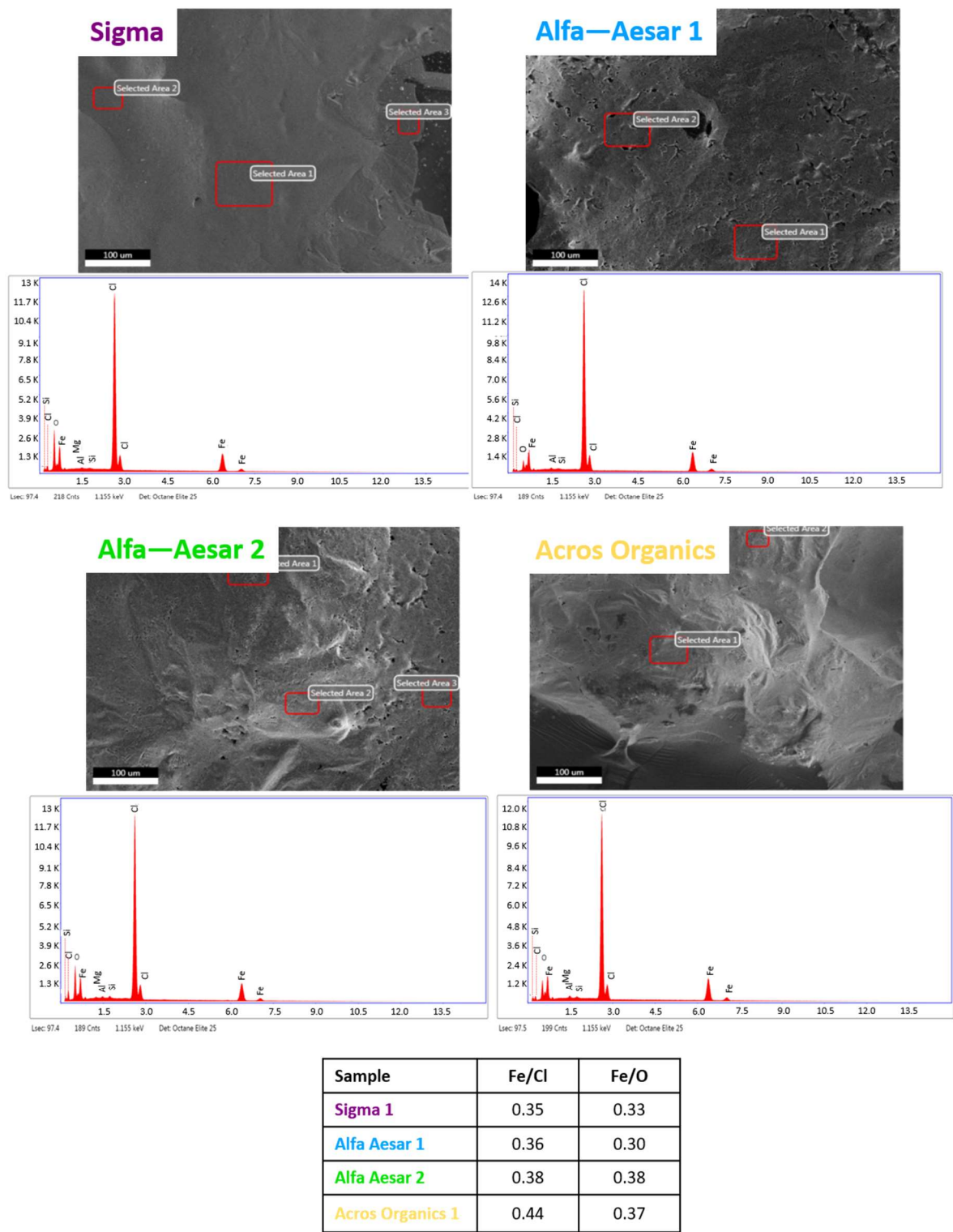
Figure 4. SEM images and EDX graphs corresponding to the iron precursors. Table summarizing the atomic ratio of Fe/Cl and Fe/O.

Hydration of $FeCl_3.6H_2O$

To better understand what happened with our iron chloride III precursors, we studied more in details its hydrolysis. Hexahydrate ferric chloride has a crystallographic structure conformed to a ferric ion surrounded by two Cl^- ions and four water molecules under the form of trans-$[FeCl_2(OH_2)_4]^+$. In the crystal, these ions and water molecules will be positioned by hydrogen bonds and electrostatic forces (Figure 5). The crystals have a space group C2/m with a=11.89±0.02, b=7.05±0.01, c=5.99±0.01 Å. The unit cell has two units type $[FeCl_2(OH_2)_4]Cl \cdot 2H_2O$.[25]
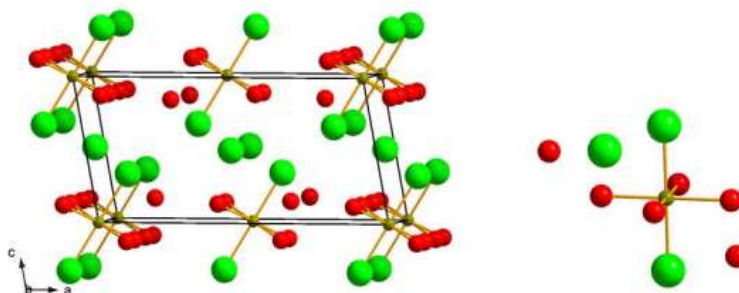
Figure 5. (Left) crystal structure of $FeCl_3 \cdot 6H_2O$ and (right) asymmetric unit. Iron is represented in brown, water in red and chloride in green.[26]

However, the hydration of iron chloride may occur with the time. Gradually, the Cl ligands are replaced by H_2O, so, the possible reactions are:

$$FeCl_3 \cdot 6H_2O \rightarrow [FeCl_2(OH_2)_4]^+ + H_2O \rightarrow [FeCl(OH_2)_5]^{2+} + Cl^- \text{ (partial hydrolysis)}$$

$$[FeCl(OH_2)_5]^{2+} + H_2O \rightarrow [Fe(OH_2)_6]^{3+} + Cl^- \text{ (complete hydrolysis)}$$
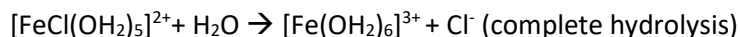
In agreement with Jolivet *et al.* during the hydration, chloride ligands are replaced by aqueous ligand to provide hexa-coordinated cations in an octahedral environment[18]

The reaction in water is : $FeCl_x \cdot nH_2O \rightarrow [Fe(H_2O)]_6 + zCl$

We may also have a hydrolysis[27], the charger transfer in the bond H_2O-M makes the O-H bond becomes weaker and the acidity of the aquo-ligand increases, finally, the deprotonation of this last ligand can be possible and several couples of acidic and basic species are present.

$$[Fe(H_2O)]_6 + H_2O \rightarrow [Fe(OH)_h(H_2O)_{6-h}]^{(z-h)+} + hH^+$$
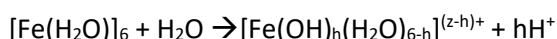
Jolivet[18] proposed a model to determine h, directly linked to the hydrolysis of iron:

$$h = \left[\frac{1}{1 + 0.014\,pH}\right] \times [1.36z - N(0.236 - 0.038pH) - \frac{2.261 - 0.02pH - \chi m}{\sqrt{\chi m}}]$$

Here, χm is the Muliken electronegativity (1.72 for iron), and z is the formal charge (+3), N, the coordination number (6). The difference in hydrolysis is not due to the initial concentration.[27]

To calculate the h of the hydrolysis of iron, the different iron precursors were dissolved in water to obtain a concentration of 0.1 M, then pH was measured.

Table 5. $pH_{measured}$, $h_{calculated}$ and main species for the different iron precursors at 0.1 M (in theory).

Reactant	$pH_{measured}$	$h_{calculated}$	Main species
Sigma1	1.97	2.66	$(Fe(OH)_{2.66}(H_2O)_{3.34})^{0.34}$
AA1	1.90	2.64	$(Fe(OH)_{2.64}(H_2O)_{3.36})^{0.36}$
AA2	1.79	2.62	$(Fe(OH)_{2.62}(H_2O)_{3.38})^{0.38}$
AO1	1.84	2.63	$(Fe(OH)_{2.63}(H_2O)_{3.37})^{0.37}$

This table shows that if the amount of water is high enough, the iron precursors may be hydrolyzed.

We have then performed XRD, FTIR and TGA of the different iron precursors to try to identify the different species inside the reactants: $[FeCl_2(OH_2)_4]^+$, $[FeCl(OH_2)_5]^{2+}$ and $[Fe(OH_2)_6]^{3+}$.

XRD

XRD patterns (Figure 6. A) of the different iron chlorides show only XRD peaks characteristics of $FeCl_3 \cdot 6H_2O$ (PDR 00-033-0645) with similar intensity. No other peaks are visible, it suggests a conservation of the crystallinity of the reactants and the presence of a unique phase. In fact, the partial replacement of Cl by OH during the hydrolysis preserves the structure.

FTIR

FTIR spectra (Figure 6.B) are quite similar: the bands around 3217 cm^{-1} and 1596 cm^{-1} are attributed to the O-H band linked to the crystalline water inside the structure. The band at 3524 cm^{-1} is related to hydroxyl-metal groups.[28] The band at 1415 cm^{-1} could be attributed to the metal-chloride bonds.[29] Between the samples, we can observe a difference in intensity of this last band which could confirm the hydrolysis. Surprisingly, the band at 840 cm_{-1} is often linked with silicon (i.e. Si-O-Si[30] and Si–N[31]), this band matches with the silicon traces detected by the SEM-EDS. The triplet between 470 and 780 cm^{-1} is characteristic of iron oxyhydroxyde (FeOOH).

Thus, the FTIR spectra confirms the contamination of the products with silicon and the partial hydration of the reactants.

TGA

TGA experiments (Figure 6.C) were performed to try to quantify the quantity of water inside the samples. The four curves are similar to other published TGA curves[32]. $FeCl_3 \cdot 6H_2O$ loses its ligands and finally forms an iron oxide product. The first step at 37 °C corresponds to the melting point of iron chloride (III) hexahydrate, the following ones are related to ligand weight loss and formation of other products: $Fe(OH)Cl_2 \cdot H_2O$ around 73 °C, $Fe(OH)_2Cl$ above around 150 °C, FeOOH above around 207 °C and finally Fe_2O_3 above 430 °C. Between room temperature and 110 °C, the weakly bonded water molecules are removed (dehydration). The strongly bonded water molecules are removed in a temperature range between 110 and 207 °C. Finally, between 210 and 600 °C, the anhydrite iron chloride is decomposed and HCl and Cl are removed.[32] Nevertheless, TGD (not presented here) helped to observe that transition temperatures are not exactly the same as a function of the precursor. Acros Organics reactant has lower transition temperatures than Alfa Aesar 2, 1 and Sigma 1. According with the previous analysis, $FeCl_3 \cdot 6H_2O$ theoretically contains 59.9 % of water. Thanks to TGA graphs, the coordinated water was evaluated to be

58.8 %, 58.9 %, 59.31 % and 59.85 % for Sigma 1, AA1, AA2 and Acros Organics 1 samples respectively. Finally, it corresponds to 1.8, 1.6, 1.0 and 0.08 % more of water inside the sample. Differences in transition temperatures could be related to the different rates of hydration. Nonetheless, TGA has to be carefully interpreted. In general, the results depend on the sample preparation, and, as previously said, iron chloride is very hygroscopic and tends to easily form aggregates. That can be difficult to obtain similar samples between the preparation and the analysis. In that case, this analysis method cannot allow to determine the amount of water, but clear differences can be noticed.
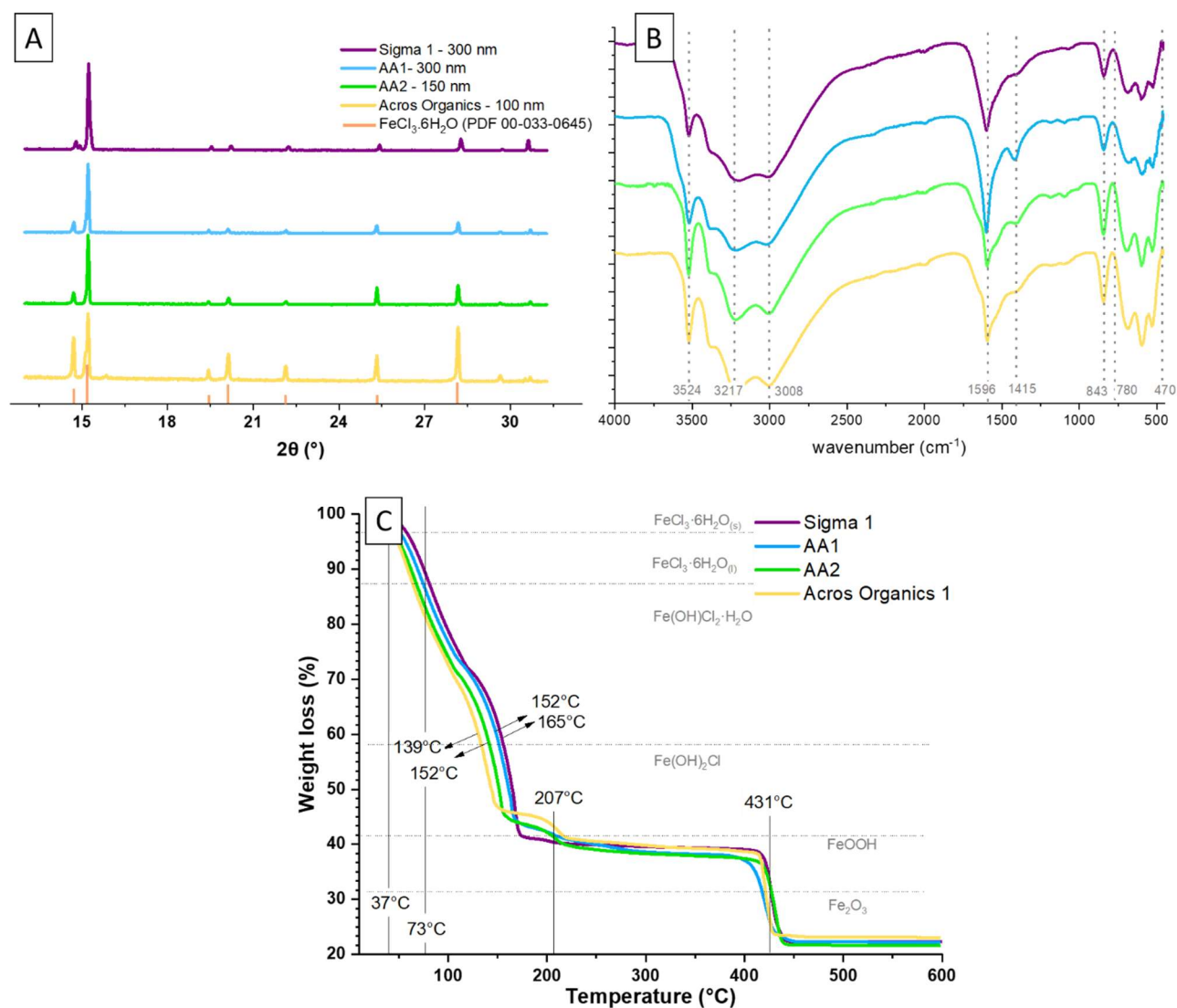
Figure 6. A. XRD patterns under air, B. FTIR spectra and C.TGA curves under air (5°C/min) of the different iron precursors.

IV. 1. 3. 5. Conclusion on the effect of the precursor origin

We have observed that different commercial batches of FeCl$_3$·6H$_2$O led to RSN with different mean diameter and nanograin size. We have characterized them by different techniques and showed that, besides the presence of some impurities, they are all hydrated. They display different hydration rates of hexahydrate iron chloride (III) and in addition, a hydrolysis of precursor is not to exclude. This hydration/hydrolysis is certainly responsible of the different observed results. In an agglomerate of

reactant particle, we can suggest a gradual modification of the composition: from the initial iron chloride (in the center) to a more hydrated form at the surface.

In agreement with reported results on the effect of water on the RSN diameter, we can conclude that the hydration of iron chloride precursor leads to smaller diameter of RSN. The variation of the nanograin size is not easy to explain but should also depend on this hydration rate.

In the formation mechanism of RSN reported in the chapter I[7], there is at first the coprecipitation of iron oxide nanoparticles (due to ammoniac resulting from urea decomposition) and there are then a heterogeneous nucleation and a growth induced by the decomposition of an intermediate iron precursor resulting from the reaction of remaining iron chloride with EG (PLS). We may advance that the different hydration rates of commercial precursors would affect these different steps. The hydration may favor the coprecipitation step leading to a higher amount of RSN resulting from coprecipitation and there is thus not enough PSL (intermediate precursor) to induce a heterogeneous nucleation. The intermediate precursor contributes only to the growth of first formed RSN, which would explain their smaller diameter and also the different observed nanograin sizes. Further experiments would be needed to confirm these hypotheses.
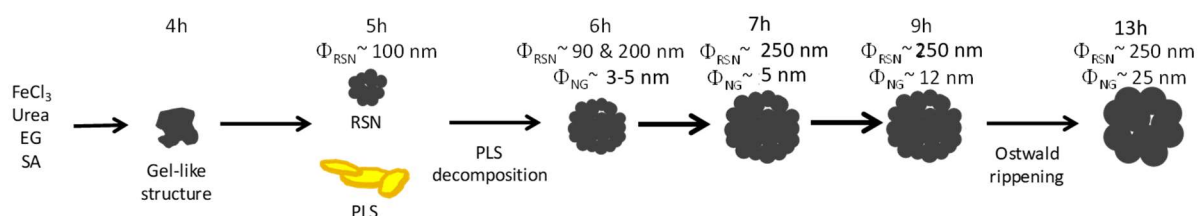
Scheme 3. Reminder: Reaction steps of the synthesis of magnetite RSN.[7]

Besides these observed differences in RSN diameter and nanograin sizes, we have evidenced another drawback of this hydration of the iron precursors, which is the formation of iron carbonates. This hydration would make them less soluble in ethylene glycol. Indeed, we discussed on our different problems (different size and carbonates presence) with our collaborators in South Korea (Pr. Piao and his students from Seoul National University). Under the same conditions, our collaborators never observed the presence of iron carbonates or a modification of the RSN size between different iron precursors. To better understand our problem, the two different teams have compared their synthesis conditions (Table 6).

The brands and lots varies and depends on the country and on the producer, but we cannot control the fabrication, so, this parameter was not considered. However, the conservation of reactants is very different: in South Korea, the group conserves reactants in a temperature and humidity controlled cabinet storage. In agreement with the previous study, it is a first point to focus.

The agitation time was surprisingly different, in the study of Gerber *et al.*, our team determined 3 hours as an optimal time to dissolve completely the reactants. Contrary, the other team decided to assure the total dissolution of the reactants by stirring all the night.

Depending on the availability of the local market, the autoclave and oven are from different providers, so the quality of the materials is different. Nonetheless, their utilization and the final results still being similar, we have not considered this parameter.

Taking into consideration all the previous factors and the analysis, we have concluded that the most important parameter was the stirring time to dissolve the reactants. With the "old" iron chloride flasks, we have observed that a stirring of the reaction mixture for overnight allowed avoiding the formation of carbonates. However, with "new" and "well stored" iron chlorides, the overnight stirring was not necessary and we can keep the initial protocol. That confirms another impact of the hydration rate of iron precursors.

Table 6. Differences between Pr. Piao team and us for the same synthesis.

Factor	Difference
Reactants	Brands and lots
Agitation Time	3 hours vs overnight
Autoclave materials	Steel of different qualities
Oven	Different methods of heating
Reaction time	21 hours vs 10.5 hours
Washing method	Centrifugation vs Magnetic decantation

Therefore, to obtain reproducible results, it is mandatory to conserve the flask in optimal conditions: under vacuum atmosphere to avoid humidity and controlled temperature (maximal suggested temperature: 35 °C). RSN syntheses for peritoneal dialysis optimization were realized with a new $FeCl_3 \cdot 6H_2O$, conserved under the previous conditions and changed all the six months.

IV. 1. 3. 6. Structural and magnetic characterizations of RSN selected for phosphate removal experiments

To overcome problems linked to hydrolysis of iron reactants we decided to take a new flask and synthesized new RSN. A typical RSN synthesis (3 h of mix and 10.5 h of reaction) leads to the expected raspberry-shaped morphology (Figure 7.A). TEM image (Figure 7.B) confirms the formation of aggregates of nanograins. These nanoclusters have a diameter around 296 ± 35 nm with nanograins of ca. 25 nm (measured from TEM images). Moreover, the homogeneous contrast in the nanostructure allows us to confirm that these objects are not hollow. In the HRTEM image (Figure 7. C.1), we can observe resolved lattice fringes. The distance between two adjacent planes in a specific direction were determined to be around 2.5 Å, corresponding to the *hkl* planes of the iron oxide spinel (*311*). Selected area electron diffraction (SAED) pattern (Figure 7. C.2) were taken from the sampling area of Figure 7. C.1. The SAED pattern shows concentric rings which evidences the good crystallinity of our nanoparticles. Moreover, the distances between the rings and the center of the pattern can all be attributed to a *hkl* plan from the spinel structure, which confirms the crystallization of our iron oxide nanoparticles in a spinel phase. Based

on these observations, we can conclude that the RSN are clusters of single crystals with similar crystallographic orientations.

Figure 7. D displays the FT-IR spectrum of the RSN sample. As for the previous reported RSN (discussion about the FTIR of RSN synthesized in the paragraph IV. 4. 2.), we can observe the characteristics bands of the O-H bond (water) at 3435 cm^{-1}, 1610 cm^{-1} and 1110 cm^{-1}. Small bands at 2911 cm^{-1} corresponds to C-H$_2$ and C-H bonds and the peak at 1100 cm^{-1} is related to C=O showing the presence of traces of EG on the surface of RSN. Finally, in the zone 800-400 cm^{-1}, the well-defined band at 580 cm^{-1} confirmed the magnetite composition.

Figure 7. D represents a typical XRD pattern of the final product. Silicon was used as reference to set and correct the Y-shift due to sample preparation. The diffraction peaks are well-defined and can be indexed to the cubic spinel structure of magnetite or maghemite (magnetite JCPDS file 19-629 and maghemite JCPDS file 39-1346). Rietveld refinement allowed to determine the crystallite size (30 nm) and the lattice parameter (a= 8.401 Å). The crystal size did not completely correspond to the ones measured from TEM images and it is related, as explained above, to the mechanism of formation of the oriented aggregates. The lattice parameter value higher than that of bulk magnetite is explained also by the presence of strains and defects in such oriented aggregates (cf. previous part and Gerber et al.[13])

Magnetization curve at 300 K between -70 kOe and 70 kOe, in Figure 7, confirms their superparamagnetic behavior (no hysteresis) and conducts to a saturation magnetization value of ca. 90 emu·g^{-1}, a value close to that of bulk magnetite (92 emu·g^{-1}).[33]
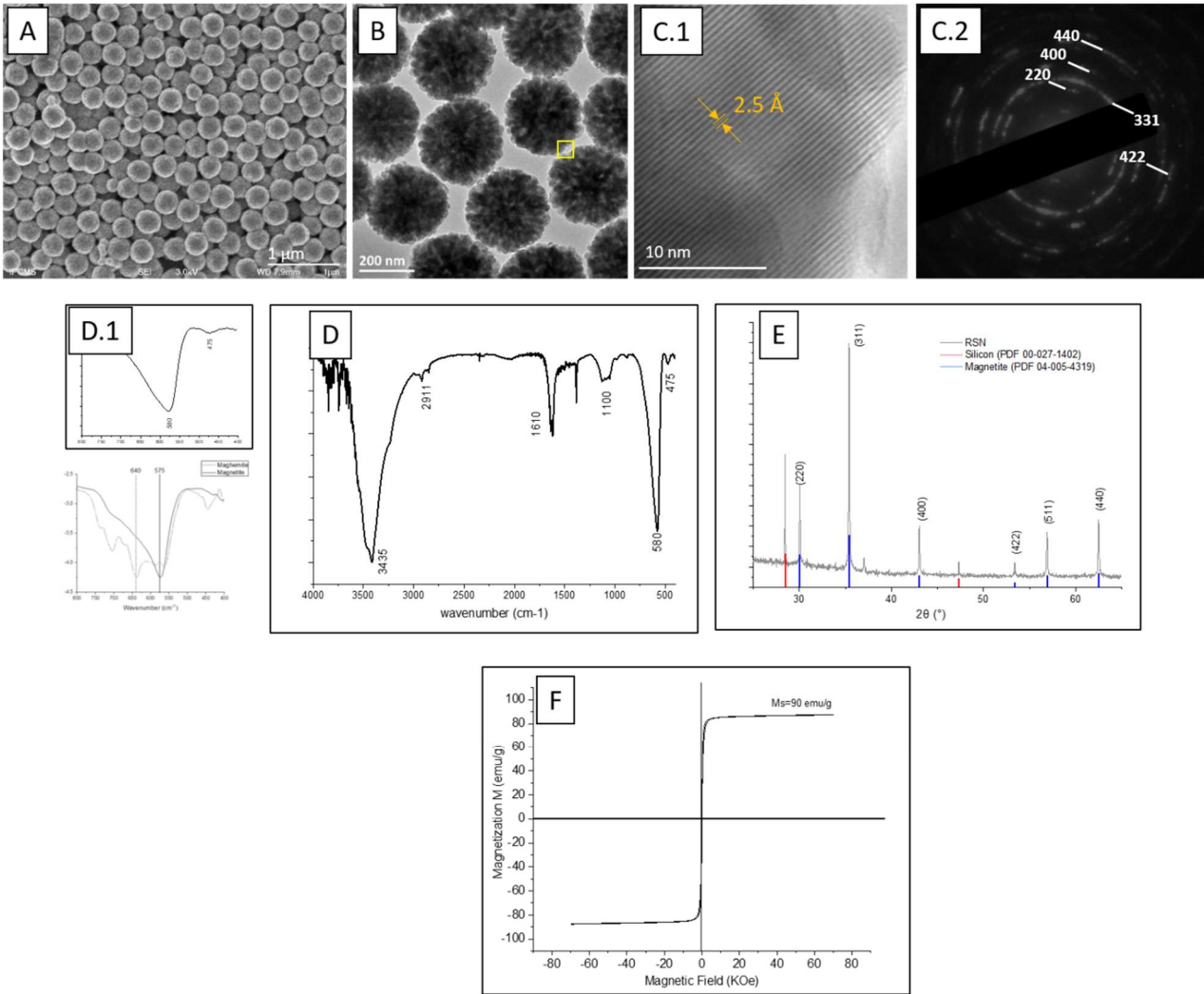
Figure 7. A. SEM, B. TEM and C.1. HRTEM images of RSN; C.2. SAED pattern; D. XRD pattern.

E. FT-IR spectrum. F. Magnetization curve at 300 K.

We compare our results with the results of Gerber et al.[13] in Table 7

Table 7. Comparison of the different RSN syntheses

	Gerber *et al.*[13] (sample RSN25)	This research (AA2 precursor)	New RSN (New precursor)
Size of RSN (nm)	245 ± 12	157 ± 42	296 ± 35
Size of grains (nm)	25 ± 3	30 ± 6	38 ± 10
Crystallite size (nm)	15.5	20.2	30
Lattice parameter (Å)	8.39	8.39	8.40
Magnetic properties Ms (emu·g^{-1})	78	70	90

We may notice that the diameter and nanograin size are again not similar to those of Gerber et al but the mean diameter is high as expected for non-hydrated precursor. The different results are explained by the different origin of precursor. One may notice that the higher nanograin size leads to a composition cole to magnetite as expected and to a higher magnetization.[16,17]

RSN for peritoneal dialysis

As we understood the role of iron precursor and the importance of a good storage, we can start the "production" of RSN optimized for PD experiments. Here, we are looking for RSN with the highest specific surface area (determined by BET measurements). As explained in the first part, NPs with a large specific surface area and a good affinity with phosphates are needed in order to capture as most phosphates as possible.

To increase the specific surface area, grains must be smaller. To modify this parameter, we know that the reaction time is the important parameter to control but we have taken into account also the stirring time (South Korea collaboration). To obtain the highest specific surface area, several experiments were performed using a new $FeCl_3 \cdot 6H_2O$ flask:

- Different stirring times to dissolve reactants (3 hours and overnight).
- Different reaction times (6 and 10.5 hours).

SEM images (Table 8) confirmed the formation of aggregates of nanoparticles. The XRD patterns of the different RSN were refined using the Rietveld method (FullProf crystallographic software) and lattice parameter were thus determined.

For experiments B, C and D, we obtained nanoclusters of around 300 nm, and in synthesis A, RSN are around of 266 nm. In experiments A and B (3 hours of stirring), there is a strong correlation between the reaction time and the size of the RSN and grain size. This result agrees with the observations of Gerber *et al.*, longer reaction time produced the bigger RSN with larger grain size.
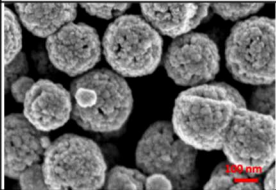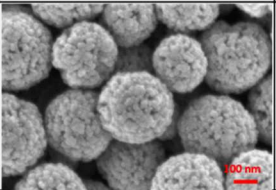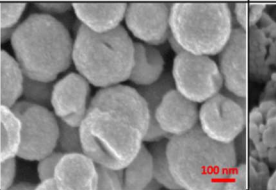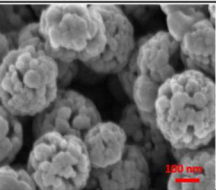
However, by considering experiments C and D with different reaction times and conducted with a similar but higher stirring time (overnight) by comparison with A and B, we notice that RSN have almost the same size, only the grain size has increased. This last result suggests that RSN reached their maximal size after 6h of reaction when 10.5 hours are needed when the reactants dissolution time is of only 3 hours.

The effect of the dissolution time (stirring time) of reactants is also visible by comparing experiments A and C, and B and D. After 6h hours of reaction, the dissolution time of 3h (A) leads to smaller RSN by comparison with that of 24h (C). By contrast, 3h of dissolution and 10.5 h of reaction leads to similar RSN size than 24h of dissolution and 6h of reaction but the grain size is higher. We may conclude that the longer is the dissolution time the faster is then the reaction.

These experiments show that the dissolution of the reactants is a very important step and affects the reaction kinetics and thus the characteristics of RSN.

The values of the lattice parameter confirm a magnetite composition for all samples. Finally, BET measurements showed specific surface area in the range 17 and 30 $m^2 \cdot g^{-1}$. As expected, the RSN with the lower nanograin size display the highest values. We conclude that the conditions leading to RSN with the highest surface specific area are: 3 hours of mixing and 10.5 hours when the temperature plateau is reached (200 °C).

Table 8. RSN synthesis of experiments A, B, C and D with 3 or 24 h of mixing and 6 or 10.5 hours of reaction time at 200 °C reaction temperature.

	A — 3h mix 6h plateau	B — 3h mix 10.5h plateau	C — Overnight mix 6h plateau	D — Overnight mix 10.5h plateau
SEM				
RSN Size	~266 nm	~317 nm	~320 nm	~310 nm
Grain Size	24 ± 5 nm	29 ± 8 nm	36 ± 12 nm	43 ± 10 nm
Lattice Parameter	8.41 Å	8.39 Å	8.40 Å	8.40 Å
Specific Surface Area	$24.2 \ m^2 \cdot g^{-1}$	$27 \ m^2 \cdot g^{-1}$	$18.9 \ m^2 \cdot g^{-1}$	$17.8 \ m^2 \cdot g^{-1}$

IV. 2. Synthesis of doped iron oxide nanostructures

The zinc and cobalt doped ferrite nanostructures were developed in collaboration with different laboratories thanks to different exchanges programs with the University of Brasilia (Brazil), the University of Seoul (South Korea) and the University of Maryland (USA).

For the peritoneal dialysis experiments, we focused on the doping of RSN with aluminum. For that, we have optimized the synthesis conditions by taking care to preserve the raspberry morphology, to be able to remove the particles with a magnet and to obtain a high specific surface area.

IV. 2. 1. Doping of RSN with Zinc (Zn-RSN)

Zinc doping is interesting to modulate the saturation magnetization. In the doped ferrite, zinc mostly occupies the tetrahedral sites. Kavas *et al.* proposed as formula as a function of doping amount: $[(Zn^{2-}_{x}Fe^{3+}_{1-x})_{Td}(Fe^{2+}_{1-x}Fe^{3+}_{1-x})_{Oh}](O^{2-})_4$ (with x, the atomic Zn concentration). The magnetic properties is modified because of the introduction of the Zn ions in the tetrahedral sites (reminder: $M=M_{Oh}-M_{Td}$, the sublattice magnetic moments). Indeed, the Zn^{2+} ions are diamagnetic (without magnetic moment), so, their insertion will decrease the contribution of the tetrahedral magnetic contribution. Naturally, M_S must increase if x increases.[34] Nevertheless, after a given x, the measured magnetization decreases. Indeed, zinc ferrite ($ZnFe_2O_4$) has a spinel structure, the absence of Fe^{3+} in Td sites (occupied by Zn) results in a weak antiferromagnetic material within Fe^{3+} and Fe^{2+} at Oh sites.[35]

The experiments of zinc doping were carried out with Rebecca Fedderwitz and Pr. Peter Kofinas from the University of Maryland. We previously observed that zinc diffusion is longer inside the RSNs, we decided to increase the reaction time from 10.5 to 12 hours.

To dope more the magnetite RSN, we tried different iron/zinc ratios. In all cases, the SEM images (Figure 8 A.1-A.3) confirm the formation of clusters of NPs with a partial conservation of the raspberry morphology. All the ratios produced a quite close nanocluster size (300 ± 103 nm, 280 ± 86 nm and 272 ± 46 nm respectively). However, the 1.2:1 and 2:1 syntheses led to a larger particle size distribution. EDS analysis showed further, for these syntheses, a very low (<1%) amount of zinc.

In order to enhance the zinc doping, the initial ratio Fe-Zn was increased: 9:1. SEM images confirmed the RSN morphology and EDS analysis showed an increase of the zinc amount (3%) even if it is always lower than expected. XRD patterns showed only the characteristic peaks of a spinel phase but no modification of the lattice parameter (respectively: 8.391; 8.391 and 8.388 Å) confirming the low Zn doping. The calculated crystallite size was 32.6 nm for the last sample, this value corresponds to the grain size of the magnetite RSN of the previous paragraph. The low amount of zinc in the doped RSN, confirmed by the XRD results and the reported difficulty to dope magnetite RSN with zinc. Other groups already indicated the difficulty to dope with Zn and the identification of metallic zinc in the final product.[12]

From these experiments and reported results, we conclude that the difficulty is the complete dissolution of the zinc chloride precursor. In future experiments, other zinc precursors will be tested as well as the mixing time.
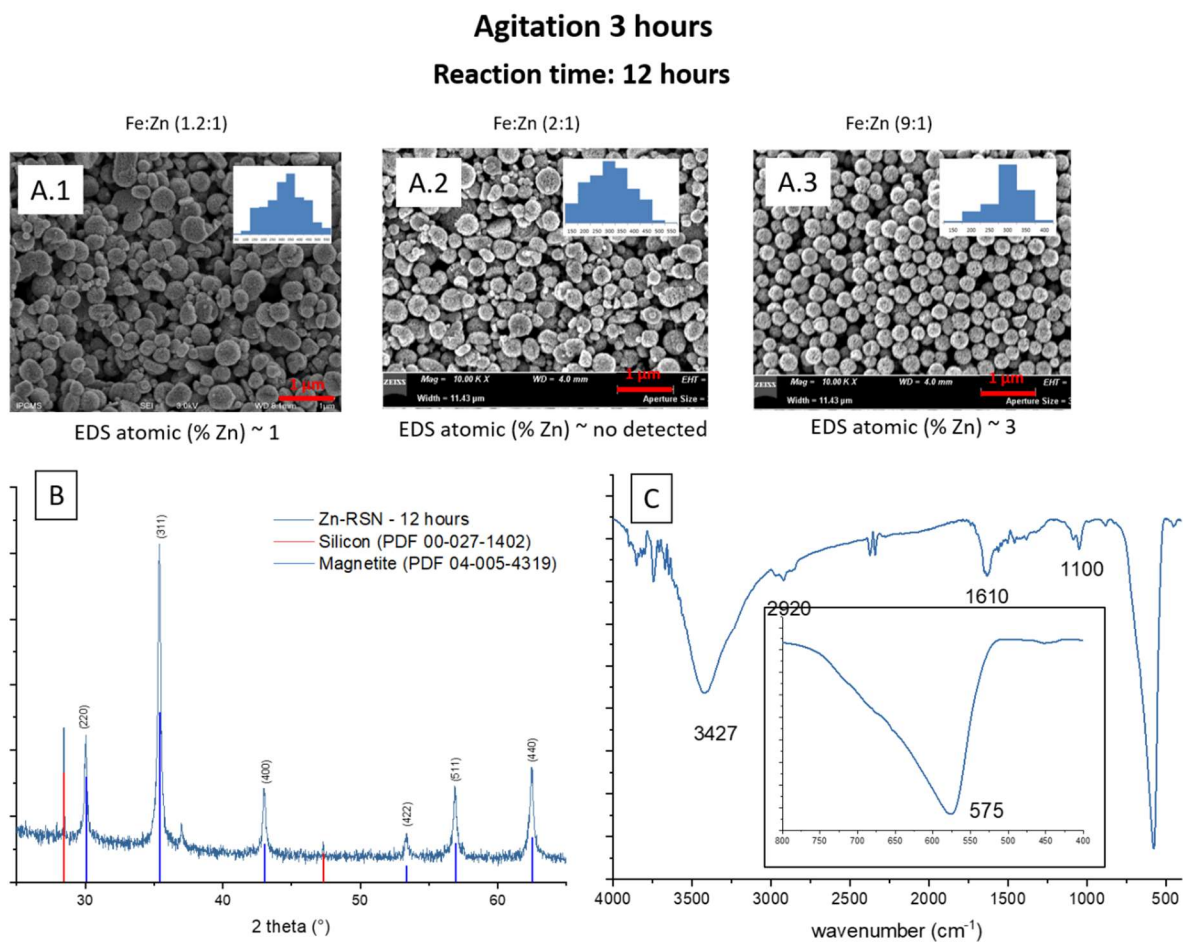
Agitation 3 hours

Reaction time: 12 hours

Figure 8. A.1-A.3. SEM images of all zinc doped RSN, B. XRD pattern and C. IR spectrum of zinc doped RSN (9:1).

IV. 2. 2. Doping of RSN with Cobalt (Co-RSN)

The ferrite $CoFe_2O_4$ drew attention because, in the bulk state, it is a well-known hard magnetic material with a high coercivity (H_C), a high Curie temperature (520 °C), a moderate saturation magnetization (80 emu·g^{-1}) and a high anisotropy constant (2.65×10^6–5.1×10^6 erg·cm^{-3}). These properties model $CoFe_2O_4$ nanoparticles as an interesting material for different applications such as biosensors, for drug delivery, magnetic hyperthermia and magnetic resonance imaging (MRI).[35–39] These characteristics are also suitable for other applications as high-density recording media, ferrofluid technologies… Inside the structure, cobalt will replace the iron II atoms. Previous studies showed that stoichiometric $CoFe_2O_3$ NPs present a higher saturation magnetization thanks to the presence of Co^{2+} ions in the octahedral sites of the spinel structure: $[(Fe^{3+})_{Td}(Co^{2+}Fe^{3+})_{Oh}](O^{2-})_4$.[40] However, at the nanosize, Co^{2+} atoms are observed to replace also some Fe^{3+} atoms in the tetrahedral sites leading to an inverse spinel structure: $(Co_xFe_{1-x})_{Td}[Co_{1-x}Fe_{1+x}]_{Oh}O_4$, where x depends on the synthesis conditions.[41]

Following the previous protocol (3h of mixing), the RSN synthesis has been performed with two different Fe:Co ratio. For a Fe:Co ratio 1:1, RSN with a mean size of 292 ± 76 nm (Figure 9. A1) are observed but the size distribution is quite large. With the Fe:Co ratio 2:1 (Figure 9. A2), the RSN size distribution is narrower and the diameter smaller: 224 ± 26 nm. Some of them are hollow and in the top of the SEM image, metal carbonate particles are identified. As we explained in the above parts, this formation is random and linked to the dissolution step of reactants which was not optimal. Even if the SEM-EDS analysis showed higher Co doping amount than with zinc doping (from 7 to 12 atomic %), the presence of carbonates fakes this value. Furthermore, we cannot remove the carbonates by classical washings. To avoid the carbonate apparition, we modified our synthesis method and increased the stirring time to favor the reactants dissolution in the reaction media.

The second serie of experiments was performed in collaboration with the Seoul National University. For the doping process, we also increased the reaction time: 21 and 30 hours. SEM images (Figure 9. B) showed RSN with close mean diameter :287 ± 25 nm for 10.5 h, 262 ± 25 nm for 21 h and 267 ± 22 nm). However, for the synthesis for 10.5 h, nanograins appear smaller and the surface less rough than the others. EDS analysis showed a decrease of the cobalt amount (7-7.5 %), this value is close to reality because no carbonate was detected. From the three experiments, the reaction time has no effect on the cobalt doping amount.

Figure 9.C displays the XRD pattern of the last sample (stirred overnight and 10.5 hours of reaction time), those of other samples are very similar and not presented. The crystallite sizes were determined by profile matching: 17, 27.8 and 36 nm for Co-RSN with reaction time of 10.5 hours, 21 hours and 30 hours respectively. The peaks are related to a spinel structure (maghemite, magnetite) without presence of another phase (same observation for the sample containing carbonates). The lattice parameter was calculated to be 8.41 A, a slightly higher value than for the synthesized RSN, this increase can be related to the insertion of cobalt in the structure.

The IR spectra confirmed the presence of the magnetite phase and the presence of traces of EG.

SQUID measurement at 300 K of the sample B.1 led to a saturation magnetization of 83.5 emu·g^{-1} for $Co_xFe_{3-x}O_4$ vs 83.8 emu·g^{-1} for similar magnetite RSN. As for other cobalt doped IONPs, a hysteresis curve

was observed confirming the cobalt doping with a coercivity value of 400 Oe. The magnetic values are consistent with the theory and the published values of other groups.
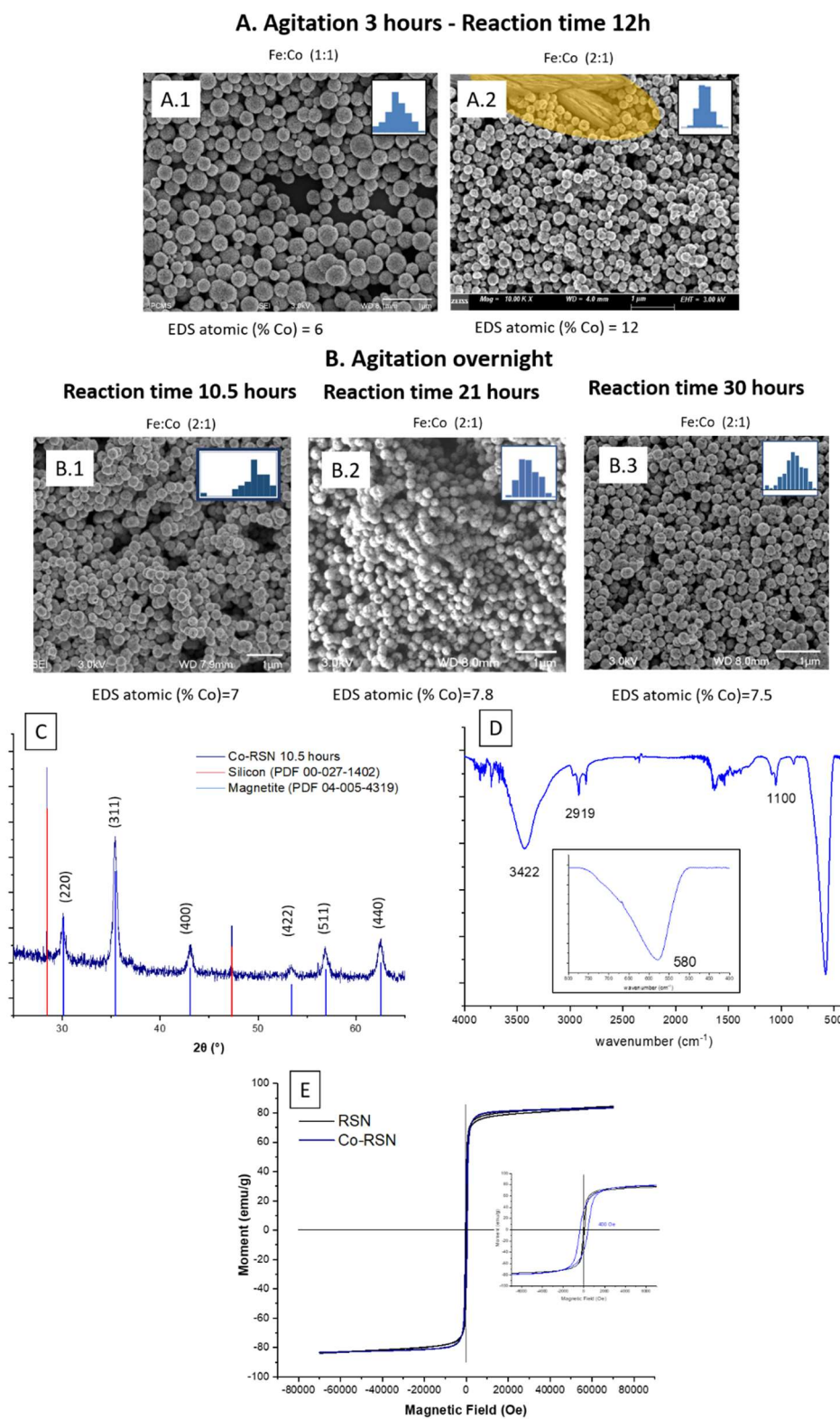
Figure 9. SEM images of cobalt doped RSN A. experiments with 3 hours stirring. B. experiments with overnight stirring. C. XRD pattern, D. FTIR spectra and E. Magnetization curve of the undoped and cobalt doped RSN at 300K.

IV. 2. 3. Doping of RSN with Aluminium (Al-RSN)

Aluminium has been shown to be a suitable doping element to enhance the phosphate removal. However, aluminum is a no-magnetic element and so, to keep the possibility of "magnetic decantation", the magnetite RSN will be doped with a small percent of aluminum. The doping of magnetite nanostructures with aluminum should be easier than with Zn and Co because their ionic radius are quite close and their valence is the same (+3).

For the doping process, we used a reaction time of 10.5 hours and a stirring time of three hours. Three Fe:Al ratio were tested. SEM images (Figure 10) present nanostructures with the morphology of no doped RSN but a broad size distribution is noticed with a mean diameter of 269 ± 45 nm for the last sample.

EDS analyses show the success of the aluminum doping with quite high doping amounts increasing with the amount of introduced Al.

However, during the washing step, samples with an initial iron ratio from 2 to 7 were hardly magnetically decanted. To facilitate this step, samples were centrifuged. With this simple observation, we can confirm that the aluminum doping modifies the magnetic properties (in particular, the saturation magnetization). The only sample which could be magnetically decanted was the last one (Fe:Al 10:1). We have therefore mainly characterized this sample called Al-RSN. This sample will be used for phosphate removal experiments.

XRD patterns (Figure 10. B) confirm the preservation of the iron oxide spinel structure without the presence of some other phases. We notice that the peaks are broader for RSN with high Al content suggesting a loss of crystallinity or smaller crystallites. The lattice parameter ($a_{of\ the\ synthesis}$= 8.389 Å) is lower than that observed usually with undoped RSN but would confirm the aluminum insertion in the spinel structure. The crystallite size is calculated to be 19.5 nm (Figure 10 A.5). suggesting that the Al doping leads to smaller crystallite size. The highest surface specific area measured for this sample (40 m²/g) confirmed the smallest nanograin size of Al-RSN by comparison with undoped RSN.

The magnetization curve at 300 K is characteristic of a superparamagnetic behavior and the saturation magnetization (Figure 10. D 64 emu·g^{-1} for $Al_xFe_{3-x}O_4$) is lower than that of undoped RSN confirming the doping magnetite by Al and previously reported results of other groups.[42–44]

Agitation 3 hours - Reaction time 10.5 hours

Fe:Al (2:1)

Fe:Al (3:1)

Fe:Al (4:1)

EDS atomic (% Al) = 45

EDS atomic (% Al) = 30

EDS atomic (% Al) = 13

Fe:Al (7:1)

Fe:Al (10:1)

EDS atomic (% Al)=16

EDS atomic (% Al)= 10
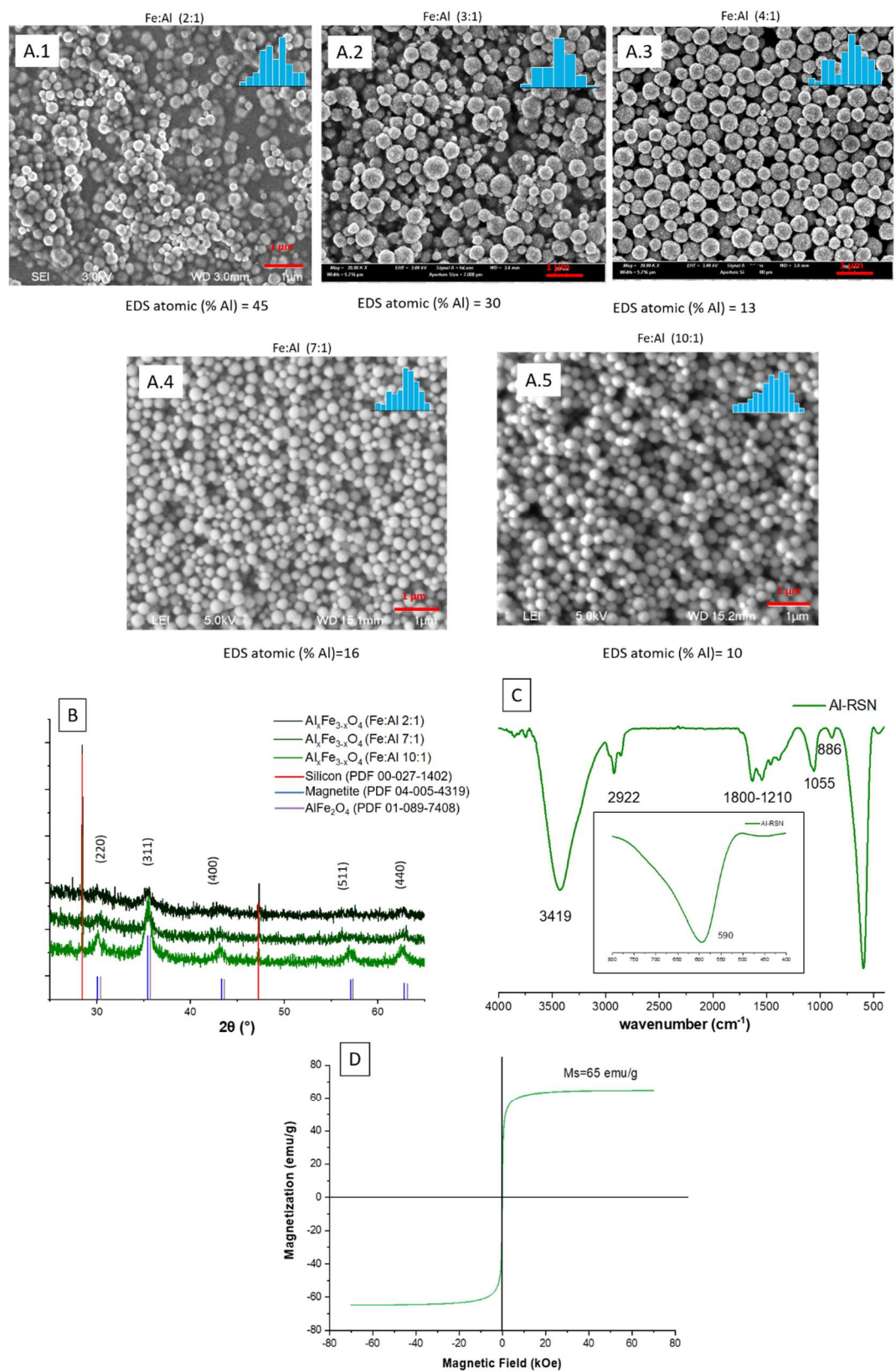
Figure 10. A.1-A.5. SEM images of Al-RSN ; B. XRD pattern, C. FTIR spectra and D. Magnetization curve of Al-RSN at 300K.

133

From these results, Al-RSN seems to be a promising material to adsorb phosphates and being applied in peritoneal dialysis treatment. This material can be attracted with a magnet and possesses a bigger specific surface area than RSN (40 vs 27 m²/g).

IV. 2. 3. Conclusion RSN

At first, we have tested the reproducibility of the synthesis of RSN by a polyol solvothermal method and evidenced the effects of different experimental parameters such as the commercial origin of the iron chloride precursor, the ageing of the precursor, the dissolution step of the reactants.

Indeed, experiments with four different iron precursors have conducted to RSN with different diameters and nanograin sizes. Using different characterization techniques, we have shown that, besides the presence of some impurities, the hexahydrate iron chlorides were hydrolyzed. The additional percent of water modifies the nature of the reactant (hydrolysis of iron chlorides) and the predicted quantity of water and iron inside the reaction. The evolution of the RSN diameter is an agreement with the reported effect of the addition of water to the reaction media: the diameter decreases when the water content increases. Its effect on the nanograin size is not so evident but our hypothesis is that it perturbates the RSN synthesis mechanism by favoring the growth step instead of a heterogeneous nucleation leading normally to bigger RSN.

Another drawback of this hydration of the iron precursor is that it favors the formation of iron carbonates in the reaction media, which are difficult to remove from the RSN.

From these different experiments, we conclude also that this hydration makes harder the dissolution of the iron precursors. Indeed, longer dissolution times (longer stirring time) and the use of "fresh" iron precursor allow obtaining RSN in a reproducible manner.

We established thus that it is mandatory to conserve the precursor flask in optimal conditions: under vacuum atmosphere to avoid humidity and controlled temperature (maximal temperature suggested: 35 °C). Performed experiments for peritoneal dialysis optimization were realized with a new $FeCl_3 \cdot 6H_2O$, conserved under the previous conditions and changed all the six months.

By taking into account these parameters, we have tuned some parameters to obtain RSN with a high surface specific area. The most adapted conditions were 3 hours of mix and 10.5 hour of reaction at 200 °C).

In a second part, we have investigated the doping of RSN by Zn, Co and Al elements. The doping of such nanostructures has not been reported much and whatever the synthesis methods, the homogenous doping of ferrite nanoparticles remains a challenge. We have used the same synthesis conditions and tune the reaction time, the dissolution time and the amount of doping elements.

- We have so concluded that that we cannot dope RSN with zinc under our synthesis conditions. The dissolution step appears crucial and other zinc precursors will be tested to improve this step.
- The RSN have been doped with small amount of cobalt (7-8 at %) by to tuning the dissolution time and reaction time. An effect of the doping on magnetic properties was evidenced. Test with different cobalt amounts have to be performed in future experiments.
- Due to the similitudes between aluminum and iron (valence, ionic size) ions, the dissolution time and the reaction time were the same than for standard RSN and high doping rates were obtained.

We observed that Al doping induces a decrease of the nanograin size leading thus to higher surface specific area. A drawback is that the doping by Al affects the saturation magnetization of RSN.

IV. 3. Phosphate removal using iron oxide nanostructures

IV. 3. 1. Experimental conditions

IV. 3. 1. 1. Preparation of phosphates solutions

Washings of RSN. After their synthesis, the RSN separated from the supernatant by magnetic decantation are dispersed in a mixture of 50-50 ethanol and warm acetone (60°C). The suspension is ultrasonicated for 5 minutes, then magnetically decanted to remove the supernatant. Different washing treatments have been tested but traces of reactant (especially EG) always remain at the RSN surface. To remove the must of EG traces, we washed the RSN 9-10 times.

Phosphate aqueous solutions. Orthophosphoric acid was used as phosphate source. A first solution at 309.9 P-mg/l was freshly prepared introducing 68.4 µl of orthophosphoric acid (85 %) in 100 ml of milli-q water. The solution was adjusted using a 2M NaOH aqueous solution to precisely set pH 7. Other phosphate solutions were prepared by dilution from this solution.

Phosphate based dialysate solutions. Some experiments were performed in the dialysis solution of second-generation double chamber "sleep safe" from Fresenius Medical Care. The difference with a dialysis solution of first generation is the storage of the solution. In the second generation, glucose is kept at very low pH, separate from bicarbonate buffer and electrolytes to avoid toxic glucose degradation products. (Glucose 126 mM, Ca^{2+} 1.75 mM, Na^+ 134 mM, Mg^{2+} 0.5 mM, Cl^- 101.5 mM).[45]

This dialysis solution is currently used in the Hautepierre hospital, pediatric department in Strasbourg.

To simulate the capture of phosphate in the dialysis solution, to the previous solution were added different volumes of a solution of phosphates ([P]=359 P-mg/L) at pH 7.

IV. 3. 1. 2. Adsorption experiments

The dispersion of RSN is added to a solution containing phosphate at a known concentration. After a magnetic stirring for different times for the kinetics study and for 24 h for the adsorption study, the RSN are separated by magnetic decantation and washed with water. Finally, the phosphate remaining in supernatants are analyzed by UV-Vis spectrophotometry using the "blue of molybdene" method described below.
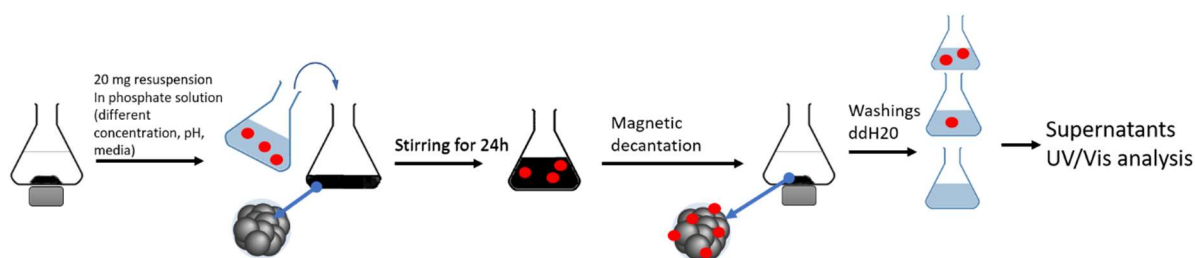
Figure 11. Process of phosphates capture.

The blue of molybdene method. This method was already performed by Daou et al.[46], in order to quantify the amount of phosphates in supernatants. This method is effective and allows quantifying very low concentrations of phosphates in water. This method is also used in different medical devices to dose phosphate in blood/urine but following the producer, the reactants could change, but the principle is the same. It consists in generating a phosphate complex, which can be quantified using UV spectroscopy.

$$7 \; H_2PO_4^- + 12 \; (NH_4)6Mo_7O_{24} + 72 \; H^+ \rightarrow 7 \; (NH_4)H_2PO_4(MoO_3)_{12} + 65 \; NH_4^+ + 36 \; H_2O$$

$$(NH_4)H_2PO_4(MoO_3)_{12} + 6 \; Sn_2^+ \rightarrow \text{'Blue of Molybdenum'} + 6 \; Sn_4^+$$
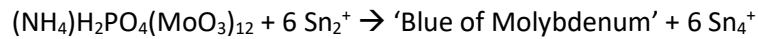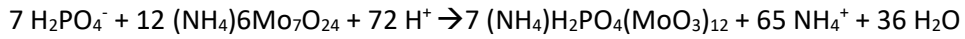
Preparation: The first reagent: 2.5 g of ammonium molybdate $((NH_4)_6Mo_7O_{24})$ were dispersed into 17.5 mL of pure water, in parallel, 28 mL of sulfonic acid $(H_2SO_4$, Carlo Erba) were dispersed in 40 mL of ddH_2O. Both solutions were mixed and diluted up to 100mL with ddH_2O.

The second reagent: 0.5 g of tin chloride dihydrate $(SnCl_2 \cdot 2H_2O)$ were dispersed in 50 mL of 85% glycerol. Both reagents were kept in glass containers and wrapped with aluminum paper to avoid premature degradation from light exposure.

500 µL of the molybdenum reagent and 500 µL of the tin reagent are mixed with the appropriate amount of the phosphates solution and filled up to 10 mL with ddH_2O. The wavelength range of measurement was 450-800 nm.
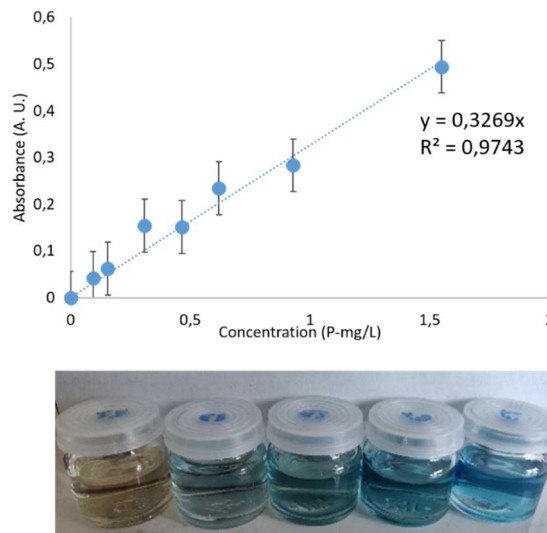
Figure 12. Calibration curve of the "bleu of molybdene" in the range 0-1.5 P-mg/L. Photo of the solutions at different concentrations.

Nota Bene: We have observed that we must carry on the experiments under specific conditions: i) the temperature must be between 20 and 25 °C to ensure the complex formation; ii) to ensure that no traces of phosphates remain on the glasses, all required glasses are cleaned before each measurement with NaOH 2M.[46] ; iii) the blue of molybdenum complex is not stable with time. Therefore, the absorbance of the blue solution must be measured after 10 minutes of stirring. Indeed, at the end of the stirring step, the complex is stable only 15 minutes.

The reference (without phosphate) undergoes also a form of degradation. Therefore, the reference has to be made again for each measurement. Finally, The 10 min timing is a first systematic error but the complexation reaction itself does not always occur at the same reaction rate leading to different values for a set concentration.

Kinetics of phosphate adsorption as a function of time. During a classical peritoneal dialysis, around 40 % of the initial concentration of phosphate serum are eliminated in 4 hours.[2] In order to faster eliminate phosphate, RSN could be used as agents, which can increase the capture and even reduce the dialysis time. To prove that RSN are adapted to dialysis session times and can help to reduce it, we characterized

the adsorption kinetics at a given phosphate concentration. For these experiments, a known amount of RSN was dispersed in a solution of phosphates with a given phosphate concentration and the amount of remaining phosphate in supernatant is analyzed at different times.

Experimentally, 20 mg of RSN are dispersed in 20 ml of a phosphate solution (50 P-mg·l^{-1} at pH 7- corresponding to the concentration of hyperphosphatemia). As we will see below, it corresponds to the concentration at which the maximum phosphate capture is reached. The mixture is stirred on a rotative-wheel for 30 minutes up to 24 hours.

Isotherm of adsorption experiments. 20 mg of RSN are dispersed in 20 ml of a phosphate solution at different concentrations. The experiments are performed in water at pH 3 and 7 and in dialysate at pH 7. The range of investigated phosphate concentrations is: 3.1-154.9 P-mg·l^{-1}. The mixtures are stirred on a rotative-wheel for 24 hours.

In a first approach, we have considered the S, L, H, C isotherm models to understand the interactions between phosphates and iron oxide. Then, different kinetics models were used to characterize more precisely the phosphate adsorption kinetics: Langmuir, Freundlich and Redlich-Peterson models. These models are described in the bibliographic chapter (chapter I).

IV. 3. 2. Results

To ensure a high adsorption of phosphate at the surface of iron oxide nanostructures, it is important to favor electrostatic interactions as detailed in bibliographic chapter. The IEP of RSN is about 5.6 as depicted in Figure 13 and is slightly shifted by comparison with the reported IEP of iron oxide usually in the range 6-7.[47] This is certainly due to the washing process, which does not completely remove all reactants (like ethylene glycol) from RNS surface. For phosphates, an increase of pH leads to a change of the main species in solution from H_3PO_4 to PO_4^{3-} (Figure 13).
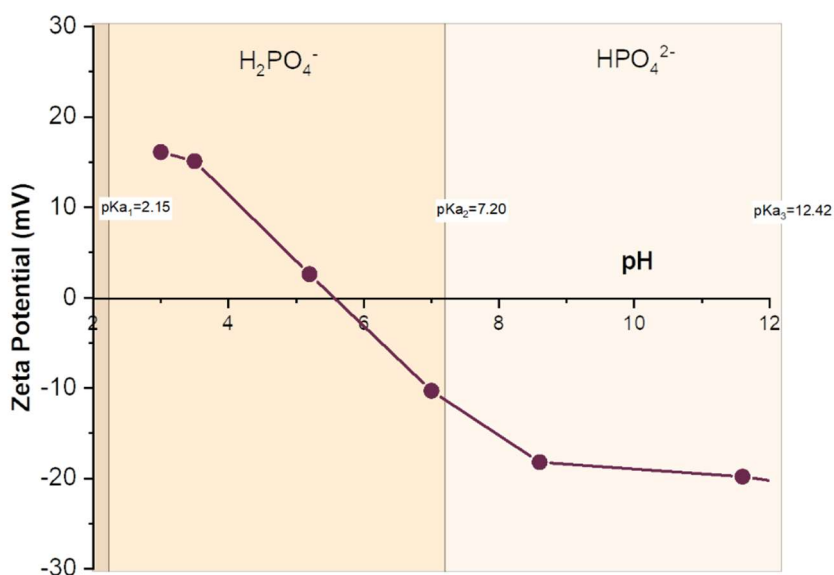
Figure 13. Zeta potential curve of RSN vs pH and phosphate species as a function of pH.

As we can see, the suitable electrostatic interactions between deprotonated phosphates and iron oxide surface are for pH<5.5. Thus, optimal adsorption conditions would be around 3 as the phosphates are deprotonated (negatively charged) and the iron oxide surface is positively charged. However, in the dialysate, the pH is around 7. At this pH, the solution contains phosphates under the forms $H_2PO_4^-$ and HPO_4^{2-}, when the surface of RSN is slightly positively charged. At such pH, the adsorption maximum is expected to be lower than at pH=3.

IV. 3. 2. 1. Phosphate removal from RSN solutions as a function of time

In a first experiment, RSN are put in contact with phosphate solutions for different times. RSN, which were used for these experiments, have a mean diameter of 319 nm and a mean nanograin size of 29 nm (surface specific area= 27 m^2/g). We notice Figure 14 that the maximum adsorption is reached after one hour. Then, the curve tends to a saturation plateau. Thus, the phosphate capture is quite fast within at maximum 2 hours.

In studies performed with other iron oxide based nanomaterials (Table 10), the maximum amount, for most of them, is reached after 5 or 15 hours. The only nanomaterial, which shows a quite similar time, is the iron hydroxide-eggshell of Mezenner et al.[48] These authors observed a maximum adsorption after 3 hours. From these results, we may advance that our iron oxide RSN adsorb the fastest the phosphates and may be adapted to reduce the duration of peritoneal dialysis treatment.

Table 9 Kinetic parameters for pseudo-first-order and pseudo-second-order models.

Our Study					
Pseudo-first-order			Pseudo-second-order		
q_e (P-mg· g^{-1})	K_1 (h^{-1})	R^2	q_e (P-mg· g^{-1})	K_2 (g·P-mg^{-1}· h^{-1})	R^2
4.0 ± 0.1	5.17 ± 0.84	0.95129	4.1 ± 0.1	5.28 ± 2.18	0.99571
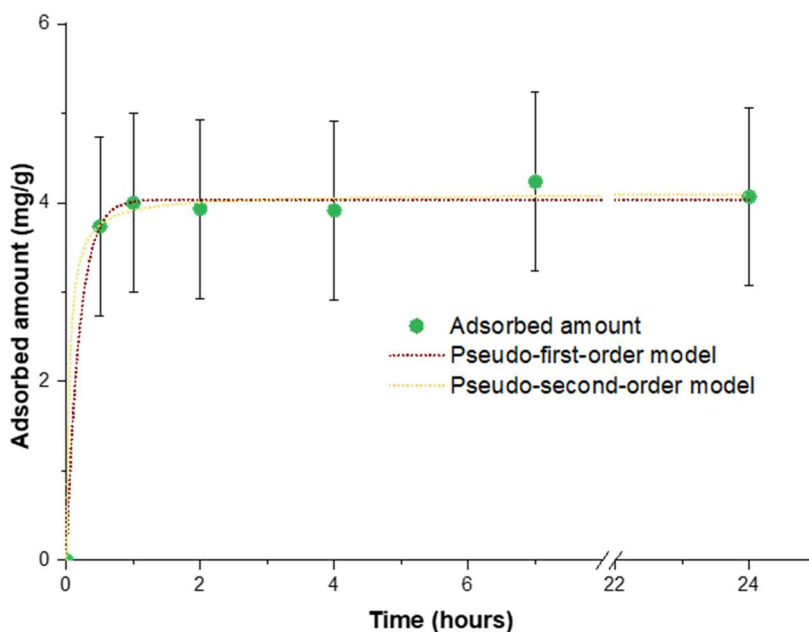
Figure 14. Adsorbed amount of phosphate by RSN in a phosphate solution (50 P-mg·L^{-1}) at pH 7 for different durations

The curves have been fitted with two kinetics equations (Chapter I). In Figure 14, we can observe that both models seem to fit quite well the experimental data. For the pseudo-first-order model, the values of the kinetic parameters are 4.0 P-mg·g^{-1} for q_e, 5.17 h^{-1} for K_1 and 0.95129 for R^2. In the same way, for the pseudo-second-order model the values are 4.1 P-mg·g^{-1} for q_e, 5.28 g·P-mg^{-1}·h^{-1} for k_2 and 0.996 for R^2. Both models give similar kinetics parameter values.

As we can note, the R^2 of pseudo-second-order model is the highest and closest to 1. This model suggests that the chemical sorption is the rate-determining parameter.[49–51] More precisely, the pseudo-second-order model describes the adsorption in two steps. The first one is a rapid adsorption on the surface of the adsorbent with abundant vacant adsorption sites. The second is a slower diffusion to finish the saturation of adsorbent sites.[52] This would be in agreement with a quick adsorption of phosphate on iron sites and then the diffusion of phosphates to fill the remaining sites.

It is difficult to compare our results with published results because the adsorption is strongly dependent on the initial concentration, the introduced amount of adsorbent and the temperature. To remove phosphates from water, different iron oxide-based materials have been designed (Table 10): for example, iron oxide impregnated strong base anion exchange resin[53], a hybrid fibrous exchanger containing hydrated ferric oxide nanoparticles[54] or hybrid anion exchanger containing triethylamine functional groups and hydrated Fe(III) oxide nanoparticles.[55] We have tried in table 3 to compare our results with these studies performed on iron oxide (nano)materials.

Table 10. Kinetics results of different iron-based materials.

Iron Material	Size	Specific Surface Area $(m^2 \cdot g^{-1})$	pH	Media	Kinetic model	q_e (P-mg·g^{-1}) and conditions	K_2 (h^{-1})
Yoon et al. Iron oxide NPs[56]	20 nm	82.2	/	water	Second	4.93 T=30 °C Adsorbent :0.6 g·L^{-1} Ce = 2 P-mg·L^{-1}	2.21
Zeng et al. Iron oxide Tailings[57]	69	48	6-6.8	water	First and second models are not adapted	/	/
Lalley et al. Bayoxide® E33 (goethite based)[6]	Rod-like structures ca. 500 nm	140	7	Water lake	Second	27.47 T=21 °C Adsorbent :5 g·L^{-1} Ce = 140 P-mg·L^{-1}	0.59
Shahid et al. Aggregates of Iron oxide NPs[5]	Aggregates of NPs of 11.6 nm	75.8	6.8	Water	No data		
Mezenner et al. Iron hydroxide-eggshell	iron hydroxide-eggshell waste 50–315 µm	/	7	water	Second	1.45 T=21 °C Adsorbent : 7.5 g·L^{-1} Ce = 53 P-mg·L^{-1}	1.58
Cao et al. Iron oxide NPs[58]	Structure of about 160 nm formed by NPs of 80 nm	/	1.62	water	Second	8.20 T=25 °C Adsorbent : 2 g·L^{-1} Ce = 10 P-mg·L^{-1}	2.52
Ajmal et al. Iron oxide NPs[59]	32–55 nm	123	7	water	Second	7.96 T=35 °C Adsorbent : / g·L^{-1} Ce = 100 P-mg·L^{-1}	1.2
Daou et al. Iron oxide NPs[60]	40 nm	30	No data				
This study RSN	300	27	7	water	Second	4.1 T=20 °C Adsorbent : 1 g·L^{-1} Ce = 50 P-mg·L^{-1}	5.28

We may notice in Table 10 that most of data fit also better with the pseudo-second-order model.[3] If we compare our material to the other iron-based materials, the k_2 value is the highest (5.28 h^{-1}), it confirms that RSN can adsorb phosphates faster.

To conclude, experimental results showed a maximum adsorption of phosphate after 2 hours which can be considered as a "fast adsorption". Such kinetic will be very suitable for the peritoneal dialysis treatment.

IV. 3. 2. 2. Phosphate removal from RSN solutions as a function of the phosphate concentration

The adsorption curves as a function of pH and phosphate concentrations are given in Figure 15. As expected and in agreement with already reported results, the adsorption is more efficient at pH =3 than at pH=7 due to more favorable electrostatic interactions. This trend was also reported by several groups with different materials: magnetite[60], goethite[61], aluminum oxide hydroxide[62] or MnO_2.[63]

The experiments have also been conducted in dyalisate at pH 7 and we may observe at first that the dyalisate composition does not affect the phosphate adsorption. One may thus advance that the phosphate adsorption is specific and that no other compounds from dyalisat adsorbed on iron oxide RSN. However, the plateau seems to be reached at lower phosphate concentration in water than in dyalisate. Therefore, the compounds in dialysate should slightly affect the adsorption kinetics and especially the last step consisting in filing the last vacant sites.
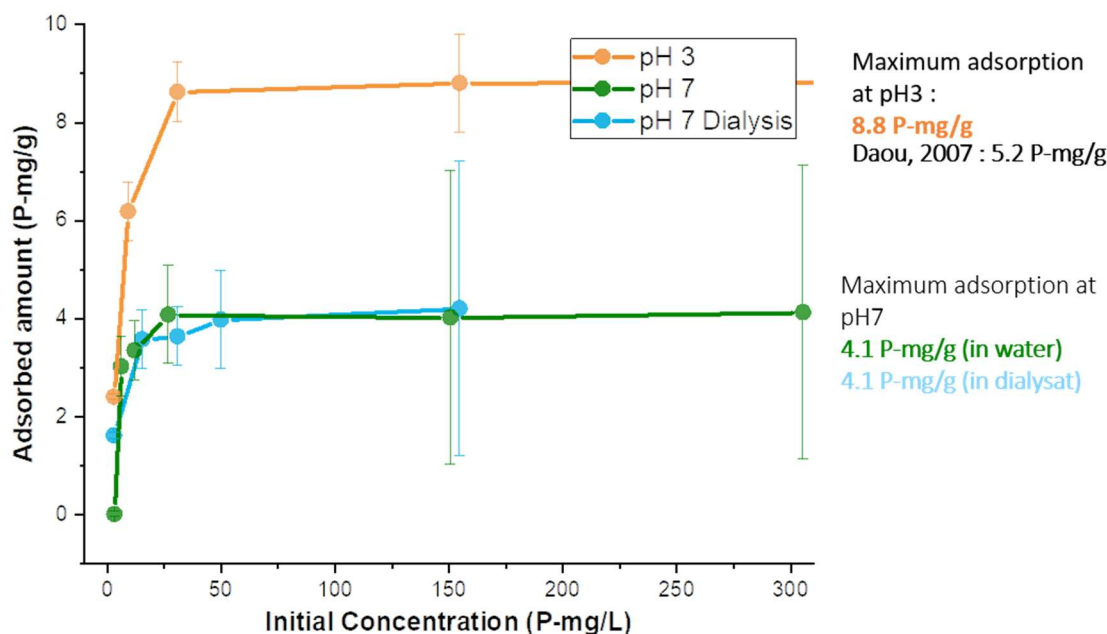
Figure 15. Adsorbed amount of phosphate by RSN as function of pH and phosphate concentrations after 24 hours. In orange, removal in water at pH 3; in green, in water at pH 7; and in blue, in the dialysis solution at pH 7.

The three curves are typical of "L" type isotherms (Chapter I). Such "L" isotherm confirms the strong affinity of phosphate for iron oxide surface and a progressive saturation of the surface when the concentration increases. A strict plateau is reached above a concentration of 50 P-mg/g whatever the pH and solution.

The curves obtained in water at pH 3 and 7 and in dialysate have been fitted with three different equilibrium models: Langmuir, Freundlich and Redlich-Peterson. The fitting curves and the adsorption parameters are presented in Figure 16 and the three curves seem better fitted with Langmuir and Redlich-Peterson models.

- For the curve in water at pH 7, the coefficient of determination (R^2) indicates that Langmuir and Redlich-Peterson are the best models. For the Langmuir isotherm, the values of adsorption parameters are 4.1 P-mg·g^{-1} for q_m and 0.42 L·mg^{-1} for K_L. For the Redlich-Peterson isotherm, the values of parameters are 0.72 L·mg^{-1} for K_R, 0.16 mg^{-1} for a_R and 1 for g.

- For the curve in the dialysis solution at pH 7, the coefficient of determination (R^2) indicates that Langmuir is the best model. For this isotherm model, the values of adsorption parameters are 4.1 P-mg·g^{-1} for q_m and 0.42 L·mg^{-1} for K_L. The data are similar to those obtained in water at pH=7 confirming that the other compounds in dialysate do not affect the phosphate adsorption.

- For the curve in water at pH 3, the coefficient of determination (R^2) indicates that Langmuir and Redlich-Peterson are the best models. For the Langmuir isotherm, the values of adsorption parameters are 8.8 P-mg·g^{-1} for q_m and 0.66 L·mg^{-1} for K_L. For the Redlich-Peterson isotherm, the values of parameters are 4.72 L·mg^{-1} for K_R, 0.52 mg^{-1} for a_R and 1 for g.

In water (pH 7)

Isotherm model	Parameters	Water (pH 7)	R²
Langmuir	q_m (P-mg/g) K_L (L/mg)	4.1 0.42	0.7256
Freundlich	K_f (mg/g) 1/n	2.7 0.08	0.28481
Redlich-Peterson	K_R (L/mg) a_R (mg-1) g	0.72 0.16 1	0.7368

In dialysis solution (pH 7)

Isotherm model	Parameters	Dialysis solution (pH 7)	R²
Langmuir	q_m (P-mg/g) K_L (L/mg)	4.1 0.42	0.9860
Freundlich	K_f (mg/g) 1/n	3.17 0.05	0.6283
Redlich-Peterson	K_R (L/mg) a_R (mg-1) g	0.72 0.16 1	0.4233

In water (pH 3)

Isotherm model	Parameters	Water (pH 3)	R²
Langmuir	q_m (P-mg/g) K_L (L/mg)	8.8 0.66	0.9869
Freundlich	K_f (mg/g) 1/n	7.74 0.02	0.3647
Redlich-Peterson	K_R (L/mg) a_R (mg-1) g	4.79 0.52 1	0.99

Figure 16. Fitting results of the isotherm adsorption curves. In red, the Langmuir model, in blue the Freundlich model and in green, the Redlich-Peterson model. Tables on the right side summarizes the parameter values corresponding to this fitting

We noticed for the Redlich-Peterson model that the best fit was possible with *g*=1, which means that the Redlich-Peterson model is reduced to the Langmuir equation. Finally, all the data are fitted with the Langmuir model. This model suggests that the adsorption sites do not interact between them and that their energies are equivalent (chapter I).

The values of K_L and q_m are higher at pH=3 than at pH 7 or in dialysate and confirmed that strong electrostatic interactions favor the phosphate adsorption.

Considering that the Langmuir model fits well our data, we can compare the K_L values by introducing the equilibrium parameter R_L. This equilibrium parameter R_L is expressed as: [64]

$$R_L = \frac{1}{1 + K_L \times C_0} .$$

With C_0, the initial concentration (P-mg·L^{-1}) and K_L the adsorption constant of Langmuir (L·mg^{-1}).

The value of R_L indicates if the phosphate adsorption is either favorable ($0 < R_L < 1$), linear ($R_L = 1$), unfavorable ($R_L > 1$), or irreversible ($R_L = 0$). The next table demonstrates that $R_L < 1$ for all the cases and confirms the favorable sorption of phosphates on the surface of RSN. More precisely, the R_L at pH 7 is higher than R_L at pH 3, it confirms a better affinity RSN-phosphates at low pH. This agrees with the electrostatic interactions previously explained: at low pH, phosphates are negatively charged and surface of RSN is positively charged.

Table 11 Equilibrium parameter values for phosphate capture in different media.

C_e	3.1	9.3	15.5	30.9	154.9
$R_{L\text{-pH 7 in water}}$	0.43	0.20	0.13	0.07	0.02
$R_{L\text{-pH 7 in dialysis solution}}$	0.43	0.20	0.13	0.07	0.02
$R_{L\text{-pH 3 in water}}$	0.33	0.14	0.09	0.05	0.01

To compare our results with the adsorption studies reported in Table 5, we have to be careful again. This adsorption strongly depends on the experimental conditions: media, temperature, initial amount of adsorbent and concentration of phosphates. The conditions and adsorption results are summarized in

Table 12.

Table 12. Adsorption isotherm results for different iron oxide-based materials.

Iron Material	Specific Surface Area ($m^2 \cdot g^{-1}$)	pH	Media and experimental conditions		Model adsorption	q_m ($P\text{-}mg \cdot g^{-1}$)	Adsorption parameters
Yoon *et al.* Iron oxide NPs[56]	82.2	/	Water T= 30 °C t= 24 h Adsorbent : 0.6 $g \cdot L^{-1}$ Ce = 2-20 $P\text{-}mg \cdot L^{-1}$		Redlich-Peterson	5.03	a_R=4.19·10^4 $L \cdot mg^{-1}$ Kr= 1.7·10^5 $mg \cdot g^{-1}$ g=0.88
Zeng *et al.* Iron oxide Tailings[57]	48	6-6.8	Water T= 20-21 °C t= 24 h Adsorbent : 2 $g \cdot L^{-1}$ Ce = 5-150 $P\text{-}mg \cdot L^{-1}$		Freundlich	12.65	K_F= 3.59 $L \cdot g^{-1}$ 1/n= 0.19
Lalley *et al.* Bayoxide® E33 (goethite based)[6]	140	7	Lake Water T= 25 °C t= 2 h Adsorbent: 2 $g \cdot L^{-1}$ Ce = 10-100 $P\text{-}mg \cdot L^{-1}$		Langmuir	37.74	K_L= 1.359 $L \cdot mg^{-1}$ R_L< 0.06
Mezenner *et al.* Iron hydroxide-eggshell[48]	/	7	Water T= 25 °C t= 4 h Adsorbent : 0.75 $g \cdot L^{-1}$ Ce = 7-140 $P\text{-}mg \cdot L^{-1}$		Freundlich	10.6	K_F=0.22 $mg\ L^{-1/n}\ g^{-1}\ L^{1/n}$ 1/n= 0.78
Cao *et al.* Iron oxide NPs[58]	/	1.6	Water T= 25 °C t= 3 weeks Adsorbent: 2 $g \cdot L^{-1}$ Ce = 10-100 $P\text{-}mg \cdot L^{-1}$		Langmuir	18.69	K_L= 0.41 $L \cdot mg^{-1}$ R_L< 0.2
Ajmal *et al.* Iron oxide NPs[59]	123	7	Water T= 25 °C t= 2 h Adsorbent : 2 $g \cdot L^{-1}$ Ce = 200-1000 $P\text{-}mg \cdot L^{-1}$		Freundlich	57.8	K_F 2.07 mg/g 1/n= 1.29
Daou et al. Iron oxide NPs[60]	30	7	Water T= RT °C t= 24 h Adsorbent : 1 $g \cdot L^{-1}$ Ce = 3-1500 $P\text{-}mg \cdot L^{-1}$		/	1.5	No data
		3			/	5.2	
This study RSN	27	7	Water	T= 20 °C t= 24 h Adsorbent : 1 $g \cdot L^{-1}$ Ce = 3.1-154.9 $P\text{-}mg \cdot L^{-1}$	Langmuir	4.1	K_L =0.42 $L \cdot mg^{-1}$ R_L< 0.43
This study RSN		7	Dialysis solution		Langmuir	4.1	K_L =0.42 $L \cdot mg^{-1}$ R_L< 0.43
This study RSN		3	Water		Langmuir	8.8	K_L =0.66 $L \cdot mg^{-1}$ R_L< 0.33

In this table, we can observe that the models, which fit better are the Langmuir and Freundlich ones. It confirms the fitting of RSN data in water and dialysis solution with the Langmuir model.

Lalley *et al.*[6] with Bayoxide® E33 and Cao *et al.*[50] with IO NPs have also fitted their curves with a Langmuir model, the R_L values (0.06 and 0.2) are much smaller than ours (0.43 and 0.33). It means that, under their conditions, their systems have a better affinity with phosphates. This could justify that the adsorbed amounts of our systems (4.1 and 8.8 $P\text{-}mg \cdot g^{-1}$) is smaller than their values (37.74 for the Bayoxide® E33 and 18.69 for the NPs of Cao). RSN have a smaller adsorbed amount of phosphates than the other iron materials. This is certainly explained by their lower surface specific area.

Adsorption amount. Maximum adsorption of RSN at pH 3 was calculated to be 8.8 P-mg·g⁻¹ (6.3 molecule·nm⁻²). At physiological pH in water and in dialysis solution, the maximum adsorbed value drops to 4.1 P-mg·g⁻¹ (2.3 P-molecule·m⁻²). We want to underline that the results in water and in the dialysis solution at pH 7 are the same, meaning that phosphate capture is not affected by the presence of any other elements in solution. Moreover, as we said, in the curve of the dialysis solution, we observe a deceleration of the capture at 50 P-mg·L⁻¹, just before the plateau. It can be justified because the media contains other elements (cations and glucose) and we will show below that RSN can adsorb glucose which may affect a little bit the phosphate diffusion to fill the last available sites. So, at this stage, we may suggest a competition between glucose and phosphate to occupy the last vacant sites.

To compare our adsorption amounts, we decided to take the study of Daou *et al).*[60] In fact, their nanoparticles have a close surface specific area (30 m²·g⁻¹) and experimental conditions are similar (T= RT °C, t= 24 h, Adsorbent: 1 g·L⁻¹, pH 3 and pH 7). The adsorption amounts with RSN are higher than those reported by Daou et al.: at pH 3, they measured 5.2 P-mg·g⁻¹ (3.26 molecule$_{phosphate}$·nm⁻²) and at pH 7, 1.5 P-mg·g⁻¹ (1.02 molecule$_{phosphate}$·nm⁻²). Therefore, RSN allows a higher adsorption of phosphates on their surface than NPs. It could be explained by a different phosphate complex (i.e. monodentate, bidentate) or the formation of a second phosphate layer or a more favorable nanostructuration of RSN (higher curvature of grains or stronger adsorption at interfaces).

Coverage of the surface (Θ). Thanks to the previous results, we can calculate the coverage of our surface thanks to the next equation:

$$\Theta_{exp} = \frac{q_m \times N_a}{M \times S_{BET}}$$

For that, q_m is the maximum adsorption (P-mg/g); Na, the number of Avogadro; M, the molar mass of phosphorus (31 g/mol). To calculate the maximum coverage, we considered the projected area of phosphate (24 Å²). The maximum and real coverages (molecule·m⁻²) and the surface occupancy (%) are given in the next table:

Table 13. Maximum and real coverage of phosphates on the iron-based materials.

Study	Conditions	Θ$_{max}$ (molecule/nm²)	Θ$_{experimental}$ (molecule/nm²)	%
Yoon *et al.*[56]	Water	4.4	1.2	27
Zeng *et al.*[57]	pH 6-6.8 in water	4.4	5.1	116
Lalley *et al.*[6]	pH 7 in lake water	4.4	5.2	119
Ajmal *et al.*[59]	pH 7 in water	4.4	9.1	207
Daou *et al.*[60]	pH 7 in water	4.4	1.02	21
	pH 3 in water	4.4	3.26	75
This study	pH 7 in water	4.4	2.9	66
	pH 7 in dialysis solution	4.4	2.9	66
	pH 3 in water	4.4	6.3	143

Table 13 shows that, at pH 7 (water and dialysis solution), the whole surface of RSN is not covered by phosphates (66% of the surface) in agreement with less favorable electrostatic interactions between phosphate and iron oxide surface. In the same way, at pH 3, the surface is covered with more of phosphates (143 % of coverage). With the other nanomaterials (Table 13), they observed also either a partial or complete coverage of the surface at any pH with values in the range 27 and 207 %.

Daou *et al.*[60] reported on the fact that the planes of Fe(+III) at iron oxide nanoparticle surface may exhibit up to 9.8 atoms of Fe/nm^2. Considering that at pH=3, we have 6.6 molecule/ nm^2, a monodentate coordination of phosphate and the RSN curvature may also explain the high coverage at pH=3.

IV. 3. 2. 3. Characterization of phosphates at the surface of RSN

We have characterized phosphates adsorbed on the iron oxide surface by zeta potential and FTIR.

After phosphatation of RSN, we can observe in Figure 17 shift of the zeta potential curve towards lower pH confirming the modification of the surface properties of RSN. The zeta potential value at pH 3 decreases from +16 mV to 3.5 mV. In agreement with Daou *et al.*[60], if the phosphatation yield is high and if after phosphatation, the global charge of surface remains positive, it may suggest that all the "Fe-OH$_2^+$" sites of the surface are not involved in phosphate capture.[46] Following his explanation, at pH 3, the phosphates can be adsorbed in the surface by two phenomena:

• the electrostatic interactions.

• the formation of the surface phosphate complex also involves the hydroxyl groups on the iron oxide surface.
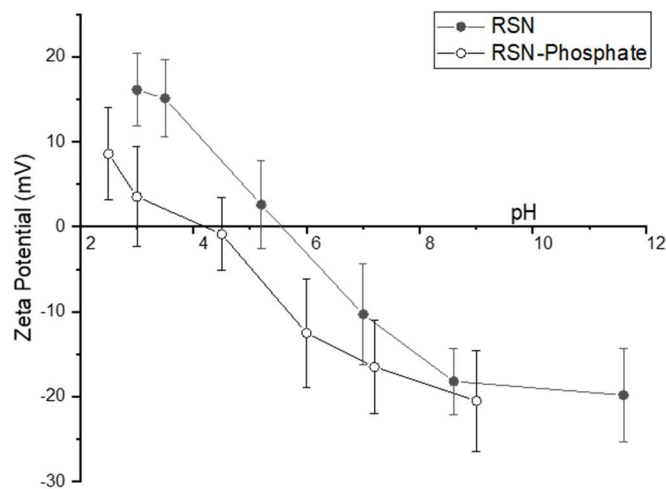
Figure 17. Zeta potential measurements as a function of pH of magnetite RSN before and after phosphatation.

FTIR. To further demonstrate the presence of phosphates onto the RSN, FTIR spectroscopy was performed (Figure 18) on different samples. All the samples containing RSN showed the typical Fe-O band centered at 580 cm^{-1}. In paragraph III.1, we showed this band corresponds to the magnetite phase. In all samples (after phosphatation in water at pH3, pH 7 or dialysis solution and glucose contact), this band was preserved even if a small shoulder is noticed towards higher wavenumbers suggesting a slightly small oxidation.

To characterize the phosphates, we focused on the zone 1300 cm^{-1}-800 cm^{-1} related to the P-O, P-OH, P=O bonds.[65] .

The FTIR spectrum of the RSN without phosphates shows also bands in the same range. In agreement with observations of other members of the groups and with the FTIR spectra of the KBr, the bands at 890, 1132 and 1058 cm^{-1} are observed in RSN and phosphated RSN IR spectra. The band at 890 cm^{-1} cannot be identified, and the bands at 1132 and 1058 cm^{-1} could be attributed to the KBr. Indeed, this strong band is present in the FTIR spectra of KBr (Figure 18, green) and has been related to a impurity in KBr.

In order to identify the band of the phosphates on the RSN, the FTIR spectrum of the RSN sample with the highest amount of phosphate on surface (RSN at pH3, [P]=154.9 P-mg/l) is displayed in Figure 18 A. and C. (range 1300 cm^{-1}-800 cm^{-1}). A deconvolution of this part was made by considering gaussien profiles.

Five gaussian curves are obtained centred at 1098 cm^{-1}, 1085 cm^{-1}, 1050 cm^{-1}, 1007 cm^{-1} and 890 cm^{-1}. We can easily identify than the band 1098 cm^{-1} can have a contribution of the KBr and the band at 890 cm^{-1} is the same than for the RSN without phosphates.

Daou *et al.*[60] found similar results with IONPS[46] and, as well, other studies with hematite, maghemite and titane oxide reported similar bands after phosphatation.[66–68] On the one hand, the bands corresponding to hydroxyl groups of water (range 3600-3200 cm^{-1} and band at 1610 cm^{-1}) decreased after phosphatation, it shows an interaction between the hydroxyl sites of the RSN and the phosphates. The modification of the bands between 1300 cm^{-1}-800 cm^{-1} confirms the presence of phosphates on the surface of RSN. To characterize the phosphate coordination on the surface (monodentate, bidentate or tridentate), the observation of a strong band at 1050 cm^{-1} suggests the presence of a monodentate or bidentate specie. However, we have a contribution of the KBr which could modify the intensity of this band. The other band at 1098 cm^{-1} has also a contribution of the KBr. The band at 1007 cm^{-1} is the only one whitout contribution of KBr. In agreement with results of Daou et al., the phosphates on the surface would be anchored at the surface. However, the pollution in the KBr did not help to identify the coordination mode of phosphates.

The same analysis on the samples at pH 7 (water and dialysis solution) is difficult as the phosphatation is lower. Only a broad and with low intensity band is visible for RSN-phosphate in water at pH 7 (Figure 18. D, turquoise blue). For the sample RSN-Phosphate in dialysis solution (pH 7, Figure 18.D, pink), a very intensive band is visible and hides the phosphate ones. As among elements in the dialysate, glucose displays IR bands in this wavenumber range, we have mixed for 2 hours, 20 mg of RSN in a solution of glucose (125 mM). For RSN-Phosphate (dialysate in pink) and RSN-glucose (in violet), the bands at 1100 cm^{-1} are similar. If we compare with the spectrum of glucose (lavender), this band is attributed to a O-C-O glucose bond. Finally, we confirm that RSN interact with the glucose from dialysis solution and due to the overlapping of glucose bands with those of phosphate, the phosphate complex cannot be identified. Nevertheless, the adsorption of glucose on RSN may explain the kinetics curve observed in dialysate: maybe more time is needed to reach the plateau.

151
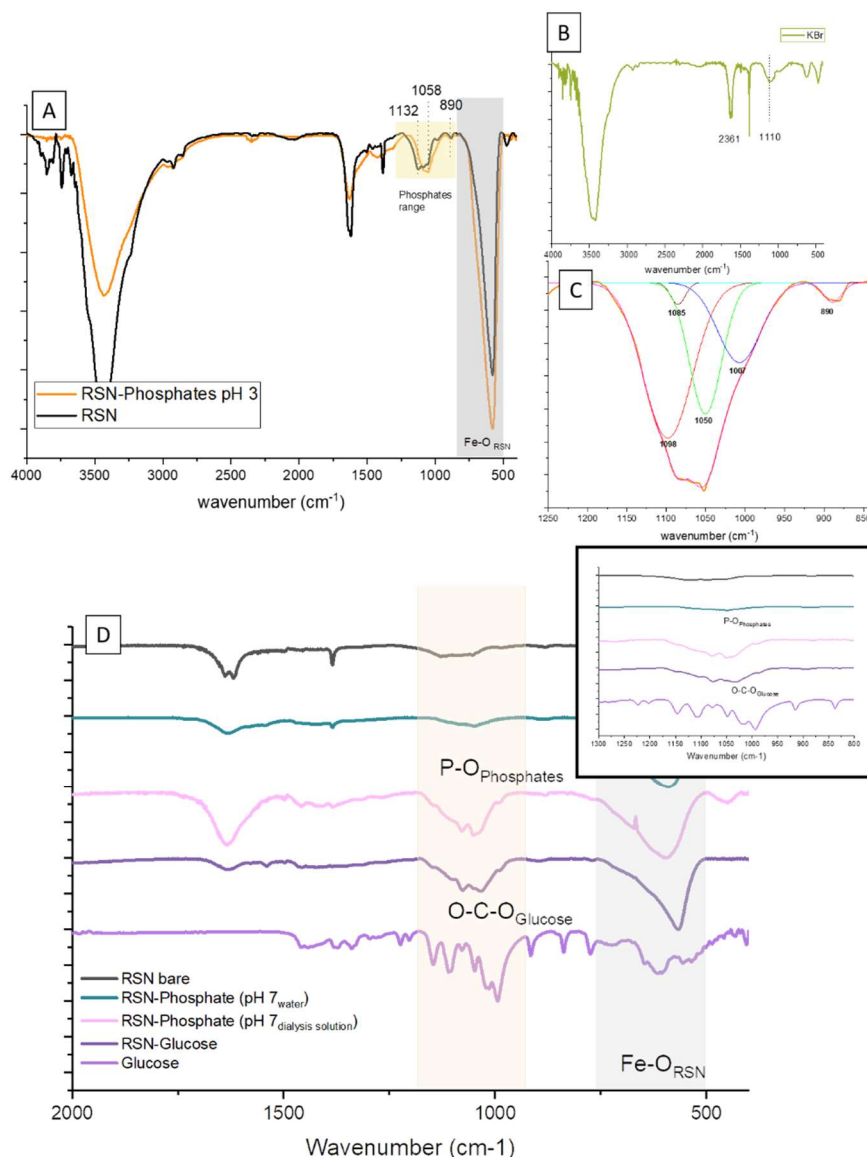
Figure 18. A. FTIR of bare RSN (black) and RSN after phosphate capture in water pH 3 (orange). **B.** FTIR spectra of the KBr. **C.** Zoom of RSN after phosphate capture in water in the range 1250-800 cm-1 and deconvolution of the bands attributed to the phosphates on the surface of the material. **D.** FTIR of bare RSN (black), RSN after phosphate capture in water (pH 7, turquoise blue), RSN after phosphate capture in the dialysis solution (pH 7, pink), RSN after contact with a glucose solution (violet) and glucose (lavender).

IV. 3. 2. 4. Conclusion on phosphate uptake by iron oxide RSN

We have investigated the adsorption of phosphates at the surface of RSN in water at pH 3 and 7 and in a dialysis solution at pH 7 as function of time and of the phosphate concentration. We have thus shown that the kinetics of adsorption followed a pseudo-second order model with a maximum adsorption after 2 hours of contact.

The adsorption isotherm of phosphates at the surface of RSN have been fitted with the Langmuir model. The maximum adsorption capacities were 4.1 and 8.8 P-mg per gram of RSN at pH 7 and pH 3, respectively. Moreover, the experiments in the dialysis solution conducted to the same results showing quite no effects of the other elements present in the dialysis solution on the phosphate adsorption. A quite high phosphate adsorption yield has been obtained with all RSN considering their low surface specific area. The phosphatation of RSN was confirmed by zeta potential measurements and FTIR spectroscopy.

These results showed that RSN are very good candidates for phosphate removal. One may notice that an increase of their surface specific area would allow to enhance the phosphate removal but we remind that the iron oxide particles have to display a high particle size to avoid their transfer in the blood vessel during the PD treatment.

However, as explained in the introduction, the aluminum doped RSN are promising for the enhancement of the phosphate adsorption. Therefore, in the next part, similar experiments were performed with Al-RSN.

IV. 3. 3. Iron oxide RSN doped with aluminum (Al-RSN) for phosphate capture

As we explained in the introduction of this chapter, the doping of ferrite is a good way to enhance the adsorption capacity of phosphate and among doping elements, Al appears promising. Mor et al. [69] have performed experiments with alumina nanoparticles (around 50 nm) and showed negative energy values of ΔG_{293K} (−1403 KJ·mol^{-1}) and ΔS_{293K} (−510.7 KJ·mol^{-1}) for the phosphate adsorption. It indicates an affinity between aluminum and phosphate.

The conception of the aluminum doped RSN and the different adsorption studies for this material were performed after the lockdown and at the end of my thesis. The results presented below must be repeated and additional points to the different curves must be added to conclude about the different models. However, they allow giving an idea about the potential of Al doped RSN.

We have used RSN doped with 10 % of Al with a mean diameter of 269 nm, a mean nanograin size of 19.5 nm and a surface specific area of 40 m²·g^{-1}. Figure 19 represents the ZP curves of RSN and Al-RSN as a function of pH, and we can clearly observe that the addition of aluminum inside the spinel iron oxide structure induces a shift of the ZP curve towards higher pH. The value of the isoelectric point is shifted from 5.6 to 7.2 and therefore at pH 7, the electrostatic interactions would be stronger and the phosphate capture should be favored.
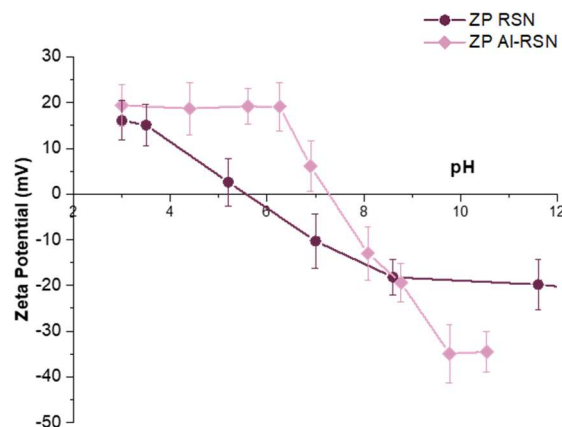
Figure 19. Zeta Potential (mV) curves of RSN (in violet) and Al-RSN (in pink) as a function of pH.

The following parts recover results of kinetics studies and adsorption isotherms under the same conditions than RSN in water. At the end, we will conclude about its possible future use in peritoneal dialysis treatment.

IV. 3. 3. 1. Phosphate removal from water solutions as a function of time with Al-RSN

As before, the use of these Al-RSN for peritoneal dialysis could be possible if the maximum adsorption takes less than 4 hours to prevent the damage of peritoneal membrane. As for RSN, Al-RSN were put in contact with a phosphate solution (50 P-mg·L^{-1}) for different times at pH 7. Regarding the behavior of Al-RSN (Figure 20, right), after 3 hours, a maximum is clearly reached. Then, the curve tends to a saturation plateau. The time needed to reach the plateau is higher than for RSN (2h). In other studies on Al-Fe materials, the maximum adsorption is reached after 5 hours[44,67,70] So, in a first sight, our Al-RSN are adapted to be applied in a peritoneal dialysis treatment.

As before with RSN, the curve is fitted with two kinetics models (Figure 20 and Table 14). In Figure 20-right, we can observe that both models seem to fit quite well the data, but the pseudo-first-order model fits better the experimental data for Al-RSN by contrast to RSN (better fit with the pseudo second order model). For the pseudo-first-order model, the values of the kinetic parameter are 9.8 P-mg·g^{-1} for q_e, 2.04 h^{-1} for K_1 and 0.97374 for R². In the same way, for the pseudo-second-order model, the values are 10.3 P-mg·g^{-1} for q_e, 0.37 g·P-mg^{-1}h^{-1} for k_2 and 0.94169 for R².
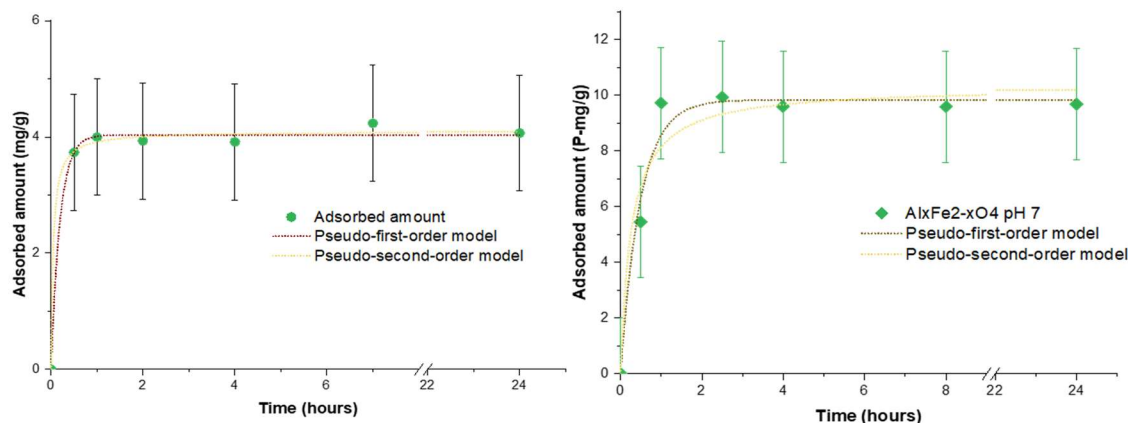
Figure 20. Adsorbed amount of phosphate by RSN and Al-RSN as a function of time in water at pH 7, [P]= 50 mg/l.

Table 14. Kinetic parameters for pseudo-first-order and pseudo-second-order models of Al-RSN.

Our Study					
Pseudo-first-order			**Pseudo-second-order**		
q_e (P-mg· g^{-1})	K_1 (h^{-1})	R²	q_e (P-mg· g^{-1})	K_2 (h^{-1})	R²
9.8 ± 0.3	2.04 ± 0.35	0.97374	10.3 ± 0.6	0.37 ± 0.18	0.94169

Even if the adsorbed phosphate amount deduced from both models is quite similar, these kinetics data are better fitted with the pseudo-first-order model with Al-RSN by contrast to RSN. Such model suggests a diffusion-controlled process. Few works have been published on the phosphate capture by iron oxide doped with aluminum nanoparticles and the main results are summarized in the next table.

Table 15. Kinetics results of different aluminum-iron oxide materials.

Iron Material	Size	Specific Surface Area ($m^2 \cdot g^{-1}$)	pH	Media	Kinetic model	q_e (P-mg·g^{-1}) and conditions	K_2 (h^{-1})
Li *et al.* AM0[4]	Goetithe wires around 500 nm	19.1	5.5	Water	Second	0.42 T=25 °C Adsorbent : 0.5 g·L^{-1} Ce = 0.5 P-mg·L^{-1}	7.60
Li *et al.* AM3[4]		22.1	5.5	Water	Second	0.44 T=25 °C Adsorbent : 0.5 g·L^{-1} Ce = 0.5 P-mg·L^{-1}	6.14
Li *et al.* AM6[4]		26.8	5.5	Water	Second	0.48 T=25 °C Adsorbent : 0.5 g·L^{-1} Ce = 0.5 P-mg·L^{-1}	5.16
Li *et al.* AM9[4]		31	5.5	Water	Second	0.51 T=25 °C Adsorbent : 0.5 g·L^{-1} Ce = 0.5 P-mg·L^{-1}	5.47
De Sousa *et al.* 50FeAl[70]	Iron oxide microsphe-res 0.85 mm	340	7	Water		No data	
Xu *et al.* Al-NP[44]	Iron oxide NPs 14.24 nm	/	<8	Water	Second	30.3 T=25 °C Adsorbent : 0.3 g·L^{-1} Ce = 10 P-mg·L^{-1}	10.20
					Second	43.86 T=25 °C Adsorbent : 0.3 g·L^{-1} Ce = 20 P-mg·L^{-1}	0.16
					Second	47.62 T=25 °C Adsorbent : 0.3 g·L^{-1} Ce = 30 P-mg·L^{-1}	1.08
This study Al-RSN	269 nm	40	7	Water	First	9.8 T=20 °C Adsorbent : 1 g·L^{-1} Ce = 50 P-mg·L^{-1}	2.04
					Second	10.3 T=20 °C Adsorbent : 1 g·L^{-1} Ce = 50 P-mg·L^{-1}	0.37
This study RSN	300	27	7	Water	Second	4.1 T=20 °C Adsorbent : 1 g·L^{-1} Ce = 50 P-mg·L^{-1}	5.28

The results in Table 15 show that most kinetics results are fitted with the pseudo-second-order model. We will need to add more points in our adsorption isotherm to conclude on the most suitable model. Finally, experimental results showed a maximum adsorption of phosphate in the first 3 hours. In spite of the value, the adsorption kinetic is adapted to the peritoneal dialysis treatment and can be accepted as a "fast adsorption".

IV. 3. 3. 2. Phosphate removal from RSN water solutions as a function of phosphate concentrations

The adsorption curves as a function of pH and phosphate concentration are given in Figure 21.

In Figure 21.B, as for RSN, we can observe an increase in the phosphate capture with the increase of the phosphate concentration up to an initial concentration of 70 P-mg·L^{-1}.Then, a plateau is reached above this concentration for both pH. As expected and in agreement with already reported results, the adsorption is more efficient at lower pH. Indeed, the electrostatic interactions are stronger at pH 3 than at pH 7.

If we compare the phosphatation behaviour of RSN and Al-RSN (Figure 21 A. and B.), the capture of phosphates with Al-RSN appears slower, and the plateau is reached after 60-70 P-mg·L-1 when for RSN, it was reached at 50. For pH 3, the maximum adsorption amount of Al-RSN is 15.5 P-mg·g^{-1}, and at pH 7, the value is 10 P-mg·g^{-1}. These values are higher than those with RSN but the surface specific area of Al-RSN is higher.

Concerning these isotherms, curves are of « L » type. Then, the curves obtained in water at pH 3 and 7 were fitted with three different equilibrium models. The fitting curves and the adsorption parameters are presented in Figure 21 and we can observe that these models do not allow fitting well the experimental curves. Nevertheless, one may notice that the Langmuir model seems to be the most suitable model. More experimental data are needed in the curves to conclude on the most adapted model and also to consider parameters resulting from the fitting.

Isotherm model	Parameters	Water (pH 3)	R²
Langmuir	q_m (mg/g) K_L (L/mg)	17.72 0.88	0,92231
Freundlich	K_f (mg/g) n	5,2 4,2	0.67187
Redlich-Peterson	K_R (L/mg) a_R (mg-1) g	1,57 0,088 1	0.88346

Isotherm model	Parameters	Water (pH 7)	R²
Langmuir	q_m (mg/g) K_L (L/mg)	10,9 0.112	0,75267
Freundlich	K_f (mg/g) n	2,93 3,76	0.44681
Redlich-Peterson	K_R (L/mg) a_R (mg-1) g	0,97 0,082 1	0.76846
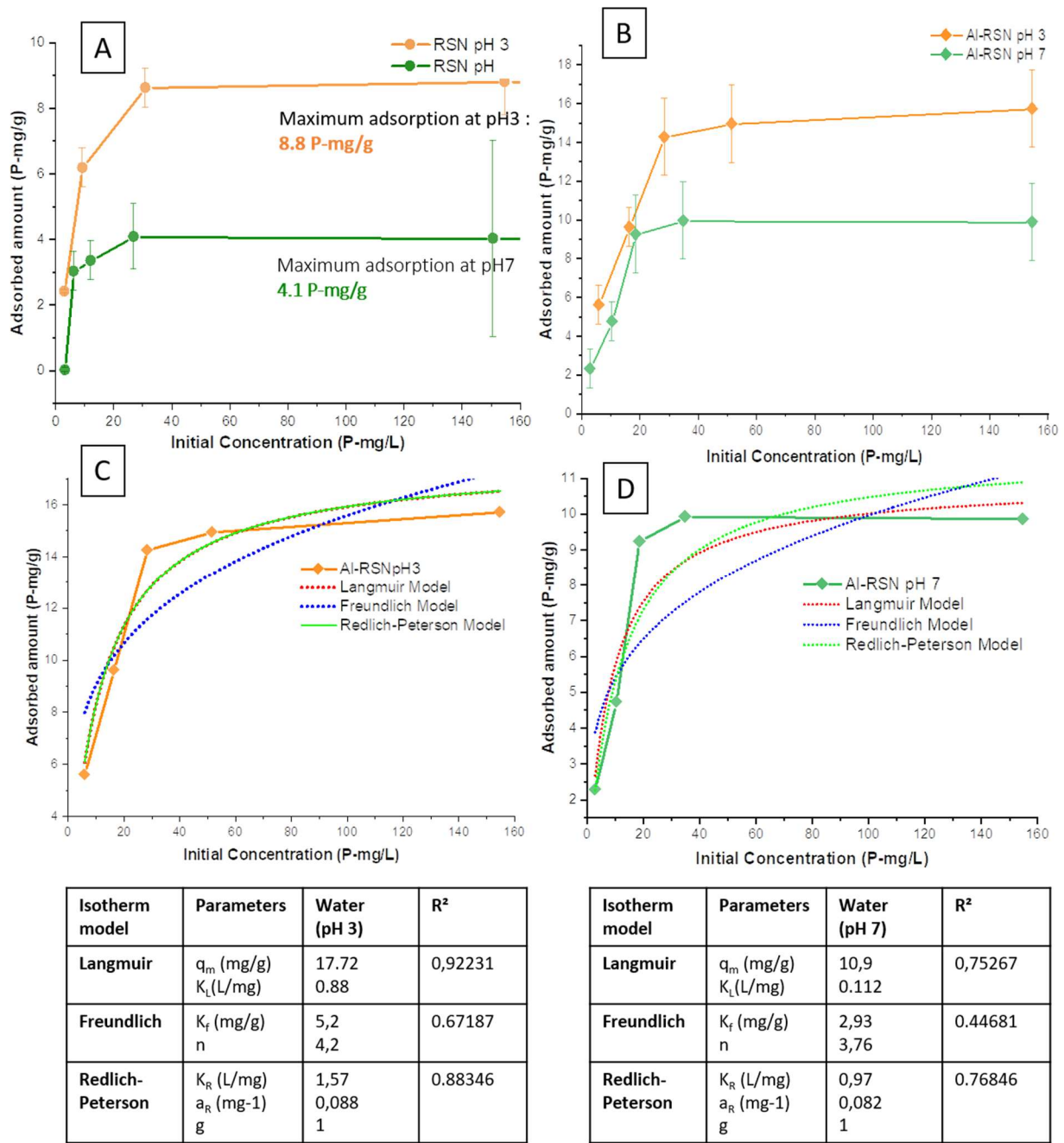
Figure 21. Adsorbed amount of phosphate by A. RSN and B. Al-RSN in different media during 24 hours. In orange, in water at pH 3; in green, in water at pH 7. C. and D. Fitting results of the isotherm adsorption curves. In red, the Langmuir model, in blue the Freundlich model and in green, the Redlich-Peterson model. Tables summarize the parameter values corresponding to this fitting.

The reported adsorption isotherm studies with similar materials are summarized in Table 16. As for RSN, the different experimental conditions make that the comparison of different results is difficult. However, we can have a general idea of the most used model and the adsorption amount of the aluminum doped ferrite materials.

Table 16. Adsorption isotherm results of different aluminum doped ferrite materials.

Iron Material	pH	Media and experimental conditions	Model adsorption	q_m (P-mg/g)	Parameters
Li *et al.* AM0[4]	5.5	Water T= 25 °C t= 24 h Adsorbent : 0.5 g·L^{-1} Ce = 0.07–1.7 P-mg·L^{-1}	Langmuir	1.21	K_L= 5.04 L·mg^{-1} R_L< 0.74
Li *et al.* AM3[4]	5.5	Water T= 25 °C t= 24 h Adsorbent : 0.5 g·L^{-1} Ce = 0.07–1.7 P-mg·L^{-1}	Langmuir	1.23	K_L= 6.41 L·mg^{-1} R_L< 0.69
Li *et al.* AM6[4]	5.5	Water T= 25 °C t= 24 h Adsorbent : 0.5 g·L^{-1} Ce = 0.07–1.7 P-mg·L^{-1}	Langmuir	1.36	K_L= 6.48 L·mg^{-1} R_L< 0.69
Li *et al.* AM9[4]	5.5	Water T= 25 °C t= 24 h Adsorbent : 0.5 g·L^{-1} Ce = 0.07–1.7 P-mg·L^{-1}	Langmuir	1.65	K_L= 4.54 L·mg^{-1} R_L< 0.76
De Sousa *et al.* 50FeAl[70]	7	Water T= 30 °C t= 24 h Adsorbent : 7.5 g·L^{-1} Ce = 1–140 P-mg·L^{-1}	Langmuir	8.21	K_L= 1.04 L·mg^{-1} R_L< 0.49
Xu *et al.* Al-NP[44]	<8	Water T= 25 °C t= overnight Adsorbent : 0.6 g·L^{-1} Ce = 1-40 P-mg·L^{-1}	Langmuir	102.15	K_L= 1.09 L·mg^{-1} R_L< 0.48
	<8	Water T= 25 °C t= overnight Adsorbent : 1.2 g·L^{-1} Ce = 1-40 P-mg·L^{-1}	Langmuir	81.31	K_L= 1.09 L·mg^{-1} R_L< 0.48

In this table, we can observe that the model which better fits the materials is the Langmuir ones. It confirms that Al-RSN data in water could be fitted with this model. This model suggests that the adsorption sites do not interact between them and that their energies are equivalent (chapter I).

Adsorption amount. At pH 7, the maximum adsorption value is 10 P-mg·g^{-1}, at pH 3, these values rises to 15.5 P-mg·g^{-1}. Both values are more important than for RSN (4.1 P-mg·g^{-1} and 8.8 P-mg·g^{-1}) but the surface specific area of Al-RSN is also higher. Thus, one interest of Al doping is to increase the surface specific area allowing a higher phosphatation capture per g of materials. We can notice that the maximum adsorption values obtained with Al-RSN are quite high by comparison with published results except for studies of Xu et al. [44]

Coverage (Θ). We can calculate the maximum coverage expected and compared with the real one. Most reported studies showed a partial coverage of the surface (11-18 %). At pH 7, the Al doped RSNs have a coverage of surface of 165% at pH 3 and 106 % at pH 7. The coverage of phosphates at pH 7 and at pH 3, is higher with Al-RSN than with RSN. These results confirm that the doping by Al of RSN allows enhancing the phosphate capture.

Table 17. **Maximum and real coverage of phosphates on the Al-RSN.**

Materials	Conditions	Θ_{max} (molecule/nm²)	Θ_{real} (molecule/nm²)	Real coverage (%)
AM0[4]	pH 5.5 in water	4.4	1.2	27.9
AM3[4]		4.4	1.1	24.6
AM6[4]		4.4	1.0	22.4
AM9[4]		4.4	1.0	23.5
50FeAl[70]	pH 7 in water	4.4	0.5	10.7
This study	pH 3 in water	4.4	7.3	165
Al-RSN	pH 7 in water	4.4	4.7	106
This study	pH 3 in water	4.4	6.3	143
RSN	pH 7 in water	4.4	2.9	66

Therefore, the Al doping increases the surface specific area of RSN and also the phosphate capture. The aluminum doping modifies the surface properties (i.e. IEP) which helps to improve the capture. So, the higher phosphate adsorption of Al-RSN is possible because these new nanostructures have a higher IEP and a higher specific surface area than RSN. A possible implication of surface Al atoms in the phosphatation is not to exclude.

IV. 3. 3. 3. Characterization of phosphates at the surface of Al-RSN

In this part, we will characterize the phosphates adsorbed on the surface by zeta potential measurements and FTIR spectroscopy.

We performed zeta potential measurements before and after phosphatation at pH 3. As observed in

Figure 22, a shift of zeta potential curve as a function of pH towards lower pH is observed. These shifts in zeta potential values confirmed a modification of the Al doped ferrite after the phosphatation step.
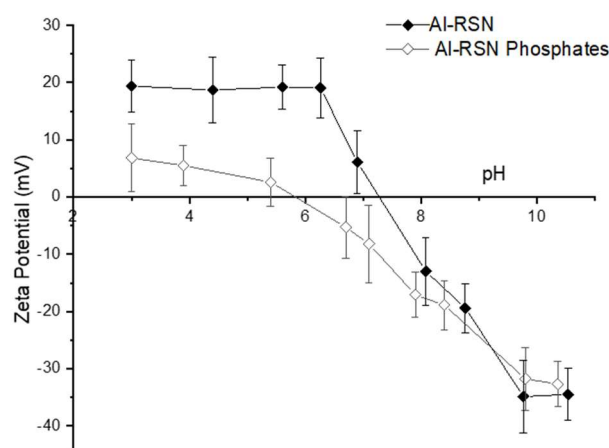

Figure 22. ZETA POTENTIAL MEASUREMENTS AS A FUNCTION OF PH OF Al- RSN BEFORE AND AFTER PHOSPHATATION AT PH = 3.

FTIR. In IR spectra in Figure 23, the intensive band at 580 cm^{-1} is attributed to the Fe-O (or Al-O) bond of the material (as for the RSN). After phosphatation, this band was quite not modified. The band between

3600 - 3200 cm^{-1} and those at 1621 cm^{-1} are associated with the vibrations of elongation of O-H bound (linked to physisorbed and chemisorbed water). Bands between 3000 and 2850 cm^{-1} are linked to C-H bonds of EG traces, other bands between 1800 and 1250 cm^{-1} to traces of ethanol/acetone used for washings.

The zone 1250-800 cm^{-1} is attributed to the P-O, P-OH, P=O bonds.[65] We can oberve in the FTIR spectra of Al-RSN, the appearence of peaks in the same zone: 1086, 1056 and 890 cm^{-1}. The band at 890 cm^{-1} was already visible in the RSN sanple, and, the band at 1086 and 1056 can also be related to a pollution of KBr. Contrary to RSN after phosphatation at pH 3 and thanks to their higher phosphatation rate, phosphated Al-RSN display a spectrum with more intense bands (Figure 23, green). A deconvolution of this zone was made considering gaussien profiles. Four peaks are obtained centred at 1104 cm^{-1}, 1053 cm^{-1}, 974 cm^{-1} and 900 cm^{-1}. Taking in consideration the contributions of KBr and Al-RSN, we have a modification of the signal for the bands at 1104, 1086 and 900 cm^{-1}.
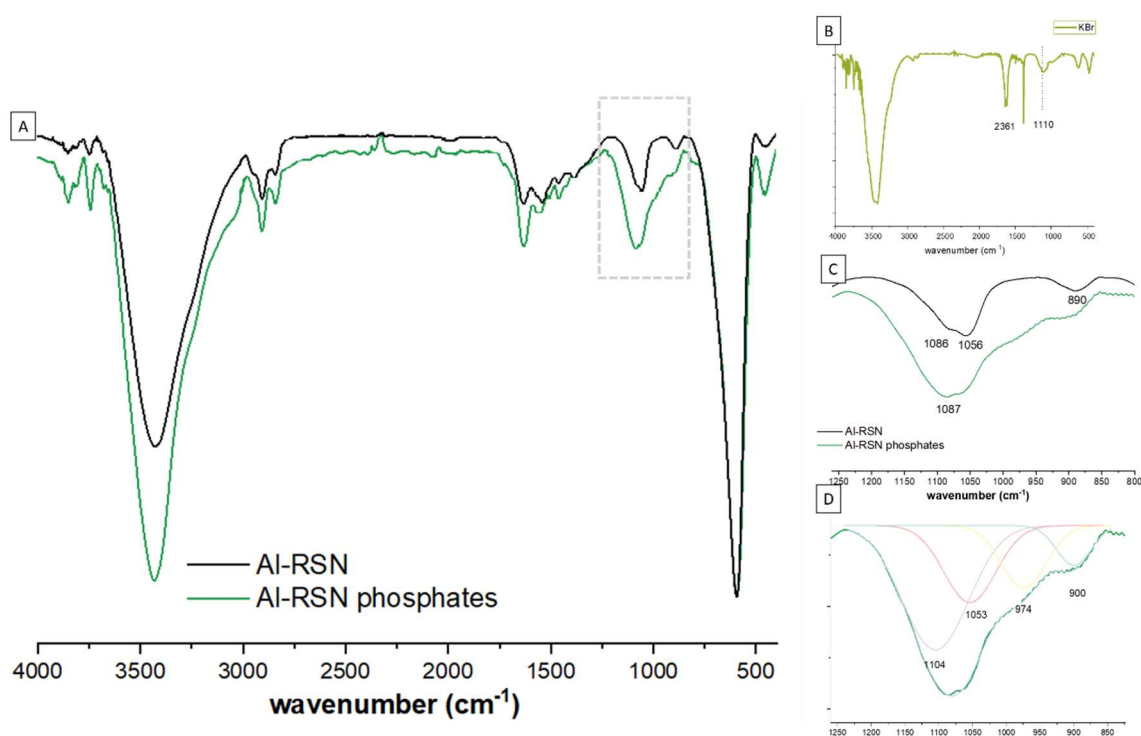
Figure 23. FTIR spectra of A. Al-RSN bare (black) and Al-RSN after phosphate capture in water at pH =7 (green). B. KBr. C. Zoom of Al-RSN after and before phosphate capture in water in the range 1250-800 cm-1 and D. Deconvolution of the bands attributed to the phosphates on the surface of the material

Other studies with hematite, maghemite and titane oxide exhibited similar bands which confirm the presence of phosphates on the surface of materials.[66,71] The large band at 1053 cm^{-1} suggests the presence of a protonated monodentate or bidentate specie.[72] However, in this case, we cannot totally confirm the intensity of this band due to the KBr contribution. In the study of phosphate adsorbed on goethite, Bruce *et al.* [73], for the sample H$_2$PO$_4^-$, the authors observed bands at 874 cm^{-1} (P-OH), 940 cm^{-1} (P-OH), 1075 cm^{-1} (P-O) and 1155 cm^{-1} (P-O). In the same study, for goethite in contact with HPO$_4^{2-}$, the observed bands were at 847 cm^{-1} (P-OH), 989 cm^{-1} (P-O) and 1077 cm^{-1} (P-O). Our bands are between two values each

time, so, we can confirm the presence of phosphates on the surface, but we cannot determine if it is a monodentate, bidentate or tridentate complex.

IV. 3. 3. 4. Conclusion of undoped and aluminum doped ferrite RSN for phosphate uptake

The investigation of the phosphatation of RSN and Al-RSN indicates that both aluminum-doped RSNs and undoped RSN are promising adsorbents with a fast adsorption of phosphate (<3 hours for Al-RSN and < 2hours for RSN) and a high phosphatation adsorption capacity.

Phosphates uptake over both adsorbents was favored at low pH and decreases with increasing pH of the solution confirming that electrostatic interactions are important to favor phosphatation of materials. The fitting of experimental curves with Al-RSN was difficult and more experimental points are needed to conclude on the suitable models.

The maximum adsorption capacity of Al-RSN deduced from experimental curves was 10 and 15.5 P-mg·g^{-1} at pH 7 and pH 3, respectively by comparison with RSN: 4.1 and 8.8 P-mg·g^{-1} at pH 7 and pH 3, respectively. We notice thus an increase of the phosphate adsorption with Al-RSN per g of materials.

However, the surface specific area of Al-RSN is higher but the phosphate coverage was determined to 162 % and 106 % at pH 3 and pH 7 respectively whereas for RSN, it was of 143% and 66% (at pH 3 and pH 7). For both pH, the coverage increased after doping. Therefore, the Al doping of RSN allows increasing the surface specific area and also enhancing the phosphatation capacity. This enhancement of the phosphate adsorption is certainly due to the shift of IEP favoring more electrostatic interactions but a contribution of surface Al ions is not to exclude.

AL-RSN and RSN are both promising absorbents for phosphate removal enhancement in the PD treatment as they combine high phosphate adsorption capacities and large diameter requested for avoiding their transfer in blood vessels.

IV. 3. 5. Preliminary *in vitro* Peritoneal Dialysis Experiments-

Our collaborators at the Hautepierre hospital (Strasbourg, France) (Dr Philippe Choquet, Master student Florence Pillods and Dr Ariane Zaloszyc) have developed a set-up allow simulating in vitro the PD treatment. The next part focused on the conception of the *in vitro* model ste-up by F. Pillods, P. Choquet and A. Zaloszyc and on the first preliminary tests.

IV. 3. 3. 1 *In vitro* Peritoneal Dialysis Model set-up

Few elaborated models of *in vitro* PD have been performed and only one was used to test the phosphates elimination using additives to the dialysis solution.[74] The advantage of *in vitro* models is that they give an estimation of the potential efficiency of a new dialysis system or fluid.

All studies representing a relevant *in vitro* model derived from the model of McGary *et al.*[74] (Figure 24). Here, the peritoneal cavity is modeled by a Plexiglas tank in which are placed the dialysis fluid at 37 ° C (usually 2 liters) and a pediatric hemodialysis filter (0.6 m^2) without its outer shell. A compartment representing arterial blood (1) at 37 °C is pumped at 150 ml/min to the dialyzer. In the dialysis compartment (2), the different exchanges are made at 37 °C, simulating the peritoneal cavity. Finally, purified blood by the dialysis goes into another compartment (3). Pressure gauges (P_{Bi} and P_{B0}) measure the initial and final flow pressures. The flow is checked by the passage of the liquid through test tubes graduated (a and b). In general, few PD *in vitro* models have been used in research to simulated some aspects of PD.[75]
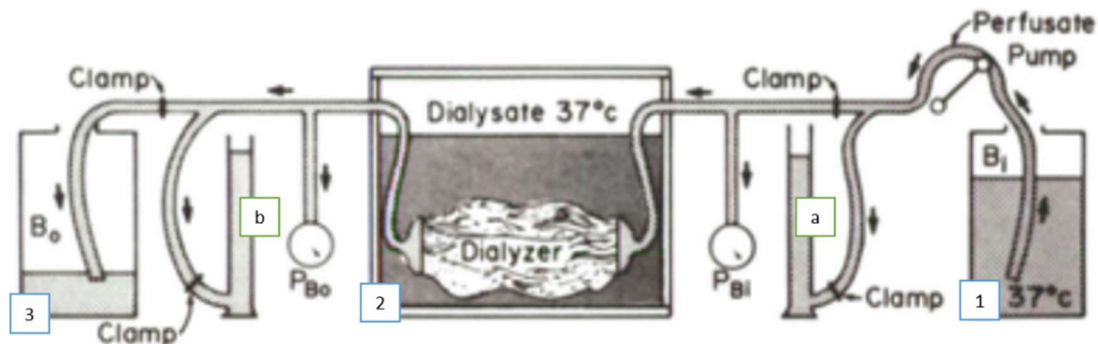
Figure 24. McGary et al. *in vitro* PD model.[74]

The *in vitro* model from the Hautepierre hospital was inspired by the McGary model.

The *in vitro* PD model of Pillods *et al.* (Scheme 4) has a structure including in order:

- A blood compartment on an elevator.
- A pipe connecting this compartment to a peristaltic pump (of variable flow).
- A vertical tubing associated with a 50 cm graduated ruler for measuring the hydrostatic pressure.
- A dialysis grid on which are fixed an incoming pipe, a leaving pipe and between the two, the dialysis membranes representing the peritoneal capillaries. This grid is placed in a peritoneal compartment, itself filled with stagnant fluid.
- A last pipe brings the circulating liquid back to the blood compartment.

163
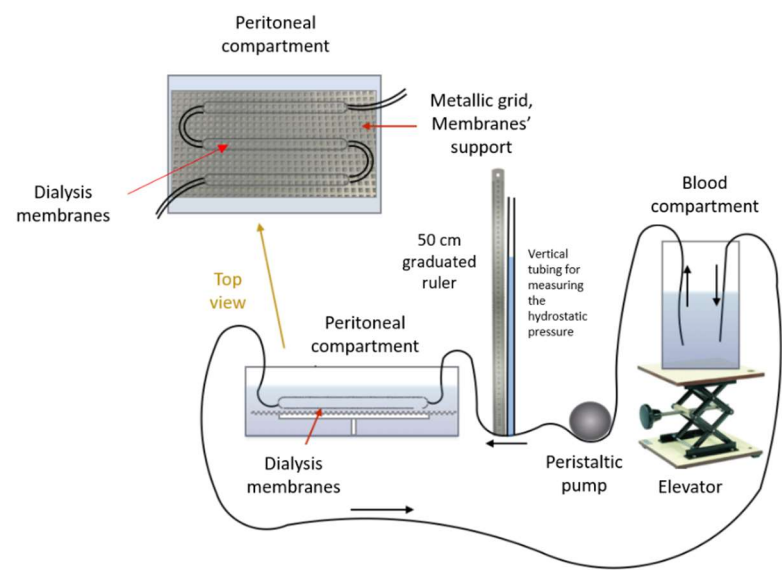
Scheme 4. *In vitro* model of peritoneal dialysis of Hautepierre hospital.

Table 18. Correspondence between the element in the model and its representation in human body.

Element in the model	Representation in human body
Dialysis membranes	Peritoneal capillaries
Blood compartment and tubes	Vessels
Elevator	Blood pressure regulators (hormones, etc.)
Peristaltic pump	Heart
Peritoneal compartment	Peritoneal cavity
Fluid in peritoneal compartment	Peritoneal fluid / dialysis fluid
Fluid in the blood compartment	Blood
Small molecular weight dye	Blood solutes (phosphates, creatinine, ions)
High molecular weight dye	Proteins that do not cross the peritoneum

We will briefly detail the components of this circuit.

Membranes

To simulate the peritoneal membrane, Pillods *et al.* used the tube-shaped cellulose dialysis membranes (SnakeSkin Dialysis Tubing, Thermo Fisher). These are usually used in chemistry to perform dialysis, allowing molecules to be selected/separated based on their molecular weight. Each membrane is characterized by a MWCO (molecular weight cut off), expressed in kilo Dalton (kDa) or Dalton (Da). This number represents the molecular weight for which 90% of the proteins are stopped by the membrane. In the PD model, the "blood solution" circulates in these dialysis tubes.

As explained in the general introduction, the capillaries are modeled by three sizes pores[76–78] and correspond to molecular weights cut off (MWCO). To choose the more representative cellulose dialysis membrane, next tables (Table 19 and Table 20) summarize different important factors to consider. Table 19 links the size of pores, the MWCO and its presence in percent in the peritoneum. Table 20 compares the commercial dialysis membranes and its match with the pores of peritoneum.

Table 19. Correspondence between the size of the pores of the peritoneum and the MWCO in molecular weight.[76]

Pore size in Angstrom (Å)	MWCO	Comments
2 to 4 (very small pores)	<200 Da	<1% of the pore surface corresponds to aquaporins.
40 to 55 (small pores)	Between 15 and 30 kDa	99% of the pore surface, 90% of water passage.
250 (large pores)	> 1000 kDa	0.01% of the pore surface.

Table 20. Correspondence between the MWCO of dialysis membranes by weight molecular size and pore size.

MWCO	Pore size (Å)	Comments
3.5 kDa	25	Size between very small pores and small pores.
10 kDa	30	Almost representative size small pores.
20 kDa	45	Representative of small pores.
25 kDa	49	Representative of small pores.

After analysis of the previous tables, the chosen membranes were 10 kDa to model the small pores because it represents 99% of peritoneum. The very small pores are not represented because they are only responsible for water transfer, nor large pores which are not involved in the exchanges.

Pression and Flow

To better simulate a PD, it is important to have, in the exchange areas, a pressure equivalent to the hydrostatic pressure of peritoneal vessels. Indeed, the osmotic pressure and the difference in concentration of a substance will condition the kinetics of this same substance.

To keep the model, the closest to the reality, the difference of hydrostatic pressure of the peritoneal membranes during dialysis, is equal to the pressure difference between peritoneal capillaries pressure and the peritoneal cavity one (when filled in an adult to approximately 1.5 ml/m², and for a children 600 ml/m² [79] of body surface area). In fact, the hydrostatic pressure of the capillaries is approximately 18 mmHg (24 cm of water).[77] For the peritoneal cavity pressure, in an adult is about 13 ± 3 cm of water (in children, this value becomes 5 cm). We therefore have a pressure difference of:

$$24 \text{ cm of } H_2O - 13 \text{ cm of } H_2O = 11 \text{ cm of } H_2O$$

In the *in vitro* PD model, the overpressure of the compartment peritoneal is zero (atmospheric pressure). To set the pressure / height, the relative height of the two compartments and the flow rate of the circulating fluid can be modified. To measure the pressure of hydrostatic fluid, an open tubing was placed, vertically juxtaposed to a 50 cm ruler whose 0 is located at the same height than the membranes (Figure 25). We then measure the pressure in cm of H_2O. To rest in real PD conditions, the pressure at the membranes must be about 11 cm of H_2O.

The blood flow of the peritoneal capillaries involved in exchanges during a PD is around 40 to 70 ml/min. [80] However, McGary *et al.* during experiments worked with flow rates of 150 ml/min. In the Hautepierre model, the flow is of the same magnitude.
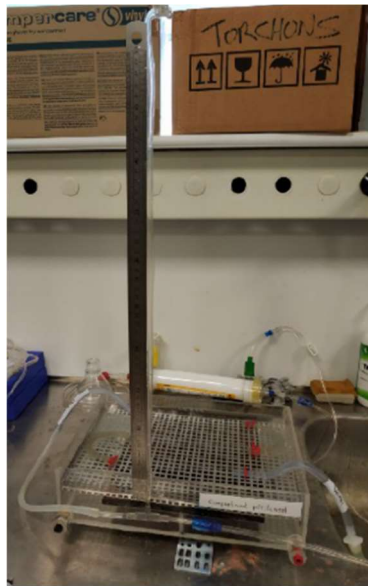

Figure 25. Vertical tubing for measuring the hydrostatic pressure

IV. 3. 3. 2. Experiments in the *in vitro* Peritoneal Dialysis model

In a first experiment in the model, Pillods *et al.* demonstrated the selectivity of the membrane pores. For that, a visual experiment showed that low molecular weight dye can freely cross the membrane, while a low molecular weight dye does not (Figure 26).

To represent the low molecular weight molecules (phosphates, urea…), methylene blue ($C_{16}H_{18}ClN_3S$) was chosen. To represent the big molecules proteins which are preserved in the "blood", bovine serum albumin (BSA) was labeled with fluorescein isothiocyanate (FITC). This set constitutes a colorant yellow. Both molecules were chosen because with the pore diameter of membranes, one of two (yellow dye) is not supposed to cross membranes.

Peritoneal dialysis (*in vitro*) was therefore carried out with the dyes in two separate routes (Figure 26). We introduced 500 ml into each blood compartment and 2.150 L into the peritoneal compartments. The flow rates were identical (320 ml/min), the relative height of the compartments and therefore the hydrostatic pressures similar. The effects of temperature and humidity were neglected since the experiments took place simultaneously.

After less than an hour, the blue dye had already slightly passed through. For the yellow dye, very slight leaks were observed at the junctions, however, this loss is not sufficient to color the water in the peritoneal compartment. The pumps were on during the day, with the same flow rate in each circuit. At night, the fluids were left stagnant.

Figure 26 represents about 500 ml of liquid recovered at the end of the experiment:

- In the BSA[FITC] circuit: liquid from the left peritoneal compartment and from the left blood compartment.
- In the methylene blue circuit: liquid from the left peritoneal compartment and from the left blood compartment.

In Figure 26, we can observe that the BSA[FITC] cannot pass through the membrane and methylene blue can. To avoid small lacks in the junctions a new prototype of junctions-membranes-pipes was set up. Before the experiments with RSN, the number of junctions was reduced. For that, Pillods *et al.* decided to use only one continuous membrane and only two junction areas (so, the number passes from eight to two, Figure 27). In addition, at the offsets, a flexible hose is introduced inside the membranes, this helps to maintain the shape and to prevent from a dramatic bending. Clamps (in white) are placed at the ends of the pipes to hold them. No coloration of the liquid in the peritoneal compartment confirms the impermeability of the route.
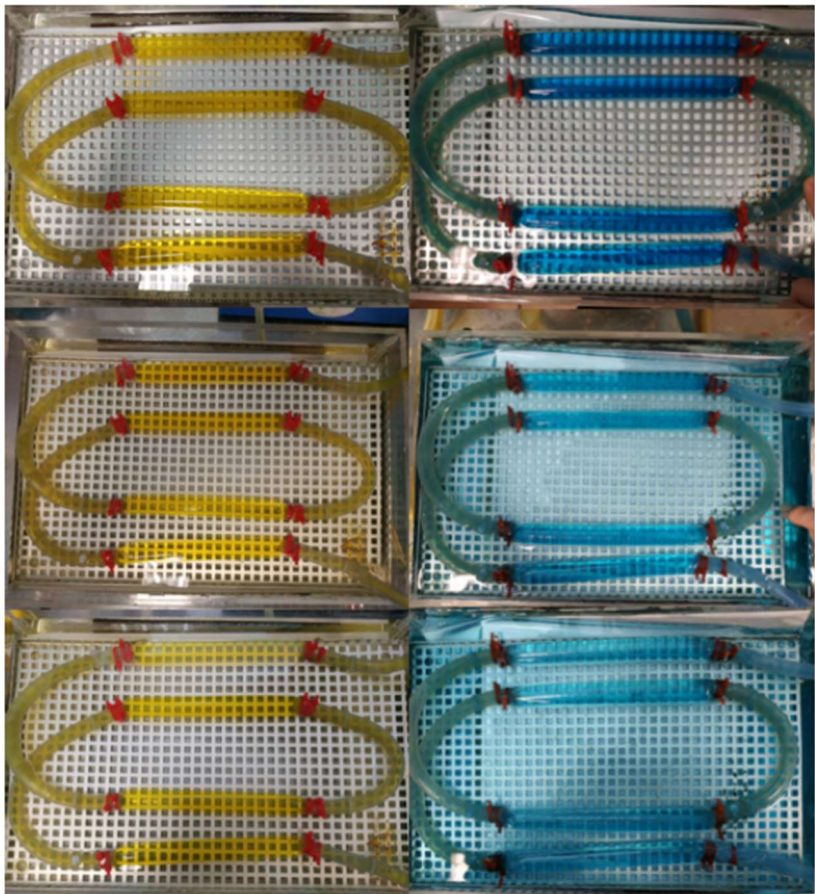

Figure 26. PHOTOS SHOWING THE GRADUAL EQUILIBRATION OF METHYLENE BLUE (RIGHT) OVER TIME IN opposition to BSA[FITC] (left).
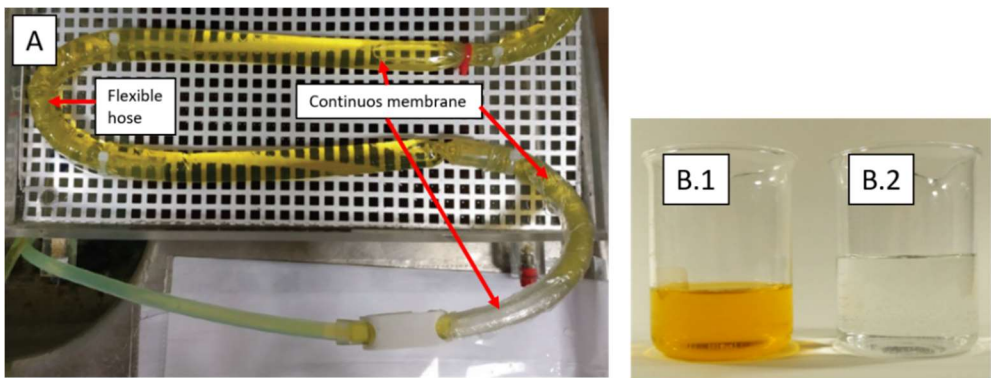

Figure 27. A. New prototype of junctions-membranes-pipes in the peritoneal compartment. B.1 BSA[FITC] solution in the blood system and in the B.2 peritoneal compartment.

Experiments with RSN

To test RSN in the *in vitro* PD model, two experiments in parallel were performed (Figure 28. A. Peritoneal compartment without RSN and B. with RSN in dialysis membranes.). For both, blood compartments contain 0.5 l of physiological with 16 P-mg/l de phosphate (pH 7). The peritoneal compartments contain 1.5 l of dialysis solution, the first is the control, the second contains the RSN divided and putted inside four dialysis tubes placed in the dialysis fluid. Other parameters (flow, hydrostatic pressure and temperature) were the same than before. Samples of the blood compartments were taken every hour for 4 hours. This time, samples were analyzed with a Dimension device Vista 2. Results are plotted in Figure 29.
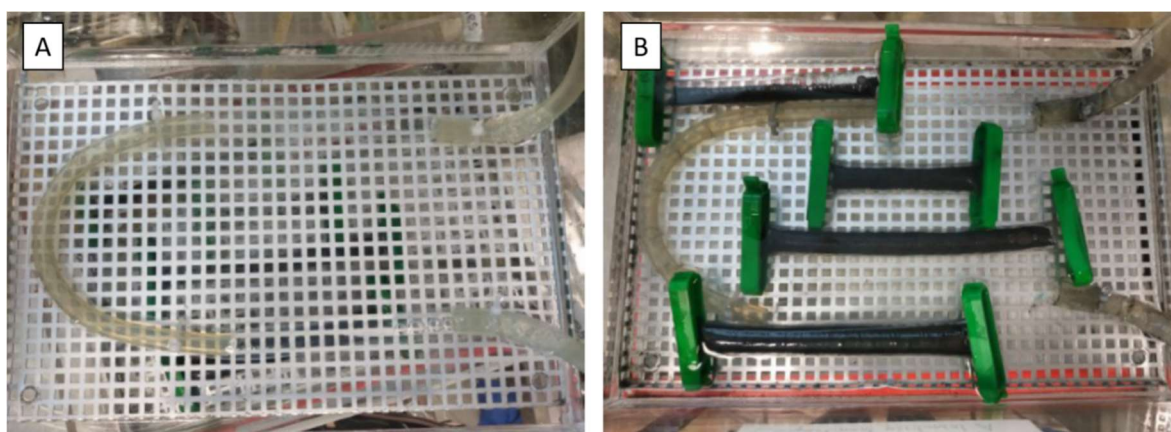
Figure 28. A. Peritoneal compartment without RSN and B. with RSN in dialysis membranes.
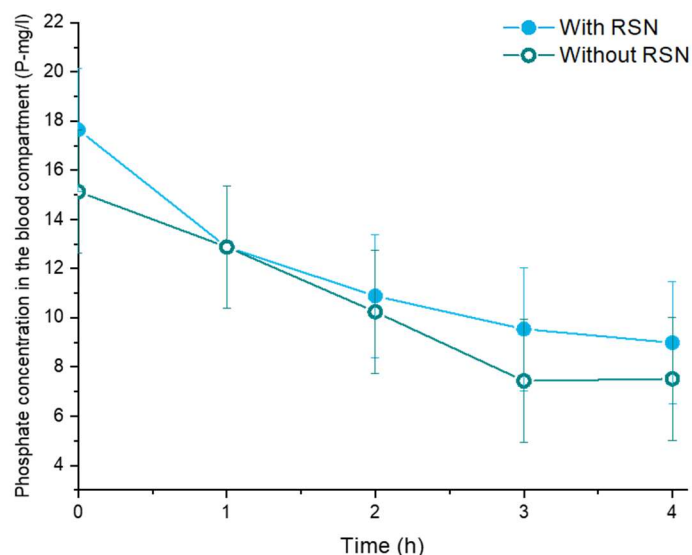
Figure 29. Results of the experiment with RSN in membranes: evolution of phosphorous concentration as a function of time.

For experiments with and without RSN, the concentration of phosphates passed from 17.7 P-mg/L to 8.9 P-mg/L. It corresponds to a reduction of 50 % of the concentration, so, we can confirm the previous experiments with dye which have successfully imitated the behavior of phosphates in the system: in the peritoneal compartment, phosphates pass from "blood" to the dialysis solution. Unfortunately, as Figure 29 shows, the experience with RSN inside membranes did not show high improvement for the phosphate

removal. Both curves follow the same variations in time, keeping similar values. To explain this, during the experiment, RSN were observed to sediment in the membranes of dialysis, contrary to the first capture experiments, this time, RSN have less mobility and were not constantly stirred to avoid the sedimentation. In a last experiment, to improve the PD with RSN, the RSN were dispersed in the peritoneal compartment (Figure 31). Moreover, to ensure a well dispersion of RSN, a stirring plate were added to the system (Figure 30, the route A is the control, the route B contains the RSN). The previous experimental conditions were conserved.
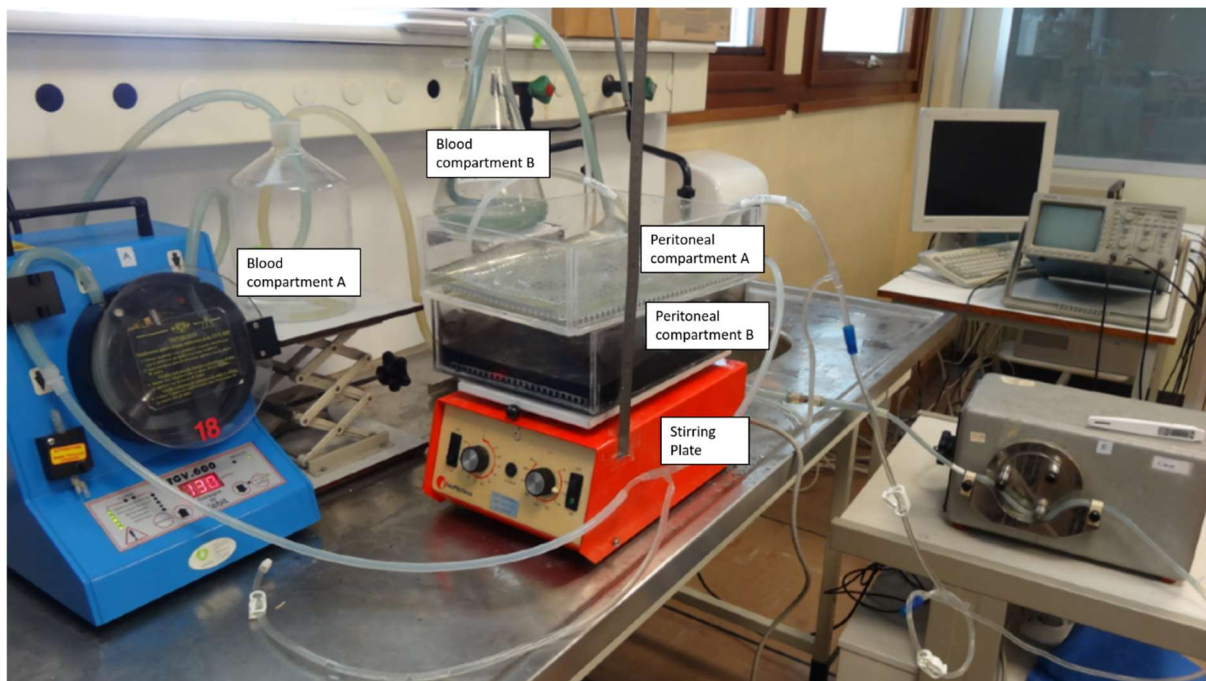
Figure 30. Route A: classical experimental conditions. Route B. experimental conditions with dialysis solution containing RSN.
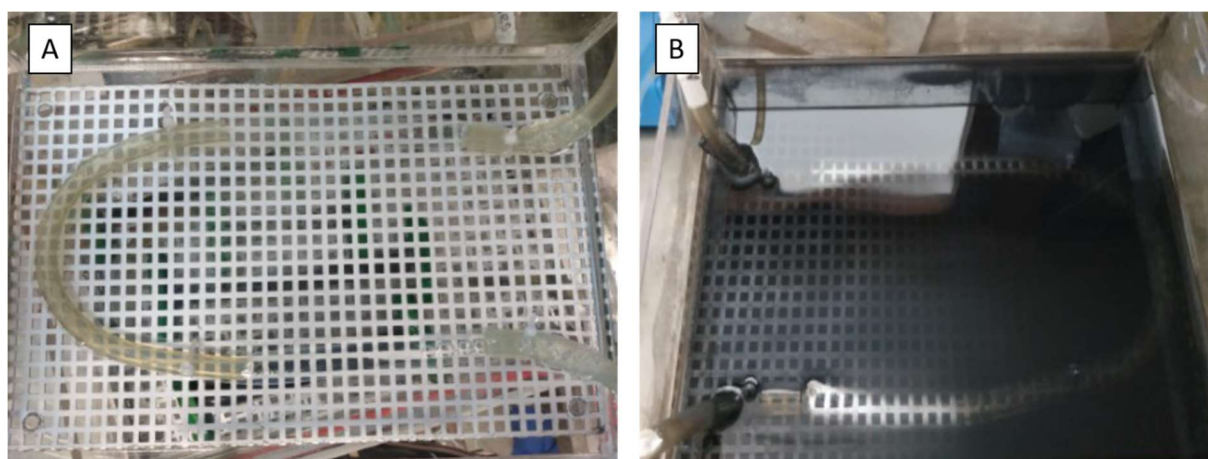
Figure 31. A. Peritoneal compartment without nanoparticles and B. with nanoparticles dispersed in compartment.

The experience with RSN did not show again an improvement of PD. This could be due to a heterogeneous dispersion of RSN in the dialysis solution. Contrary to the promising results of the RSN in tubes, PD is not improved with RSN, as before, both curves followed the same variations: a diminution of phosphate concentration of 50 % after 4 hours (Figure 32). To understand this result, we supposed that the concentration of RSN in the liquid was lower than for the experiments in tubes, or the phosphate

concentrations were very low. In both cases, it impacts the efficiency of the RSNs. During the realization of this collaboration, we faced some difficulties about vocabulary definitions between chemists and medical stuff. The most interesting difference was the word "phosphate", the heart of this study. Indeed, in order to facilitate the quantifications, in chemistry, the usual units are "P-mg/l", when in medicine are "mg/l", orally both groups called it "phosphates" until the moment when quantifications did not match. Indeed, due to a misunderstanding, the blood compartments were at 16 P-mg/l while the norm for phosphatemia is 30 to 45 P-mg/l in an adult. We were limited by low concentrations because the weight of RSN at our disposal was 2.5 g, which is enough to capture 8 mg of phosphorus (at pH 7). Nevertheless, for the low concentrations used, maybe the variations of concentration were small compared to the confidence interval of the measurements by the analyzer.

Figure 32. Results of the experiment with nanoparticles dispersed in the dialysis solution: evolution of phosphorous concentration as a function of time.

Conclusion

Diagnosed patients with chronical or end-stage renal failure cannot naturally level the concentration of certain ions or molecules in their blood (Chapter I). Among them, phosphate is one of the most dangerous and is generally in excess. Among 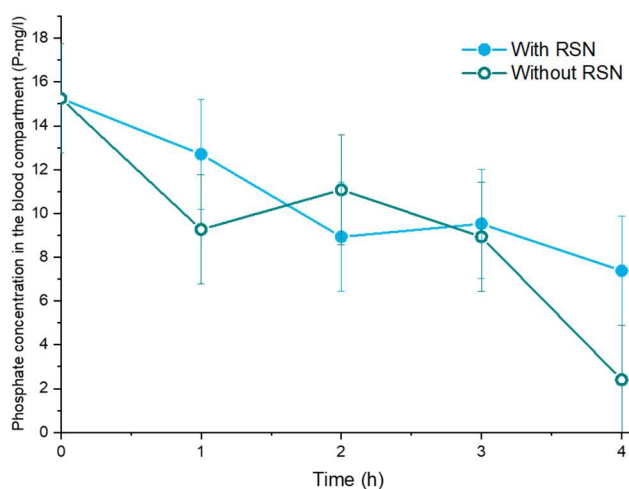treatment to purify the blood, one promising is the peritoneal dialysis which is less efficient than the classical one hemodialysis but presents many advantages as more comfortable for patients and more suitable for children and new-born babies. This study investigates the use of iron oxide nanostructures as an adsorbent to improve the phosphate removal in this treatment. The synthesis of iron oxide and aluminum-doped ferrite raspberry-shaped nanostructures (RSN and Al-RSN) was optimized using a solvothermal-polyol method. We demonstrated thus the impact of synthesis parameters such as the nature of the iron precursor, the reaction time and the mixing/solubilisation step. Then, the phosphate removal properties of these nanostructures were tested by studying their adsorption capacity and kinetics.

The RSN showed great affinity for phosphate with a maximum adsorption capacity of 4.1 P-mg/g (pH 7) and 8.8 P-mg/g (pH 3). Additional tests in the dialysis solution demonstrated that the adsorption was selective. Indeed, the presence of other cations and organic molecules in dialysate did not interfere with the phosphate adsorption efficacy.

The Al-RSN allowed a higher enhancement of adsorption capacity with 10 P-mg/g (pH 7) and 15.5 P-mg/g (pH 3). The Al doping shifts the IEP of RSN and allows thus favorable electrostatic interactions. In addition, the surface specific area of Al-RSN is higher.

In addition, it was demonstrated that the phosphate maximum absorption was reached in less than 3 hours for both undoped and Al doped RSN. These overall results showed that such nanostructures are promising for the phosphate removal in the peritoneal dialysis treatment.

Finally, an in vitro model set-up was designed and constructed by the group of Dr. Philippe Choquet (Hautepierre Hospital, Strasbourg, France). Preliminary tests were performed to test the RSN efficacy in simulated conditions of peritoneal dialysis treatment. Further experiments are needed to optimize the device and compare our RSN in *in vitro* conditions.

References

(1)   Elias, R. M.; Alvares, V. R. C.; Moysés, R. M. A. Phosphate Removal During Conventional Hemodialysis: A Decades-Old Misconception. *KBR* **2018**, *43* (1), 110–114.

(2)   Kuhlmann, M. K. Phosphate Elimination in Modalities of Hemodialysis and Peritoneal Dialysis. *Blood Purif.* **2010**, *29* (2), 137–144.

(3)   Li, M.; Liu, J.; Xu, Y.; Qian, G. Phosphate Adsorption on Metal Oxides and Metal Hydroxides: A Comparative Review. *Environ. Rev.* **2016**, *24* (3), 319–332.

(4)   Li, M.; Liu, H.; Chen, T.; Wei, L.; Wang, C.; Hu, W.; Wang, H. The Transformation of α-(Al, Fe)OOH in Natural Fire: Effect of Al Substitution Amount on Fixation of Phosphate. *Chemical Geology* **2019**, *524*, 368–382.

(5)   Shahid, M. K.; Kim, Y.; Choi, Y.-G. Magnetite Synthesis Using Iron Oxide Waste and Its Application for Phosphate Adsorption with Column and Batch Reactors. *Chemical Engineering Research and Design* **2019**, *148*, 169–179.

(6)   Lalley, J.; Han, C.; Li, X.; Dionysiou, D. D.; Nadagouda, M. N. Phosphate Adsorption Using Modified Iron Oxide-Based Sorbents in Lake Water: Kinetics, Equilibrium, and Column Tests. *Chemical Engineering Journal* **2016**, *284*, 1386–1396.

(7)   Gerber, O.; Pichon, B. P.; Ihiawakrim, D.; Florea, I.; Moldovan, S.; Ersen, O.; Begin, D.; Grenèche, J.-M.; Lemonnier, S.; Barraud, E.; Begin-Colin, S. Synthesis Engineering of Iron Oxide Raspberry-Shaped Nanostructures. *Nanoscale* **2016**, *9* (1), 305–313.

(8)   Yan, L.; Yang, K.; Shan, R.; Yan, T.; Wei, J.; Yu, S.; Yu, H.; Du, B. Kinetic, Isotherm and Thermodynamic Investigations of Phosphate Adsorption onto Core–Shell Fe3O4@LDHs Composites with Easy Magnetic Separation Assistance. *Journal of Colloid and Interface Science* **2015**, *448*, 508–516.

(9)   Su, Y.; Yang, W.; Sun, W.; Li, Q.; Shang, J. K. Synthesis of Mesoporous Cerium–Zirconium Binary Oxide Nanoadsorbents by a Solvothermal Process and Their Effective Adsorption of Phosphate from Water. *Chemical Engineering Journal* **2015**, *268*, 270–279.

(10)   Lai, L.; Xie, Q.; Chi, L.; Gu, W.; Wu, D. Adsorption of Phosphate from Water by Easily Separable Fe3O4@SiO2 Core/Shell Magnetic Nanoparticles Functionalized with Hydrous Lanthanum Oxide. *Journal of Colloid and Interface Science* **2016**, *465*, 76–82.

(11)   Gerber, O.; Bégin-Colin, S.; Pichon, B. P.; Barraud, E.; Lemonnier, S.; Pham-Huu, C.; Daffos, B.; Simon, P.; Come, J.; Bégin, D. Design of Fe3–XO4 Raspberry Decorated Graphene Nanocomposites with High Performances in Lithium-Ion Battery. *Journal of Energy Chemistry* **2016**, *25* (2), 272–277.

(12)   Nguyen, X. S.; Zhang, G.; Yang, X. Mesocrystalline Zn-Doped Fe3O4 Hollow Submicrospheres: Formation Mechanism and Enhanced Photo-Fenton Catalytic Performance. *ACS Applied Materials & Interfaces* **2017**, *9* (10), 8900–8909.

(13)   Gerber, O.; Pichon, B. P.; Ulhaq, C.; Grenèche, J.-M.; Lefevre, C.; Florea, I.; Ersen, O.; Begin, D.; Lemonnier, S.; Barraud, E.; Begin-Colin, S. Low Oxidation State and Enhanced Magnetic Properties Induced by Raspberry Shaped Nanostructures of Iron Oxide. *J. Phys. Chem. C* **2015**, *119* (43), 24665–24673.

(14)   Tartaj, P.; Morales, M. a del P.; Veintemillas-Verdaguer, S.; o, T. G. lez-Carre; Serna, C. J. The Preparation of Magnetic Nanoparticles for Applications in Biomedicine. *J. Phys. D: Appl. Phys.* **2003**, *36* (13), R182–R197.

(15)   Nakamoto, K. *Infrared and Raman Spectra of Inorganic and Coordination Compounds*, 4th ed.; John Willey and Sons: New York, 1986.

(16)   Daou, T. J.; Pourroy, G.; Bégin-Colin, S.; Grenèche, J. M.; Ulhaq-Bouillet, C.; Legaré, P.; Bernhardt, P.; Leuvrey, C.; Rogez, G. Hydrothermal Synthesis of Monodisperse Magnetite Nanoparticles. *Chem. Mater.* **2006**, *18* (18), 4399–4404.

(17)   Baaziz, W.; Pichon, B. P.; Fleutot, S.; Liu, Y.; Lefevre, C.; Greneche, J.-M.; Toumi, M.; Mhiri, T.; Begin-Colin, S. Magnetic Iron Oxide Nanoparticles: Reproducible Tuning of the Size and Nanosized-Dependent Composition, Defects, and Spin Canting. *J. Phys. Chem. C* **2014**, *118* (7), 3795–3810.

(18)   Jolivet, J.-P.; Henry, M. *De la solution à l'oxyde - Condensation des cations en solution aqueuse. Chimie de surface des oxyde*; EDP Sciences, 1994.

(19)   Ammar, S.; Helfen, A.; Jouini, N.; Fiévet, F.; Rosenman, I.; Villain, F.; Molinié, P.; Danot, M. Magnetic Properties of Ultrafine Cobalt Ferrite Particles Synthesized by Hydrolysis in a Polyol MediumBasis of a Presentation given at Materials Discussion No. 3, 26–29 September, 2000, University of Cambridge, UK. *Journal of Materials Chemistry* **2001**, *11* (1), 186–192.

(20)   Feldmann, C.; Jungk, H.-O. Polyol-Mediated Preparation of Nanoscale Oxide Particles. *Angewandte Chemie International Edition* **2001**, *40* (2), 359–362.

(21)   Cao, S.-W.; Zhu, Y.-J.; Chang, J. Fe3O4 Polyhedral Nanoparticles with a High Magnetization Synthesized in Mixed Solvent Ethylene Glycol–Water System. *New J. Chem.* **2008**, *32* (9), 1526–1530.

(22)   Yu, D.; Sun, X.; Zou, J.; Wang, Z.; Wang, F.; Tang, K. Oriented Assembly of Fe3O4 Nanoparticles into Monodisperse Hollow Single-Crystal Microspheres. *J. Phys. Chem. B* **2006**, *110* (43), 21667–21671.

(23)   Ueda, M.; Ikeda, A. Effect of Microstructure and Cr Content in Steel on CO2 Corrosion. *NACE, Houston, TX* **1996**, *CORROSION*.

(24)   Li, W.; Qiao, X.; Zheng, Q.; Zhang, T. One-Step Synthesis of MFe2O4 (M=Fe, Co) Hollow Spheres by Template-Free Solvothermal Method. *Journal of Alloys and Compounds* **2011**, *509* (21), 6206–6211.

(25)   Lind, M. D. Crystal Structure of Ferric Chloride Hexahydrate. *J. Chem. Phys.* **1967**, *47* (3), 990–993.

(26)   Louvain, N.; Fakhry, A.; Bonnet, P.; El-Ghozzi, M.; Guérin, K.; Sougrati, M.-T.; Jumas, J.-C.; Willmann, P. One-Shot versus Stepwise Gas–Solid Synthesis of Iron Trifluoride: Investigation of Pure Molecular F2 Fluorination of Chloride Precursors. *CrystEngComm* **2013**, *15* (18), 3664–3671.

(27)   Perton, F. Architecture de Nanoparticules Hybrides Pour Une Imagerie et/Ou Thérapie Multimodales. Thèse, Strasbourg, 2016.

(28)   Guzman, A.; Zuazo, I.; Feller, A.; Olindo, R.; Sievers, C.; Lercher, J. A. On the Formation of the Acid Sites in Lanthanum Exchanged X Zeolites Used for Isobutane/Cis-2-Butene Alkylation. *Microporous and Mesoporous Materials* **2005**, *83* (1), 309–318.

(29)   Yassin, F. A.; El Kady, F. Y.; Ahmed, H. S.; Mohamed, L. K.; Shaban, S. A.; Elfadaly, A. K. Highly Effective Ionic Liquids for Biodiesel Production from Waste Vegetable Oils. *Egyptian Journal of Petroleum* **2015**, *24* (1), 103–111.

(30)   Capeletti, L. B.; Zimnoch, J. H. Fourier Transform Infrared and Raman Characterization of Silica-Based Materials. *Applications of Molecular Spectroscopy to Current Research in the Chemical and Biological Sciences* **2016**.

(31)   Scardera, G.; Puzzer, T.; Conibeer, G.; Green, M. A. Fourier Transform Infrared Spectroscopy of Annealed Silicon-Rich Silicon Nitride Thin Films. *Journal of Applied Physics* **2008**, *104* (10), 104310.

(32)   Müller, M.; Villalba, J. C.; Anaissi, F. J. Thermal Decomposition (TG-DTA) of Iron Salts [FeCl3.6H2O] and [Fe(NO3)3.9H2O] with Morphologic and Chemical Analysis of Final Product. *Semina: Ciências Exatas e Tecnológicas* **2014**, *35* (1), 9–14.

(33)   Kingery, W. D.; Uhlmann, D. R.; Bowen, H. K. *Introduction to Ceramics*, 2nd ed.; New York : Wiley, 1976.

(34)   Kavas, H.; Baykal, A.; Toprak, M. S.; Köseoğlu, Y.; Sertkol, M.; Aktaş, B. Cation Distribution and Magnetic Properties of Zn Doped NiFe2O4 Nanoparticles Synthesized by PEG-Assisted Hydrothermal Route. *Journal of Alloys and Compounds* **2009**, *479* (1), 49–55.

(35)   Kremenović, A.; Antić, B.; Vulić, P.; Blanuša, J.; Tomic, A. ZnFe2O4 Antiferromagnetic Structure Redetermination. *Journal of Magnetism and Magnetic Materials* **2017**, *426*, 264–266.

(36)   Mohamed, R. M.; Rashad, M. M.; Haraz, F. A.; Sigmund, W. Structure and Magnetic Properties of Nanocrystalline Cobalt Ferrite Powders Synthesized Using Organic Acid Precursor Method. *Journal of Magnetism and Magnetic Materials* **2010**, *322* (14), 2058–2064.

(37)   Swatsitang, E.; Phokha, S.; Hunpratub, S.; Usher, B.; Bootchanont, A.; Maensiri, S.; Chindaprasirt, P. Characterization and Magnetic Properties of Cobalt Ferrite Nanoparticles. *Journal of Alloys and Compounds* **2016**, *664*, 792–797.

(38)   Ma, J.; Zhao, J.; Li, W.; Zhang, S.; Tian, Z.; Basov, S. Preparation of Cobalt Ferrite Nanoparticles via a Novel Solvothermal Approach Using Divalent Iron Salt as Precursors. *Materials Research Bulletin* **2013**, *48* (2), 214–217.

(39)   Chakroune, N.; Viau, G.; Ammar, S.; Jouini, N.; Gredin, P.; Vaulay, M. J.; Fiévet, F. Synthesis, Characterization and Magnetic Properties of Disk-Shaped Particles of a Cobalt Alkoxide: CoII(C2H4O2). *New J. Chem.* **2005**, *29* (2), 355–361.

(40)   Baaziz, W. Synthèse et Caractérisation Des Nanoparticules Spinelles et Coeur-Coquille à Base d'oxyde de Fer et de Cobalt. These de doctorat, Strasbourg, 2011.

(41)   Amiri, S.; Shokrollahi, H. The Role of Cobalt Ferrite Magnetic Nanoparticles in Medical Science. *Materials Science and Engineering: C* **2013**, *33* (1), 1–8.

(42)   Aghazadeh, M.; Karimzadeh, I.; Reza Ganjali, M.; Malekinezhad, A. Al3+ Doped Fe3O4 Nanoparticles: A Novel Preparation Method, Structural, Magnetic and Electrochemical Characterizations. *Int. J. Electrochem. Sci.* **2017**, *12*, 8033–8044.

(43)   Ehsani, M. H.; Esmaeili, S.; Aghazadeh, M.; Kameli, P.; Tehrani, F. S.; Karimzadeh, I. An Investigation on the Impact of Al Doping on the Structural and Magnetic Properties of Fe3O4 Nanoparticles. *Appl. Phys. A* **2019**, *125* (4), 280. https://doi.org/10.1007/s00339-019-2572-2.

(44)   Xu, J.; Luu, L.; Tang, Y. Phosphate Removal Using Aluminum-Doped Magnetic Nanoparticles. *Desalination and water treatment* **2017**, *58*.

(45)   Schaefer, B.; Bartosova, M.; Macher-Goeppinger, S.; Sallay, P.; Vörös, P.; Ranchin, B.; Vondrak, K.; Ariceta, G.; Zaloszyc, A.; Bayazit, A. K.; Querfeld, U.; Cerkauskiene, R.; Testa, S.; Taylan, C.; VandeWalle, J.; Yap, Y.; Krmar, R. T.; Büscher, R.; Mühlig, A. K.; Drozdz, D.; Caliskan, S.; Lasitschka, F.; Fathallah-Shaykh, S.; Verrina, E.; Klaus, G.; Arbeiter, K.; Bhayadia, R.; Melk, A.; Romero, P.; Warady, B. A.; Schaefer, F.; Ujszaszi,

A.; Schmitt, C. P. Neutral PH and Low–Glucose Degradation Product Dialysis Fluids Induce Major Early Alterations of the Peritoneal Membrane in Children on Peritoneal Dialysis. *Kidney International* **2018**, *94*

(46)   Daou, T. J. Synthèse et Fonctionnalisation de Nanoparticules d'oxydes de Fer Magnétiques. Thesis, Strasbourg 1, 2007.

(47)   Illés, E.; Tombácz, E. The Effect of Humic Acid Adsorption on PH-Dependent Surface Charging and Aggregation of Magnetite Nanoparticles. *JCIS* **2006**, *295* (1), 115–123.

(48)   Mezenner, N. Y.; Bensmaili, A. Kinetics and Thermodynamic Study of Phosphate Adsorption on Iron Hydroxide-Eggshell Waste. *Chemical Engineering Journal* **2009**, *147* (2), 87–96.

(49)   Netzahuatl-Muñoz, A. R.; Cristiani-Urbina, M. del C.; Cristiani-Urbina, E. Chromium Biosorption from Cr(VI) Aqueous Solutions by Cupressus Lusitanica Bark: Kinetics, Equilibrium and Thermodynamic Studies. *PLoS ONE* **2015**, *10* (9), e0137086.

(50)   Febrianto, J.; Kosasih, A. N.; Sunarso, J.; Ju, Y.-H.; Indraswati, N.; Ismadji, S. Equilibrium and Kinetic Studies in Adsorption of Heavy Metals Using Biosorbent: A Summary of Recent Studies. *J. Hazard. Mater.* **2009**, *162* (2–3), 616–645.

(51)   Azimvand, J.; Didehban, K.; Mirshokraie, S. Safranin-O Removal from Aqueous Solutions Using Lignin Nanoparticle-g-Polyacrylic Acid Adsorbent: Synthesis, Properties, and Application. *Adsorption Science & Technology* **2018**, *36* (7–8), 1422–1440.

(52)   Long, F.; Gong, J.-L.; Zeng, G.-M.; Chen, L.; Wang, X.-Y.; Deng, J.-H.; Niu, Q.-Y.; Zhang, H.-Y.; Zhang, X.-R. Removal of Phosphate from Aqueous Solution by Magnetic Fe–Zr Binary Oxide. *Chemical Engineering Journal* **2011**, *171* (2), 448–455.

(53)   Nur, T.; Johir, M. A. H.; Loganathan, P.; Nguyen, T.; Vigneswaran, S.; Kandasamy, J. Phosphate Removal from Water Using an Iron Oxide Impregnated Strong Base Anion Exchange Resin. *Journal of Industrial and Engineering Chemistry* **2014**, *20* (4), 1301–1307.

(54)   You, X.; Farran, A.; Guaya, D.; Valderrama, C.; Soldatov, V.; Cortina, J. L. Phosphate Removal from Aqueous Solutions Using a Hybrid Fibrous Exchanger Containing Hydrated Ferric Oxide Nanoparticles. *Journal of Environmental Chemical Engineering* **2016**, *4* (1), 388–397.

(55)   Wiriyathamcharoen, S.; Sarkar, S.; Jiemvarangkul, P.; Nguyen, T. T.; Klysubun, W.; Padungthon, S. Synthesis Optimization of Hybrid Anion Exchanger Containing Triethylamine Functional Groups and Hydrated Fe(III) Oxide Nanoparticles for Simultaneous Nitrate and Phosphate Removal. *Chemical Engineering Journal* **2020**, *381*, 122671.

(56)   Yoon, S.-Y.; Lee, C.-G.; Park, J.-A.; Kim, J.-H.; Kim, S.-B.; Lee, S.-H.; Choi, J.-W. Kinetic, Equilibrium and Thermodynamic Studies for Phosphate Adsorption to Magnetic Iron Oxide Nanoparticles. *Chemical Engineering Journal* **2014**, *236*, 341–347.

(57)   Zeng, L.; Li, X.; Liu, J. Adsorptive Removal of Phosphate from Aqueous Solutions Using Iron Oxide Tailings. *Water Research* **2004**, *38* (5), 1318–1326.

(58)   Cao, D.; Jin, X.; Gan, L.; Wang, T.; Chen, Z. Removal of Phosphate Using Iron Oxide Nanoparticles Synthesized by Eucalyptus Leaf Extract in the Presence of CTAB Surfactant. *Chemosphere* **2016**, *159*, 23–31.

(59)   Ajmal, Z.; Muhmood, A.; Usman, M.; Kizito, S.; Lu, J.; Dong, R.; Wu, S. Phosphate Removal from Aqueous Solution Using Iron Oxides: Adsorption, Desorption and Regeneration Characteristics. *Journal of Colloid and Interface Science* **2018**, *528*, 145–155.

(60)   Daou, T. J.; Begin-Colin, S.; Grenèche, J. M.; Thomas, F.; Derory, A.; Bernhardt, P.; Legaré, P.; Pourroy, G. Phosphate Adsorption Properties of Magnetite-Based Nanoparticles. *Chem. Mater.* **2007**, *19* (18), 4494–4505.

(61)   Hawke, D.; Carpenter, P. D.; Hunter, K. A. Competitive Adsorption of Phosphate on Goethite in Marine Electrolytes. *Environ. Sci. Technol* **1989**, *23* (2), 187–191.

(62)   Tanada, S.; Kabayama, M.; Kawasaki, N.; Sakiyama, T.; Nakamura, T.; Araki, M.; Tamura, T. Removal of Phosphate by Aluminum Oxide Hydroxide. *Journal of Colloid and Interface Science* **2003**, *257* (1), 135–140.

(63)   Yao, W.; Millero, F. J. Adsorption of Phosphate on Manganese Dioxide in Seawater. *Environ. Sci. Technol.* **1996**, *30* (2), 536–541.

(64)   Adsorption Equilibrium, Kinetics and Thermodynamics of Methylene Blue from Aqueous Solutions Using Date Palm Leaves. *Energy Procedia* **2013**, *36*, 898–907.

(65)   Guerra-López, J.; González, R.; Gómez, A.; Pomés, R.; Punte, G.; Della Védova, C. O. Effects of Nickel on Calcium Phosphate Formation. *Journal of Solid State Chemistry* **2000**, *151* (2), 163–169.

(66)   Tejedor-Tejedor, M. I.; Anderson, M. A. The Protonation of Phosphate on the Surface of Goethite as Studied by CIR-FTIR and Electrophoretic Mobility. *Langmuir* **1990**, *6* (3), 602–611.

(67)   Li, L.; Stanforth, R. Distinguishing Adsorption and Surface Precipitation of Phosphate on Goethite (α-FeOOH). *JCIS* **2000**, *230* (1), 12–21.

(68)   Guerrero, G.; Mutin, P. H.; Vioux, A. Anchoring of Phosphonate and Phosphinate Coupling Molecules on Titania Particles. *Chem. Mater.* **2001**, *13* (11), 4367–4373.

(69)   Mor, S.; Chhoden, K.; Negi, P.; Ravindra, K. Utilization of Nano-Alumina and Activated Charcoal for Phosphate Removal from Wastewater. *Environmental Nanotechnology, Monitoring & Management* **2017**, *7*, 15–23.

(70)   Sousa, A. F. de; Braga, T. P.; Gomes, E. C. C.; Valentini, A.; Longhinotti, E. Adsorption of Phosphate Using Mesoporous Spheres Containing Iron and Aluminum Oxide. *Chemical Engineering Journal* **2012**, *210*, 143–149.

(71)   Guerrero, G.; Mutin, P. H.; Vioux, A. Anchoring of Phosphonate and Phosphinate Coupling Molecules on Titania Particles. *Chem. Mater.* **2001**, *13* (11), 4367–4373.

(72)   Tronc, E.; Ezzir, A.; Cherkaoui, R.; Chanéac, C.; Noguès, M.; Kachkachi, H.; Fiorani, D.; Testa, A. M.; Grenèche, J. M.; Jolivet, J. P. Surface-Related Properties of γ-Fe2O3 Nanoparticles. *Journal of Magnetism and Magnetic Materials* **2000**, *221* (1), 63–79.

(73)   Bruce, I. J.; Taylor, J.; Todd, M.; Davies, M. J.; Borioni, E.; Sangregorio, C.; Sen, T. Synthesis, Characterisation and Application of Silica-Magnetite Nanocomposites. *Journal of Magnetism and Magnetic Materials* **2004**, *284*, 145–160.

(74)   McGary, T. J.; Nolph, K. D.; Moore, H. L.; Kartinos, N. J. Polycation as an Alternative Osmotic Agent and Phosphate Binder in Peritoneal Dialysis. *Uremia Investigation* **2009**, *8* (2), 79–84.

(75)   Bajo, M. A.; Pérez-Lozano, M. L.; Albar-Vizcaino, P.; del Peso, G.; Castro, M.-J.; Gonzalez-Mateo, G.; Fernández-Perpén, A.; Aguilera, A.; Sánchez-Villanueva, R.; Sánchez-Tomero, J. A.; López-Cabrera, M.; Peter, M. E.; Passlick-Deetjen, J.; Selgas, R. Low-GDP Peritoneal Dialysis Fluid ('balance') Has Less Impact in Vitro and Ex Vivo on Epithelial-to-Mesenchymal Transition (EMT) of Mesothelial Cells than a Standard Fluid. *Nephrol. Dial. Transplant.* **2011**, *26* (1), 282–291.

(76)   Rippe, B. A Three-Pore Model of Peritoneal Transport. *Perit Dial Int* **1993**, *13 Suppl 2*, S35-38.

(77)   *The Textbook of Peritoneal Dialysis*; Gokal, R., Nolph, K. D., Eds.; Springer Netherlands, 1994.

(78)   Waniewski, J. Mathematical Modeling of Fluid and Solute Transport in Hemodialysis and Peritoneal Dialysis. *Journal of Membrane Science* **2006**, *274* (1), 24–37.

(79)   Fischbach, M.; Warady, B. A. Peritoneal Dialysis Prescription in Children: Bedside Principles for Optimal Practice. *Pediatr Nephrol* **2009**, *24* (9), 1633–1642.

(80)   Bazaev, N. A.; Grinval'd, V. M.; Selishchev, S. V.; Strokov, A. G. A Wearable Device for Low-Flow Detoxification of Human Body by Peritoneal Dialysis. *Biomed Eng* **2018**, *52* (3), 147–151.

Chapter V
DEPOLLUTION PERSPECTIVE

The nanomaterials, that we have developed during this PhD research project, could be also re-used/developed for depollution applications. Therefore, we have further designed them by adapting their functionalization or by combining them with other materials for pollutants removal applications.

V.1 Design of core-shell (RSN@STMS) composite materials

In order to facilitate the removal of functionalized stellate mesoporous silica (STMS) from any media, the strategy could be to pair STMS with a magnetic compound. In fact, we showed in the previous chapter that raspberry shaped nanostructures (RSN) display a high saturation magnetization and a superparamagnetic behavior which is essential to ensure a good colloidal stability of RSN suspension. To be able to extract easily functionalized STMS from liquid media, we have investigated the coating of RSN by a mesoporous silica shell and thus designed a core@shell (RSN@STMS) composite material. At first, we have considered the MS coating methods developed for iron oxide nanoparticles (IONPs), then selected a method and performed coating experiments of RSN.

V. 1. 1. MS coating methods of RSN

The first encapsulation of IONPs made by thermal decomposition within MS shells was reported 12 years ago by the team of Pr. Hyeon *et al.* [1] In this procedure, IONPs are capped with oleic acid and dispersed in chloroform. To this solution, an aqueous solution of CTAB was added. The CTAB surfactant not only ensured the water-phase transfer of the hydrophobic NPs by forming a double shell around oleic acid coated IONPs but also allowed the generation of micelles acting as templates (or structure directing agents) for the build-up of the resulting MS network. Under aqueous basic conditions and upon addition of TEOS precursor, mesoporous silica with ordered porous structure formed around the positively charged CTAB coated IONPs and around the templating micelles.

Also in 2008, Deng and Zhao[2] described for the first time the coating of a mesoporous silica shell around iron oxide nanoclusters (NC) (300 nm diameter made of 15 nm IONPs). In a first step, the authors deposited a non-porous silica shell (nSiO2, 20 nm thickness) by a classical sol-gel process on acidified NC. Then, they formed a mesoporous silica (MS) shell (70 nm) by a sol-gel modified procedure in the presence of CTAB surfactant as a pore structuring agent. After CTAB extraction in acetone, NC@nSiO2@MS (500 nm size, 2.3 nm pore size, 365 m²·g^{-1} and 0.29 cm³·g^{-1}) composite particles were obtained. Perpendicular orientation of the aligned mesopores were interestingly formed. The authors explained it by a minimization of surface energy of the CTAB/silicate rod like complexes. About magnetic properties, the silica coating was shown to decrease their M_S from 80.7 to 53.3 emu·g^{-1}. Despite of this lower value, the magnetization saturation remained high enough to ensure a strong and rapid magnetic response to an external applied magnetic field. In this work, these NC@nSiO2@MS were used as adsorbents for a rapid magnetic removal in solution of microcystins, a family of disocyclic

heptapeptides (1000 Da) and well-known for their high toxicity. After this work, other groups also used the strategy of a "modified sol-gel process" to coat a mesoporous silica shell and new protocols emerged. In Table 1, the different published methods to coat a mesoporous silica shell around IO nanoclusters synthesized by a polyol process are reported.

Table 1. Different reported methods to coat nanoclusters with a silica shell.

Ref.	Material	Surface/treatment of the IO nanoclusters	Silica coating method	Silica precursor	Surfactant	Size (nm)	Magnetic properties (Ms in emu·g⁻¹)	Specific surface area (m²·g⁻¹)
2	NC@nSiO$_2$	Acidification of the surface	Sol-gel process		/	370	/	/
	NC@nSiO$_2$@MS	Silica non-porous shell	Sol-gel process		CTAB	480	53.3	365
3	NC@nSiO$_2$	Citration of the surface	Sol-gel process		/	200	/	/
	NC@nSiO$_2$@MS	Silica non-porous shell	Oil-in-water		CTAC	400 nm	~15.2	396
4	NC@nSiO$_2$	Acidification of the surface	Sol-gel process	TEOS	/	/	/	/
	NC@nSiO$_2$@MS	Silica non-porous shell	Sol-gel process		CTAB	360	45.9	378
5	NC@Resorcinol@MS	Resorcinol	Oil-in-water		CTAB	460-860	/	460 nm : 623
6	NC@MS	EDTA (?)	Oil-in-water		CTAB	150	30	456
7	NC@MS	EDTA (?)	Oil-in-water		CTAB	470	35.6	526
8	NC@MS	Citration of the surface	Oil-in-water		CTAB	324	/	265

The control of large pore size MS shell and their perpendicular orientation to the surface around magnetic IO nanoclusters is quite recent (since 2013) and still remains an important objective. Probably, the most advanced research team for such systems is the group of Pr. Dongyuan Zhao[9]. In 2015, magnetic nanoclusters are covered with a non-porous silica shell (NC@nSiO$_2$) to facilitate the deposition of the mesoporous silica shell. Then, a large pore mesoporous silica shell with radially oriented mesopores was deposited around the NC@nSiO$_2$ via the biphasic oil-in-water strategy. Finally, the system obtained is noted NC@nSiO2@MS.[3] By comparison with the previous described methods of Deng and Zhao which occurs in water, here the solvent is a mix of water and an organic solvent (as hexane).

To deposit a mesoporous silica shell around NC, other groups followed the oil-in-water strategy with or without an intermediary condensed silica shell to stabilize the nanoclusters (or added another shell, as resorcinol for the work of Yue *et al.* [5]). In another work of the group of Zhao, the authors showed that by tuning the stirring speed from 170 to 500 rpm, micelle sizes could be tailored through swelling effect and, consequently, the large pore size could be adjusted from 5 to 9 nm.[5]

For "oil-in-water" process, the formation mechanism is better known. CTAB template molecules, used for the pores formation, will create a double layer around the NCs@nSiO2 thanks to electrostatic

interactions between the negatively charges silica surface and the positive charge of CTA⁺. Excess of CTA⁺ will create cylindrical micelles (Figure 1) containing organic phase into micelles. Thanks to the stirring speed, more or less organic phase is going into the micelle, which determines the pore size of the mesoporous silica.[5] By electrostatic interactions, TEOS, negatively charged, will polymerize around micelles. After extraction of all the CTAB templates, mesoporous silica is obtained.
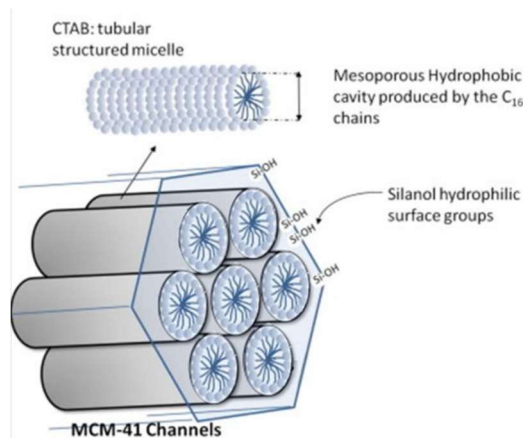

Figure 1. CTAB micelles structures.[10]

As expected, the addition of a mesoporous silica shell notably increases the size of the objects, this can limit its applications in medical treatments, but for environmental depollution, this size is totally compatible with applications and the submicron and micron scale is even preferred. In addition, the specific surface area shifts from 20-30 $m^2 \cdot g^{-1}$ for NCs to 365-526 $m^2 \cdot g^{-1}$. These last values are close to the previous synthesized STMS (500 $m^2 \cdot g^{-1}$) and are suitable to transpose the functionalization strategy of STMS developed in chapters 2 and 3. On the other hand, the magnetic properties are also modified and magnetization saturation decreases from 80 to 15-50 $emu \cdot g^{-1}$. This decrease has to be monitored to ensure an effective magnetic removal.

From these reported methods, a good colloidal stability of RSN is mandatory to ensure a homogeneous silica coating and we will thus coat RSN with citrates (ensuring a colloidal stability by electrostatic interactions). Concerning the coating strategy of RSN (Scheme 1), we also decided to put a first layer of non-porous silica coating to protect RSN from the media (acidic, corrosive…). Then, a second mesoporous silica layer was chosen to ensure a large specific surface area. For this last step, two strategies are possible in agreement with the previous reported results (Table 1): the first one is the "oil-in-water"[6] and the second one, the "Stöber modified" with CTAB.[4] We decided to deposit the MS shell following the "oil-in-water" process because this strategy affords several advantages which are an easy modification of pores size and a simple experimental protocol.
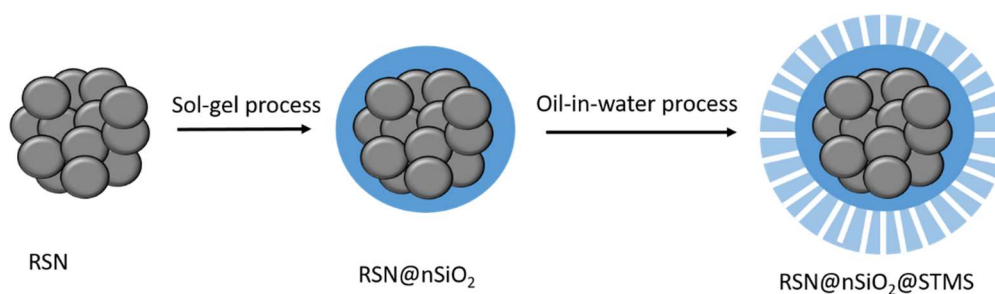
Scheme 1. Main steps to synthesize RSN@SiO₂ composite materials. The first step corresponds to the non-porous silica shell, the second to the mesoporous silica shell.

V. 1. 2. Experimental conditions

Products. Trisodium citrate (>99 %) from Roth, Ammonium hydroxide Sodium (NH₄OH) from Fluka, cetyltrimethylammonium bromide (CTAB), tetraethyl orthosilicate (TEOS) was purchased from Alfa Aesar, trimethylamine (TEA, >99 %) from Sigma Aldrich.

Citrate Coating. 10 mg of RSNs (synthesis method in chapter IV) are treated with 0.45 M sodium citrate solution (30 mL) under mechanical stirring for 20 minutes. The process is repeated 3 times. Finally, the RSN-citrate are washed 2 times with water.

Deposition of a non-porous silica shell (RSN@nSiO₂). The previous RSN@citrate are then dispersed in a cosolvent of 2 mL of water and 8 mL of ethanol. Then, NH₄OH at 25% (100 μL) and TEOS (100 μL) are added to the solution. The solution is stirred for 6 hours. The RSN@nSiO₂ are washed 2 times with EtOH and 2 times with water and conserved in EtOH.

Deposition of a porous silica shell (RSN@nSiO₂@STMS). The previous nano-objects are introduced in a 100 mL triple necked flask with 10 mL of water. The contents are dispersed thanks to ultrasonication. A solution of CTAB (0.2 g), TEA (68.9 μL) and 10 mL of water is added drop by drop into the flask under vigorous mechanical agitation. The solution is stirred at room temperature for 1 h. Then a solution of TEOS (25 μL) in 10 mL of hexane is introduced slowly. The reaction is heated at 60°C for 24 h in an oil bath. RSN@nSiO₂@mSiO₂ are washed 3 times with water. For the CTAB extraction, the synthesized particles are placed in the same flask with 15 mL of NH₄NO₃ solution (20 mg·mL⁻¹ in EtOH) and the solution is heated at 60°C for 1 h under mechanical agitation. The synthetized particles are washed with water/EtOH (1:1 in volume) and conserved in EtOH.

V. 1. 3. Results

Citrate coating. The RSN used in this study display a mean diameter of 326 nm and a mean nanograin size of 25 nm (Figure 2). The coverage of the RSN surface with citrate molecules to ensure IONPs colloidal stability is well known and provides electrostatic interactions between RSN at pH 6.6. According to zeta potential (ZP) measurements at pH =6.6, bare RSNs have a ZP value of -7.8 ± 4.6 mV, this value is shifted to -40.1 ± 5.2 mV after their citration. As a reminder: if the absolute value of the zeta potential is higher than 30 mV, the colloidal solution can be considered as stable.

The colloidal stability of citrate-coated RSNs suspension is confirmed by granulometric measurements (Figure 2.C). The size distribution is quite monomodal with no aggregation and the mean hydrodynamic size is 498 nm, higher than that determined by TEM (324 nm). The difference between both measurements cannot be explained only by the presence of the solvation layer around the citrated RSN and some low aggregation should occur. That confirms that citrate molecules ensure a good colloidal stability of RSNs in suspension.

The presence of citrates was confirmed by FTIR spectroscopy (Figure 2. D). In the IR spectrum of citrated RSN, we can observe the typical bond of Fe-O at 580 cm^{-1}. The comparison of IR spectra before and after citration of RSN showed the appearance of additional bands in the range 1488-1220 cm^{-1} (linked to the C-O bond) and at 1591 cm^{-1} (v_{asCOO^-}: 1620 cm^{-1}) which confirmed the presence of citrates on the RSN. We can observe that the small bands in the range 3010-2830 cm^{-1}, linked to the C-H bond of citrate and/or ethylene glycol, stayed on the RSN. These results confirmed the presence of citrates on the surface of RSN.
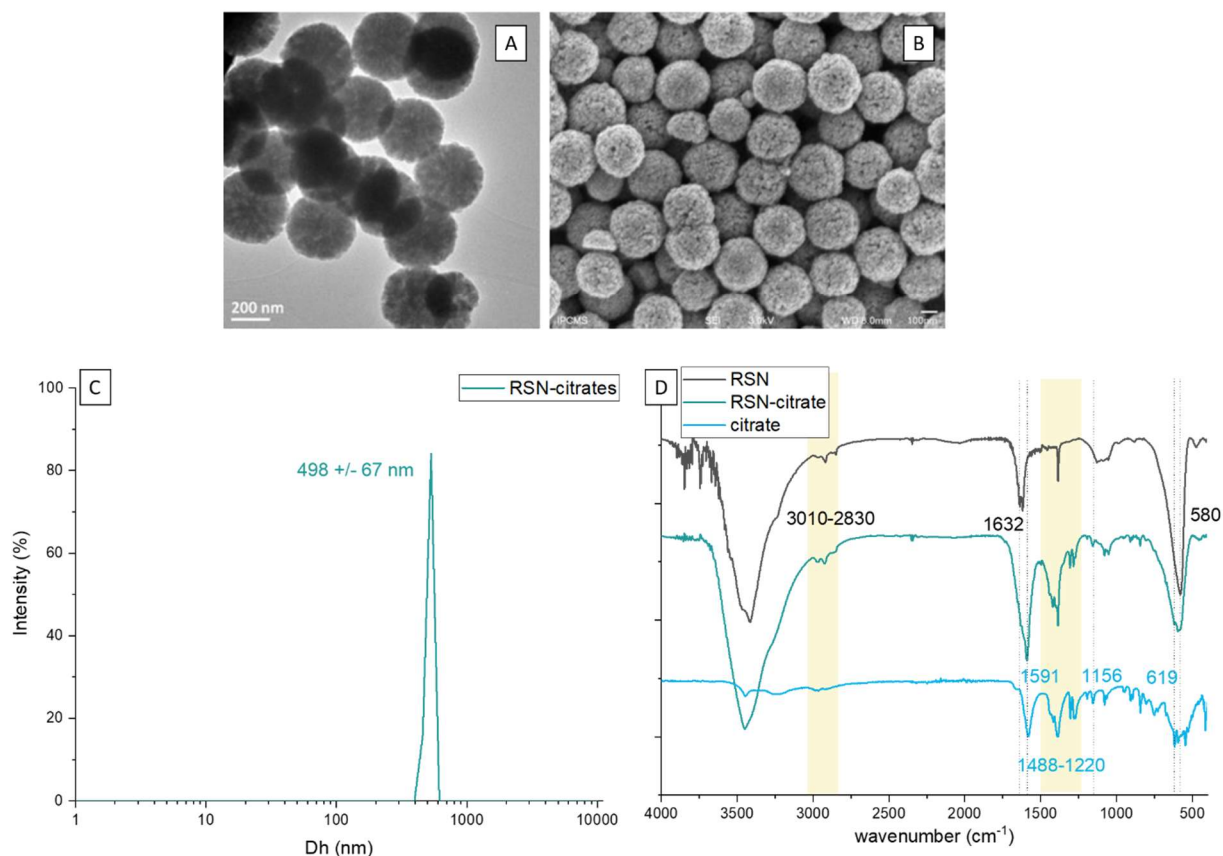
Figure 2. A. TEM and B SEM images of the RSN. C. granulometric measurement of citrate coated RSN. D. FTIR spectra of RSN, citrate coated RSN and citrates.

Coating step with non-porous silica shell (RSN@nSiO₂)

The condensed silica shell synthetized around the citrated RSNs is a quite reproducible process. In fact, the coating has been realized several times, and at each synthesis, a silica shell has been observed by TEM (Figure 3). The silica shell is a very thin layer not always clearly visible and displays an average thickness of about 10 nm.
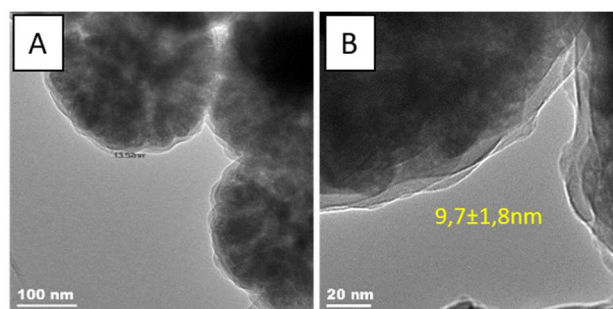

Figure 3. TEM images of the non-porous silica shell at the surface of RSN (RSN@nSiO₂).

Coating step with a mesoporous silica shell (RSN@nSiO₂@STMS)

Contrary to the STMS synthesis previously reported, here, the MS shell has been synthesized thanks to an organic template. Magnetic stirring cannot be applied in our case because RSNs are very sensitive to an external static magnetic field and they would aggregate on the stirring magnet effect. TEM images of the so-obtained composite particles are presented in Figure 4. RSN@nSiO2@STMS images show the presence of a regular silica shell around single RSNs and around aggregates of 2 RSN. The

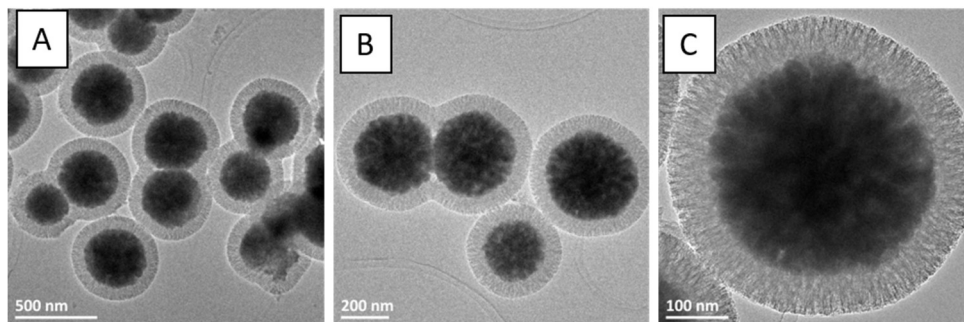silica layer is considered as a "radial" mesoporous silica because pores mostly start from the RSN surface.

Figure 4. TEM images of RSN@nSiO$_2$@STMS

V. 1. 4. Conclusion

To conclude, the synthesis of a composite nanomaterial consisting in an iron oxide magnetic core displaying a high saturation magnetization and coated with one or two silica shells was achieved. The reproducibility of the condensed silica coating (RSN@nSiO$_2$) has also been successful thanks to a pre-treatment of RSN with trisodium citrate to improve their colloidal stability. For the mesoporous silica shell, the "oil-in-water" approach allows getting the suitable pore morphology and structure of silica (large pore radially oriented) and can thus be used for further depollution experiments.

V. 2. Design of Nanomaterials for PAH or endocrine disruptors removal from liquid media

V. 2. 1. Endocrine Disruptors and PAH molecules

In this research study, we were interested in the design of nanocomposite to capture endocrine disruptors (ED). In the next lines, we will explain the diversity of this category of micropollutants, their complexity and dangerousness. Finally, we will focus on removal of the polycyclic aromatic hydrocarbon (PAH), a family of endocrine disruptors.

About micropollutants in water, European regulations (European Water Framework Directive) impose on countries to achieve "good chemical status" and "good ecological status" of waterbodies. It means the respect of the limit concentrations for micropollutants. Regarding at the lists, many of these substances are endocrine disruptors. Today, a clear and universal definition remains highly subject to the goodwill of the authorities (such as the world health organization (WHO), international program on chemical safety (IPCS) or the European parliament). For this work, we kept the latest definition adopted in Europe (June 2016). A substance is an ED if:

- It has adverse effects on human health.
- It acts on the hormonal system.
- a causal link must exist between the adverse effect and the mode of action.

As we have summarized in the Scheme 2, the real danger of the ED is that they mimic the role of real hormones into the hormone receptors, and this causes a wrong answer of the cells. These erroneous answers are reflected as responses at inappropriate times or the modulation of the gene's levels.[11–15] Consequently, these modifications may lead to major diseases and dysfunctions.
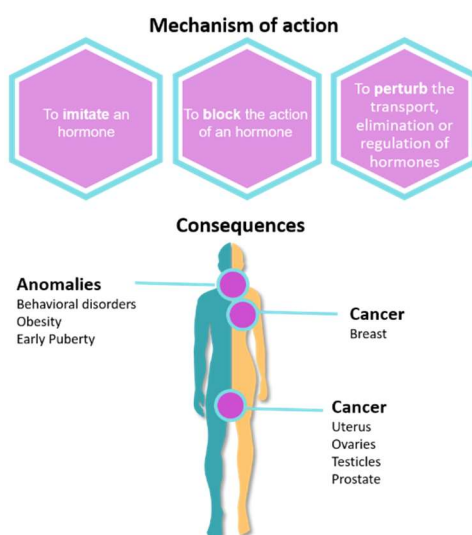
Scheme 2. Mechanism of action and consequences of endocrine disruptors.

Sources of these substances are multiple and the pathways into human body are diverse. In water, air or soils potential ED are under the form of synthetic hormones, pesticides, residues of chemical industry or products from combustion. They can enter the body by ingestion, inhalation and skin contact.

Nowadays, the big danger of these substances is clearly highlighted. In theory, regulations must be very strict. In practice, ED are considered as a "new" problem and regulations have been still too lax. The dangerousness of many substances is recognized since 1991, but only after 2014, governments actively focused on reinforcing regulations. In 2020, the European authorities finally confirmed 19 chemical substances as ED, 84 substances are under investigation and 9 are confirmed as ED in at least one country of the European member states. In agreement with the scientist community, these lists represent only 3% of the total ED.

Endocrine disruptors are classified in different families, nevertheless, for the next parts, it has been decided to focus mainly on polycyclic aromatic hydrocarbons (PAH). PAHs are organic molecules composed from, at least, two aromatic rings. These molecules are mostly colorless, white or pale-yellow solids. They form a ubiquitous group of several hundred chemically related compounds, environmentally persistent with various structures and varied toxicity.[16–18] Many PAHs are confirmed as harmful to health by different structures of public health supervision. For example, benzo[a]pyrene, which is present in the air (< 10 pg·m^{-3}), in rivers (<1ng·L^{-1}), seas (0.01 to 0.1 ng·L^{-1}) and rainwater (10ng·L^{-1}) is considered as a priority pollutant by the European Food Safety Authority (EFSA) and as a carcinogen by the International Center for Research on Cancer (IARC) of the World Health Organization (WHO). Benzo[a]pyrene is present in fossil fuels and emitted during volcanic eruptions and forest fires, it is also synthesized by plants, bacteria and algae.[19] We can also cite the dibenz[a,h]anthracene which is present in the air (<0.5 ng·m^{-3}), in the seas (<0.1 ng·L^{-1}) and rainwater (<50 ng·L^{-1}) also considered priority by EFSA. The main anthropogenic sources of this compound in the environment are exhaust fumes from diesel engines. The quantities of aerosol of dibenzo[a,h]anthracene released into the atmosphere are respectively 8.3 µg and 0.33 µg per kilometer traveled for cars (filtered and not). It is also released into the atmosphere by cigarette fumes, exhaust from petrol engines or even boiler fumes.[19]

Hence, the endocrine disruptors address a problem which gets the attention of science and technology. Since the years 2000, several groups already proposed materials to capture and/or degrade these pollutants. In 2017, Xu *et al.* also used the photocatalytic degradation of captured organic micropollutants (like bisphenol A or S, diphenyl sulfoxide or phthalates) with gold nanoclusters supported on TiO$_2$ nanoparticles.[20] In the same way, Rodovalho *et al.* used iron oxide NPs which have been previously coated with polydimethylsiloxane (PDMS).[21] The group of Chalasani also presented a method with iron oxide core to degrade organic micropollutants by photocatalysis with Fe$_3$O$_4$@TiO$_2$-cyclodextrine nanomaterials.[22] As well, the use of functionalized silica for pollutant removal has been reviewed by Cashin *et al.*, they showed a large panel of grafting and surface and application for depollution.

In our study on the conception of materials for the PAH capture, we focused on the promotion of π-stacking interaction between PAH molecules and the functionalized materials. For these interactions, it exists three main conformations: sandwich, T-shaped or parallel displaced (Figure 5). The energy of the interaction is between 8 and 12 kJ.mol^{-1}, depending on the conformation.[23–25]
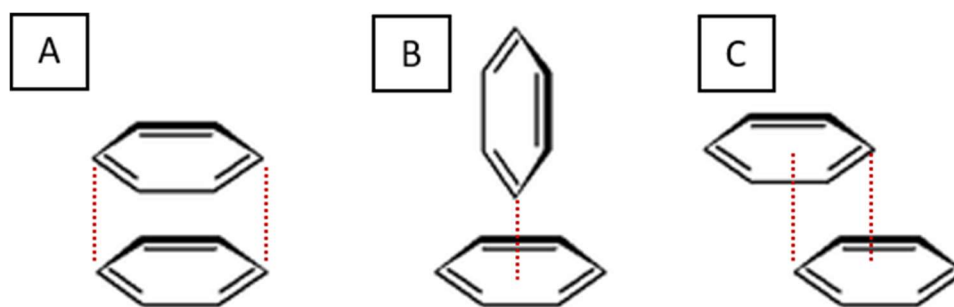
Figure 5. Conformation of π-stacking A. sandwich B. T-shaped and C. parallel displaced. Modified from Molčanov *et al.*[26]

We have thus investigated the functionalization of the different nano-objects, that we have developed in these PhD works or their combination with other materials in order to be able to remove high amount of PAH from liquid media. We have thus functionalized STMs or RSN with designed molecules or combined RSN with graphene, both being able to ensure π-stacking with PAH.

In this study, we have functionalized silica STMS with Trimethoxy(2-phenylethyl)silane (STMS@TMOPES), the RSN were coated with polydopamine (RSN@PDA) and tannic acid (RSN@TA), and finally, we searched to deposit those RSN on graphene layers (FLG@RSN). The choice of the ligand to test the capture of PAH has been driven thanks to the work of Orm about removal of PAH.[25]

Finally, the FLG@RSN were utilized for first experiments on PAH removal. For that, we performed the capture of naphthalene and fluorene in water and in methanol.

The next scheme summarizes these different experiments:

STMS

TMOPES

STMS@TMOPES

RSN

Polydopamine

RSN@PDA

Tannic Acid

RSN@TA

FLG@RSN

Synthesis of nanomaterials
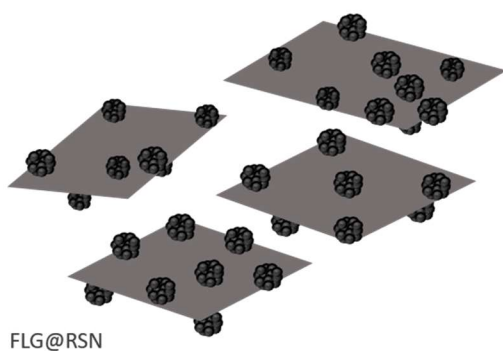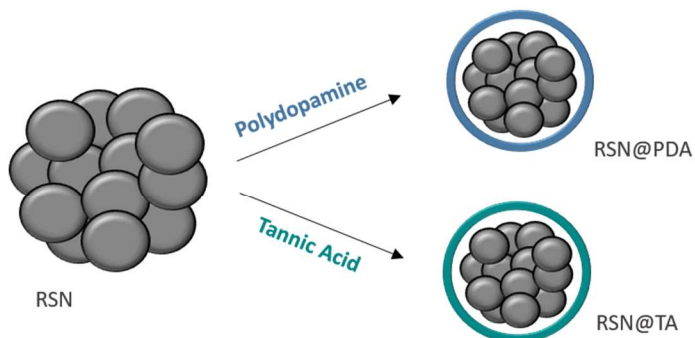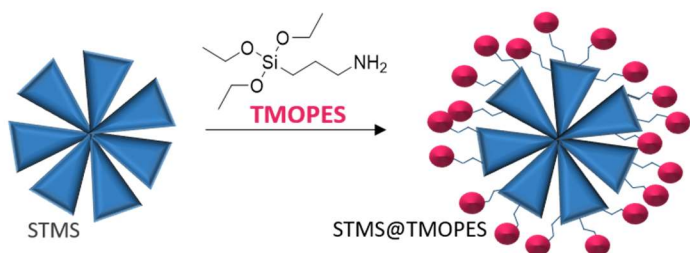
PAH Capture
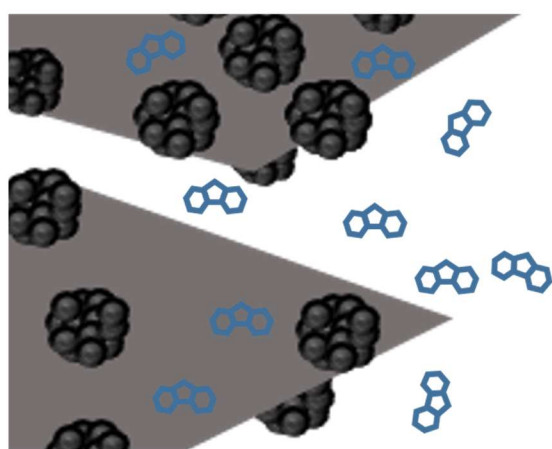
FLG@RSN

In **water**-naphthalene capture
In **methanol**-naphthalene capture

Naphthalene

Visual abstract of this part.

189

V. 2. 2. Experimental conditions

V. 2. 2. 1. Functionnalization of Silica Nanoparticles

STMS@Trimethoxy(2-phenylethyl)silane (TMOPES). The typical procedure for the grafting of STMS with TMOPES ligand is adapted from previous reported experiments (DFoB and CE grafting). 250 mg of STMS are added to 7 mL of EtOH with 1.2 mL of NH_4OH (0.7 M). The mixture is stirred for 5 min and different quantities of TMOPES are added for different monolayer coverage percentage (Table 2). The mixture is stirred for 2 hours. Finally, functionalized STMS are washed twice with 30 mL of ethanol.

Table 2. TMOPES volumes to different STMS coverage

Synthesis	Theoretical coverage (%)	TMOPES volume (µl)
STMS@TMOPES-A	30	45.5
STMS@TMOPES-B	50	75.8
STMS@TMOPES-C	70	106
STMS@TMOPES-D	90	136

V. 2. 2. 2. RSN Functionalization

RSN@POLYDOPAMINE (PDA). Bare RSN, prepared as described in chapter IV, were coated following the previous citration protocol. Dried citrate coated RSN were then dispersed in 10mM tris-base buffer solution (200 mL), checked to have a pH of 8-9, and then dopamine hydrochloride (DA-HCl, 50 mg) was added and stirred for an hour. Particles were separated with a magnet, rinsed with deionized water several times, and stored in water. This procedure is adapted from the work of Zheng *et al.*[27]

RSN@Tannic acid (TA). 25 mg of bare RSN and 45 mg of TA were introduced in 25 ml of water at pH 7. Following the work of Liao *et al* [28]., the whole mixture was mechanically stirred during 3 h and 15 h. The thickness of the TA shell (and for their work, the carbon shell) is proportional to the impregnation time. RSN@TA were then washed with water and ethanol.

V. 2. 2. 3. Raspberry-shaped Nanostructures on few layer graphene (FLG@RSN)

Synthesis of FLG@RSN. 50.77 mg of graphene dispersed in water (FLG provided by Dr. Dominique Bégin "Groupe Nanostructures Carbonées et Catalyse"-ICPEES) were dried using the freeze-dried method. When graphene is completely dried, 10 ml of ethylene glycol are added and the whole mixture is stirred until complete dispersion of graphene. Then, iron chloride (273.35 mg), succinic acid (37.79 mg) and urea (601.69 mg) are inserted into the mixture. The solution is stirred vigorously for 3 hours. The solution was carefully sealed in a Teflon lined stainless autoclave (15 mL capacity) and slowly heated at 200°C at 1.5°C/min. This temperature was mainteMaintened for 10.5 hours. The autoclave is cooled down to room temperature outside of the oven for 3 hours. The black sediment is separated by magnetic decantation. On a first approach, it is washed 3 times with ethanol and 3 times with deionized water to eliminate organic and inorganic impurities.

NB: The provided FLG were previously coated with tannic acid to ensure their well-dispersion in water. In further experiments, we could find some effects linked to its presence.

Depollution experiments

To test the capacity of our material to capture PAH and easily quantify the captured amount, four solutions were prepared: two of naphthalene and two of fluorene (in water and in methanol as solvent respectively). Four calibration curves were plotted to quantify the two molecules for further experiments.

The solutions and supernatant were analyzed in a UV-Vis spectrophotometer between 200 and 400 nm.

Naphthalene solutions

Naphthalene in water. 8.10 mg of naphthalene (purity 99%) were dissolved in 1 liter of ultra-filtered water (C_i = 8 mg·L^{-1}). To completely solubilize the naphthalene, the solution was continuously stirred at 60°C during 72 hours in an oil silicone bath under temperature control. This solution was used to obtain solutions at different concentrations [0.1-8] mg·L^{-1} by dilution in a total volume of 20 mL.

Naphthalene in methanol. 6.6 mg of naphthalene (purity 99 %) were dispersed in 20 mL of methanol (C_i = 329 mg·L^{-1}), the flask was handled stirred. Initial concentration. The calibration curve was plotted with secondary solution prepared thanks to this solution. The concentration range is from 2 to 10 mg·L^{-1}.

Fluorene solutions

Fluorene in water. This time, 3.6 mg of fluorene (purity 98 %) were dispersed on 2 L of water (C_i = 1.5 mg·L^{-1}). Following the same procedure of naphthalene, this solution was stirred at 60°C during 72 hours in an oil silicone bath under temperature control. For the calibration curve, the range of solution was from 0.183 to 1.5 mg·L^{-1}.

Fluorene in methanol. As for naphthalene, to have a solution at 329 mg·L^{-1}, 6.69 mg of naphthalene were dispersed in 20 mL of methanol in a flask and handled stirred for some seconds until completely dissolution. For the calibration curve, the concentration range is 2-10 mg·L^{-1}.

Removal of PAH

The FLG@RSN were considered to remove naphthalene in water and in methanol. In water, 2 and 4 mg of FLG@RSN were dispersed in 5 mL a solution of naphthalene at 8 mg·L^{-1}. The whole was mechanically stirred for 24 hours.

To remove naphthalene in the methanol solution, 2, 4 and 8 mg of the same nanocomposite suspension were dispersed in 5 mL volume of a solution of naphthalene in methanol at 5 mg/L. The solution was stirred for 24 hours.

The nanomaterials were separated from the different solutions by magnetic decantation and supernatants were analyzed by UV-Vis spectroscopy.

Magnetic Hyperthermia and Photothermia

The solutions have a concentration in water of 3.35 mg·ml^{-1}, 1.92 mg·ml^{-1} and 1.44 mg·ml^{-1} for FLG@RSN, graphene and RSN respectively. For magnetic hyperthermia, the device was set at 300 Gauss and a frequency of 536 kHz, the measurement was performed for 250 seconds. For photothermia, the solutions were irradiated with a 1064 nm laser at 1 W·cm^{-2}.

V. 2. 3. Results

V. 2. 3. 1. Functionalization of Silica Nanoparticles

In the previous studies, we showed various ways to functionalize silica surface. Based on our previous experience, our first strategy in this section was the modification of silica surface with Trimethoxy(2-phenylethyl) silane molecule. The used STMS have a mean size of 110 nm with a specific surface area of 500 m²·g^{-1} (Figure 6).

STMS@Trimethoxy(2-phenylethyl) silane

The choice of the ligand to test the capture of PAH has been driven thanks to the work of Orm[25] about removal of PAH. Hence, trimethoxy(2-phenylethyl)silane (TMOPES- Scheme 3) was grafted on the silica shell via the silane group. This synthesis was already performed by other groups: Yoo *et al.* used this molecule to protect quantum-dots (previously grafted on the surface of silica NPs) and used these particles in LEDs.[29] In 2011, Johnson *et al.* already modified the surface of mesoporous silica materials with TMOPES for the detection of volatile hydrocarbon solvents via fluorescence and reflecting methods.[30]
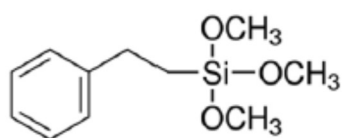
Scheme 3. Trimethoxy(2-phenylethyl)silane (TMOPES).

The FTIR spectra in Figure 6 A showed that all the grafted samples display a well-defined band at 460 cm^{-1} corresponding to the Si-O bond of STMS. An increase of the intensity of the band at 810 cm^{-1} (attributed to the bending vibration of Si-O bond) confirms the grafting of TMOPES on the surface of STMS. In addition to this, the appearance of a band at 1236 cm^{-1} is attributed to TMOPES on the surface of STMS. To further confirm the grafting of TMOPES on the surface of STMS, TGA was performed. Figure 6.B shows the TGA curve of our grafted STMS and several weight losses are observed. The first one around 100°C can be attributed to solvents evaporation (ethanol or water). The second weight loss at around 525°C might match with the degradation of organic components like the organic part of TMOPES. Thus, these TGA analyses confirm the presence of the organic ligands on STMS particles. The analysis of this weight loss suggests the same grafting for all the samples, with an average grafting rate of 51.5 μg_{TMOPES}·mg$^{-1}_{SiO2}$ (490 nmol$_{TMOPES}$·mg$^{-1}_{SiO2}$; 0.5 ligand·nm^{-2}). This grafting is suitable for the capture of pollutants.

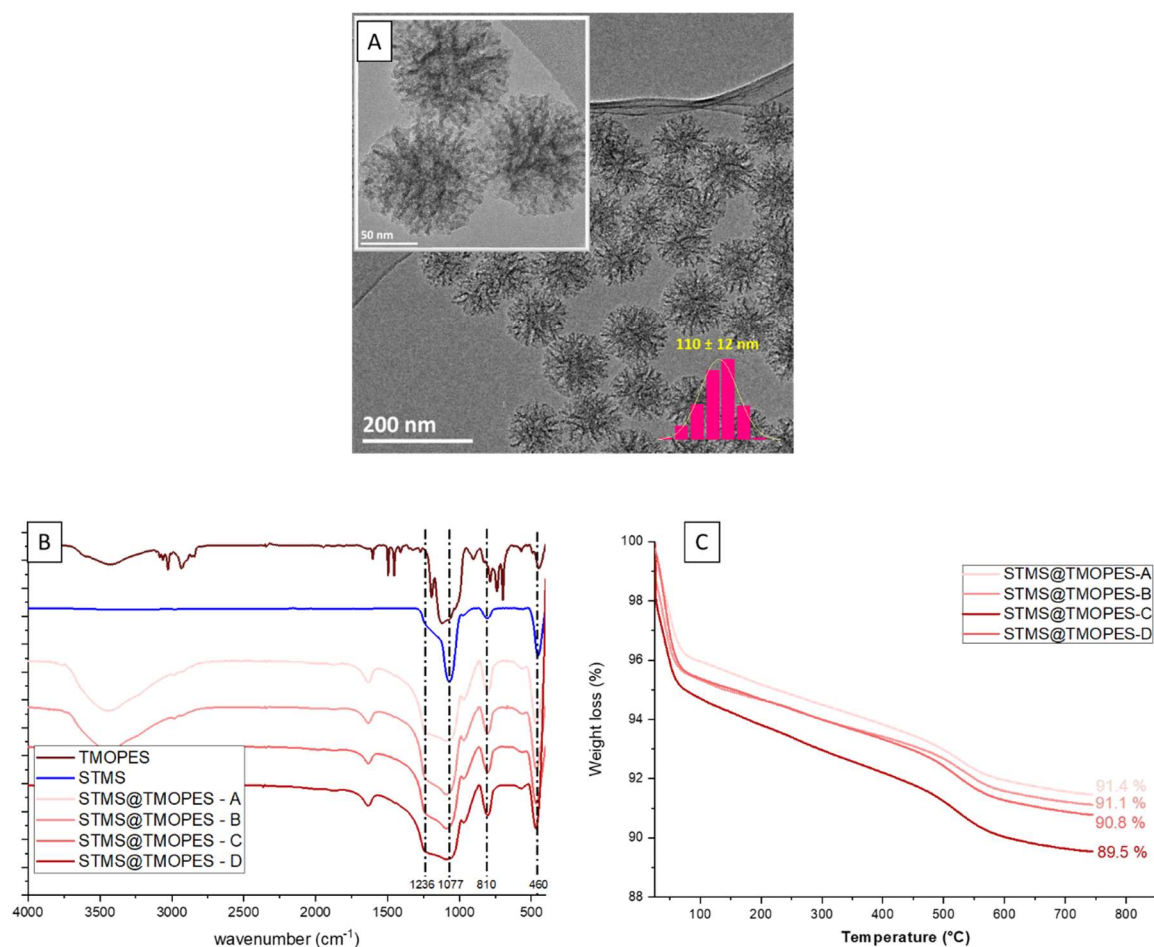**Figure 6. A. TEM images of the STMS. B. FTIR and C. ATG (10 °C·min⁻¹ under air) of TMOPES (black) and STMS of different synthesis.**

Table 3. Grafting of TMOPES on STMS of the different synthesis.

Synthesis	Δm (%)	Grafting (µg·mg⁻¹)	Grafting* (nmol·mg⁻¹)
STMS@TMOPES-A	4.8	52.5	500
STMS@TMOPES-B	4.4	48.2	459
STMS@TMOPES-C	4.8	52.8	502
STMS@TMOPES-D	4.7	52.5	500

*Molar mass of organic part of TMOPES: 105 g.mol⁻¹

To conclude, the ligand TMOPES was successfully grafted onto STMS. However, for different initial weight of TMOPES, the grafting rates converged all to the same result which is ca. 500 nmol·mg⁻¹. Some experiments (no presented here) were performed to remove toluene from water. The analysis of solutions by UV-Vis spectrophotometry showed a decrease of the absorbance peaks for all the grafted STMS. Unfortunately, we faced some difficulties in performing toluene quantification due to the fact that toluene is a high volatile molecule. Therefore, the obtained results did not represent the real capacities of the functionalized silica NPs.

V. 2. 3. 2. RSN functionalization

In order to make use of the magnetic properties to facilitate the removal of pollutants from different media, we investigated the functionalization of RSNs with molecules presenting aromatic rings. As for the previous material, we are looking for a capture by the π-stacking with HAP.

RSN@Polydopamine (PDA)
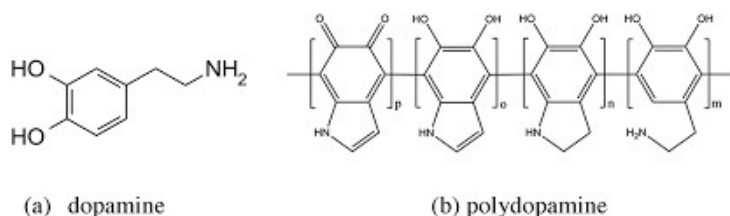
(a) dopamine   (b) polydopamine

Scheme 4. (a). Dopamine and (b). Polydopamine molecules.

We choose in a first assay the polydopamine (PDA) functionalization. Some groups already used PDA to functionalize membranes and improve capture of pollutants (i.e. ethylene blue as the representative target contaminant).[31]

It is always important to have a colloidal suspension of RSN before functionalization. For that, we have citrated RSN. In addition, citrates allow to negatively charge the RSN and then, the positive charged PDA can interact with citrated RSN through electrostatic interaction and thus encapsulate the citrated RSN. In fact, the dopamine is added in a 10mM tris buffer solution containing citrated RSN (pH 8-9) and in this solution, polymerization of dopamine takes place around the citrated RSN.

The zeta potential measurement of bare RSN at pH =7 is at -10 mV while RSN coated with citrates exhibit a zeta potential value of -40 mV. Finally, PDA coated RSN exhibit a zeta potential value of 7 mV. This distinct difference in zeta potential values confirms of the coating of RSN by citrates and then by PDA. Granulometric measurements were difficult and the mean hydrodynamic diameter was 1131±97 nm evidencing both a particle aggregation and sedimentation.

In TEM images of coated RSN (Figure 7.A. and B.), a layer of ca. 6 nm is visible around the RSN.

The FTIR spectrum of PDA coated RSN (Figure 7.C) displays the typical Fe-O band at 580 cm^{-1} (identical to that of the bare RSN (black)). The bands between 1740 and 920 cm^{-1} of the citrated RSN (curve blue) are modified in the RSN-PDA sample. The most remarkable modification is for the bands centered at 1591 and 1384 cm^{-1}. The majority of the bands linked to the citrates are overlapped with the new bands. If we consider the Figure 7.D (FTIR of the polydopamine[32]), in the same zone, the bands are similar to the new bands of the sample after PDA coating.

From the zeta potential measurements, the TEM observations and IR spectra, we can confirm the coating of polydopamine around the RSN.
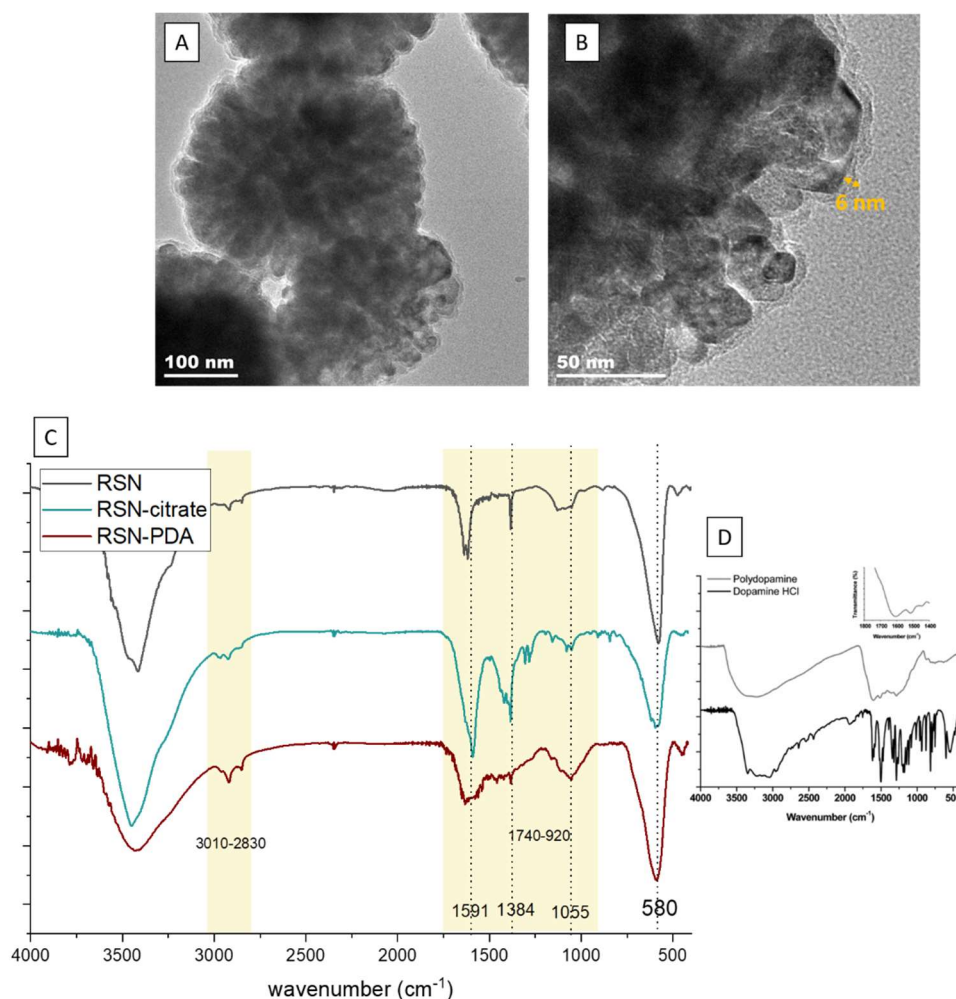
Figure 7. A. and B. TEM images of the RSN coated by PDA. C.FTIR spectra of RSN particles: bare (black) coated with citrate (blue) and with polydopamine (red). D. FTIR spectra of dopamine and polydopamine of Dreyer et al.[32]

In conclusion, it was possible to coat RSN with a thin layer of PDA (observed by TEM and confirmed by FTIR). However, the unstable colloidal suspensions suggest a deposition around agglomerates of RSN. In addition, the conception of this material is expensive because dopamine (reactant) is expensive. This is not because of the price; the problem is the conservation of the dopamine after opening of the flask. In fact, the dopamine is very sensitive to air and it oxidizes very fast. Consequently, each experiment means a new flask. The optimization of this material by ensuring a well layer deposition on RSN, profiles the RSN-PDA as material to capture PAH pollutants. This property will be ensured by the aromatic rings of the PDA and the cycles of the PAH (π-stacking interactions).

RSN@Tannic acid (TA)

Tannic acid (TA) is a form of tannin, a type of polyphenol and a good candidate to replace
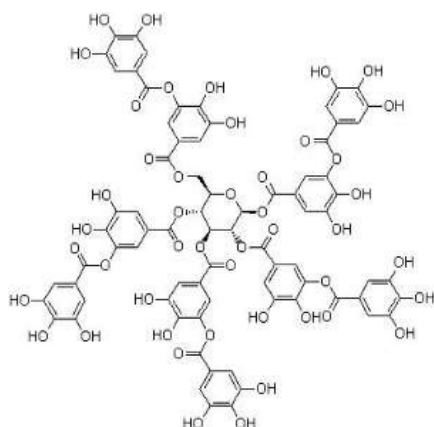
Scheme 5. Tannic acid

polydopamine. This molecule is composed of several aromatic rings and hydroxides groups (Scheme 5). It is often used as a fixative of dyes, reactant in the manufacture of inks, rubber, and imitation horns. Some materials, which integrates TA in their surface, were used for environmental projects: TA immobilized on powdered activated carbon (TA-PAC) to adsorb Cr(VI) in water[33,34] and graphene hydrogel functionalized with TA for organic dye adsorption in water media.[35]

TA has a low cost, and the conditions of storage are easy to perform. Because of that, we can consider that TA is a low-cost option to PDA.

Functionalization of RSN can be done by the bonding of the catechol functions of tannic acid on the surface. Indeed, these functions have a great affinity with iron and will allow their grafting on the surface.[36]

The zeta potential measurement did not exhibit an important change of charge (from -10 mV of bare RSN to -7 mV with TA coated RSN). This small difference in surface charge does not allow to ensure the coating. However, contrary to RSN-PDA, the granulometric measurements of RSN-TA indicates a hydrodynamic diameter of 400±97 nm. This value agrees with the size of RSN by TEM (32 nm) and suggests the success of the coating by TA. The FTIR spectrum of RSN@TA (Figure 8, wine-red curve) presents a modification of the bands in the range 1540-790 cm^{-1} of the RSN sample (black curve) which may be linked to the tannic acid (violet curve). Moreover, an increase in the intensity of the bands between 3050 and 2800 cm^{-1} is visible in the RSN-TA sample. The bands in the range 3600-3100 cm^{-1} (O-H bond) could be attributed to the phenolic and catechol group of tannic acid and to the physisorbed water.[37–39] Bands between 3050 and 2800 cm^{-1} are linked to the stretching vibrations of the O-C and C-H bonds and could confirm the presence of the tannic acid group. However, they were previously related to ethylene glycol. Between 1528 and 1238 cm^{-1}, the new bands of the RSN-TA sample are related to C=C bonds of the aromatic rings of the TA. Finally, the band at 1052 cm^{-1} in the spectrum belong to phenol groups, this bond could be shifted (compared to the TA spectra).[40,41] FTIR spectra suggested thus the presence of TA on RSN.
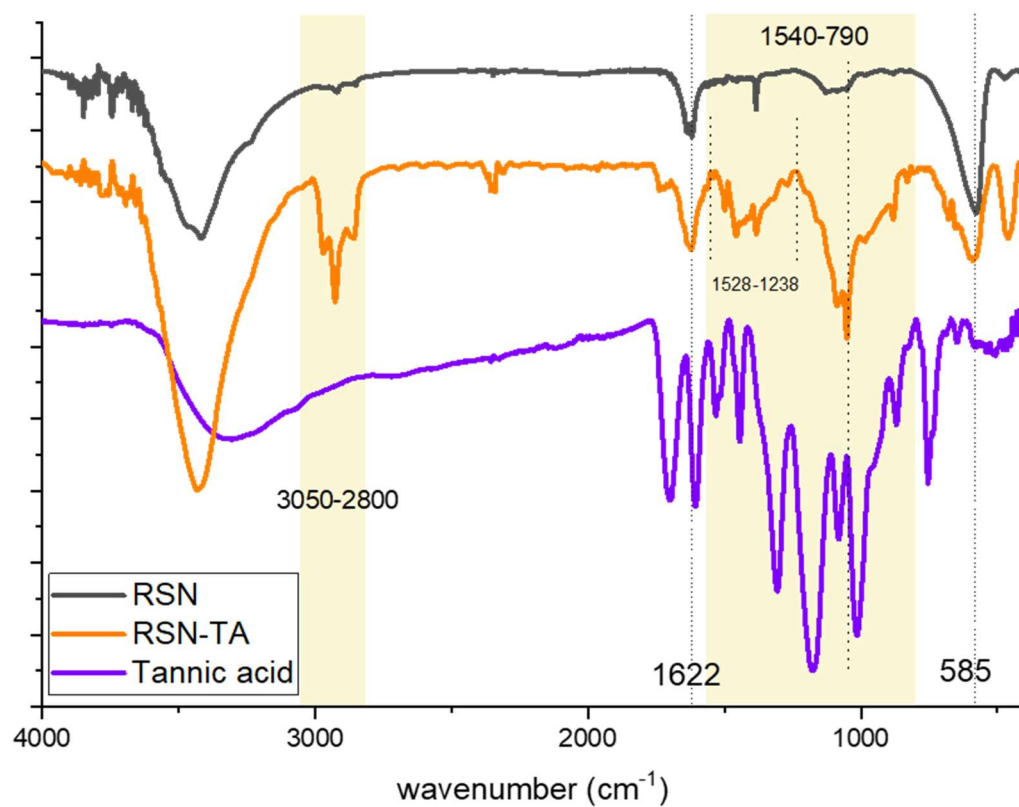
Figure 8. FTIR spectra of bare RSN particles (black), RSN coated with tannic acid (wine-red) and tannic acid (violet).

To conclude, FTIR spectroscopy and granulometric measurements would confirm the functionalization of RSN with TA even if the TEM images did not show a layer as for the PDA coating.

V. 2. 3. 3. FLG@RSN composite materials

Nowadays, one widespread technique allowing the capture of endocrine disruptors is the use of activated carbon. This material consists essentially of carbonaceous material with a porous structure. It is the result of a heat treatment in a strictly controlled atmosphere: thermal activation (drying, carbonization at 500-600 °C and mild oxidation at 850-1000°C) of various natural materials (coal, lignite, wood, etc.).[42] This treatment gives to the carbon the property of binding certain molecules brought into contact since it has a large specific surface which induces a strong adsorbent power. The use of activated carbon for the PAHs depollution of aqueous media nevertheless has its limits. Indeed, this material is not reusable and it has a limited lifespan. It can be regenerated by oxidation/removal of the organic matter adsorbed on its surface, but this operation destroys a part of the carbon material and reduces its efficiency by 5 to 10 %.[43] In addition, it cannot be used when liquid media are « charged » and/or consist in slurries.

In fact, graphene is a crystalline allotropic form of carbon that has many interesting properties including its high specific surface (which may be of 300-1000 $m^2 \cdot g^{-1}$)[44], with a very large system of delocalization of electrons. It shows an excellent mechanical / thermal stability compared to other materials. It was theorized in 1947 by Phillipe Wallace and first synthesized in 2004 by Andre Gem at the University of Manchester. This success earned him the Nobel Prize in Physics in 2010 and allowed the emergence of new methods of capturing PAHs. Indeed, several papers have already reported on the suitability of graphene and graphene oxide for environmental applications and especially for PAHs removal. [45–47]

As graphene has already been proved adapted for PAHs removal, we investigate here the possibility to add magnetic properties to graphene. The combination of the interesting magnetic properties of RSN with few layer graphene will allow composite materials recovery by magnetic decantation. The synthesis of such composite materials has already been reported for supercapacitors and lithium-batteries applications. [48,49]

Such composite materials have been obtained by performing the synthesis of RSN in presence of graphene. SEM images (Figure 9 A. and B.) show that RSN are clearly visible on the graphene sheets. The layers of graphene are well separated and RSN are homogenously distributed on the graphene sheets. RSN display a mean size of 324 ± 40 nm. The space between RSN leave enough place for PAH molecules to interact with graphene. In addition, the density of RSN on graphene sheets can be easily modulated. Figure 9. C shows the possible magnetic decantation of this material and proves that RSN clearly add magnetic properties to graphene layers which will facilitate their removal from solutions.
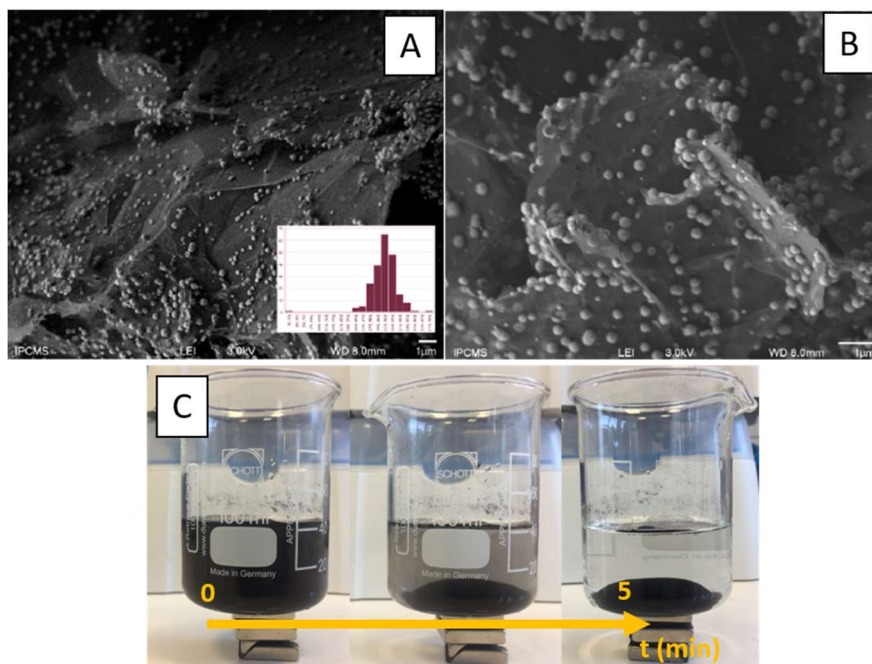
Figure 9. A. and B.) SEM images of FGL@RSN composites. C) Magnetic decantation of FLG@RSN under the application of a magnet.

The XRD pattern of FLG@RSN (Figure 10. A, dark grey curve) showed the typical diffraction peaks of the spinel iron oxide phase. Contrary to the previous characterized RSN (Figure 10, black curve), XRD peaks are larger suggesting smaller grains. A mean crystallite size of 12 nm is determined by profile matching of the XRD pattern. The calculated lattice parameter 8.39 Å is close to that of the magnetite phase (8.396 Å). An additional peak at 26.5° is attributed to (002) reflection of the hexagonal crystalline structure of graphene. [50,51]
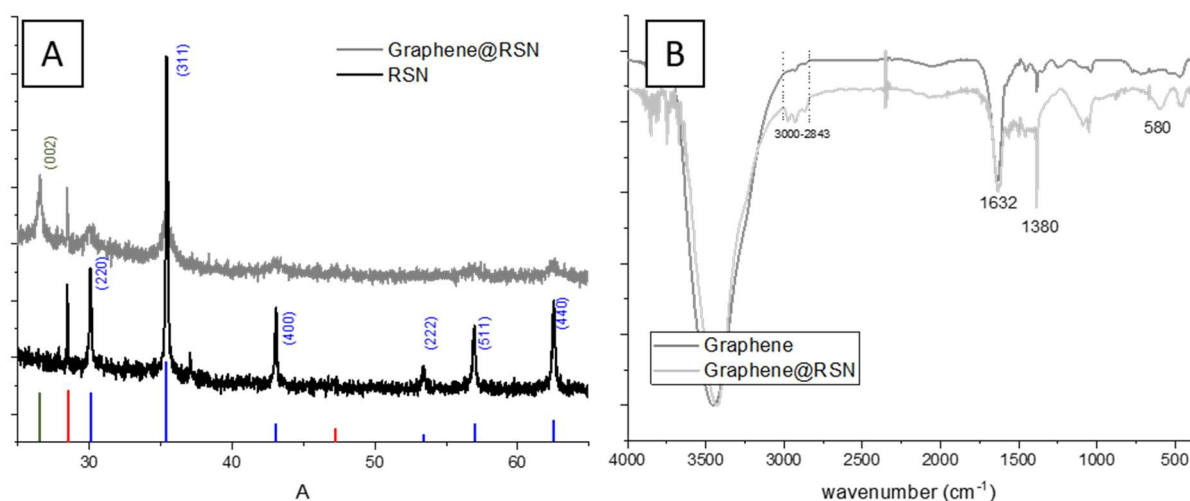

Figure 10. A. XRD pattern and B. FTIR spectrum of FLG@RSN.

In the FT-IR spectrum of the FLG@RSN sample (Figure 10. B, dark grey curve), the three bands in the range 3000-2843 cm^{-1} correspond to the C-H stretch vibrations of the methylene group attributed to

graphene.[52] Band at 1632 cm^{-1} could correspond to the C=C bond or aromatic cycles of graphene or to the C=O bond of the tannic acid. Indeed, the FLG were previously coated with tannic acid to ensure their colloidal stability in water. After the synthesis of our composite material FLG@RSN, the TA is always present even after the washing step. Another band at 1100 cm^{-1} could be related to traces of EG in the sample. Finally, a small band at 580 cm^{-1} is linked to the Fe-O bond of RSN.

Depollution experiments using FLG@RSN composite materials

UV-Vis spectrophotometry and calibrations curves

We want to emphasize that, in the best of our knowledge, no other groups quantified naphthalene and/or fluorene in methanol or water using UV-Vis spectrophotometry.

Naphthalene

In figure 11, we can see an absorption maximum which increases with the naphthalene concentration at 275 nm in water (Figure 11. A) and at 276 nm in methanol (Figure 11. B). In agreement with different studies, these peaks match with naphthalene.[53,54] The evolution of this peak with the concentration allowed us to plot calibration curves in the different media. The calibration curves have a coefficient of determination of 0.9962 and 0.9926 in water and methanol respectively. Thus, we can consider the curves as linear and useful for quantification in further experiments.
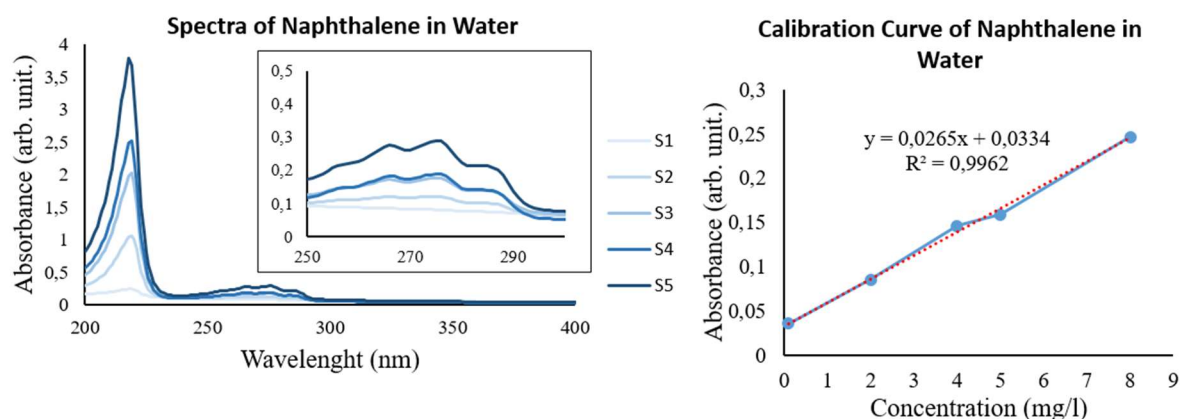
Figure 11. UV-Vis spectra and calibration curves of naphthalene in A. water and B. methanol.

Fluorene

Following the same principle, fluorene solutions were analyzed, and the absorption maximum was found at 260 nm in water and at 263 nm in methanol (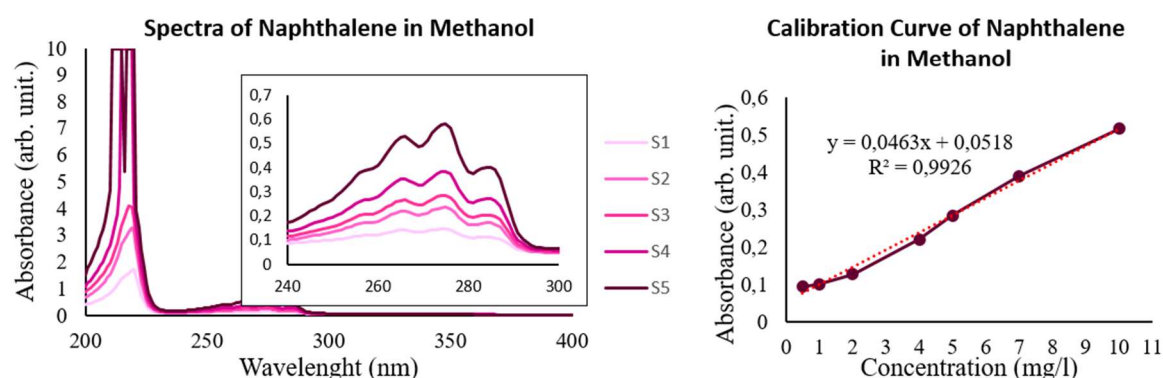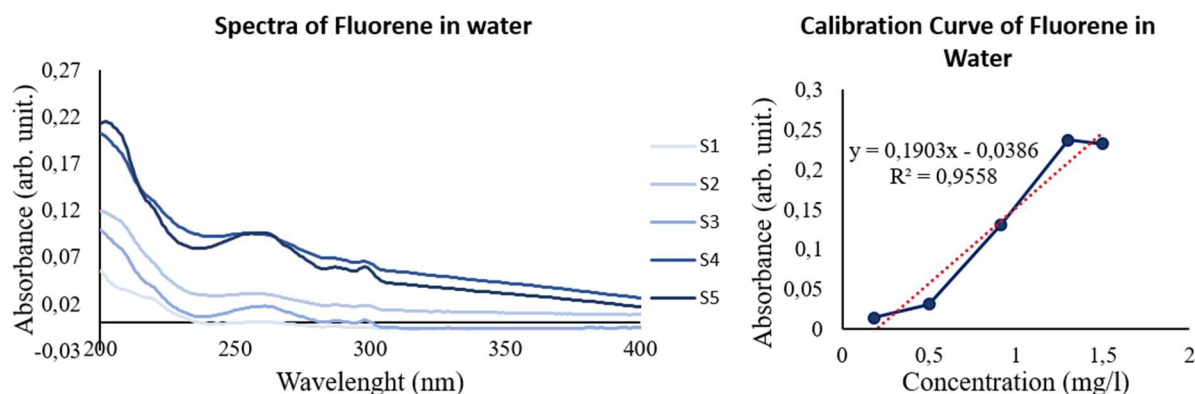Figure 12). Contrary to naphthalene in water, the curve is not linear and cannot be used to quantify fluorene in water. However, the curve in methanol is linear and the coefficient of determination values 0.9995. So, this curve can be used.

A. Fluorene in water

B. Fluorene in methanol
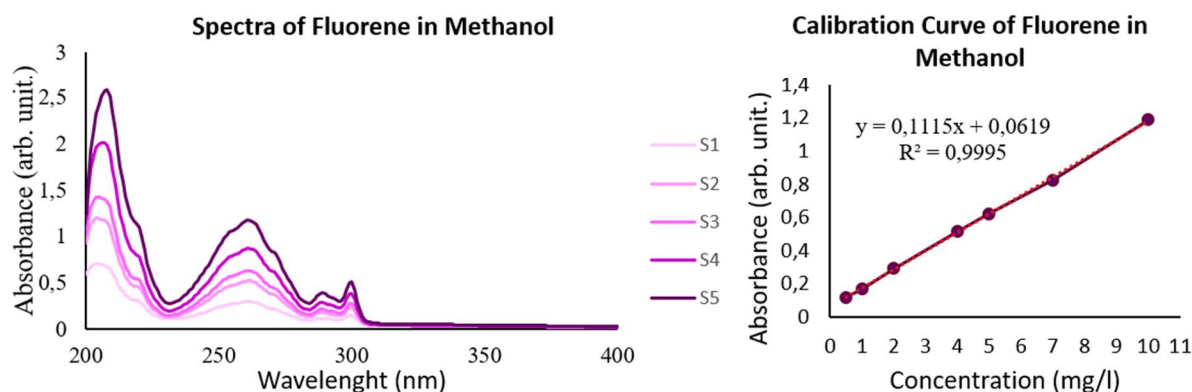
Figure 12. UV-Vis Spectrum and calibration curve of fluorene in A. water and B. methanol.

Removal experiments of PAHs

Naphthalene

2 mg and 4 mg of FLG@RSN were dispersed in an initial solution of naphthalene in water. According to graphs in Figure 13, the UV-Vis spectra of the supernatants are different of those of the initial solutions. At a first sight, we can consider that the molecule capture reached around 100 %. However, besides the broad band at 260 nm, a band at 200 nm is also noticed which overlaps a little bit with the band at 260 nm. Several groups reported the UV-Vis spectrum of graphene in water[55,56] and, surprisingly, the band below 250 nm in our spectra is similar to that of graphene. Probably, the supernatant contained "invisible" traces of FLG@RSN which altered the UV-Vis spectrophotometric analysis. In this case, the band of graphene overlaps that of naphthalene. To confirm the presence of FGL in supernatant, other analytical methods will be needed.

The result of the experiment in methanol is given in Figure 13.B. It shows the spectrum of supernatants in methanol. The capacity of capture was calculated to be of 7.80 $nmol_{naphthalene} \cdot mg^{-1}_{FLG@RSN}$ (1 $\mu g_{naphthalene} \cdot mg^{-1}_{FLG@RSN}$), 5.15 $nmol_{naphthalene} \cdot mg^{-1}_{FLG@RSN}$ (0.66 $nmol_{naphthalene} \cdot mg^{-1}_{FLG@RSN}$) and 1.87 $nmol_{naphthalene} \cdot mg^{-1}_{FLG@RSN}$ (024 $nmol_{naphthalene} \cdot mg^{-1}_{FLG@RSN}$) for 2, 4 and 8 mg naphthalene solutions in methanol respectively. The amount of composite materials has a surprising influence: the increase of the amount of material reduces the capture capacity of the material. It could be justified by possible π-π stacking interactions between graphene sheets which reduce the surface of capture or by the interactions between the acid tannic on the surface of sheets. Regardless, these preliminary first results confirm the possibility to capture naphthalene with FLG@RSN.
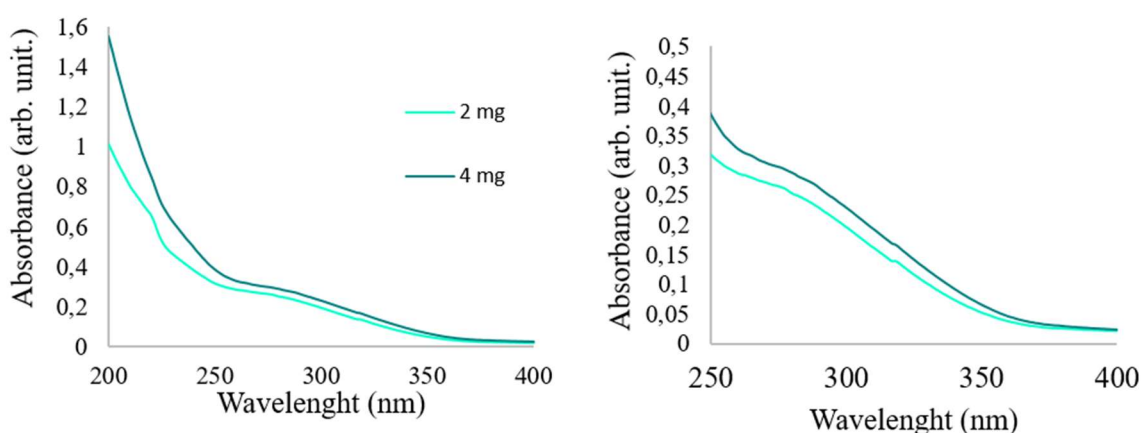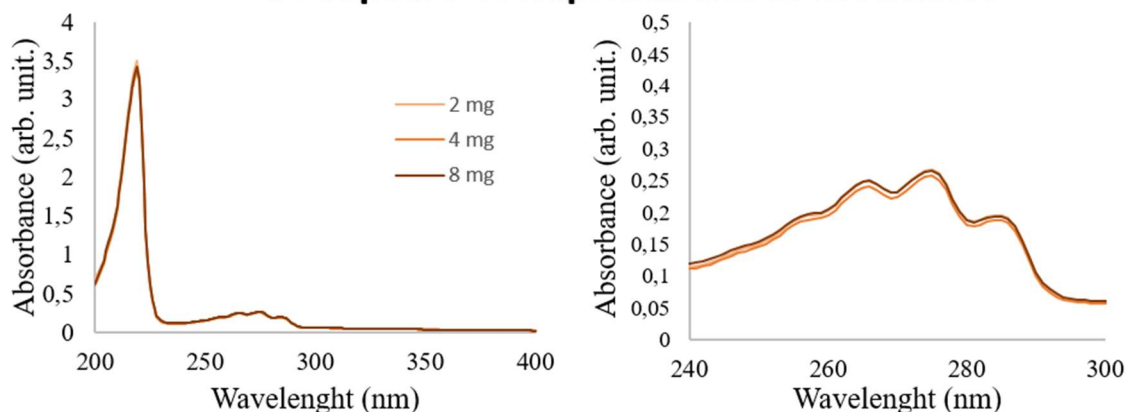

Figure 13. UV-Vis spectra of treated Naphthalene in A. water and B. in methanol.

V. 2. 3. 4. Evaluation of the potential of heating of the composite materials by magnetic hyperthermia and photothermia

Iron oxide nanoparticles have well known to release heat under the application of an alternative magnetic field (magnetic hyperthermia)[57,58] and may also release heat under a laser irradiation (photothermia). Graphene may also release heat under laser irradiation.[59] Therefore, we have performed magnetic hyperthermia and photothermia experiments to evaluate the heating potential of our materials.

To compare the three samples, the samples FLG@RSN and RSN contain the same iron amount. In the same way, the samples FLG@RSN and FLG contains the same graphene amount.

The magnetic hyperthermia experiments (Figure 14.A) showed a more important increase of temperature for the sample FLG@RSN ($\Delta T=20$ °C) than for the RSN one ($\Delta T=3$ °C). Without particular surprise, the sample FLG, being not endowed with magnetic feature, did not present a temperature increase. Comparing the samples, we can suggest that the "heating" phenomenon is due to the RSN on the graphene, however, the FLG must play a "conductive-amplifying" role to allow this important heat but another explanation would be that under the alternating magnetic field, there is a rotation of FLG coated with RSN. The friction would induce a macroscopic heating. Apparently, no other magnetic hyperthermia studies by other groups have been performed on FLG @IONPs to compare our results.

The photothermia experiments achieved with a power of P = 1 W·cm^{-2} show a temperature increase for the three samples. The difference in temperature is very close for the three samples: 9.7, 12.3 and 11.5 °C for FLG@RSN, FLG and RSN samples. It is interesting to observe a similar increase in the samples, but there are not a "accumulative" effect as expected. The group of Pan *et al.* also observed an increase of temperature with a FLG@IONPs material.[60]
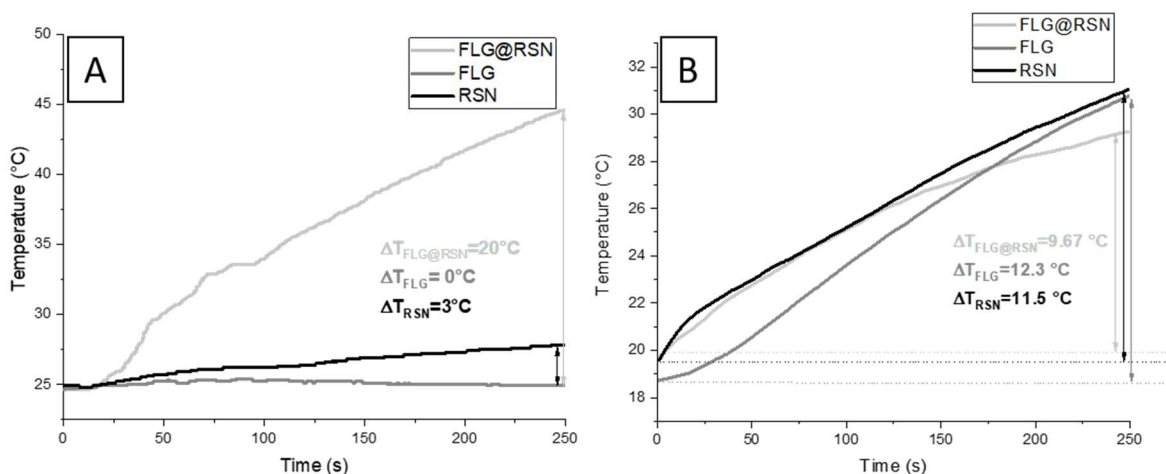
Figure 14. Heating curves by A. magnetic hyperthermia and B. photothermia of FLG@RSN, FLG and RSN samples.

Such experiments are interesting as in 2016, Rodovalho *et al.* showed the desorption of toluene from IO NPs coated with PDMS thanks to the magnetic hyperthermia. In fact, the sample was introduced into the magnetic hyperthermia apparatus (the frequency was 300 kHz and the field amplitude was 98 G for a quantity of 5 mg of nanomaterial), the authors observed an increase in temperature of 75 °C in

100 seconds and they evaluated this temperature as sufficient to desorb toluene. They also performed recycling experiments using hyperthermia. However, they did not clearly express a complete removal from the nanoparticles.[21]

V. 2. 4. Conclusion

In this chapter, we succeeded in synthesizing different materials which are potential adsorbents of PAHs molecules. We have demonstrated that the strategies that we have developed for coating STMS particles by molecules for Fe and Na removal can be extended to the functionalization of STMS for PAH removal. We have also coated magnetic RSN by a silica coating which led to magnetic MS particles promising for capture of PAHs and removal of the particles from liquid media by applying a magnetic field.

The coating of RSN by molecules for PAHs capture was not so easy because of the low colloidal stability of RSN and the presence of EG at their surface. However, the presence of molecules suitable for PAHs removal has been evidenced. Further studies are needed to evaluate their potential for PAHs removal. Finally, we designed FLG@RSN composite particles for the PAH capture because of the reported properties of graphene in the endocrine disruptors capture. In those experiments, FLG@RSN showed a capacity to remove a part of pollutants (naphthalene) from the initial solutions. However, further experiments are needed to validate and possibly increase the capture yield.

References

(1) Kim, J.; Kim, H. S.; Lee, N.; Kim, T.; Kim, H.; Yu, T.; Song, I. C.; Moon, W. K.; Hyeon, T. Multifunctional Uniform Nanoparticles Composed of a Magnetite Nanocrystal Core and a Mesoporous Silica Shell for Magnetic Resonance and Fluorescence Imaging and for Drug Delivery. *Angewandte Chemie* **2008**, *120* (44), 8566–8569.

(2) Deng, Y.; Qi, D.; Deng, C.; Zhang, X.; Zhao, D. Superparamagnetic High-Magnetization Microspheres with an Fe3O4@SiO2 Core and Perpendicularly Aligned Mesoporous SiO2 Shell for Removal of Microcystins. *J. Am. Chem. Soc.* **2008**, *130* (1), 28–29.

(3) Yang, J.; Shen, D.; Wei, Y.; Li, W.; Zhang, F.; Kong, B.; Zhang, S.; Teng, W.; Fan, J.; Zhang, W.; Dou, S.; Zhao, D. Monodisperse Core-Shell Structured Magnetic Mesoporous Aluminosilicate Nanospheres with Large Dendritic Mesochannels. *Nano Res.* **2015**, *8* (8), 2503–2514.

(4) Yang, P.; Quan, Z.; Hou, Z.; Li, C.; Kang, X.; Cheng, Z.; Lin, J. A Magnetic, Luminescent and Mesoporous Core–Shell Structured Composite Material as Drug Carrier. *Biomaterials* **2009**, *30* (27), 4786–4795.

(5) Yue, Q.; Li, J.; Luo, W.; Zhang, Y.; Elzatahry, A. A.; Wang, X.; Wang, C.; Li, W.; Cheng, X.; Alghamdi, A.; Abdullah, A. M.; Deng, Y.; Zhao, D. An Interface Coassembly in Biliquid Phase: Toward Core–Shell Magnetic Mesoporous Silica Microspheres with Tunable Pore Size. *J. Am. Chem. Soc.* **2015**, *137* (41), 13282–13289.

(6) Xiong, L.; Bi, J.; Tang, Y.; Qiao, S.-Z. Magnetic Core–Shell Silica Nanoparticles with Large Radial Mesopores for SiRNA Delivery. *Small* **2016**, *12* (34), 4735–4742.

(7) Yuan, Q.; Li, N.; Chi, Y.; Geng, W.; Yan, W.; Zhao, Y.; Li, X.; Dong, B. Effect of Large Pore Size of Multifunctional Mesoporous Microsphere on Removal of Heavy Metal Ions. *Journal of Hazardous Materials* **2013**, *254–255*, 157–165.

(8) Seo, B.; Lee, C.; Yoo, D.; Kofinas, P.; Piao, Y. A Magnetically Recoverable Photocatalyst Prepared by Supporting TiO2 Nanoparticles on a Superparamagnetic Iron Oxide Nanocluster Core@fibrous Silica Shell Nanocomposite. *RSC Adv.* **2017**, *7* (16), 9587–9595.

(9) Sun, Z.; Zhou, X.; Luo, W.; Yue, Q.; Zhang, Y.; Cheng, X.; Li, W.; Kong, B.; Deng, Y.; Zhao, D. Interfacial Engineering of Magnetic Particles with Porous Shells: Towards Magnetic Core – Porous Shell Microparticles. *Nano Today* **2016**, *11* (4), 464–482.

(10) Ribeiro-Santos, T. A.; Henriques, F. F.; Villarroel-Rocha, J.; de Castro, M. C. M.; Magalhães, W. F.; Windmöller, D.; Sapag, K.; Lago, R. M.; Araujo, M. H. Hydrophobic Channels Produced by Micelle-Structured CTAB inside MCM-41 Mesopores: A Unique Trap for the Hazardous Hormone Ethinyl Estradiol. *Chemical Engineering Journal* **2016**, *283*, 1203–1209.

(11) Rogers, J. A.; Metz, L.; Yong, V. W. Review: Endocrine Disrupting Chemicals and Immune Responses: A Focus on Bisphenol-A and Its Potential Mechanisms. *Molecular Immunology* **2013**, *53* (4), 421–430.

(12) Kabir, E. R.; Rahman, M. S.; Rahman, I. A Review on Endocrine Disruptors and Their Possible Impacts on Human Health. *Environmental Toxicology and Pharmacology* **2015**, *40* (1), 241–258.

(13) Schug, T. T.; Janesick, A.; Blumberg, B.; Heindel, J. J. Endocrine Disrupting Chemicals and Disease Susceptibility. *The Journal of Steroid Biochemistry and Molecular Biology* **2011**, *127* (3), 204–215.

(14) Boelsterli, U. A. *Mechanistic Toxicology: The Molecular Basis of How Chemicals Disrupt Biological Targets, Second Edition*; CRC Press, 2007.

(15) Safe S H. Endocrine Disruptors and Human Health--Is There a Problem? An Update. *Environmental Health Perspectives* **2000**, *108* (6), 487–493.

(16) Rajpara, R. K.; Dudhagara, D. R.; Bhatt, J. K.; Gosai, H. B.; Dave, B. P. Polycyclic Aromatic Hydrocarbons (PAHs) at the Gulf of Kutch, Gujarat, India: Occurrence, Source Apportionment, and Toxicity of PAHs as an Emerging Issue. *Marine Pollution Bulletin* **2017**, *119* (2), 231–238.

(17)   Abdel-Shafy, H. I.; Mansour, M. S. M. A Review on Polycyclic Aromatic Hydrocarbons: Source, Environmental Impact, Effect on Human Health and Remediation. *Egyptian Journal of Petroleum* **2016**, *25* (1), 107–123.

(18)   Richter-Brockmann, S.; Achten, C. Analysis and Toxicity of 59 PAH in Petrogenic and Pyrogenic Environmental Samples Including Dibenzopyrenes, 7H-Benzo[c]Fluorene, 5-Methylchrysene and 1-Methylpyrene. *Chemosphere* **2018**, *200*, 495–503.

(19)   INERIS - Santé, Expertise en toxicologie chronique https://substances.ineris.fr/fr/page/21 (accessed Oct 7, 2020).

(20)   Xu, F.; Chen, J.; Kalytchuk, S.; Chu, L.; Shao, Y.; Kong, D.; Chu, K.-H.; Sit, P. H.-L.; Teoh, W. Y. Supported Gold Clusters as Effective and Reusable Photocatalysts for the Abatement of Endocrine-Disrupting Chemicals under Visible Light. *Journal of Catalysis* **2017**, *354*, 1–12.

(21)   Rodovalho, F. L.; Capistrano, G.; Gomes, J. A.; Sodré, F. F.; Chaker, J. A.; Campos, A. F. C.; Bakuzis, A. F.; Sousa, M. H. Elaboration of Magneto-Thermally Recyclable Nanosorbents for Remote Removal of Toluene in Contaminated Water Using Magnetic Hyperthermia. *Chemical Engineering Journal* **2016**, *302*, 725–732.

(22)   Chalasani, R.; Vasudevan, S. Cyclodextrin-Functionalized Fe3O4@TiO2: Reusable, Magnetic Nanoparticles for Photocatalytic Degradation of Endocrine-Disrupting Chemicals in Water Supplies. *ACS Nano* **2013**, *7* (5), 4093–4104.

(23)   Burley, S. K.; Petsko, G. A. Aromatic-Aromatic Interaction: A Mechanism of Protein Structure Stabilization. *Science* **1985**, *229* (4708), 23–28.

(24)   Rodovalho, F. L.; Capistrano, G.; Gomes, J. A.; Sodré, F. F.; Chaker, J. A.; Campos, A. F. C.; Bakuzis, A. F.; Sousa, M. H. Elaboration of Magneto-Thermally Recyclable Nanosorbents for Remote Removal of Toluene in Contaminated Water Using Magnetic Hyperthermia. *Chemical Engineering Journal* **2016**, *302*, 725–732.

(25)   Bou Orm, N. Nano-Matériaux Hybrides Pour l'élimination de Micro-Polluants Organiques (HAP) Dans Les Effluents Aqueux. These de doctorat, Lyon 1, 2012.

(26)   Molčanov, K.; Sabljić, I.; Kojić-Prodić, B. Face-to-Face π-Stacking in the Multicomponent Crystals of Chloranilic Acid, Alkali Hydrogenchloranilates, and Water. *CrystEngComm* **2011**, *13* (12), 4211–4217.

(27)   Zheng, R.; Wang, S.; Tian, Y.; Jiang, X.; Fu, D.; Shen, S.; Yang, W. Polydopamine-Coated Magnetic Composite Particles with an Enhanced Photothermal Effect | ACS Applied Materials & Interfaces. *ACS Appl. Mater. Interfaces* **2015**, *7* (29), 15876–15884.

(28)   Liao, C.; Xu, Q.; Wu, C.; Fang, D.; Chen, S.; Chen, S.; Luo, J.; Li, L. Core–Shell Nano-Structured Carbon Composites Based on Tannic Acid for Lithium-Ion Batteries. *J. Mater. Chem. A* **2016**, *4* (43), 17215–17224.

(29)   Yoo, H.; Seong Jang, H.; Lee, K.; Woo, K. Quantum Dot-Layer-Encapsulated and Phenyl-Functionalized Silica Spheres for Highly Luminous, Colour Rendering, and Stable White Light-Emitting Diodes. *Nanoscale* **2015**, *7* (30), 12860–12867.

(30)   Johnson, B. J.; Anderson, N. E.; Charles, P. T.; Malanoski, A. P.; Melde, B. J.; Nasir, M.; Deschamps, J. R. Porphyrin-Embedded Silicate Materials for Detection of Hydrocarbon Solvents. *Sensors (Basel)* **2011**, *11* (1), 886–904.

(31)   Capozzi, L. C.; Mehmood, F. M.; Giagnorio, M.; Tiraferri, A.; Cerruti, M.; Sangermano, M. Ultrafiltration Membranes Functionalized with Polydopamine with Enhanced Contaminant Removal by Adsorption. *Macromolecular Materials and Engineering* **2017**, *302* (5), 1600481.

(32)   Dreyer, D. R.; Miller, D. J.; Freeman, B. D.; Paul, D. R.; Bielawski, C. W. Elucidating the Structure of Poly(Dopamine). *Langmuir* **2012**, *28* (15), 6428–6435.

(33)   Gong, X.; Li, W.; Wang, K.; Hu, J. Study of the Adsorption of Cr(VI) by Tannic Acid Immobilised Powdered Activated Carbon from Micro-Polluted Water in the Presence of Dissolved Humic Acid. *Bioresource Technology* **2013**, *141*, 145–151.

(34)   Li, W.; Gong, X.; Li, X.; Zhang, D.; Gong, H. Removal of Cr(VI) from Low-Temperature Micro-Polluted Surface Water by Tannic Acid Immobilized Powdered Activated Carbon. *Bioresource Technology* **2012**, *113*, 106–113.

(35)   Tang, C.-Y.; Yu, P.; Tang, L.-S.; Wang, Q.-Y.; Bao, R.-Y.; Liu, Z.-Y.; Yang, M.-B.; Yang, W. Tannic Acid Functionalized Graphene Hydrogel for Organic Dye Adsorption. *Ecotoxicology and Environmental Safety* **2018**, *165*, 299–306.

(36)   Elhabiri, M.; Carrër, C.; Marmolle, F.; Traboulsi, H. Complexation of Iron(III) by Catecholate-Type Polyphenols. *Inorganica Chimica Acta* **2007**, *360* (1), 353–359.

(37)   Kim, S.; Kim, H.-J. Curing Behavior and Viscoelastic Properties of Pine and Wattle Tannin-Based Adhesives Studied by Dynamic Mechanical Thermal Analysis and FT-IR-ATR Spectroscopy. *Journal of Adhesion Science and Technology* **2003**, *17* (10), 1369–1383.

(38)   Silverstein, R. M.; Bassler, G. C. Spectrometric Identification of Organic Compounds. *J. Chem. Educ.* **1962**, *39* (11), 549.

(39)   Özacar, M.; Şengil, İ. A.; Türkmenler, H. Equilibrium and Kinetic Data, and Adsorption Mechanism for Adsorption of Lead onto Valonia Tannin Resin. *Chemical Engineering Journal* **2008**, *143* (1), 32–42.

(40)   Garro^Galvez, J. M.; Fechtal, M.; Riedl, B. Gallic Acid as a Model of Tannins in Condensation with Formaldehyde. *Thermochimica Acta* **1996**, *274* (25), 149–163.

(41)   Holopainen, T.; Alvila, L.; Rainio, J.; Pakkanen, T. T. IR Spectroscopy as a Quantitative and Predictive Analysis Method of Phenol–Formaldehyde Resol Resins. *Journal of Applied Polymer Science* **1998**, *69* (11), 2175–2185.

(42)   Gestion de l'eau par les industriels https://www.techniques-ingenieur.fr/base-documentaire/environnement-securite-th5/gestion-de-l-eau-par-les-industriels-42447210/ (accessed Oct 7, 2020).

(43)   BeClood.com. Accueil Memento degremont® de SUEZ https://www.suezwaterhandbook.fr/ (accessed Oct 7, 2020).

(44)   Lee, X. J.; Hiew, B. Y. Z.; Lai, K. C.; Lee, L. Y.; Gan, S.; Thangalazhy-Gopakumar, S.; Rigby, S. Review on Graphene and Its Derivatives: Synthesis Methods and Potential Industrial Implementation. *Journal of the Taiwan Institute of Chemical Engineers* **2019**, *98*, 163–180.

(45)   Jawaid, M.; Ahmad, A.; Lokhat, D. *Graphene-Based Nanotechnologies for Energy and Environmental Applications*; Elsevier, 2019.

(46)   Li, B.; Ou, P.; Wei, Y.; Zhang, X.; Song, J. Polycyclic Aromatic Hydrocarbons Adsorption onto Graphene: A DFT and AIMD Study. *Materials* **2018**, *11* (5), 726.

(47)   Wang, J.; Chen, Z.; Chen, B. Adsorption of Polycyclic Aromatic Hydrocarbons by Graphene and Graphene Oxide Nanosheets. *Environ. Sci. Technol.* **2014**, *48* (9), 4817–4825.

(48)   Gerber, O.; Bégin-Colin, S.; Pichon, B. P.; Barraud, E.; Lemonnier, S.; Pham-Huu, C.; Daffos, B.; Simon, P.; Come, J.; Bégin, D. Design of Fe3–XO4 Raspberry Decorated Graphene Nanocomposites with High Performances in Lithium-Ion Battery. *Journal of Energy Chemistry* **2016**, *25* (2), 272–277.

(49)   Pardieu, E.; Pronkin, S.; Dolci, M.; Dintzer, T.; Pichon, B. P.; Begin, D.; Pham-Huu, C.; Schaaf, P.; Begin-Colin, S.; Boulmedais, F. Hybrid Layer-by-Layer Composites Based on a Conducting Polyelectrolyte and Fe3O4 Nanostructures Grafted onto Graphene for Supercapacitor Application. *J. Mater. Chem. A* **2015**, *3* (45), 22877–22885.

(50)   Murugan, A. V.; Muraliganth, T.; Manthiram, A. Rapid, Facile Microwave-Solvothermal Synthesis of Graphene Nanosheets and Their Polyaniline Nanocomposites for Energy Strorage. *Chem. Mater.* **2009**, *21* (21), 5004–5006.

(51)   Wu, M.-S.; Lin, C.-J.; Ho, C.-L. Multilayered Architecture of Graphene Nanosheets and MnO2 Nanowires as an Electrode Material for High-Performance Supercapacitors. *Electrochimica Acta* **2012**, *81*, 44–48.

(52) Naebe, M.; Wang, J.; Amini, A.; Khayyam, H.; Hameed, N.; Li, L. H.; Chen, Y.; Fox, B. Mechanical Property and Structure of Covalent Functionalised Graphene/Epoxy Nanocomposites. *Scientific Reports* **2014**, *4* (1), 4375.

(53) Sun, H.; Jiang, J.; Xiao, Y.; Du, J. Efficient Removal of Polycyclic Aromatic Hydrocarbons, Dyes, and Heavy Metal Ions by a Homopolymer Vesicle. *ACS Appl. Mater. Interfaces* **2018**, *10* (1), 713–722.

(54) Evans, C. H.; Partyka, M.; Van Stam, J. Naphthalene Complexation by β-Cyclodextrin: Influence of Added Short Chain Branched and Linear Alcohols. *Journal of Inclusion Phenomena* **2000**, *38* (1), 381–396.

(55) Ammar, A.; Al-Enizi, A. M.; AlMaadeed, M. A.; Karim, A. Influence of Graphene Oxide on Mechanical, Morphological, Barrier, and Electrical Properties of Polymer Membranes. *Arabian Journal of Chemistry* **2016**, *9* (2), 274–286.

(56) Lai, Q.; Zhu, S.; Luo, X.; Zou, M.; Huang, S. Ultraviolet-Visible Spectroscopy of Graphene Oxides. *AIP Advances* **2012**, *2* (3), 032146.

(57) Gazeau, F.; Lévy, M.; Wilhelm, C. Optimizing Magnetic Nanoparticle Design for Nanothermotherapy. *Nanomedicine (Lond)* **2008**, *3* (6), 831–844.

(58) Ménard, M.; Meyer, F.; Parkhomenko, K.; Leuvrey, C.; Francius, G.; Bégin-Colin, S.; Mertz, D. Mesoporous Silica Templated-Albumin Nanoparticles with High Doxorubicin Payload for Drug Delivery Assessed with a 3-D Tumor Cell Model. *Biochimica et Biophysica Acta (BBA) - General Subjects* **2019**, *1863* (2), 332–341.

(59) Cázares Cortés, E. D. C. Synthèse de Nanogels Biocompatibles et Multi-Stimulables Pour La Libération Contrôlée d'une Molécule Modèle Par Hyperthermie Magnétique et Photothermie. These de doctorat, Paris 6, 2017.

General Conclusions

The objective of this thesis was to develop new functional materials highly efficient and, if possible, recyclable for iron, phosphate and sodium removal from biological media (blood).

Since several years, the removal of molecules and ions are mainly focusing on environmental applications for purification purposes. Similar removal processes could, in theory, also be used in medical science. Indeed, there are several issues concerning problems of purification in human body. These issues have different origins: genetic illness, dysfunction of organs, endocrinal problems, medication errors or an overconsumption of such molecules/minerals. Depending on the overdose level, the age of the patient and the element, the consequences are not the same. When for one, the excess is traduced by aches and pains, for the other, it can be dramatic or deadly. Thanks to our knowledge in nanoparticle design and functionalization, we proposed the application of iron oxide particles with a raspberry-shaped morphology and stellate mesoporous silica nanoparticles to improve medical treatments and specially to purify blood from toxic elements. To ensure a specific medical purification, their design was optimized. In this frame, the surface functionalization, the size and the chemical composition were tuned in order to get materials which could be adapted in medical treatments for the purification of blood.

We have targeted three elements toxic when in excess in blood: iron, sodium and phosphates. With the newly designed nanocomposites, we look to improve two different medical treatments aiming at extracting these elements with a high and controlled yield: chelatotherapy (iron) and peritoneal dialysis (sodium and phosphate).

In chapter II, we have synthesized stellate mesoporous silica nanoparticles and optimized the grafting of a chelating ligand of iron: desferrioxamine at their surface to enhance the iron capture. Here, we successful synthesize STMS particles with a mean diameter of 100 nm and a surface specific area of 500 $m^2 \cdot g^{-1}$. Their functionalization was optimized by three easy steps. We have so obtained NPs (called DFoB-STMS) with a high grafting rate (730 $nmol_{DFoB} \cdot mg_{SiO2}^{-1}$). These materials showed a fast capture of iron (<30 min) and a specific capture of iron over other cations (Fe^{3+} > Al^{3+} >> Mg^{2+}, Na^+...). Such nanomaterials could also be applied in iron environmental purification. Indeed, iron is an important micronutrient in aquatic environment. As for humans, high iron levels have been found to cause pathological problems in fishes. They may also affect aquatic species indirectly by killing off their food sources. Consequently, iron excess can also increase mortality in ecosystems. The DFoB-STMS nanobjects that we have developed here, could be used as a possible way to depollute water from iron. However, one problem could be the very small size of these nanoparticles. And, the recollection using a centrifuge could be not easy-to-use for applications in larger scales but we have shown that we can coat highly magnetic nanoparticles by a mesoporous silica shell which should facilitate a magnetic handling of such nanomaterials.

Following the same principle than for Chapter II, Chapter III deals with the functionalization of STMS with crown-ether 15-5 (CE-STMS,) and cryptand [2.2.1] (C_{221}-STMS). We succeeded in grafting 742 $nmol_{CE} \cdot mg_{SiO2}^{-1}$ but CE-STMS was found to be not adapted for water media and an optimal sodium

capture was only observed in a cosolvent methanol-water. That is why, we chose another ligand cryptand [2.2.1] but we faced grafting problems. We have tested different grafting methods and the best solution was to coat MS with PEI and then to couple cryptand on PEI using HBTU cross-linker. Thus a grafting rate of 219 $nmol_{C221} \cdot mg_{SiO2}^{-1}$ has been obtained. In addition, C_{221}-STMS particles presented good colloidal stability in water, which allows the possibility to use them in aqueous media. The uptake of sodium in water was therefore successful with these C_{221}-STMS particles. In addition, in an equivalent of dialysis media, they were shown to allow a specific capture of sodium ($Na^+ > Mg^{2+} > Ca^{2+}$). For the first recyclability experiments: removal of 40 % of sodium in cages was obtained. In the future, we need to optimize the grafting rate of C_{221} and solutions are to use longer chains as linkers between STMS and cryptands. This would bring more flexibility for the coupling of C_{221} but also for the Na chelation.

With these promising results, we can imagine grafting other cryptands or crown-ether on the surface of STMS to remove selectively other cations in excess (as iron and sodium) or radioactive elements in other applications such purification in environment. Indeed, it is also interesting to remove sodium from drinking water in order to avoid high blood pressure, risks of heart disease or stroke. Another striking subject concerning sodium is the sea water desalinization. Indeed, actual methods are very costly (osmosis, exchange membranes…) and not very effective. Moreover, the water pollution of rivers, lakes and groundwater, combined to an exponential demographic explosion, provoke an urgent need of a new drinking water source. Consequently, sodium removal becomes an interesting axis of research to provide drinking water from seawater. As for DFoB-STMS, CE-STMS and C_{221}-STMS could be an axis to improve desalination. They are highly selective for few elements (sodium, calcium, potassium) and can be used in large scales. Nevertheless, we cannot omit the high cost of cryptands as an additional dissuasive factor (in addition to the previous already exposed reasons).

In chapter IV, we have treated the different issues of phosphates in blood. In the first part, we have optimized the synthesis of RSN and RSN doped with Zn, Co and Al. We showed the issues of RSN synthesis by evidencing the influence of the origin and ageing of the iron precursor: a hydration of precursor has been demonstrated which has an effect on the size of RSN and on the synthesis mechanism of RSN. Other parameters were shown crucial, and in particular for the RSN doping, such as the mixing time to dissolve the reactants and the reaction times. After the control of the experimental parameters, we focused on the synthesis of RSN with the highest specific surface area and defined a new protocol.

The doping with Zn was difficult in our experimental conditions due certainly to a problem of dissolution of the zinc precursor. Other zinc precursor should be tested. The doping by cobalt was realized by acting on the reactant mixing time. The doping by Al was easy due to the common features between Al and Fe ions but Al decreases the magnetization of RSN and thus low Al content are required.

In the second part of chapter IV, we showed the potential of our two materials to remove phosphates in the peritoneal dialysis. For this, we showed that both materials may remove a high amount of phosphates in less than 3 hours. Moreover, the aluminum doping increases the RSN specific surface

area and shifts the isoelectric point, which enhance the electrostatic interactions between deprotonated phosphates and the protonated surface of iron oxide RSN. Therefore, higher phosphate removal capacity was noticed with Al-RSN. A set-up to simulate in vitro PD has been build and preliminary tests have been performed to optimize the device. Now, it would be interesting to test in this device Al-RSN for phosphate capture as well as C_{221}-STMS for Na capture.

Besides these experiments, we may observe that even if we presented phosphates as a problem of health, phosphates are one the most important biomolecules in life involved in a wide range of metabolic pathways. Nevertheless, in high concentration, phosphates can cause severe damage to the ecosystem and to the human body. Indeed, the constant progress and development of the agriculture and industry fields, increase the amount of released phosphate in nature, hence the amount of wastewater. When discharged into lakes, rivers or any other natural water sources, damages are dealt both to the environment and indirectly to the human health. Therefore, such Al-RSN could be also tested for phosphate environmental depollution.

In the last chapter, we firstly focused on the "optimization" of these nanomaterials for environmental applications only. Core-shell RSN@SiO$_2$ nanocomposites were designed to increase the size of the previous functionalized STMS (to be able to apply them in environmental projects) and to facilitate their magnetic extraction from media. The idea is to adapt the previous grafting protocols on these new systems to graft different specific ligands to remove other toxic metals or molecules.

In the second part, we have grafted at the surface of STMS particles and of RSN, designed molecules to remove polycyclic aromatic hydrocarbons (PAH), which are highly polluting molecules. For that, we chose molecules able to create π-stacking interactions between the grafted molecules and the PAH. The selected molecules were TMOPES for STMS and Polydopamine and Tannic acid for RSN. We have also combined graphene and RSN for PAH removal: graphene is expected to capture PAH and the magnetic RSN should ensure an easily removal of the composite from water thanks to their magnetic properties. The first tests with naphthalene were encouraging and the system needs to be further optimize. However, these results are a proof of principle of the high potential of these materials for further depollution projects. Furthermore, other groups have shown the capacities of graphene oxide to interact with phosphates and thus FLG@RSN composites would be interesting to test for dephosphatation. Based on these results, our synthesized FLG@RSN could find interesting applications in peritoneal dialysis treatment and phosphate depollution.

Annexe
Characterization methods

FTIR Spectrometry

This method (abbreviated FTIR) was used as a clue to determine the chemical composition of the RSN and STMS, the phosphates, citrates, glucose, polydopamine and tannic acid on the surface of RSN or Al-RSN, the grafting of DFoB and TMOPES on STMS and to compare the different iron chlorides precursors. This method was also used to perform the washings of RSN and Al-RSN after the reaction. However, for a long period, we were affronted to an impurity on the KBr support, this last avoid the complete interpretation of the phosphates anchoring.

It is based on the absorption of frequencies of bonds depending on the shape of the bonds, the molecular potential energy surfaces, the amos mass and the associated vibronic coupling. A particular signal is associated to the interaction bond, this information helped to recognize the nature of the bond.

This method allowed us to show the presence of phosphates on the surface of RSN, the efficiency of washings for RSN and the presence of organic molecules grafted on the surface of STMS.

The IR spectra were recorded in a Perkin Elmer Spectrum Instrument: FTIR via KBr disks containing the sample. ATR via pressing the sample.

Granulometry and Zeta Potential measurements

Granulometry measurements

Stable suspensions of nanoparticles are required to the surface modification, or for further applications. The granulometric measurements by dynamic light scattering (DLS) or photon correlation spectroscopy (PCS) ensures a result to help the verification of the colloidal stability. The principle

k : Boltzman constant
T : Temperature, for the measurement : 25°C
η : dynamic viscosity of the media
D : Difussion coefficient

consists on linking the intensity of an incident scattered beam by the nanoparticles versus time. Then, the hydrodynamic diameter Dh is determined by the Stokes-Einstein equation:

$$Dh = \frac{kT}{3\pi\eta D}$$

This value takes part of the size of the NP, the molecules on surface and the ionic double layer.

In case of a colloidal suspension, a laser beam in contact with the suspension is diffused by particles: small particles will diffuse faster than big particles, so, a captor will register the scattered light density fluctuation versus time. The variation will be fitted to calculate the delay time which is related to the diffusion coefficient by parameters concerning the instrument.

The zetasizer Nano ZS from Malvern DLS was used to characterize the properties of colloidal suspensions: the hydrodynamic diameter and the dispersity in size in intensity mode with a laser emitting at 623 nm, 25°C and detector position at 173°. Measurements of surface Zeta potential were performed to get insights into the surface charge of the particles.

The next tables summarize the parameter used during the measurements of DLS:

	Dynamic Viscosity (25°C)	Refractive Index
Water	0.8872 cP	1.330
Ethanol	1.2 cP	1.361

	Refractive Index	Absorption
IO	2.420	0.1
Silica	1.460	0.010

Zeta Potential measurements

Colloidal suspensions are formed from particles (solid, liquid or gas) in suspension in a solution. In case of a colloidal suspension formed of a liquid as matrix and a solid as particle, the zeta-potential is the difference of potential between the medium and the charged layer around the particles. It is often the only value that can be used to describe double-layer properties of a colloidal dispersion. I want to underline the importance of pH in these measurements: for a higher pH more negative charges will be present in solution, contrary to a low pH, the units are usually in millivolts (mV).

This measurement is used to indicate the stability of colloidal solutions. For small particles, a high absolute value is synonym of stability because of the electrostatic repulsion between particles; contrary, a small absolute value attractive forces can be stronger, so particles will be attracted and aggregate. A solution with a zeta-potential of 0 mV corresponds to the isoelectric point (IEP), in other words, they are around the same quantity of positive and negative charges and particles tend to aggregate. As general indicator, a solution with an absolute value superior to 25 mV, the colloidal solution is considered as stable.

Zeta potential can only be calculated from models or by experiments, based on electropheric mobility. To determine this value, an electric field is applied across the diluted suspension, particles will migrate toward the opposite charged electrode.

ICP-AES (Inductively coupled plasma-atomic emission spectroscopy)

Quantification of element samples (Na, Fe, K, Al, Ca) inside the different supernatants was performed in a Varian 720ES at RePSeM, inorganic plateform, UMR 7178, by Dr. Caroline Bertagnolli.

This method uses the intensity of the light emitted from a plasma at a particular wavelength (unique for an element) to determine the concentration of the sample.

Depending on the samples, dilutions can be modified in order to work with less of 5% of volume of organic solvents.

N$_2$ Adsorption Isotherm

To characterize the porosity of the silica nanoparticles, adsorption and desorption of nitrogen isotherms were measured on a ASAP 2420 V instrument with around 100 mg of STMS nanoparticles. The Brunauer-Emmett-Teller (BET) model was used to calculate the surface area, and the pore size was obtained according to BJH (Barrett, Joyner and Halenda) model.

Relaxometry-Nuclear Magnetic resonance (NMR)

In this work, relaxometry was used to quantify the iron concentration in solutions, depending on the source, preparation of samples is different, nevertheless, the measured solutions contain all a volume of 200 µl, 2% of HNO3 and were heated at 37°C at least 15 minutes.

The relaxation time T1 was measured on a Brucker Minispec Instrument (60MHz, 1.41T). The T1 measurement uses the inversion-recovery sequence: a pulse inversion of 180° followed by a measurement at 90° after a delay tau.

The protole was set up with a first value of 100 ms, the following measurements were adjusted in function of the T1 measured, in general 3 repetitions are needed to obtain an acceptable amplitude value (error < 5%)

Scattering Electronic Microscope

The Scattering Electronic Microscope allows to record images of the solid materials at different magnifications. Contrary to the TEM, in the SEM images, the recorded images have different dimensions.

In this technique, a beam of electrons interacts with atoms in the surface of the sample. To register an image, the different detectors will recover elements of different source: retro diffusion of electrons of the incident beam, emission secondary electrons, emission of X-Ray, emission of photons UV-Vis… The whole allows the construction of an image.

During this thesis, the SEM recorded images of the ensemble of the RSN and FLG@RSN synthesis and the aspect of the iron chloride precursors. A drop of the RSN dispersed on methanol was deposited on

a silicium support. Thanks to the SEM micrographs, the size of RSN were measured. For that, only the RSN in the first plan were measured.

The SEM use were the JEOL 6700F and the Zeiss GeminiSEM 500.

Spectrophotometry UV-Visible

UV-Visible spectrophotometry is a method to quantify the absorbance of light of a chemical substance by measuring the intensity of light as a beam of light passes through sample solution. For absorbance measurements, the instrument must be settled at the wavelength of maximal absorption ([λmax-150nm ; λmax+150nm]).

To calculate concentration with absorption light, Beer-Lambert law was considered to express in equation: $$A = \varepsilon \times l \times C$$

Where:

ε: molar attenuation coefficient (L mol^{-1} cm^{-1})

C: concentration of solution (mol L^{-1})

A: value of absorption light (no units, since $A = log_{10} P_0 / P$)

An unknown concentration of a test sample can be determined by measuring the amount of light that a sample absorbs and applying Beer's law. In contract, in highly concentrated samples, the law may not be followed very well due to saturation effects, changes in the refractive index and other effects and no solute-solute interactions, in the other hand it requires relatively low analyte concentration (<0.01 M). Moreover, no apparent chemical deviations, when an analyte associates dissociates or react with the solvent creating another chemical species.

The solutions were analyzed) with quartz optical cell (Hellma) using either a CARY50 Probe Varian absorption spectrophotometer or an Agilent CARY5000 absorption spectrophotometer maintained at 25.0°C (Lauda E200 thermostat).

Magnetic measurements

The magnetic measurements were performed in a superconductive quantum interface device (SQUID). With this device, the behavior of a sample can be recorded under different conditions such as temperature or an external magnetic field.

The used SQUID was a Quantum Design – MPMS 3-SQUID-VSM. M(H) curves were recorded for the RSN and doped RSN at 300 K. This analysis allowed to confirm the superparamagnetic (or not) behavior of the RSN, to measure the saturation magnetization (Ms) and to give a coercive field (Hc) and remnant magnetization (Mr).

Transmission Electronic Microscope

A transmission electron microscope JEOL 2100 high-resolution microscope operating at 200 kV was used to characterize the size and morphology of the STMS silica and ferrite RSN.

This technique used a beam of electrons which are transmitted through the sample. The detector will reconstruct an image thanks to the interaction of electrons with the sample.

TEM is a very local analysis to record 2D micrographs which allows to calculate the mean size of the different batches of nanoparticles for RSMS and grains for RSN. Thanks to this technique, we can also observe the lattices fringes of nanograins by recording high resolution images (HRTEM).

EDS (energy dispersive spectroscopy) was used to evaluate the composition of the NPs. In this technique, the emission of a photon is followed by the relaxation time of an atom after the removal of a core electron.

Thermogravimetric Analysis

TGA is a quantitative measurement of mass loss when a sample is heated. With this method, it is possible to calculate the hydration of a sample, the organic composition of a sample, the different reactions depending on the temperature. For this thesis, the TGA was used to quantify the organic grafting on STMS (DFoB, CE, C221, TMOPES), moreover, to estimates the water amount inside the different precursors of iron chloride.

This instrument is composed by a thermosensitive balance which saved continuously the mass variation. Depending on the model, constructors speak about horizontal and vertical balance

TGA was performed on a TA SDT 600 instrument to measure the loss mass of the sample when the temperature changed. Consequently, the amount of organic compound grafted on functionalized inorganic STMS nanoparticles can be quantified.

X-Ray Diffractometer

The XRD patterns provided by a X-ray diffractions provides a clue about the chemical structure thanks to the position and the intensity of the diffraction peaks. Each peak is linked to a specific reflection of a Bragg plan of the crystal. This last follows the Bragg law: $2d_{hkl}\sin\theta=\lambda n$, where d_{hkl} is the inter-reticular distance, θ is the Bragg angle and n, the diffraction order. For the user XR diffractometer, λ, the wavelength corresponds to $K\alpha=1.5406$ Å.

The ensemble of XRD patterns were used to identify the different spinel structures, thanks to a profile matching with the software Fullprof, we calculated the crystallite size and the lattice parameter of the different ferrites. This refinement consists of the comparation of the experimental and the theory XRD patterns. To match both patterns, the software Fullprof uses the LeBail method and the modifies Thompson-Cox-Hasting pseudo-Voigt profile function.

The XRD was a Bruker D8 Advance.

Annexe
Supporting Information of Chapter II

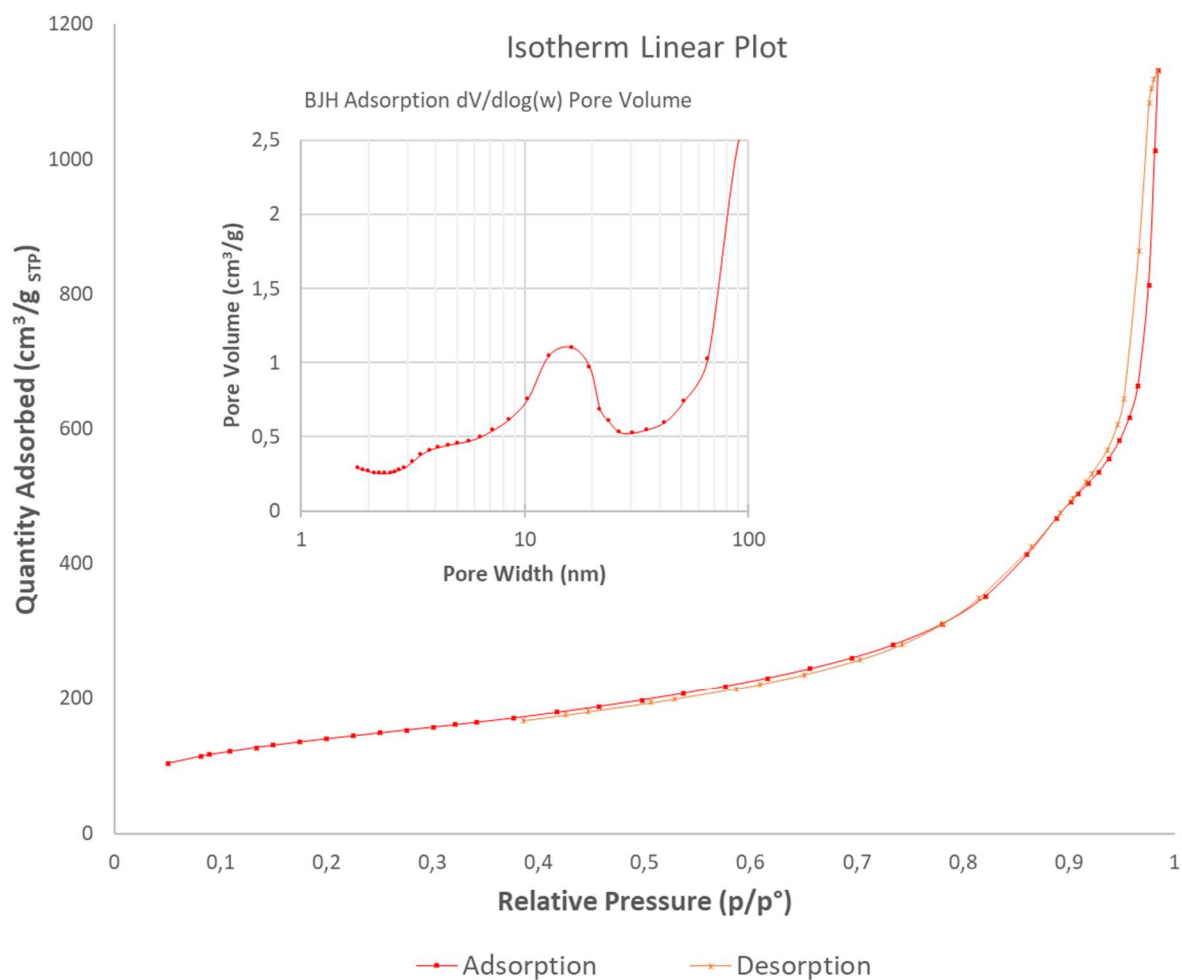## Figure S1. N$_2$ BET isotherm adsorption of STMS NPs.

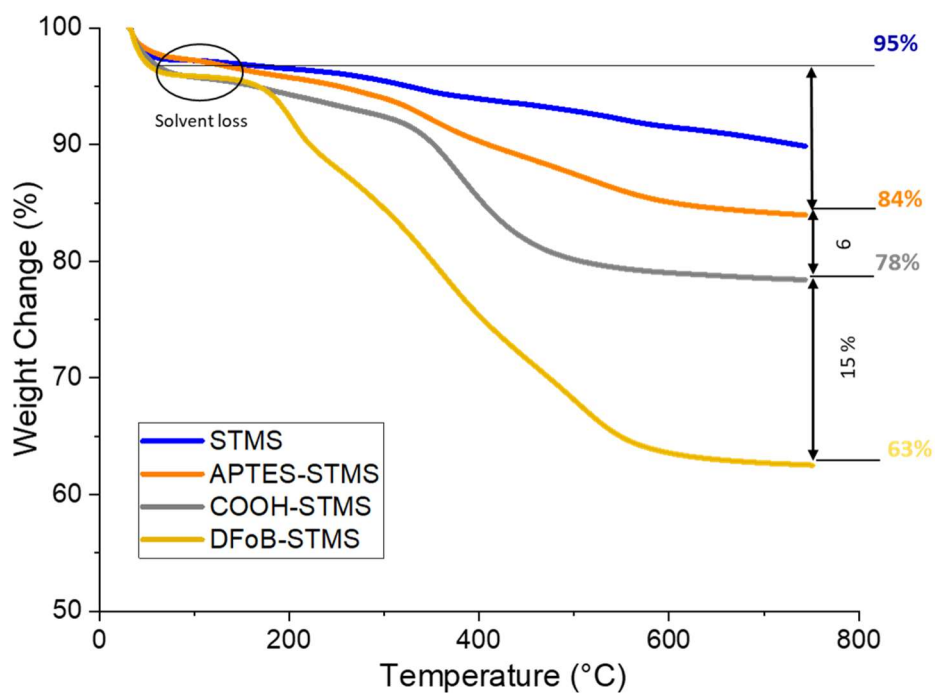# Figure S2. TGA: evaluation of number of functions grafted.

Table S1 Thermogravimetric analysis

$$\textbf{Grafting rate} \left(\frac{\mu g \text{ function}}{mg \text{ STMS}} \right) = \frac{\text{amount of function grafted (}\mu g)}{\text{amount of STMS (mg)}}$$

Step	SiO_2 (wt%)	APTES (wt%)	COOH (wt%)	DFoB (wt%)
APTES-STMS	84	9		
COOH-STMS	78	8.4	8.6	
DFoB-STMS	63	6.8	6.9	15

1. The calculation of APTES (wt%) is based on the constant of SiO_2.

2. The calculation of COOH (wt%) is based on the constant of SiO_2 and APTES-SiO_2.

3. The calculation of DFoB(wt%) is based on the constant of SiO_2 and APTES-SiO_2 and COOH-SiO_2.

Table S2 CHNS Analysis

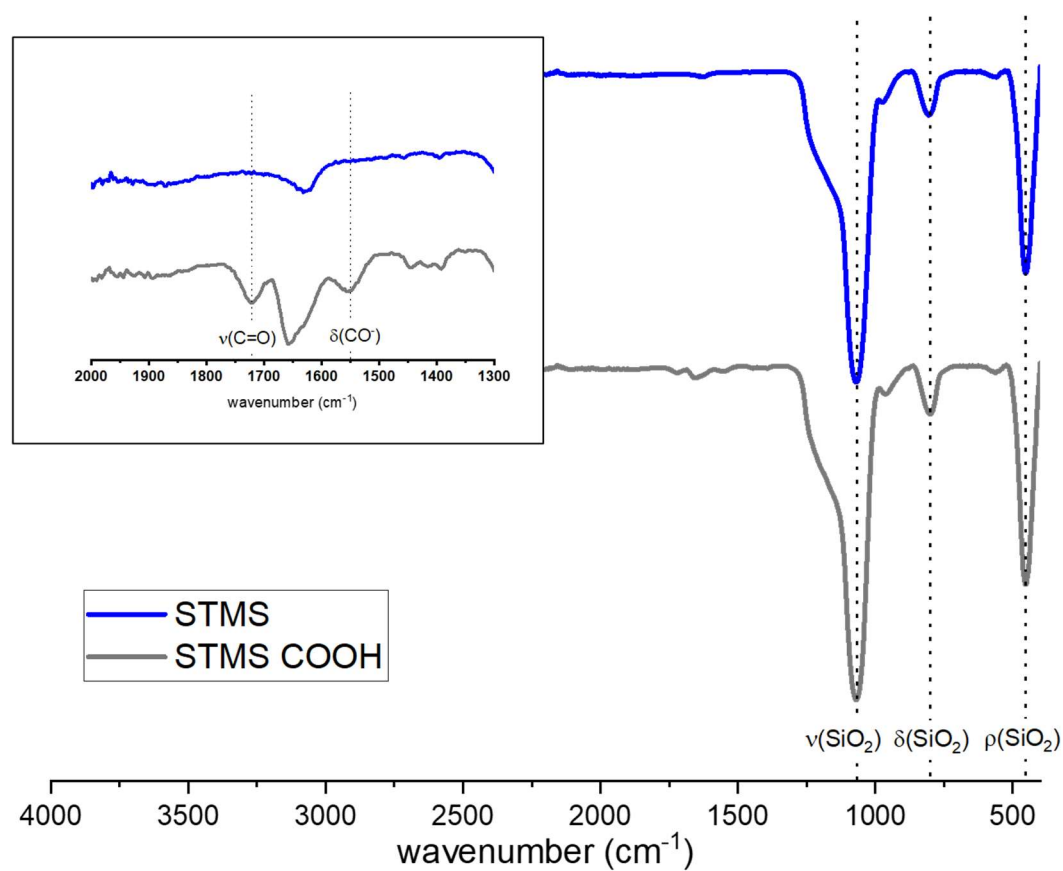| Sample	N (wt %)	C (wt %)	H (wt %)
APTES-STMS 1	2.82	7.65	2.04
APTES-STMS 2	2.81	7.75	2.06

Initially, we have $2.82 \cdot 10^{-2}$ ($g_N/g_{APTES-STMS}$).

So, 2 $mmol_N/g_{APTES-STMS}$ $\rightarrow$ 2.38 $mmol_N/g_{STMS}$ (0.84 g of STMS in 1 g of APTES-STMS).

We know the specific surface area of STMS is: 498 m²/g

So, we grafted $4.76 \cdot 10\text{-}3$ $mmol_N/m^2$ $\rightarrow 4.76 \cdot 10\text{-}24$ mol_N/nm^2 = 2.75 N/nm² ~ 2.75 $NH2_{functions}/nm^2$

Figure S3. FTIR of STMS and COOH-STMS

Assignment	Band in STMS sample (cm^{-1})	Band in COOH-STMS sample (cm^{-1})
Si-O rocking	449	452
Si-O bending	804	803
Si-O stretching	1073	1066
C-O$^-$ bending	/	1548
C=O stretching	/	1722

S4. Calibration curve UV-Vis Spectroscopy measurement

The supernatants containing FeNTA could be directly assayed by UV-Vis spectroscopy (λ_{max} = 270 nm). However, for our study, the absorption spectrum of the FeNTA ferric complex is flooded by another peak (linked to HEPES-FeNTA) at about 210 nm. To overcome this issue, it was necessary to titrate iron(III) spectroscopically at other wavelengths. For the analysis of FeNTA supernatants, 1.1 eq of DFoB in solution (DFoB$_{free}$) were added to 1 ml of the supernatant solution. The color changed from light yellow to orange confirming the ligand exchange. The solutions were then analyzed by the UV-Vis absorption spectrophotometry (CARY50 Probe Varian). A standard calibration curve was first obtained by measuring the absorbance values at 430 nm (λ_{max} of the Fe**DFoB** complex) in a HEPES buffer (50 mM, 3 ml). For this purpose, a HEPES solution (50 mM, pH 7.4) containing a known amount of Fe(III) (6.6×10^{-3} M) was prepared and increasing amounts of a DFoB$_{free}$ solution (1.27×10^{-2} M) were added. The absorbance of the mixture DFoB+Fe^{3+} (FoB complex) was measured. Using a linear regression, the extinction coefficient for the complex FoB was determined to be ε_{430} = 2950 M$^{-1}\cdot$cm^{-1}, which is slightly higher than the values determined in water by other groups[1]. Thus, the iron exchange ratio was determined to be 1.02 mol of DFoB$_{free}$ for 1 mol Fe**NTA**.

Calibration curve FoB in HEPES

- **Molar extinction coefficient**
  ε_{430nm} = 2950 cm$^{-1}\cdot$M^{-1}
- **Exchange Stoichiometry**
  Fe**NTA:**DFoB 1:1.02
- **Exchange kinetics**
  Instantaneous
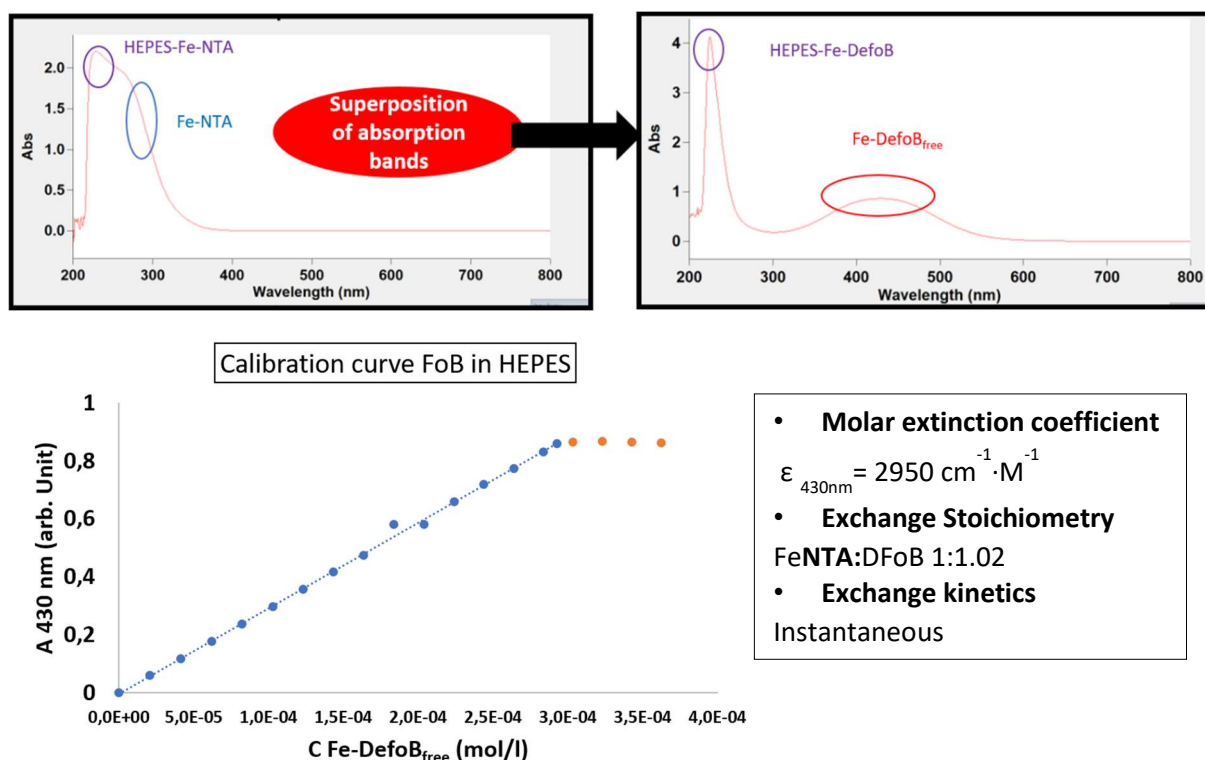
(1)   Evans, P.; Kayyali, R.; Hider, R. C.; Eccleston, J.; Porter, J. B. Mechanisms for the Shuttling of Plasma Non-Transferrin-Bound Iron (NTBI) onto Deferoxamine by Deferiprone. *Translational Research* **2010**, *156* (2), 55–67.

Annexe
Supporting Information of Chapter IV

Washings of RSN

RSN washing is an essential research to avoid toxicity problems linked to unreactive and side products. In our reaction, EG is linked to several toxicities. To use RSN in bioapplications, the surface must be mandatory clean. Several technics were performed to recover the RSN-bare faster and with the easiest method. To know the efficacity of washings, the ratio Fe-O/C=O$_{EG}$ is calculated, for all the methods, this ratio increased with the washings.

Two different methods were used. The first consist on several washings, the 3 first consisted on the classical previously determined by the team (3x Ethanol), the other 6 washings are a cosolvent EtOH:Acetone (1:3) or only warm acetone (65 °C): for each washing, nanoparticles are ultrasonicated during 3 minutes and magnetically precipitated. Here, 50 mL of the solvent are added in a tube containing RSN, this tube is ultrasonicated between 4-5 minutes and, finally, RSN are separated from the solvent with a magnet. The second method was performed by Dr. Geoffrey Cotin during his post-doc in the group. The principle is very easy: acetone is used to remove the organic molecules excess after the nanoparticles synthesis by thermal decomposition, so to remove the most of secondary elements, nanoparticles are mechanically stirred in a big volume of acetone for 60 minutes. To improve the washings, after this time, RSN are magnetically precipitated and redispersed in the same volume of acetone. This process was repeated 3 times. The evolution of washings is followed by FT-IR.

The next table summarizes the recovered results of washings. For the first method, comparing the three different solvents, we can conclude thanks to the final Fe-O/C=O ratio: The most efficient washings were the mix ethanol-acetone (8.2) and the hot acetone (7.8). In fact, the initial washings (water+ethanol) were not sufficient, as we can see, a big quantity of EG stayed in the surface of RSN (Fe-O/EG= 0.66). Another interesting point is the acetone role during washings: without acetone, more washings are needed to remove ethylene glycol, however, a of ethanol-acetone or only acetone are sufficient. We also observed than more than 12 washings, the ratio did not increase, we can conclude than the globality of ethylene glycol was removed.

For the second method, as before, the diminution and deformation of EG Band is observed, so, an augmentation of the ratio Fe-O/EG after several washes is noted. Moreover, the band at 1100 cm-1 started being deformed since the end of the second washing (L2-60), we can consider the majority of

EG has been removed. The final reported value of the ratio is 7.30 (W3-180 minutes), the band of EG is completely deformed and its shape is close to these of KBr (which presents Impurities-Chapter IV).

To conclude about the washings, several washings with acetone are needed. Two methods are possible to remove ethylene glycol. It is interesting to compare them: even if the first method is shorter, the constant ^presence of the experimenter is needed to ensure the different steps and dead time is very short (less than 5 minutes), on the other hand, the other method only requires around 20 minutes of presence time, for further scaled-up experiments, this last method could be very interesting.
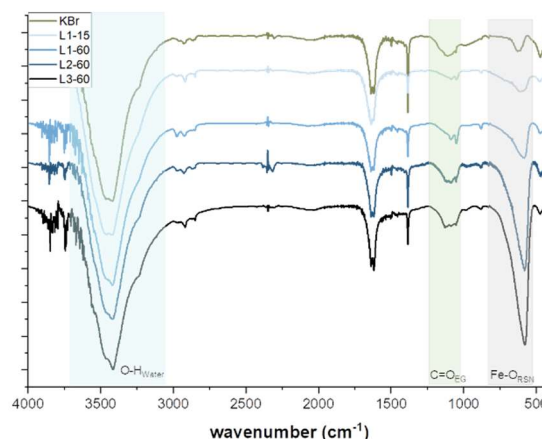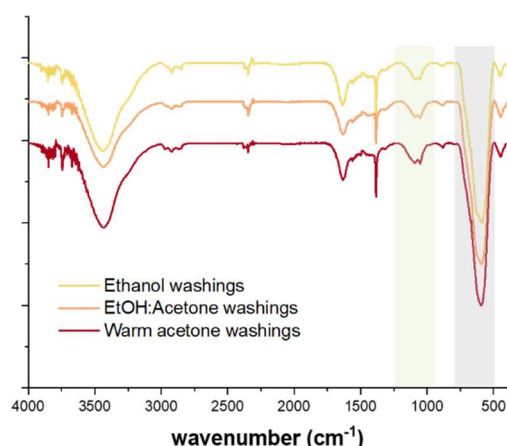
Washing	Water x3 EtOH x3	Water x3 EtOH x9	**Water x3 EtOH x3 EtOH:Ac (50:50) x6**	**Water x3 EtOH x3 Ac x6**	EtOH x1 EtOH:Ac (50:50) x6	EtOH x1 Ac x6	**Constant stirring Method (x3)**
Total number of washings	6	**12**			7		**3**
Temperature	**RT**			**~60°C**	RT		**60°C**
Stirring	Ultrasonication 4min						**Mechanic stirring 1h**
Time (approx.)	1h	**2h**			1h		**3h**
Ratio Fe-O/EG (FTIR)	**0.66**	**5.4**	**8.2**	7.8	**3.3**	**6.7**	**6.7**

Ingénierie de nanocomposites recyclables pour l'élimination de polluants

Contexte

Les nanomatériaux de silice et d'oxyde de fer sont souvent utilisés dans les traitements de purification de l'eau, de l'air et des sols. D'une part, les nanoparticules de silice mésoporeuse (MS) sont considérées comme l'un des adsorbants les plus polyvalents et les plus efficaces pour l'élimination des polluants environnementaux. Récemment, ces matériaux (fonctionnalisés ou non) ont été appliqués comme adsorbants de polluants. L'avantage de ces matériaux est leur grande surface spécifique, un bas prix de production et leur facilité de fonctionnalisation. D'autre part, les nanoparticules d'oxyde de fer présentent des propriétés magnétiques intéressantes combinées à une facilité particulière de modifier leur surface ou à des affinités avec certains éléments. Ceci en fait un composé de choix pour purifier des milieux pollués. En raison des propriétés intéressantes des nanomatériaux à base de silice et d'oxyde de fer, ils sont choisis pour des applications de purification environnementale.

D'un autre côté, certains problèmes de purification existent également en médecine. Donc, tels nanomatériaux pourraient également améliorer les traitements de purification du sang. Dans ce contexte, nous considérons deux problèmes de santé : l'hémochromatose traitée par chélatothérapie et l'insuffisance rénale traitée par dialyse péritonéale.

• L'hémochromatose est une maladie génétique. Ici, l'organisme ne peut pas réguler naturellement les niveaux de fer. L'excès de fer est stocké dans les différents organes et cause leur dysfonctionnement (cirrhose, problèmes hépatiques). Les traitements actuels de chélatothérapie présentent de nombreux effets secondaires dus au court temps de circulation du médicament dans l'organisme. Ainsi, pour améliorer ce traitement, des biomatériaux peuvent être conçus pour augmenter le temps de circulation des chélateurs.

• L'insuffisance rénale consiste en un dysfonctionnement d'au moins un rein. La conséquence immédiate est que le sang cesse d'être purifié ce qui conduit à une accumulation de toxines supérieur aux niveaux standard. La dialyse vise à éliminer les éléments très nocifs du sang, tels que le sodium et le phosphate. Cependant, parmi les deux types de dialyse, l'hémodialyse est plus efficace que la dialyse péritonéale. Quoi qu'il en soit, la dialyse péritonéale possède des avantages économiques et de confort pour les patients. De plus, elle peut être appliquée chez les enfants et les nouveau-nés (impossible avec l'hémodialyse). Pour améliorer la purification du sodium et du phosphate, l'objectif est de concevoir des matériaux et de les introduire dans la solution de dialyse afin d'améliorer l'élimination de ces éléments du sang.

Dans ce contexte, l'objectif de ma thèse est de développer de nouveaux matériaux fonctionnels hautement performants et, si possible, recyclables pour l'élimination du fer, du phosphate et du sodium des milieux biologiques (sang). Les particules magnétiques d'oxyde de fer seront conçues pour l'élimination du phosphate tandis que la silice mésoporeuse sera recouverte de ligands chélateurs conçus pour l'élimination du fer et du sodium.

Le premier chapitre (partie bibliographique), décrit le principe de la dialyse péritonéale. Ensuite, les nano-objets qui seront utilisés pour faire face à ces défis sont décrits. Ils sont constitués de silice mésoporeuse recouverte de ligands chélateurs et de particules magnétiques d'oxyde de fer en forme de framboise.

Le deuxième chapitre est centré sur l'élaboration de particules de silice mésoporeuse stellaire greffées avec de la desferrioxamine. Ce matériau a été conçu pour résoudre les problèmes de purification rencontrés lors de l'absorption de l'excès de fer dans le corps.

Le troisième chapitre est consacré à l'amélioration de l'extraction du sodium par dialyse péritonéale. Les précédentes particules de silice mésoporeuse stellaire ont été greffées avec des molécules porteuses de fonctions sodium chélatantes (couronne-éther et cryptand).

Le quatrième chapitre traite de la conception de nanoparticules d'oxyde de fer magnétiques pour l'absorption de phosphate dans la dialyse péritonéale, dans un premier temps. Des nanostructures d'oxyde de fer de morphologie framboise et présentant une saturation magnétique élevée ont été sélectionnées et leur synthèse reproductible a été étudiée. Le dopage des particules d'oxyde de fer avec de l'aluminium s'est avéré prometteur pour améliorer la capture du phosphate. Deuxièmement, la capture de phosphates avec les objets d'oxyde de fer synthétisés sont caractérisés et utilisés dans un modèle in vitro de dialyse péritonéale.

Enfin, le dernier chapitre présente des expériences préliminaires qui ont été réalisées afin de tester notre nano-objet pour l'élimination des polluants de l'eau et des milieux liquides. Dans la première partie du chapitre, le revêtement de particules magnétiques en forme de framboise d'oxyde de fer avec de la silice mésoporeuse a été étudié. Ici, le but était de combiner la grande surface spécifique et les propriétés de surface de la silice mésoporeuse avec les propriétés magnétiques des particules. Après le greffage du ligand en surface, nous étions censés obtenir des particules conçues avec des propriétés chélatantes élevées qui sont faciles à éliminer des milieux pollués en appliquant un champ magnétique. La deuxième partie de ce chapitre consiste en la conception de nanomatériaux capables de capter les hydrocarbures aromatiques polycycliques (HAP). Nous avons conçu plusieurs matériaux tels que : de la silice mésoporeuse greffée avec des ligands, des particules d'oxyde de fer enrobées et des particules d'oxyde de fer supportées sur une couche de graphène. Ce type de matériau pourrait aider à purifier l'eau et l'air ou à être appliqué dans le processus de quantification des HAP.

Objectifs

Pendant cette thèse, des matériaux innovants, avec une grande surface spécifique et dont la surface puisse être adaptée pour capter et relarguer les différents polluants ont été développés. Différents aspects sont combinés lors de ce projet : de la recherche fondamentale (interactions particules-polluants, modèles d'isotherme d'adsorption, complexation des métaux), le développement de nouveaux matériaux (particules magnétiques ou à base de silice mésoporeuse recyclables et à forte capacité de sorption/désorption des polluants) et la mise en œuvre d'une technologie (récupération magnétique facile et recyclage des composites) qui peuvent offrir de nouvelles perspectives pour la dépollution industrielle, améliorer les rendements des traitements médicaux et faciliter le dosage des polluants. Des protocoles analytiques ont été ainsi développés en utilisant, dans la grande majorité, la spectrophotométrie UV-Visible car c'est une méthode très facile à prendre en main, rapide et non destructive des échantillons.

Dans le cadre de ma thèse, nous avons travaillé en collaboration avec différents laboratoires de recherche qui maitrisent certaines techniques d'analyse (DSA-IPHC), comportements moléculaires (LIMA), synthèse des molécules chélatantes (ICS). Nous avons aussi collaboré avec l'hôpital de Hautepierre à Strasbourg sur la problématique de captation des phosphates pour la dialyse péritonéale et avec la startup Mexbrain sur l'extraction du fer du cerveau.

Pour la captation du sodium et du fer, nous développerons des particules de silice mésoporeuse fonctionnalisées par des molécules portant des fonctions chélatantes et nous montrerons que la silice mésoporeuse peut se retrouver aussi à la surface de particules magnétiques permettant ainsi lors extraction facile des milieux pollués. Pour la captation des phosphates, nous utiliserons des nanostructures d'oxyde de fer de morphologie framboise, les phosphates s'adsorbant très facile à la surface de l'oxyde de fer. Dans le cas de la captation des HAP, nous développerons différents matériaux qui sont des potentiels bons candidats à des futures expériences de captation.

Objectifs

Chapitre II : Nanoparticules de silice mésoporeuse stellaire hautement chélatantes pour l'élimination spécifique du fer des milieux biologiques (article publié)

Des nanoparticules (**NPs**) de silice à large porosités (Stellate Mesoporous Silica **STMS**) ont été synthétisées par la méthode de Zhang[1]: un procédé sol-gel en présence d'un surfactant (CTATos). Cette synthèse nous permet d'obtenir des NPs d'environ 100 nm, avec une taille de pore ~15nm et une surface spécifique de 500 m²/g (Figure 1). Elles ont été fonctionnalisées avec la déferoxamine (**DFoB**), un chélatant spécifique du fer, pour la captation du fer dans des milieux biologiques comme le sang. Plusieurs modifications de surface de la silice sont nécessaires afin de greffer la DefoB sur la surface des NPs : 1) greffage de l'APTES ((3-Aminopropyl)triethoxysilane) qui conduit à la présence de fonction amine en surface, 2) greffage d'une molécule permettant d'avoir des fonctions acide carboxylique en surface 3) couplage de la DefoB.

Les analyses thermogravimétriques montrent que la perte de masse est liée aux différents ligands greffés à la surface de la silice et permet leur quantification (Figure 1). Grâce à ceci, la masse de chélatant greffé calculée est de 410 $\mu g_{DFoB}.mg_{SiO2}^{-1}$ (730 $nmol_{DFoB}.mg_{SiO2}^{-1}$). D'autres mesures comme le potentiel zêta au même pH montre une évolution en fonction des différents greffages et permet de confirmer les différents greffages. Les mesures granulométriques par DLS (dynamic light scattering) dans l'eau montrent la stabilité colloïdale des NPs et l'augmentation de leur diamètre hydrodynamique au fur et à mesure des différents greffages.
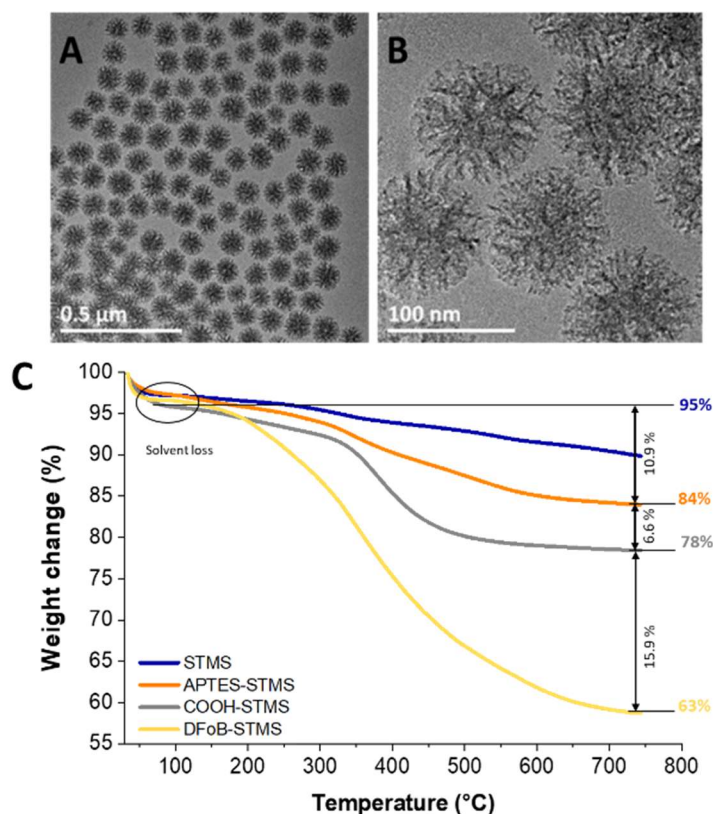

Figure 1 A) et B) Image MET des STMS. B) Analyse Thermogravimétrique des différentes étapes de greffage

Pour l'évaluation de la captation du fer par ces silices chélatantes, une analyse du fer par spectrophotométrie UV-Visible ou par ICP-AES a été faite selon les conditions expérimentales.

Pour les tests à pH 7, un protocole de mesure a été mis en place par spectrométrie UV-Visible car il se forme un complexe coloré (Fe+DFoB=FoB, λ_{max}=430 nm). Il est ainsi possible de tracer une droite d'étalonnage afin de doser le fer en solution, sans problèmes d'interférence liés à des interactions entre le solvant et le complexe qui présentent des bandes d'adsorption à des faibles longueurs d'onde (environ 200 nm).

Pour les études de captation du fer dans des conditions physiologiques, nous avons utilisé comme source de fer, un complexe de fer stable dans l'eau : le Fe-NTA (acide nitroacétique). Des composés tels que des chlorures de fer ne peuvent pas être utilisés car ils s'hydrolysent rapidement dans l'eau et de plus, dans le sang, le fer est généralement complexé à des protéines par exemple. Nous avons choisi un complexe de fer avec une constante de complexation relativement faible (log K_{FeNTA} = 6.0 à pH7.4 et log K_{FeNTA} ~15-16)[2]). La constante de complexation correspondante à la DFoB est : log $K_{Fe(III)DFoB}$ = 30[3]; pFe = 26.5, with pFe = -log[Fe]$_{free}$ pour [Fe]$_0$ = 10^{-6} M et [DFoB]$_0$ = 10^{-5} M à pH 7.4)[3,4].

Une étude de cinétique dans des conditions 0.85 : 1 FeNTA :DFoB montre que l'échange de ligands entre le Fe-NTA et les STMS@DefoB se fait en 30 minutes (valeur limitée par les contraintes expérimentales), les particules STMS@DefoB montrent une grande efficacité de captation (78.6 % avec une capacité de capture de 480 nmol$_{Fe}$·mg$_{SiO2}^{-1}$). Une étude sur les effets de la surface sur la captation a montré que jusqu'à une stœchiométrie 1 :1, les molécules de DFoB capte les ions de fer, pour un excès de fer par rapport aux DFoB greffés, les molécules de NH$_2$ (positivement chargées et liées aux APTES-SRMS), captent aussi le complexe FeNTA.
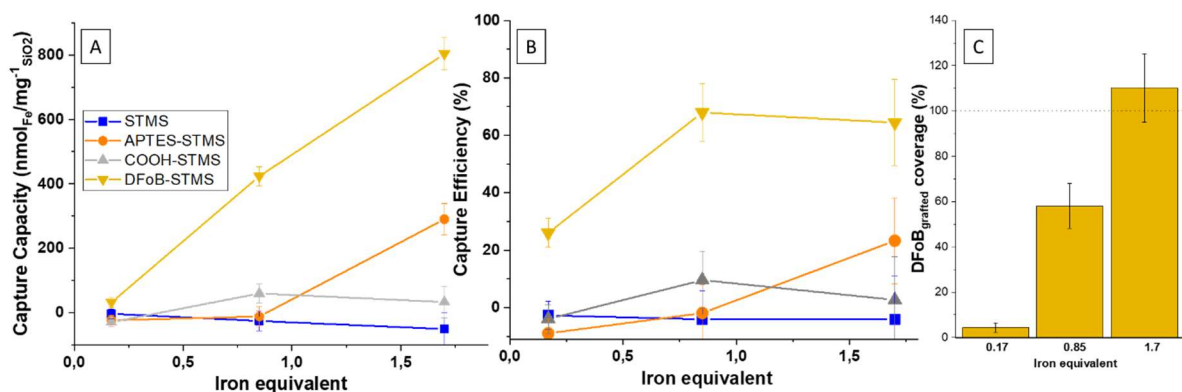

Figure 2 A. Capacité de capture et efficacité de capture des STMS (bleu) bleu), APTES-STMS (orange), COOH-STMS (gris) et DFoB-STMS (jaune) pour différents ratios FeNTA: DFoB greffés (0,17: 1, 0,85: 1 et 1,7: 1) avec un temps d'imprégnation de 30 minutes à 25 ° C, pH 7,4. C) La couverture représente le pourcentage de molécules DFoB occupées par les cations Fe3 +. L'expérience a été répétée trois fois.

Ces nanopartciules ont montré aussi une forte sélectivité lors de la caption de fer dans une solution contenant plusieurs ions. Dans une étude, la sélectivité de chélation du Fe (III) par rapport à d'autres cations d'intérêt biologique tels que Al^{3+}, Zn^{2+}, Cu^{2+}, Ca^{2+} ou Na$^+$ a été évaluée. En effet, le sang est un système complexe composé de nombreux ions métalliques essentiels au fonctionnement de l'organisme. L'idée principale est donc d'établir si les NP DFoB-STMS sont capables de capturer

sélectivement le fer (III) dans un environnement multi-éléments complexe. Deux milieux différents ont été utilisés pour démontrer que notre matériau peut capturer le fer sans autre perturbation ionique. La solution multi-éléments consistait en une solution contenant différents ions biologiques à la même concentration initiale, et l'expérience de la solution de Bracht consiste en une préparation qui imite la composition ionique du cerveau.

Pour la solution multi-éléments, la capacité de capture et l'efficacité de capture du fer sont plus faibles que dans les expériences précédentes car l'aluminium a également une constante de complexation élevée (même si pour FeDFoB la constante de complexation est plus élevée) conduisant à une capture du Al^{3+}. Les résultats ont montré une réduction de la capture du fer (capacité de capture 229 $nmol_{Fe3+} \cdot mg_{SiO2}^{-1}$ et efficacité de capture d'environ 44%). Concernant les autres ions (Na^+, K^+, Mg^{2+}, Ca^{2+} et Zn^{2+}) leur captation était moins importante, en accord avec une constante de complexation plus faible. Pour l'étude dans la solution de Barth, les valeurs de capacité de capture et d'efficacité (428 $nmol_{Fe3+} \cdot mg_{SiO2}^{-1}$ et 69%) sont conformes aux résultats des études cinétiques et stœchiométriques. Comme l'échantillon ne présentait pas d'aluminium au départ, un lien étroit pourrait être suggéré entre la capture du fer avec et sans présence d'aluminium, ce lien n'existait pas pour les autres ions dans les deux milieux différents.

Pour les investigations futures, nous devrons garantir la sécurité de ce traitement car l'élimination de certains autres ions pourrait être risquée. Par exemple, une élimination de sodium pourrait produire des problèmes cardiovasculaires sous forme d'épisodes d'hypotension.

Pour la recyclabilité, la captation (coordination) se fait à pH physiologique en utilisant le Fe-NTA comme source de fer, la décoordination du fer se fait en milieu très acide (pH 1), car le complexe FoB est moins stable sous ces conditions. Néanmoins les courbes de complexation/décomplexation ont été compliquées avec, à chaque cycle, plus de fer capté que relargué/décomplexé. L'hypothèse a été que la surface des silices ne portait pas que des molécules chélatantes mais aussi des fonctions ammonium de l'APTES ou COOH de la 2eme étape qui pouvaient interagir avec le fer. Nous avons réalisé des expériences de captation du fer sur les particules silice fonctionnalisées par les différentes molécules et nous avons pu montrer que le fer était bien capté par les particules fonctionnalisées par l'APTES. Notre hypothèse est donc qu'en plus de la complexation grâce à la DefoB, les fonctions amines qui n'ont pas pu être couplées captent le complexe Fe-NTA via des interactions électrostatiques. Pour la décoordination, un relargage d'environ 30% sur les 3 répétitions de fer préalablement capté a été possible. Un meilleur relargage du fer n'est pas envisageable car les NPs à ce pH s'agglomèrent et le fer qui est décoordiné ne peut pas diffuser, donc, lors du retour à pH physiologique, il est à nouveau capté par les NPs.

Conclusion.

Ces nanomatériaux pourraient également être appliqué dans la purification environnementale de fer. En effet, le fer est un micronutriment important. En ce qui concerne les êtres vivants, des niveaux élevés de fer causent des problèmes pathologiques, et dans les milieux aquatiques, le fer développe un excès d'algues qui peut affecter indirectement les espèces aquatiques. Par conséquent, l'excès de

fer peut également augmenter la mortalité dans les écosystèmes. Les nanobjets DFoB-STMS que nous avons développés ici, pourraient être utilisé comme moyen possible de dépolluer l'eau du fer. Cependant, un problème lors de l'application pourrait être la très petite taille de ces nanoparticules. De plus, la recollection à l'aide d'une centrifugeuse pourrait ne pas être facile à mettre en place à grande échelle. Afin de surmonter ces problématiques, nous avons montré que nous pouvons revêtir les RSN (hautement magnétiques) par une coquille de silice mésoporeuse qui devrait faciliter une manipulation magnétique de ces nanomatériaux.

Chapitre III : Greffage d'éther- couronne et de cryptand sur des nanoparticules de silice mésoporeuse stellaires pour une purification efficace et sélective du cation sodium

Dans ce travail, nous émettons l'hypothèse que de telles silices STMS fonctionnalisés avec de l'éther-couronne ou des cryptands pourraient contribuer efficacement à éliminer le sodium des environnements biologiques. Ainsi, nous avons réalisé dans une première approche le greffage de l'éther 15-couronne-5 (CE) sur STMS, et dans une seconde approche, du cryptand [2.2.1] (nommé cryptand221 et abrégé C_{221}). Les deux macrocycles sont bien connus pour leur capacité à se lier fortement aux cations sodium[14 ,15]. Ainsi, dans ce travail, nous présentons la stratégie chimique pour greffer efficacement CE et C_{221} à la surface du STMS. Le greffage de CE s'est avéré efficace par la méthode EDC (greffage : 223 $\mu g_{CE} \cdot mg_{SiO2}^{-1}$ qui correspond à $nmol_{CE} \cdot mg_{SiO2}^{-1}$). Contrairement, aux CE, le C_{221} n'a pas pu être greffé avec de l'EDC. D'autres essais ont été menés pour le couplage du C_{221} : EDC+NHS et HBTU. Afin de faciliter

Greffage des ether-couronne (CE) sur les STMS. Après la synthèse STMS et la fonctionnalisation APTES (décrite dans la partie précédente), le greffage de la couronne-éther portant des groupements carboxyliques a été réalisé sur la surface APTES-STMS via un couplage de type peptidique. Pour l'éther couronne, les fonctions acides sur les ligands ont été activées par l'agent activateur carbo-diimide EDC formant un produit intermédiaire réactif qui a réagi avec les fonctions amines sur la surface APTES-STMS. Comme on le voit ci-dessus, le ATG (figure 3.A) et le potentiel zeta (figure 3.B) ont donné des résultats similaires qui sont : 129 $\mu g_{APTES} \cdot mg_{SiO2}^{-1}$ et +16 meV, respectivement. De plus, la figure 3. C démontre que les suspensions CE-STMS présentent une bonne stabilité colloïdale avec une taille hydrodynamique moyenne d'env. 271 nm.
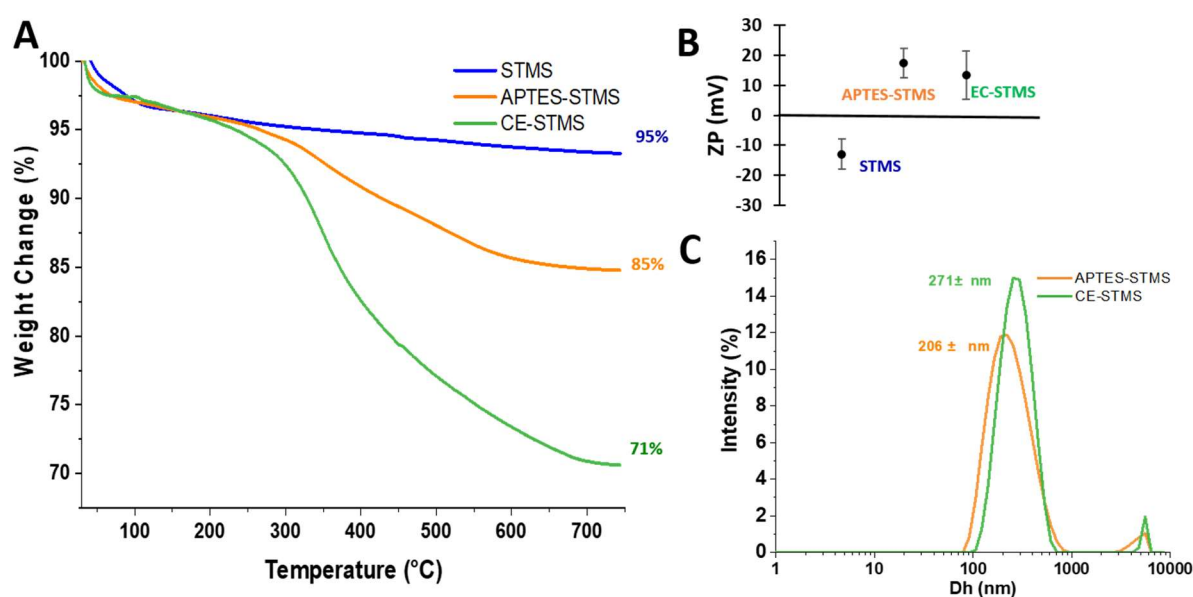

Figure 3. A. ATG et B. Potentiel zeta de STMS (bleu), APTES-STMS (orange), CE-STMS (vert) et C.Distribution de taille DLS d'APTES-STMS (orange) et CE-STMS (vert).

<u>Captation du sodium par les CE.</u> Nous avons testé la capture du sodium par le CE-STMS dans ce co-solvant (20:80) (log Ks_{Na-CE}=3.25[5])pour deux stœchiométries Na: EC 0,9:1 et 4,7:1. Les résultats présentés dans le tableau 1 montrent que la capture du sodium a été améliorée, passant d'une capture de capacité de 245 $nmol_{Na+}·mg_{SiO2}^{-1}$, pour la stœchiométrie Na: EC 0,9:1, à 1600 $nmol_{Na+}·mg_{SiO2}^{-1}$ pour Na: EC 4,7:1 (couverture des CE greffés de 25 et 216 %). Cela montre que le greffage de CE à la surface du STMS par rapport au CE libre n'affecte pas la capacité de chélater efficacement les cations sodium. Des expériences intéressantes dans un environnement cosolvant et un grand excès de sodium indiquent une occupation en Na de 216 % d'éther-couronne greffé, beaucoup plus que les sites d'occupation initiaux. Des interactions non-spécifiques avec la surface de la silice pourraient justifier cette captation.

Dans le but d'être plus réaliste pour les applications de DP, nous avons évalué la capture de sodium dans des solutions aqueuses à différents pH (pH = 7 et 5) et stœchiométries Na:CE (0,9:1 et 4,7:1). Nous avons trouvé dans l'eau pour des conditions de stœchiométrie 0,9:1 à pH = 7, seulement une capacité de capture de 28 $nmol_{Na+}·mg_{SiO2}^{-1}$ (correspondant à 2,8 % d'efficacité et à 3,7 % de couverture). Afin de déplacer l'équilibre de capture, les EC-STMS NPs ont été introduites dans une solution avec un excès de sodium plus important à une stœchiométrie Na:CE 4,7:1 à pH = 7, ce qui a conduit à une amélioration de la capacité de capture à 124 $nmol_{Na+}·mg_{SiO2}^{-1}$ (correspondant à 16.7 % de couverture de capture), dans une solution légèrement acide (pH 5) les résultats restent similaires (108 $nmol_{Na+}·mg_{SiO2}^{-1}$). En effet, la faible constante de complexation du sodium dans l'eau (log Ks_{Na-CE}=0.58)[5] expliquerait ces résultats.

<u>Le greffage du cryptand C_{221}</u> a été réalisé avec des stratégies similaires à celles de l'éther-couronne : nous avons cherché à créer une liaison peptidique entre la fonction carboxylique du C_{221} et l'amine des NH_2-STMS NPs. Pour cela, nous avons utilisé différentes stratégies : EDC et EDC-NHS.
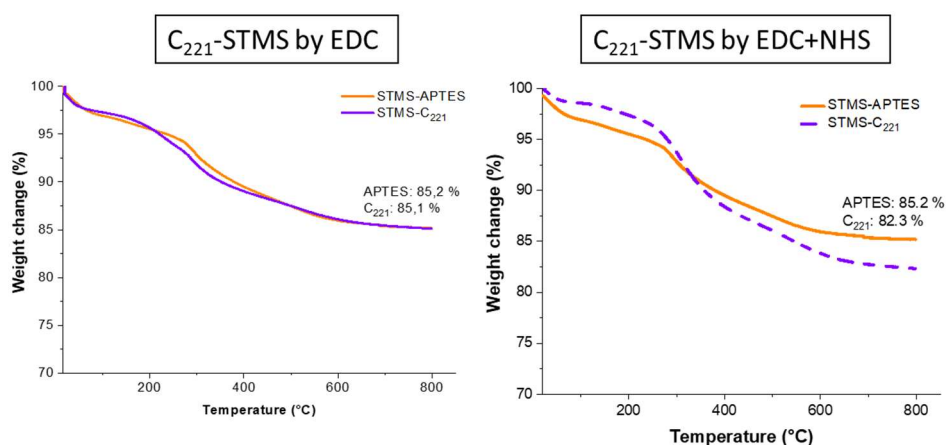

Figure 4. Analyse Thermogravimétrique des greffage de cryptand par EDC et EDC+NHS.

Comme pour les autres greffages, le greffage du C_{221} a été évalué par analyse thermogravimétrique (Figure 2, courbe violette pour le cryptand). Cette analyse a montré comme résultat : 1,2 $µg_{C221}·mg^{-1}_{STMS}$ (2,7 $nmol_{C221}·mg^{-1}_{SiO2}$) par la méthode EDC et 35 $µg_{C221}·mg^{-1}_{STMS}$ (80 $mmol_{C221}·mg^{-1}_{SiO2}$) par EDC+NHS. Pour comprendre ce faible greffage, nous pensons que comme le cryptand est une plus

grosse molécule que CE, elle a donc une plus grande contrainte stérique. Il est possible que les produits intermédiaires ne soient pas suffisamment stables dans le temps.

Pour améliorer le greffage, il faut un groupe intermédiaire peut-être plus stable, plus de fonctions amines à la surface du STMS, ou des fonctions avec plus de flexibilité (c'est-à-dire des chaînes carbonées plus longues).

Afin d'augmenter le nombre de groupements amine à la surface du STMS et augmenter la flexibilité des chaînes, nous avons modifié la fonction APTES par PEI: un polymère contenant des fonctions amines primaires et secondaires. De même, nous avons cherché à créer un intermédiaire de réaction qui soit encore plus stable : le HOBT.

Cette nouvelle stratégie de greffage montre un meilleur greffage. Le taux de greffage était d'environ 181 $\mu g_{PEI} \cdot mg_{SiO2}^{-1}$ (perte de poids de 79,6%) et d'environ 96 μg de C_{221} par mg de STMS (219 $\mu mol_{C221}.mg_{SiO2}^{-1}$). Le potentiel zêta valide les étapes critiques de la fonctionnalisation. Ces résultats sont parfaitement cohérents avec l'incorporation de groupements ammonium et de molécules non chargées (C_{221}). Enfin, le C_{221}-STMS a formé des suspensions colloïdales dans l'eau avec des diamètres hydrodynamiques de ca. 190 nm (figure 5.C). Cette stabilité colloïdale est très favorable pour la captation du sodium en milieu aqueux.
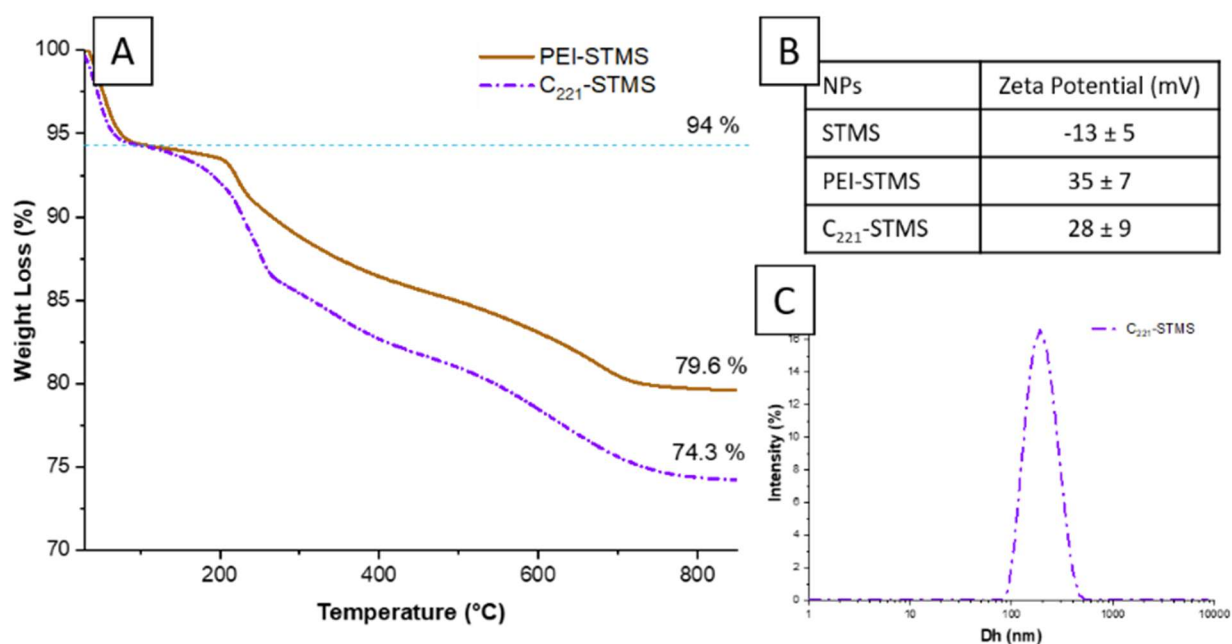

Figure 5. A) Analyse Thermogravimétrique du greffage du cryptand par HBTU (C221-STMS) et du PEI-STMS. B) Tableau du potentiel zéta de chacune des étapes du greffage et C) Granulométrie de l'échantillon C221-STMS. l'échantillon C221-STMS.

<u>Captation du sodium par les C_{221}.</u> Contrairement à l'étude avec les CE-STMS, des expériences avec C_{221}-STMS ont été réalisées directement dans l'eau. Comme pour les CE-STMS, pour démontrer les potentielles applications pour la dialyse péritonéale, nous avons évalué la capture du sodium dans des solutions aqueuses à différentes stœchiométries Na: C_{221} (0,9:1 et 4,7:1) et au même pH (pH 7).

Cette fois, dans l'eau pour des conditions de stœchiométrie 0,9:1, la capacité de capture a été trouvée à 34,1 $nmol_{Na+} \cdot mg_{SiO2}^{-1}$ (correspondant à 12,5% d'efficacité et à 15,5% de couverture). Dans le cas d'un excès de sodium plus important (Na: C_{221} 4,7:1), la capacité de capture est passée à 368 $nmol_{Na+} \cdot mg_{SiO2}^{-1}$ (correspondant à 26,2% d'efficacité et 168% de couverture cryptand). Par rapport aux résultats précédents de CE-STMS, le matériau contenant des cryptands est plus performant en stœchiométrie 0,9: 1 (Na: macrocyclegrafted). Cependant, pour l'expérience avec un excès de sodium (4,7 éq.) La capacité de capture est plus importante que prévu (168% de couvrance). Comme pour le système précédent, nous avons la capture du soidum par les macrocycles et une adsorption supplémentaire par d'autres parties des nanomatériaux. Pour voir une possible capture par NH2 de PEI-APTES, d'autres expériences seront améliorées. Enfin, ces derniers résultats sont supérieurs à ceux du CE-STMS dans les mêmes conditions. Il suggère le fort potentiel de ces nanomatériaux dans le traitement de dialyse péritonéale.
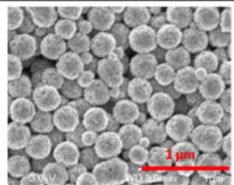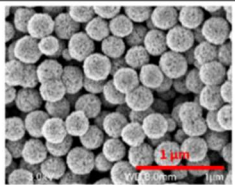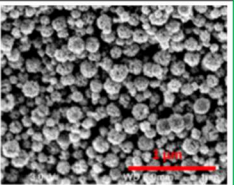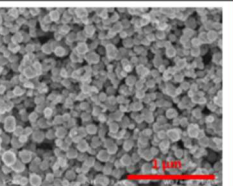
Conclusion

Suivant le même principe que pour le chapitre II, le chapitre III traite de la fonctionnalisation du STMS avec couronne-éther 15-5 (CE-STMS,) et cryptand [2.2.1] (C221-STMS). Avec ces résultats prometteurs, on peut imaginer greffer d'autres cryptands ou couronne-éther à la surface de STMS pour éliminer sélectivement d'autres cations en excès (comme le fer et le sodium) ou des éléments radioactifs dans d'autres applications telles purification dans l'environnement. En effet, il est également intéressant d'éliminer le sodium de l'eau buvable et éviter l'hypertension artérielle, les risques de maladie cardiaque ou d'accident vasculaire. Un autre sujet marquant concernant le sodium est le dessalement de l'eau de mer. En effet, les méthodes actuelles sont très coûteuses (osmose, membranes d'échange…) et peu efficaces. De plus, la pollution de l'eau des rivières, des lacs et les eaux souterraines, combinées à une explosion démographique exponentielle, provoquent un besoin urgent d'un nouveau source d'eau potable. Par conséquent, l'élimination du sodium devient un axe de recherche intéressant pour rendre potable l'eau de mer. Comme pour DFoB-STMS, CE-STMS et C221-STMS, le dessalement pourrait être un axe de recherche. Ces nanoobjets sont très sélectifs pour quelques éléments (sodium, calcium, potassium) et pourraient être utilisés dans grandes échelles. Néanmoins, nous ne pouvons pas omettre le coût élevé des cryptands comme facteur dissuasif supplémentaire (en plus des raisons précédentes déjà exposées).

Chapitre IV : Étude de l'amélioration de la capture du phosphate dans le processus de dialyse péritonéale à l'aide de nanostructures d'oxyde de fer

La synthèse des nanostructures d'oxyde de fer de morphologie framboise (RSN) est une synthèse solvothermale-polyol en autoclave qui nous permet d'obtenir des agglomérats contrôlés (environ 300 nm) de nanocristaux partageant des orientations cristallographiques. Elles présentent un comportement superparamagnétique avec une aimantation à saturation largement supérieure à celle des mêmes nanocristaux isolés (non agrégés). Cette forte aimantation facilitera leur extraction magnétique de divers milieux (eaux usées, boues, …). Le but est d'obtenir une grande surface spécifique afin de pouvoir capter le maximum de phosphates à pH physiologique en conservant une aimantation élevée.

Lors des premiers travaux de synthèse dans l'équipe « NPs fonctionnalisées », des RSN de diamètre moyen 250 nm constituées de nanograins de 5 nm ou 25 nm suivant le temps de réaction ont été obtenues selon les conditions de synthèse décrites dans la référence.[6] Lors du début de ma thèse, en reprenant ces conditions, nous avons obtenu des résultats différents selon l'origine commercial du chlorure de fer hydraté utilisé. Les résultats et les différents pots utilisés sont résumés dans le tableau suivant.

Table 1. Taille moyenne des cristallites (déduite des motifs DRX) et diamètre moyen du RSN en fonction du précurseur de fer utilisé et des images MEB représentatives de la synthèse.

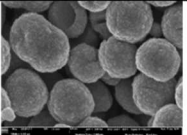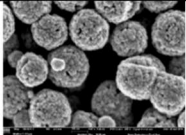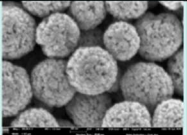| Brand and lot	Sigma-1	Alfa Aesar-1	Alfa Aesar-2	Acros Organics-1
RSN size (nm)	291±52	296±35	157±42	~100
Grain size (nm)	38±7	26±6	30±6	27±9
Crystallite size (nm)	32.4	19.9	20.2	25.4
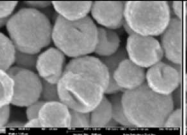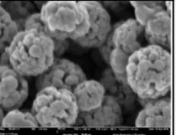
La synthèse est donc dépendante du fournisseur de $FeCl_3.6H_2O$ ou encore de la date d'ouverture du pot (effet de vieillissement). Différentes analyses non concluantes ont été faites sur les différents pots afin de mettre en évidence une pollution ou dégradation. Notre hypothèse est que les réactifs de fer seraient plus ou moins hydratés mais cela a été difficile à mettre en évidence. Des études sur l'hydrolyse de nos chlorures de fer ont été menés et ont permis de conclure qu'un stockage non optimal change le degré d'hydratation des molécules ce qui modifie son comportement lors de la synthèse.

Ensuite, nous avons eu aussi des problèmes lors des synthèses avec notamment la formation de carbonates. Ces carbonates se formaient surtout lors des essais de dopage de l'oxyde de fer par du cobalt ou Zn. Une collaboration avec un laboratoire coréen m'a permis de comprendre que le temps

de mélangeage des réactifs avant de lancer la synthèse hydrothermale était important : un temps de mélangeage/solubilisation de 24 h au lieu de 3 h permet d'éviter la formation de carbonates.

Pour travailler dans des conditions de synthèse reproductibles, un nouveau pot de chlorure de fer a été commandé et stocké sous les meilleures conditions. Le tableau suivant résume les conditions de synthèse testées ainsi que les résultats des différentes conditions de synthèse.

Table 2. Synthèse RSN des expériences avec 3 ou 24 h de mélange et 6 ou 10,5 heures de temps de réaction.

Mixing Time	3h			24h	
Experimental Time (200°C)	5h	6h	10h30	6h	10h30
SEM					
RSN Size (nm)	~280	~266	317	~320	~310
Grain Size (nm)	/	24.4	28.5	36.5	42.6
Specific Surface Area (m²/g)	13.8	27.2	29.6	18.9	17.8

En analysant le tableau, nous observons une dépendance de la taille de grains avec le temps de mélange : plus il est long, plus les tailles de grains seront grandes pour un même temps de réaction. En ce qui concerne le temps de réaction : pour les 3 heures de mélange, nous observons une dépendance de la taille des RSN et donc, de la surface spécifique en fonction du temps de réaction, néanmoins, après les 24h de mélange, cette dépendance n'est plus observable. Suite à ces résultats, afin d'obtenir la plus grande surface spécifique pour la captation, le temps de mélange idéal est de 3h avec un temps de réaction de 10h30.

<u>Dopage à l'aluminium.</u> L'aluminium s'est révélé être un élément dopant approprié pour améliorer l'élimination du phosphate. Cependant, l'aluminium est un élément non magnétique et ainsi, pour garder la possibilité de décanter magnétiquement, les RSN en oxyde de fer seront dopés avec un faible pourcentage d'aluminium. Le dopage des nanostructures de magnétite avec de l'aluminium devrait être plus facile qu'avec du Zn et du Co car leur rayon ionique est assez proche et leur valence est la même (+3).

Pour le processus de dopage, nous avons utilisé un temps de réaction de 10,5 heures et un temps d'agitation de trois heures. Trois rapports Fe: Al ont été testés. L'image MEB (figure 6) présentent des nanostructures avec la morphologie d'un RSN non dopé mais une large distribution de taille est observée avec un diamètre moyen de 269 ± 45 nm pour le dernier échantillon. De plus, il y a eu une préservation de la structure spinelle d'oxyde de fer sans la présence de certaines autres phases. On remarque que les pics sont plus larges pour les RSN à haute teneur en Al suggérant une perte de cristallinité ou des cristallites plus petites. Le paramètre de réseau (a=8.389 Å) est inférieur à celui observé habituellement avec RSN non dopé mais confirmerait l'insertion d'aluminium dans la structure spinelle. La taille de cristallite calculée est de 19,5 nm, ceci suggère que le dopage à l'aluminum conduit

à une plus petite taille de cristallite. La plus grande surface spécifique mesurée pour cet échantillon (40 m²/g) a confirmé la plus petite taille de nanograin d'Al-RSN par comparaison avec RSN non dopé. La courbe d'aimantation à 300 K est caractéristique d'un comportement superparamagnétique et l'aimantation à saturation (Figure 10. D 64 emu·g^{-1} pour Al-RSN) est inférieure à celle du RSN non dopé confirmant le dopage de la magnétite par Al et les résultats précédemment rapportés de autres groupes.[7–9]

D'après ces résultats, l'Al-RSN semble être un matériau prometteur pour adsorber les phosphates et appliqué dans le traitement de dialyse péritonéale. Ce matériau peut être attiré par un aimant et possède une surface spécifique plus grande que RSN (40 vs 27 m²/g).
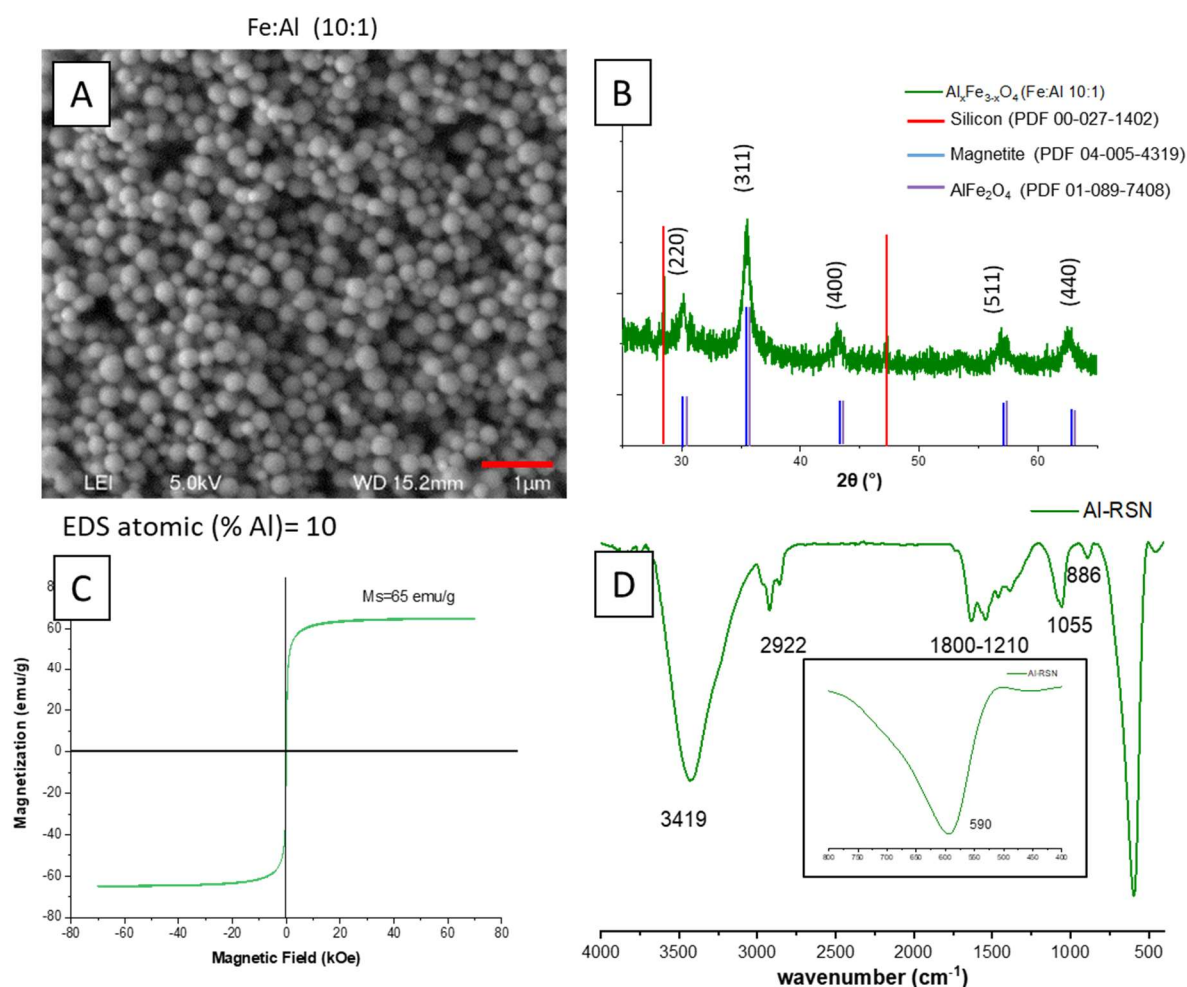
Figure 6. A) Images MEB d'Al-RSN; B) XRD difractogramme, C) spectres FTIR et D) courbe de magnétisation de Al-RSN à 300K.

Captation des phosphates. Nous avons suivi le protocole de dosage du phosphate par spectroscopie UV-Vis mis en place par le Dr. Daou[9] dans sa thèse. Un complexe appelé bleu de molybdène, coloré bleu (λ_{max}=680 nm) est formé et il est ensuite possible de tracer une droite d'étalonnage afin de doser le phosphate en solution. Deux droites d'étalonnage ont été tracées : une dans l'eau et une deuxième dans la solution de dialysat pour la DP.

Ici, nous avons adapté notre système à une étude faite par le Dr. Toufic Jean DAOU à pH 3 sur des nanoparticules d'oxyde de fer synthétisées par coprécipitation (taille : 40 nm ; surface spécifique : 30 m²/g)[10] pour la captation et le dosage de l'ion phosphate. Afin de comparer ces résultats à ceux obtenus avec nos RSN, nous avons travaillé dans l'eau à pH 3, pH 7 (pour les applications biomédicales), et dans la solution de dialysat à pH 7.

Les résultats montrent que la captation phosphate à pH 3 (8,8 P-mg/g) est supérieure à celle à pH7 (résultat en accord avec l'étude de Daou en 2007[10]). En plus ces RSN permettent de capter plus de phosphate qu'avec les NPs de Daou et al.[10] Néanmoins, il faut travailler à pH 7 pour les applications biomédicales : dans l'eau et dans le dialysat, nous obtenons les mêmes valeurs à saturation (4,1 P-mg/g).

Une étude sur les phosphates en surface des RSN montre qu'à pH 7 (eau et solution de dialyse), toute la surface de RSN n'est pas recouverte de phosphates (66% de la surface). Ceci est en accord avec des interactions électrostatiques moins favorables entre le phosphate et la surface d'oxyde de fer. De la même manière, à pH 3, la surface est recouverte de plus de phosphates (143% de couverture). Avec autres nanomatériaux d'oxyde de fer, on a observé une couverture partielle ou complète de la surface à tout pH avec des valeurs comprises entre 27 et 207%.[10–14]

Vu ces résultats très prometteurs, nous avons cherché à développer un deuxième système en dopant les RSN avec de l'aluminium (Al-RSN) afin d'augmenter la capacité de captation de phosphates.

En comparaison avec les RSN, les Al-RSN à pH 7 et 3 permettent une meilleure capture dans les mêmes conditions. Pour ces nanomatériaux, une adsorption maximale à pH 3 de 15,5 P-mg·g^{-1} a été mesurée, ainsi qu'à pH 7, l'adsorption maximale est de 10 P-mg·g^{-1}. Afin de comprendre l'effet du dopage à l'aluminium, la couverture maximale attendue a été calculée et comparée à la réelle. La plupart des études rapportées ont montré une couverture partielle de la surface (11-18%)[9,15,16]. A pH 7, les RSN dopées à l'aluminium ont une couverture de surface de 165% à pH 3 et de 106% à pH 7. La couverture des phosphates à pH 7 et à pH 3, est plus élevée avec Al-RSN qu'avec RSN. Ces résultats confirment que le dopage par Al de RSN permet d'améliorer la capture des phosphates.

Finalement, le dopage Al augmente la surface spécifique du RSN et également la capture du phosphate. Le dopage en aluminium modifie les propriétés de surface (c'est-à-dire, le point isoélectrique) ce qui contribue à améliorer la captation. Ainsi, l'adsorption de phosphate plus élevée d'Al-RSN est possible car ces nouvelles nanostructures ont un point isoélectrique et une surface spécifique plus élevés que le RSN. Une implication possible des atomes d'Al de surface dans la phosphatation n'est pas à exclure.
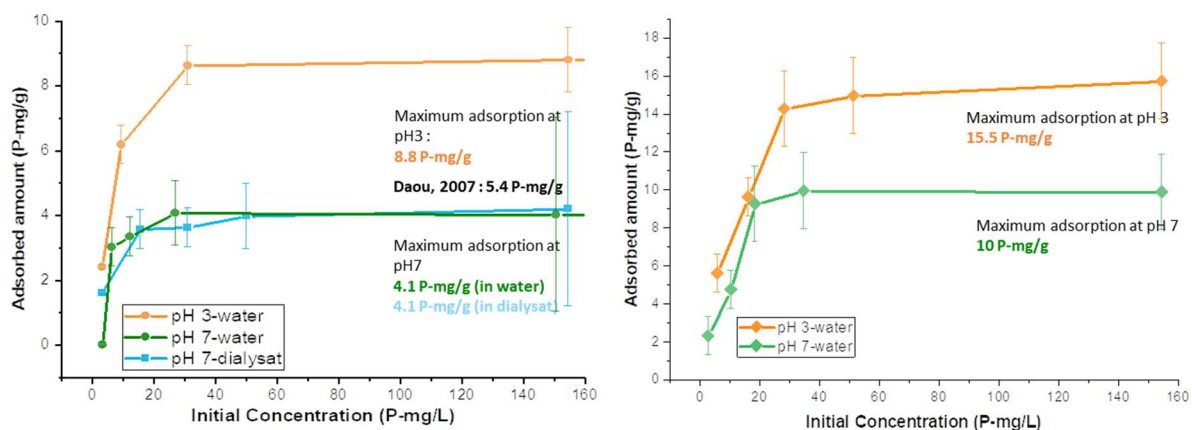
Figure 4 Isothermes d'adsorption des RSN et Al-RSN à pH différent (3 and 7) dans l'eau ou dans une solution de dialyse.

Conclusion

Dans le chapitre IV, nous avons traité les différents problèmes des phosphates dans le sang. Dans la première partie, nous avons optimisé la synthèse de RSN et RSN dopés avec Zn, Co et Al. Nous avons montré les enjeux de la synthèse RSN en mettant en évidence l'influence de l'origine et du vieillissement du précurseur de fer: une hydratation du précurseur a été démontré, de plus, son effet sur la taille du RSN et sur le mécanisme de synthèse du RSN. Autres paramètres se sont avérés cruciaux lors de la synthèse : le temps de mélange pour dissoudre les réactifs et le temps de réaction. Après le contrôle des paramètres expérimentaux, nous nous sommes concentrés sur la synthèse de RSN afin d'obtenir la plus grande surface spécifique.

Le dopage au Zn a été difficile dans nos conditions expérimentales en raison certainement d'un problème de dissolution du précurseur de zinc. D'autres précurseurs de zinc doivent être testés. Le dopage au cobalt a été réalisé en agissant sur le temps de mélange du réactif. Le dopage par Al était facile en raison des caractéristiques communes entre les ions Al et Fe mais Al diminue la magnétisation du RSN et donc une faible teneur en Al est nécessaire.

Dans la deuxième partie du chapitre IV, nous avons montré le potentiel de nos deux matériaux à éliminer les phosphates dans la dialyse péritonéale. Pour cela, nous avons montré que les deux matériaux peuvent éliminer une grande quantité de phosphates en moins de 3 heures. De plus, le dopage aluminium augmente la surface spécifique RSN et décale le point isoélectrique. Ceci améliore les interactions électrostatiques entre les phosphates déprotonés et la surface protonée de l'oxyde de fer RSN. Par conséquent, une capacité d'élimination du phosphate plus élevée a été observée avec Al-RSN. Un modèle *in vitro* de la dialyse péritonéale a été construit et des tests préliminaires avec les RSN ont été effectués. Désormais, il serait intéressant de tester dans cet appareil Al-RSN pour la capture de phosphate ainsi que C_{221}- STMS pour la capture de Na.

Outre ces expériences, nous pouvons observer que même si nous présentions les phosphates comme un problème de santé, le phosphate est l'une des biomolécules les plus importantes, et est impliquées dans un large nombre de réactions métaboliques. Néanmoins, à forte concentration, les phosphates

peuvent causer de graves dommages à l'écosystème et au corps humain. En effet, le progrès et le développement constants des domaines de l'agriculture et de l'industrie, augmenter la quantité de phosphate libéré dans la nature, d'où la quantité d'eaux usées. Une fois déchargé dans les lacs, les rivières ou toute autre source d'eau naturelle, les dommages sont causés à la fois à l'environnement et indirectement à la santé humaine. Par conséquent, un tel Al-RSN pourrait également être testé pour la dépollution des phosphates.

Chapitre V : Conception de matériaux composites cœur-coquille (RSN@STMS)

Afin de faciliter l'élimination de la silice mésoporeuse stellaire fonctionnalisée (STMS) de n'importe quel milieu, la stratégie pourrait être d'apparier STMS avec un composé magnétique. En effet, nous avons montré dans le chapitre précédent que les nanostructures en forme de framboise (RSN) affichent une aimantation à saturation élevée et un comportement superparamagnétique qui est essentiel pour assurer une bonne stabilité colloïdale de la suspension RSN. Pour pouvoir extraire des STMS facilement fonctionnalisés à partir de milieux liquides, nous avons étudié le revêtement de RSN par une coque de silice mésoporeuse et ainsi conçu un matériau composite core@shell (RSN@STMS). Dans un premier temps, nous avons examiné les méthodes de revêtement MS développées pour les nanoparticules d'oxyde de fer (IONP), puis sélectionné une méthode pour réaliser des revêtements de silice.

A partir des méthodes rapportées, une bonne stabilité colloïdale du RSN est obligatoire pour assurer un revêtement de silice homogène et nous allons donc enduire le RSN de citrates (assurant une stabilité colloïdale par interactions électrostatiques). Concernant la stratégie de revêtement du RSN, nous avons également décidé de mettre une première couche de revêtement de silice non poreuse pour protéger le RSN des milieux (acides, corrosifs…). Ensuite, une deuxième couche de silice mésoporeuse a été choisie pour assurer une grande surface spécifique. Pour cette dernière étape, deux stratégies sont possibles en accord avec les résultats rapportés précédemment : la première est le « oil-in-water »[17] et la seconde, le « Stöber modifié » avec CTAB.[18] Nous avons décidé déposer la coquille MS suivant le procédé «oil-in-water» car cette stratégie présente plusieurs avantages qui sont une modification aisée de la taille des pores et un protocole expérimental simple.

Lors des expériences, le dépôt d'une coquille de silice condensée synthétisée autour des RSN citratées est un processus reproductible. En effet, le revêtement a été réalisé plusieurs fois, et à chaque synthèse, une coquille de silice a été observée par TEM (figure 5). La coque de silice est une couche très fine pas toujours bien visible et présente une épaisseur moyenne d'environ 10 nm.

Contrairement à la synthèse STMS précédemment rapportée, ici, la coquille mesoporeuse MS a été synthétisée grâce à un template organique. L'agitation magnétique ne peut pas être appliquée dans notre cas car les RSN sont très sensibles à un champ magnétique statique externe et ils s'agrégeraient sous l'effet de l'aimant d'agitation. Les images TEM des particules composites ainsi obtenues sont présentées sur la figure 5. Les images RSN @ nSiO2 @ STMS montrent la présence d'une coquille de silice régulière autour des RSN simples et autour des agrégats de 2 RSN. La couche de silice est considérée comme une silice mésoporeuse « radiale » car les pores partent principalement de la surface du RSN.
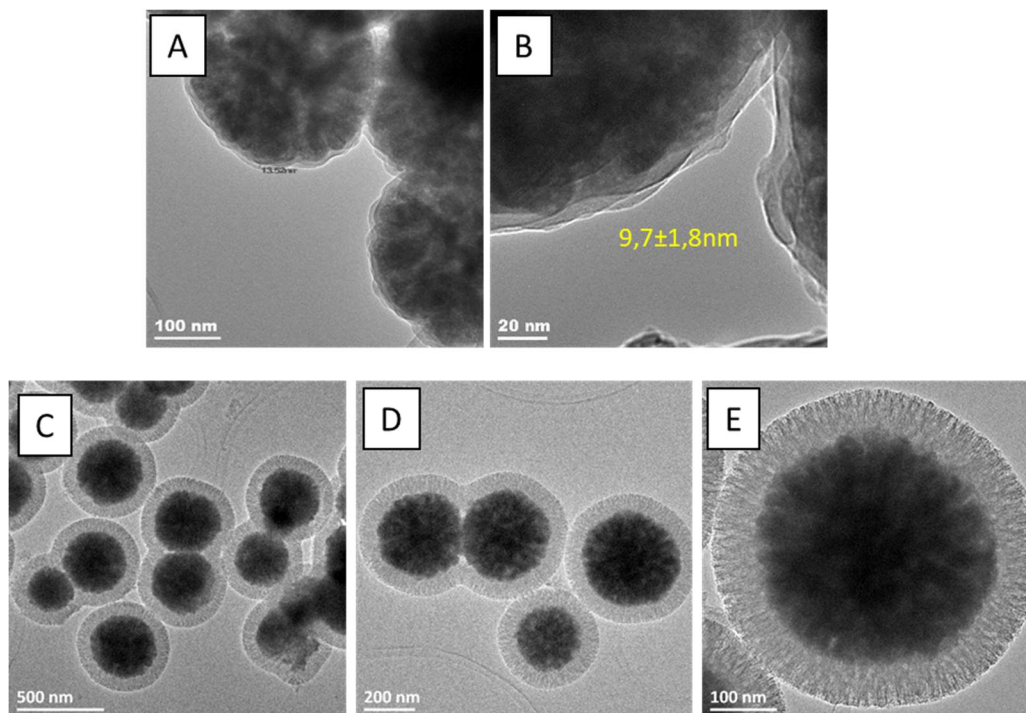
Figure 5. A. B. Images TEM de la coque de silice non poreuse à la surface du RSN (RSN@nSiO2). C. D. E. Images TEM de RSN@nSiO2@STMS.

Pour conclure, il a été possible de synthétiser un nanomatériau composite constitué d'un noyau magnétique en oxyde de fer présentant une aimantation à forte saturation et recouvert de deux coquilles de silice a été réalisée. La reproductibilité du revêtement de silice condensée (RSN @ nSiO2) a également été réussie grâce à un prétraitement des RSN avec du citrate trisodique pour améliorer leur stabilité colloïdale. Pour la coque de silice mésoporeuse, l'approche «oil-in-water» permet d'obtenir la morphologie et la structure des pores appropriées de la silice (grands pores orientés radialement) et peut ainsi être utilisée pour d'autres expériences de dépollution.

Dans ce dernier chapitre, nous nous sommes d'abord concentrés sur « l'optimisation » de ces nanomatériaux pour applications environnementales uniquement. Les nanocomposites cœur-coquille RSN @ SiO2 ont été conçus pour augmenter la taille des anciens STMS fonctionnalisés (pour pouvoir les appliquer dans des projets environnementaux) et faciliter leur extraction magnétique des médias. L'idée est d'adapter les protocoles de greffage précédents sur ces nouveaux systèmes pour greffer différents ligands spécifiques pour éliminer d'autres métaux ou molécules toxiques.

Chapitre V : Conception de nanomatériaux pour l'élimination des perturbateurs endocriniens des milieux liquides

Nous nous sommes intéressés à la conception de nanocomposites pour capturer les perturbateurs endocriniens. Aujourd'hui, une définition claire et universelle reste fortement soumise à la bonne volonté des autorités (telles que l'Organisation mondiale de la santé (OMS), le programme international sur la sécurité chimique (IPCS) ou le Parlement européen). Pour ce travail, nous avons conservé la dernière définition adoptée en Europe (juin 2016). Une substance est un perturbateur endocrinien si i) Il a des effets néfastes sur la santé humaine. Ii) Il agit sur le système hormonal.

Comme nous l'avons résumé dans le schéma 2, le vrai danger de la dysfonction érectile est qu'elle imite le rôle des hormones réelles dans les récepteurs hormonaux, ce qui provoque une mauvaise réponse des cellules. Ces réponses erronées se traduisent par des réponses à des moments inappropriés ou la modulation des niveaux du gène. Enfin, nous nous sommes concentrés sur l'élimination des hydrocarbures aromatiques polycycliques (HAP), un groupe de perturbateurs endocriniens. En fait, les HAP présentent des cycles aromatiques. Ces aromatiques présentent un grand intérêt car ils peuvent favoriser l'interaction π-stacking entre les molécules de HAP et les matériaux fonctionnalisés, pour ceci, nous avons choisi le graphène.

Dans cette étude, nous avons fonctionnalisé la silice STMS avec du triméthoxy (2-phényléthyl) silane (STMS @ TMOPES), les RSN ont été enduits de polydopamine (RSN@PDA) et d'acide tannique (RSN@TA), et enfin, nous avons cherché à déposer ces RSN sur des couches de graphène (FLG@RSN). Le choix du ligand pour tester la capture des HAP a été motivé grâce aux travaux d'Orm sur l'élimination des HAP.[19]

Dans ce travail, nous cherchons à ajouter des propriétés magnétiques au graphène. Les propriétés magnétiques intéressantes du RSN permettront une récupération par décantation magnétique. De plus, par hyperthermie magnétique, ces nanoclusters chauffent de manière macroscopique ce qui pourrait permettre de casser ces liaisons π-π pour réutiliser les nanocomposites. La synthèse de ces nanostructures a déjà été rapportée pour des applications de supercondensateurs.[20,21]

Les images SEM de la figure 9. A et B ont montré RSN sur les feuilles de graphène (FLG@RSN). Les RSN ont une taille de 324 ± 40 nm. On peut observer une distribution relative homogène de RSN sur les feuilles de graphène. Cela pourrait laisser suffisamment de place aux molécules pour interagir avec le graphène.

La figure 5. C montre également la décantation magnétique de ce matériau. En fait, nous avons précédemment essayé de séparer le graphène de l'eau / méthanol. Ces expériences montrent la grande difficulté de centrifuger le matériau, par conséquent, l'ajout de propriétés magnétiques grâce au RSN est très intéressant pour d'autres expériences.
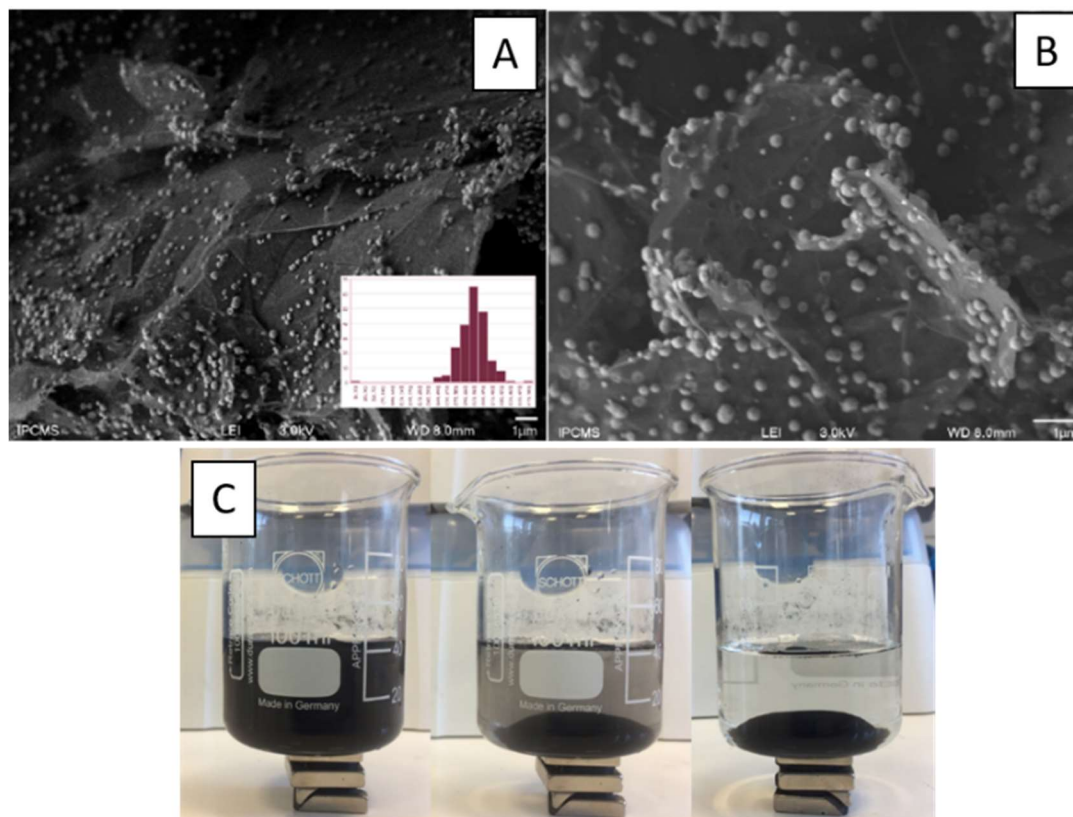

Figure 6. A et B. Images MEB des FLG@RSN. C. Effet d'un aimant sur une solution contenant les nanomatériaux à différents temps.

2 mg et 4 mg de FLG@RSN ont été dispersés dans une solution initiale de naphtalène dans l'eau. L'analyse des résultats montrent une captation d'environ 100%. Cependant, sur les spectres UV, on remarque également une bande à 200 nm qui chevauche un peu la bande à 260 nm. Plusieurs groupes ont rapporté le spectre UV-Vis du graphène dans l'eau et, étonnamment, la bande en dessous de 250 nm dans nos spectres est similaire à celle du graphène. Probablement, le surnageant contenait des traces « invisibles » de FLG @ RSN qui ont modifié l'analyse spectrophotométrique UV-Vis. Dans ce cas, la bande de graphène chevauche celle du naphtalène. Pour confirmer la présence de FGL dans le surnageant, d'autres méthodes analytiques seront nécessaires.

Le résultat de l'expérience dans le méthanol montre une capacité de capture de 7,80 $nmol_{naphtalène} \cdot mg^{-1}_{FLG@RSN}$ (1 $\mu g_{naphtalène} \cdot mg^{-1}_{FLG@RSN}$), 5,15 $nmol_{naphtalène} \cdot mg^{-1}_{FLG@RSN}$ (0,66 $nmol_{naphtalène} \cdot mg^{-1}_{FLG@RSN}$) et 1,87 $nmol_{naphtalène} \cdot mg^{-1}_{FLG@RSN}$ (024 $nmol_{naphtalène} \cdot mg^{-1}_{FLG@RSN}$) pour des solutions de 2, 4 et 8 mg de naphtalène dans le méthanol respectivement. La quantité de matériaux composites a une influence surprenante : l'augmentation de la quantité de matériau réduit la capacité de capture du matériau. Elle pourrait se justifier par d'éventuelles interactions d'empilement π-π entre les feuilles de graphène qui réduisent

la surface de capture ou par les interactions entre l'acide tannique à la surface des feuilles. Quoi qu'il en soit, ces premiers résultats préliminaires confirment la possibilité de capturer le naphtalène avec FLG@RSN.

Conclusion

Pour cette partie, nous avons greffé à la surface de particules STMS et de RSN, des molécules conçues pour éliminer les hydrocarbures aromatiques polycycliques (HAP), molécules hautement polluantes. Pour cela, nous avons choisi molécules capables de créer des interactions π-stacking entre les molécules greffées et les HAP. La sélection molécules étaient TMOPES pour STMS et polydopamine et acide tannique pour RSN. Nous avons également combiné graphène et RSN pour l'élimination des HAP le graphène devrait capturer les HAP et le RSN magnétique devrait assurent une élimination facile du composite de l'eau grâce à leurs propriétés magnétiques. Les premiers tests avec le naphtalène étaient encourageants et le système doit encore être optimisé. Cependant, ces résultats sont une preuve de principe du fort potentiel de ces matériaux pour d'autres projets de dépollution.

En outre, d'autres groupes ont montré les capacités de l'oxyde de graphène à interagir avec les phosphates et ainsi les composites FLG@RSN seraient intéressants à tester pour la déphosphatation. Sur la base de ces résultats, notre le FLG@RSN synthétisé pourrait trouver des applications intéressantes dans le traitement de dialyse péritonéale et la dépollution des phosphates.

Conclusions générales

L'objectif de cette thèse était de développer de nouveaux matériaux fonctionnels hautement performants et, si possible, recyclable pour l'élimination du fer, du phosphate et du sodium des milieux biologiques (sang).

Depuis plusieurs années, l'élimination des molécules et des ions se concentre principalement sur l'environnement applications à des fins de purification. Des processus d'élimination similaires pourraient, en théorie, également être utilisés dans le domaine médical science. En effet, il existe plusieurs problèmes concernant les problèmes de purification dans le corps humain. Ces problèmes ont des origines différentes : maladie génétique, dysfonctionnement des organes, problèmes endocriniens, erreurs de médication ou surconsommation de ces molécules / minéraux. Selon le taux de surdosage, l'âge du patient et l'élément, les conséquences ne sont pas les mêmes. Quand pour un, l'excès se traduit par des courbatures et des douleurs, pour l'autre, cela peut être dramatique ou mortel. Grâce à nos connaissances en conception de nanoparticules et fonctionnalisation, nous avons proposé l'application de particules d'oxyde de fer de morphologie en forme de framboise et nanoparticules de silice mésoporeuses étoilées pour améliorer les traitements médicaux et surtout pour purifier le sang des éléments toxiques. Pour assurer une purification médicale spécifique, leur conception a été optimisée. Dans ce cadre, la fonctionnalisation de surface, la taille et la composition chimique ont été ajustées afin d'obtenir des matériaux qui pourrait être adapté dans les traitements médicaux pour la purification du sang.

Nous avons ciblé trois éléments toxiques en excès dans le sang : le fer, le sodium et les phosphates. Avec le nanocomposites nouvellement conçus, nous cherchons à améliorer deux traitements médicaux différents visant à extraire ces éléments à rendement élevé et contrôlé : chélatothérapie (fer) et dialyse péritonéale (sodium et phosphate).

Références

(1)   Zhang, K.; Xu, L.-L.; Jiang, J.-G.; Calin, N.; Lam, K.-F.; Zhang, S.-J.; Wu, H.-H.; Wu, G.-D.; Albela, B.; Bonneviot, L.; Wu, P. Facile Large-Scale Synthesis of Monodisperse Mesoporous Silica Nanospheres with Tunable Pore Structure. *J. Am. Chem. Soc.* **2013**, *135* (7), 2427–2430.

(2)   Elhabiri, M.; Carrër, C.; Marmolle, F.; Traboulsi, H. Complexation of Iron(III) by Catecholate-Type Polyphenols. *Inorganica Chimica Acta* **2007**, *360* (1), 353–359.

(3)   Farkas, E.; Enyedy, É. A.; Csóka, H. A Comparison between the Chelating Properties of Some Dihydroxamic Acids, Desferrioxamine B and Acetohydroxamic Acid. *Polyhedron* **1999**, *18* (18), 2391–2398.

(4)   Evers, A.; Hancock, R. D.; Martell, A. E.; Motekaitis, R. J. Metal Ion Recognition in Ligands with Negatively Charged Oxygen Donor Groups. Complexation of Iron(III), Gallium(III), Indium(III), Aluminum(III), and Other Highly Charged Metal Ions. *Inorg. Chem.* **1989**, *28* (11), 2189–2195.

(5)   Dishong, D. M.; Gokel, G. W. Crown Cation Complex Effects. 16. Solvent Dependence of the 15-Crown-5 and 18-Crown-6 Equilibriums with Sodium Cation. *J. Org. Chem.* **1982**, *47* (1), 147–148.

(6)   Gerber, O.; Pichon, B. P.; Ihiawakrim, D.; Florea, I.; Moldovan, S.; Ersen, O.; Begin, D.; Grenèche, J.-M.; Lemonnier, S.; Barraud, E.; Begin-Colin, S. Synthesis Engineering of Iron Oxide Raspberry-Shaped Nanostructures. *Nanoscale* **2016**, *9* (1), 305–313.

(7)   Aghazadeh, M.; Karimzadeh, I.; Reza Ganjali, M.; Malekinezhad, A. Al3+ Doped Fe3O4 Nanoparticles: A Novel Preparation Method, Structural, Magnetic and Electrochemical Characterizations. *Int. J. Electrochem. Sci.* **2017**, *12*, 8033–8044.

(8)   Ehsani, M. H.; Esmaeili, S.; Aghazadeh, M.; Kameli, P.; Tehrani, F. S.; Karimzadeh, I. An Investigation on the Impact of Al Doping on the Structural and Magnetic Properties of Fe3O4 Nanoparticles. *Appl. Phys. A* **2019**, *125* (4), 280.

(9)   Xu, J.; Luu, L.; Tang, Y. Phosphate Removal Using Aluminum-Doped Magnetic Nanoparticles. *Desalination and water treatment* **2017**, *58*.

(10)   Daou, T. J.; Begin-Colin, S.; Grenèche, J. M.; Thomas, F.; Derory, A.; Bernhardt, P.; Legaré, P.; Pourroy, G. Phosphate Adsorption Properties of Magnetite-Based Nanoparticles. *Chem. Mater.* **2007**, *19* (18), 4494–4505.

(11)   Yoon, S.-Y.; Lee, C.-G.; Park, J.-A.; Kim, J.-H.; Kim, S.-B.; Lee, S.-H.; Choi, J.-W. Kinetic, Equilibrium and Thermodynamic Studies for Phosphate Adsorption to Magnetic Iron Oxide Nanoparticles. *Chemical Engineering Journal* **2014**, *236*, 341–347.

(12)   Zeng, L.; Li, X.; Liu, J. Adsorptive Removal of Phosphate from Aqueous Solutions Using Iron Oxide Tailings. *Water Research* **2004**, *38* (5), 1318–1326.

(13)   Lalley, J.; Han, C.; Li, X.; Dionysiou, D. D.; Nadagouda, M. N. Phosphate Adsorption Using Modified Iron Oxide-Based Sorbents in Lake Water: Kinetics, Equilibrium, and Column Tests. *Chemical Engineering Journal* **2016**, *284*, 1386–1396.

(14)   Ajmal, Z.; Muhmood, A.; Usman, M.; Kizito, S.; Lu, J.; Dong, R.; Wu, S. Phosphate Removal from Aqueous Solution Using Iron Oxides: Adsorption, Desorption and Regeneration Characteristics. *Journal of Colloid and Interface Science* **2018**, *528*, 145–155.

(15)   Li, M.; Liu, H.; Chen, T.; Wei, L.; Wang, C.; Hu, W.; Wang, H. The Transformation of α-(Al, Fe)OOH in Natural Fire: Effect of Al Substitution Amount on Fixation of Phosphate. *Chemical Geology* **2019**, *524*, 368–382.

(16)   Sousa, A. F. de; Braga, T. P.; Gomes, E. C. C.; Valentini, A.; Longhinotti, E. Adsorption of Phosphate Using Mesoporous Spheres Containing Iron and Aluminum Oxide. *Chemical Engineering Journal* **2012**, *210*, 143–149.

(17)   Xiong, L.; Bi, J.; Tang, Y.; Qiao, S.-Z. Magnetic Core–Shell Silica Nanoparticles with Large Radial Mesopores for SiRNA Delivery. *Small* **2016**, *12* (34), 4735–4742.

(18)   Yang, P.; Quan, Z.; Hou, Z.; Li, C.; Kang, X.; Cheng, Z.; Lin, J. A Magnetic, Luminescent and Mesoporous Core–Shell Structured Composite Material as Drug Carrier. *Biomaterials* **2009**, *30* (27), 4786–4795.

(19)   Bou Orm, N. Nano-Matériaux Hybrides Pour l'élimination de Micro-Polluants Organiques (HAP) Dans Les Effluents Aqueux. These de doctorat, Lyon 1, 2012.

(20)   Pardieu, E.; Pronkin, S.; Dolci, M.; Dintzer, T.; Pichon, B. P.; Begin, D.; Pham-Huu, C.; Schaaf, P.; Begin-Colin, S.; Boulmedais, F. Hybrid Layer-by-Layer Composites Based on a Conducting Polyelectrolyte and Fe3O4 Nanostructures Grafted onto Graphene for Supercapacitor Application. *J. Mater. Chem. A* **2015**, *3* (45), 22877–22885.

(21)   Gerber, O.; Bégin-Colin, S.; Pichon, B. P.; Barraud, E.; Lemonnier, S.; Pham-Huu, C.; Daffos, B.; Simon, P.; Come, J.; Bégin, D. Design of Fe3–XO4 Raspberry Decorated Graphene Nanocomposites with High Performances in Lithium-Ion Battery. *Journal of Energy Chemistry* **2016**, *25* (2), 272–277.

École doctorale
Physique, chimie-physique | ED 182
Université de Strasbourg

Paula DUEÑAS RAMÍREZ

Ingénierie de nanocomposites recyclables pour l'élimination de polluants

Résumé

Les nanoparticules d'oxyde de fer et de silice retrouvent aujourd'hui des nombreuses applications dans différents domaines grâce aux propriétés magnétiques, leur surface spécifique et leur biocompatibilité. Ce projet de thèse comporte des recherches de captation de métaux ou des molécules dans différentes situations. Le fil conducteur de ces projets est l'amélioration de traitements qui cherchent à extraire certains éléments (métaux ou molécules) qui ne peuvent pas être évacués naturellement et qui continue en circulation : l'excès de fer pour le traitement de l'hémochromatose, excès de sodium et de phosphates pour l'amélioration de la dialyse péritonéale, ainsi que des nombreuses perspectives de dépollution environnementale et la captation des hydrocarbures aromatiques polycycliques (HAP),une famille de perturbateurs endocriniens.

Mots-Clefs : Nanoparticules magnétiques, nanoparticules de silice, dépollution, fer, sodium, phosphate, hémochromatose, dialyse péritonéale, HAP.

Résumé en anglais

The iron oxide and silica nanoparticles found today many applications in different fields thanks to the magnetic properties, their specific surface area and their biocompatibility. This thesis project involves research on the capture of metals or molecules in different situations. The common thread of these projects is the improvement of treatments which seek to extract certain elements (metals or molecules) which cannot be evacuated naturally and which continue in circulation: excess iron for the treatment of hemochromatosis, excess of sodium and phosphates for the improvement of peritoneal dialysis, as well as many perspectives of environmental depollution and uptake of polycyclic aromatic hydrocarbons (PAH), a family of endocrine disruptors.

Keywords: Magnetic nanoparticles, silica nanoparticles, depollution, iron, sodium, phosphate, hemochromatosis, peritoneal dialysis, PAH.